The Design of Complex Intermetallic Structures or:

How I Learned to Stop Worrying and Love Chemical Frustration

By

Gordon G. C. Peterson

A dissertation submitted in partial fulfillment of

the requirements for the degree of

Doctor of Philosophy

(Chemistry)

at the

UNIVERSITY OF WISCONSIN-MADISON

2020

Date of final oral examination: 02/25/2020

The dissertation is approved by the following members of the Final Oral Committee:

Daniel C. Fredrickson, Professor, Chemistry
Mark Ediger, Professor, Chemistry
Thomas Brunold, Professor, Chemistry
Kyoung-Shin Choi, Professor, Chemistry

The Design of Complex Intermetallic Structures or:

How I Learned to Stop Worrying and Love Chemical Frustration

Gordon G. C. Peterson

Under the supervision of Professor Daniel C. Fredrickson

At the University of Wisconsin-Madison

Since the advent of automated diffractometers and area detectors, the work time required to collect and produce a crystallographic model from a dataset of reflections and intensities has been reduced from upwards of a few years to just a few hours. Yet despite this technological leap, both methods ultimately yield a simple Fourier map, giving the magnitudes and locations of electron densities within a unit cell, but offering no chemical insight into the forces underlying their arrangement. Intermetallics, compounds formed form a mixture of metallic elements, show a particularly wide diversity of structural features, suggesting that multiple complicated factors govern their formation. The equally impressive variety of applications for intermetallics as superconductors, permanent magnets, thermoelectrics, catalysts, and super-hard materials (among many others) drives the desire to develop new intermetallic compounds, as well as a conceptual framework for understanding the origins of their assembly.

In this thesis, we discuss how chemical frustration can help us understand the forces controlling intermetallic structure and guide the discovery of new structurally complex phases. Here, we consider the chemical frustration of a ternary chemical system to be analogous to the geometrical frustration of three antiferromagnetically paired spins at the corners of an equilateral triangle. This model suggests that because each pair of elements has a preferred of bonding arrangement, space within a ternary crystal

structure must be divided into immiscible domains based on different binary bonding schemes. The fusion of these domains into a single structure is paramount to the intergrowth concept, which views each domain as a fragment of a structurally-related parent phase. In such a system, the geometrical arrangements necessary for both domains to cohabitate a single unit cell naturally lead to complicated structural features.

Why, then, do domains choose to intergrow at all? Phase segregation into two separate binary compounds would appear to solve the problems of merging incompatible bonding domains, and yet many intergrowths are experimentally observed. We view the answer to the problem through the lens of the Hume-Rothery rules for solids, which state that three factors can promote stability in intermetallics: electron count, atomic size effects, and electronegativity effects.

In the following Chapters of this thesis, we will explore each of these effects, and how they act to enable the formation of the elaborately structured phases presented in this work. First, we describe the chemical frustration idea in detail, elaborating upon the three computational techniques we will use to test our insight into the stabilizing effects born from the Hume-Rothery rules. In Chapter 2, we go on to specifically explore how electron counts stabilize the structure of $Fe_{14}Pd_{17}Al_{69}$, leading to the electron-hole matching method for inducing complexity in intermetallics. Next, we see how the formation of the intergrowth subnitride $Mn_{39}Si_9N_x$ detailed in Chapter 3 is facilitated by the favorable epitaxy between intermetallic Mn-Si domains and N-centered octahedra. Finally, in Chapter 4 we present the synthesis and structure of $Ca_3Cu_{7.8}Al_{26.2}$, and investigate how a combination of electron count, atomic size, and electronegativity effects combine to enable a reaction between the binary parent compounds $CaAl_4$ and $CuAl_2$.

To my English-teacher parents, who told me to do science.

Acknowledgments

When I left home for the first time to move to Ithaca, it was one of the hardest times of my overall very pleasant life. I doubted myself, felt like I didn't belong, and strongly considered leaving more than once during my first semester. Eventually, I made a home, and grew to love Cornell and the friends I had made there, which had the unfortunate side effect of making it challenging yet again to leave Ithaca behind and uproot to Wisconsin. Now, after my five and a half years in Madison, the bittersweet feeling of moving away from all the people I've connected to here in favor of the greener bayous of Houston strikes again with renewed and unique vigor. First and foremost, I want to thank all my friends from Buffalo, Ithaca, and everywhere along the way for showing me that distance and a change of scenery is not the same as moving on, and thank you to my friends in Madison who have made graduate school one of the best times of my life. To all of you, I humbly ask that we never change.

Arriving in Madison in 2014, I was pretty sure I wanted to join a properties-focused materials group, which I'm sure would have been a lovely Ph.D. experience through and through. Though it was on my list, I was not initially planning on joining Danny's group; I wanted to try something different than I had in my undergraduate research with Stephen Lee, who is by all accounts an incredible teacher and a wonderful person. As it turns out, Danny is also, by all accounts, a phenomenal teacher, passionate scientist, charismatic extraordinaire, and all-around wonderful person, and through our interactions in classes, group meetings, casual office digressions, and painstakingly meticulous revisions of formal manuscript, I believe I have learned true appreciate for a clean diffraction pattern, a converged calculation, proper use of hyphens, and all seven seasons of *Star Trek: The Next Generation*. To Danny, thank you for your lessons, your mentorship, your wisdom, and your patience.

It's weird going from the youngest member of a research group to the oldest: watching everyone age and leave until suddenly you're somehow supposed to be the expert and find a job or something. The ten generations of Fredrickson Group members that I have had the pleasure to work with have offered more support, friendship, insight, and comradery over the years than I could ever hope to articulate in text, although I would be remiss to not try. To Rie, Brandon, Kale, Yiming, Vince, Anastasiya, and Katie, thank you for welcoming me into the group with blank stares when I neglected to tell you that I had joined, for your endless patience re-teaching me the how to use VASP every time I forgot to delete POSCAR element line, and for a willingness to sit through most of *Wizard People, Dear Reader* on any given Saturday. To Leland and Hillary, thank you for the long nights spent together in the computer and Argonne National labs, respectively, for the years spent learning and growing together, and most importantly for your friendship during the transition into graduate school and beyond. To Erdong, Kendall, Mary, Amber, Keyu, Kyana, Jonathan, Brandon-2, Danica, Emmett, Yuanzuo, Alex, Dan, Ken, Scott, Cheng, and Yueai, thank you for the time you have donated editing manuscripts, rescheduling meetings, and listening to practice talks to help me finish this thesis these past few crazy months, and thank you for developing so quickly into wonderful young scientists. It has made me feel old and realize it's time to go.

Finally, thank you to my family. To my grandmother, aunts, uncles, cousins, in-laws, and everyone else connected to Stow, Ohio or Lewiston, Idaho, thank you for asking me to describe intermetallics at Thanksgiving not because of its scientific merit but simply because you care. To Sarah, thank you for your endless supply of love, support, and roasted Brussels sprouts. To my parents, thank you for everything. I aspire to be you more like you every day.

Table of Contents

List of Figures

Chapter 1.

Chapter 2.

Chapter 3.

List of Tables

Appendix B.

Chapter 1.

Introduction

1.1 Intergrowth Phases in Intermetallics

A foundational principle of chemistry states that, in the long term, all chemical systems tend towards an energetic minimum.[1] This is especially true in the solid state, where most synthetic techniques tend to yield thermodynamically stable products, and metastable phases are long-lived due to the physical constraints of a crystal lattice.[2] It is then, perhaps, a surprise to see such a remarkable diversity of crystalline structure as is exhibited by these compounds in such a way that cannot be simply explained by the classical notions of hard sphere atomic packing. This variety of structure is a hallmark of intermetallics, those compounds formed from a combination of transition metal elements, and defines their simultaneously wide range of physical properties[3] such as thermoelectrics,[4-7] superconductivity,[8-10] magnetism,[11-16] magnetocaloric effects,[17,18] and superhardness,[19,20] while also supporting near infinite possibilities for stoichiometry, crystal system, and atomic arrangements, making connections between structure and properties uniquely challenging to draw.

The central research goal of the Fredrickson group is to bridge this gap by helping to develop chemically intuitive conceptual frameworks that further our ability to understand the driving forces

underlying the formation of intermetallic compounds. One potential avenue to this end is seen through an examination of some of the most complex intermetallic structures, which can be viewed as built from a combination of multiple distinct bonding arrangements. For example, Figure 1.1 shows the structure of Nb_3Al_2C,[21] which contains tetrahedrally close-packed (tcp) regions of $Al@Nb_{12}$ icosahedra (pink) joined through shared triangular faces with domains of C-centered Nb octahedra. The ternary phase is entirely constructed from these two motifs, with Nb-Al interactions spatially separated from the structure's C atoms, segregating the two domains even within the same structure.

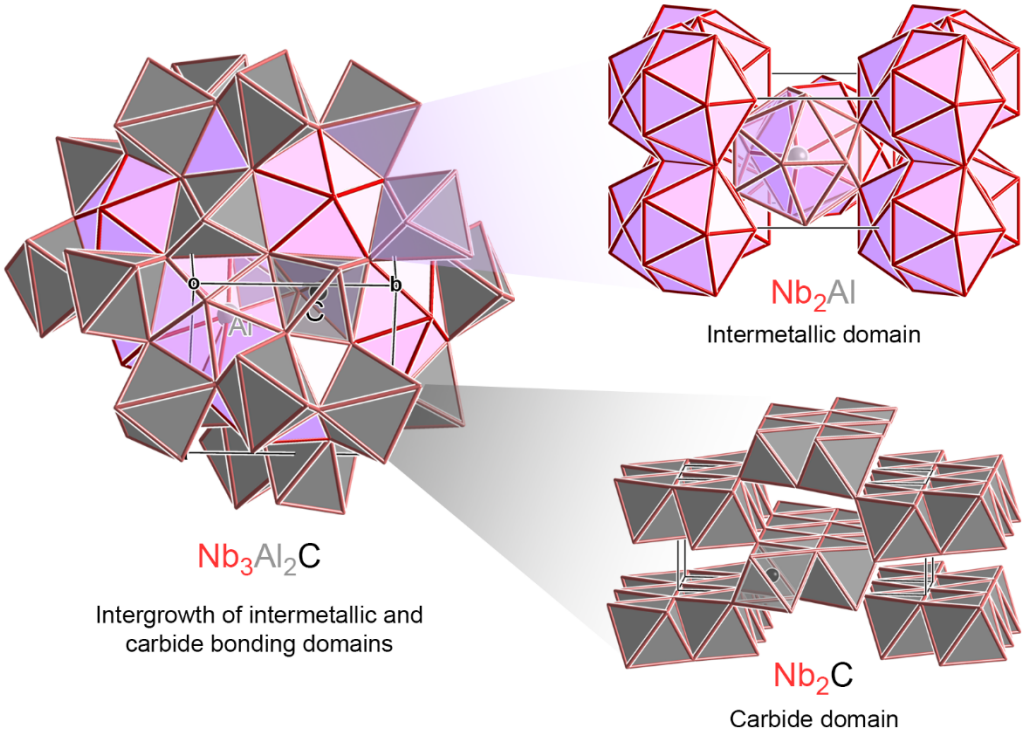

Figure 1.1. The intergrowth concept, as observed in Nb_3Al_2C, which has distinct separation of tetrahedrally close-packed intermetallic domains (pink) and octahedral carbide domains (gray).

Perhaps more intriguingly, these two structural motifs are intimately connected to Nb_2Al and Nb_2C binary structures found nearby on the phase diagram.[22,23] Nb_2Al is built from analogous Al-centered Nb

icosahedra to those in Nb_3Al_2C; in fact this tcp arrangement is often seen in T-E intermetallic phases (T = transition metal, E = main group metal). Nb_2C, on the other hand, is constructed of layered C@Nb_6 octahedra (like those that decorate the tcp surface in Nb_3Al_2C), in line with the preference of C atoms for an octahedral coordination environment seen in other metal carbide phases.[24,25] We can therefore consider the structure of Nb_3Al_2C to be an arrangement of tcp and octahedral structural fragments drawn from the parent binaries Nb_2Al and Nb_2C, respectively. We can thus identify Nb_3Al_2C as an intergrowth phase.[26,27] The intergrowth concept is a useful tool for analyzing the structure of ternary intermetallics, and begins to hints at a reason behind their complexity.

1.2 The Chemical Frustration Model

The impetus to synthesize complex intermetallics is motivated not only by their structural intrigue, but by the observation that desirable properties can sometimes be correlated to unit cell size and disorder.[28] As intergrowth phases are naturally more complex than their parent binaries, they are desirable synthetic targets in this regard, and some have been shown to exhibit a combination of properties born from their parent binaries, suggesting the potential for tunable and multifunctional materials.[29,30] Methods for inducing intergrowth in crystalline structure are therefore at a premium, and the correlation between complexity and the coexistence of competing bonding types is leveraged for materials design through the chemical frustration model.

The concept of chemical frustration can be drawn analogous to the geometrical frustration within an antiferromagnetically ordered triangle of atoms, as shown in Figure 1.2a.[31] When placed at the corners of an equilateral triangle, only two of the three atomic contacts can favorably pair antiferromagnetically at

one time.[32] Extending this idea to an example ternary system, T-Ni-P, we can represent the phase diagram by yet another triangular arrangement. Each edge of this phase diagram contains binary phases with a preferred bonding scheme; for example, we might observe intermetallic bonding arrangements in a T-Ni binary phase, whereas Ni-rich phosphide phases, such as Ni_2P, are largely based on the tiling of tricapped P-centered trigonal prisms.[33] In a hypothetical ternary phase combining all three elements in the middle of the triangle then, the system is stuck trying to conjoin these incompatible bonding domains within the same unit cell.

An overview of reported structures, however, does reveal two compounds which manage to beautifully integrate metallic T-Ni and phosphide Ni-P domains into a single ternary structure, shown in Figure 1.2b. The $Mo_2Ni_6P_3$ structure contains the familiar tricapped trigonal prisms of Ni_2P, while also building columns of a $MoNi_4$-like face-centered cubic (fcc) domain that runs along **b**.[34] $Zr_2Ni_{12}P_7$, on the other hand, merges columns of P-centered tricapped trigonal prisms with pseudo-hexagonal fragments of a $ZrNi_{3.5}P_{1.5}$ motif evoking the $CaCu_5$ structure,[35] one of the most common structure types for rare-earth containing intermetallics.[36,37] In this way, these structures illustrate how intergrowth structures are able to blend two dissimilar bonding domains, while simultaneously maintaining the preferred coordination environments from each binary parent structure.

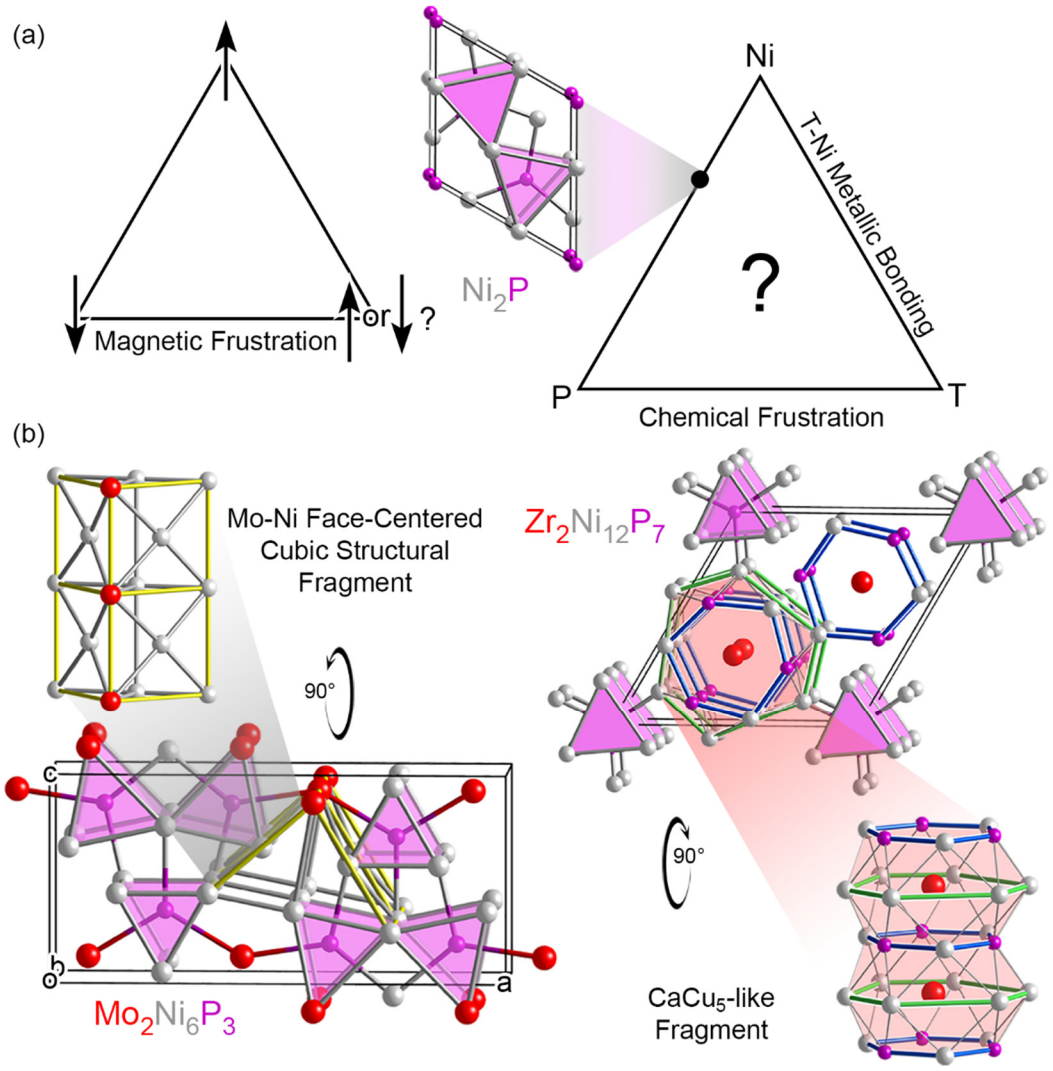

Figure 1.2. The chemical frustration model, illustrated for the T-Ni-P system (T = transition metal). (a) The similarities between the concepts of geometrical frustration in a magnetic system and chemical frustration in a ternary phase diagram. (b) The ternary T-Ni-P phases $Mo_2Ni_6P_3$ and $Zr_2Ni_{12}P_7$, which exhibit domains of the Ni_2P structure intergrown with domains of face-centered cubic $MoNi_4$ and $CaCu_5$-type $ZrNi_{3.5}P_{1.5}$, respectively.

1.3 Methods to Induce Chemical Frustration

Just because a structure *can* increase complexity through intergrowth, it may not necessarily be favorable. In fact, basic "like dissolves like" chemical intuition would tell us that, rather than mesh incompatible bonding domains within a single structure, a compound should simply prefer to segregate

into distinct phases that can each occupy their desired arrangement unperturbed. Yet, again and again we see ternary structures form in complicated intergrowth arrangements; what forces could be acting to stabilize such a product? Understanding what such factors act to stabilize such structures could suggest useful synthetic and theoretical tools for the creation and prediction of complex intermetallics.

To answer this question, we can draw some inspiration from the rules for solid solutions proposed by William Hume-Rothery in 1931.[38] These state that the ability of solids to favorably mix with each other is based on the compatibility of three key factors: atomic size, valence electron count, and electronegativity. Though these rules were intended to apply to the mixing of elements within a solid solution, we can extend them to intermetallic systems where they give us a chemically intuitive starting point evaluating the forces stabilizing solid state structure. In particular, if these three factors govern the favorability of mixing two elements together in a solid solution, the same could be true for two domains within an intergrowth structure.

1.3.1 Chemical Pressure and Epitaxial Stabilization

Previous work in the Fredrickson group has, in fact, made great headway into analyzing the effects of these factors on the structures of intermetallics.[39-41] Starting with atomic size, we have developed a model for the analysis of chemical pressure (CP), a calculation performed by finding the change in energy of a structure relative to the change in volume, and dividing up the subsequent pressure map into pairwise atomic interactions.[36,41,42] This CP method is a powerful tool that can be used for the visualization of the atomic packing strains between individual atoms in a crystal structure. An example CP scheme is shown for Ni_2P in Figure 1.3a, where the calculated chemical pressures have been plotted as atom-centered

spherical harmonics. In this plot, black lobes correspond to negative pressures, where contacts are overly long and the structure would prefer to shorten the interatomic distance, such as those seen along Ni-Ni contacts in the Ni_2P CP scheme. The white lobes between Ni and P atoms, on the other hand, indicate positive pressures, where distances are too short and lengthening of the contact is preferred. The size of each lobe corresponds to the magnitude of the pressure along that direction, and we can see that the opposing pressures of the Ni_2P CP scheme hold the structure in balance against one another; the Ni-Ni contacts cannot shorten without also contracting the already too short Ni-P distances.

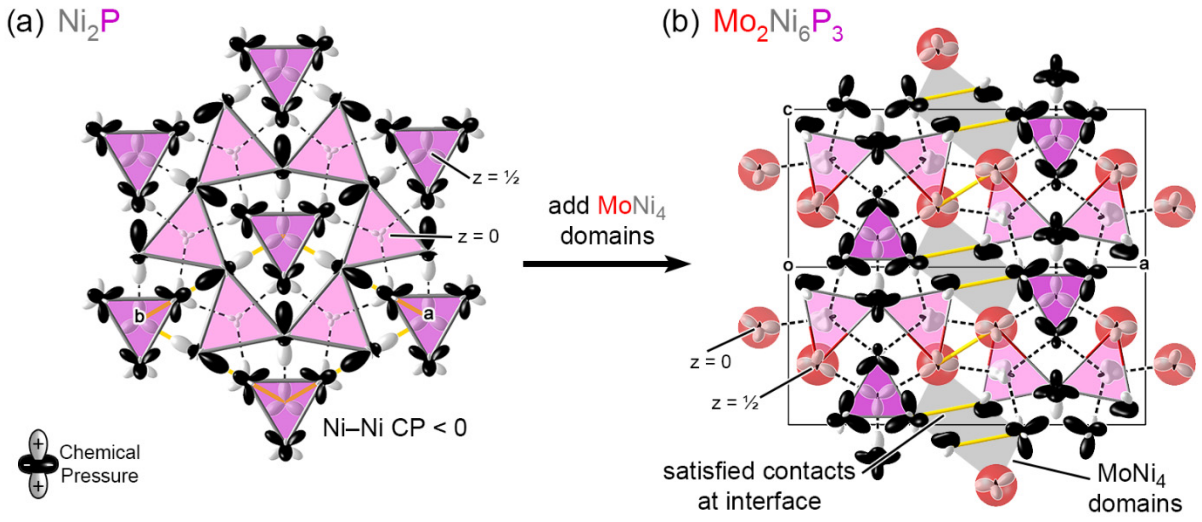

Figure 1.3. Epitaxial stabilization as a mechanism for the stabilization of $Mo_2Ni_6P_3$. The negative Ni-Ni chemical pressures shown at the interfaces of the Ni_2P and $MoNi_4$ domains (yellow contacts) in $Mo_2Ni_6P_3$ are relieved relative to the Ni-Ni interactions in Ni_2P, helping to stabilize the intergrowth of these domains. (adapted from Warden, H. M. *Proposal Narrative* **2018**)

Chemical pressure schemes are at their most useful, however, when used to compare the strain of atomic packing between related structures. In Figure 1.3b, the CP scheme of $Mo_2Ni_6P_3$, the intergrowth structure formed through insertion of fcc-like domains of $MoNi_4$ into the Ni_2P structure is shown. While the pressures within the Ni_2P-like domains of the ternary structure still show similar pressure features to

those of the binary, we can see in this scheme that the CPs of atoms at the interfaces between Ni_2P and $MoNi_4$ domains in the structure are very small, indicating that the strains in their atomic packing have been satisfied through intergrowth. The relief of interfacial chemical pressure trough the intergrowth of bonding domains with complementary chemical pressure schemes, dubbed epitaxial stabilization, is one method for creating complex intermetallic structures that can be generalized through CP analysis.

1.3.2 Valence Electron Counting and the 18−*n* rule

The valence electron count of an intermetallic phase provides an additional Hume-Rothery inspired factor for controlling structure, offering another factor to leverage for inducing chemical frustration and intergrowth. This strategy applies especially well to T-E intermetallics, such as in the CaF_2-type structure of $NiSi_2$, where the summation of 10 electrons from the Ni atom and 8 electrons from the two Si atoms indicates a stable 18-electron configuration on the Ni atom.[43,44] In most T-E compounds, however, adherence to the 18-electron rule is not quite so straightforward; in CsCl-type CoAl, for example, there are only a total of 12 electrons per Co atom, 6 electrons short of a full configuration. However, as Figure 1.4 shows, the Fermi level for the CoAl structure falls into a pseudogap in the density of states curve, indicative of electronic stability.

To rationalize this inconsistency, we turn to the reversed approximation Molecular Orbital method,[45] which uses linear combinations of filled delocalized crystal orbitals to reconstruct target atomic orbitals within a crystal structure. Targeting the valence 4s, 4p, and 3d orbitals for CoAl, we can see on the right side of Figure 1.4 that we are able to reproduce their characteristic shapes, although six of these orbitals (highlighted in red), cannot be entirely localized to the central Co atom, and show significant density on

neighboring Co and Al atoms. This indicates that, while these orbitals are filled, they are supported through bonding interactions with neighboring Co atoms that are bridged by Al squares, isolobal to a sp^3d^2 σ-bond. From this, we can conclude that the Co atoms in CoAl are in fact reaching an 18-electron configuration, but doing so by creating six shared isolobal Co-Co bonds, analogous to a C atom reaching a filled octet in a molecular compound by making four covalent connections. This idea outlines the basis for the 18–*n* rule, where main group metal-rich T-E compounds are expected to be electronically stable when the structure contains 18–*n* electrons per T atom, with *n* equal to the number of isolobal T-T bonds formed.[46]

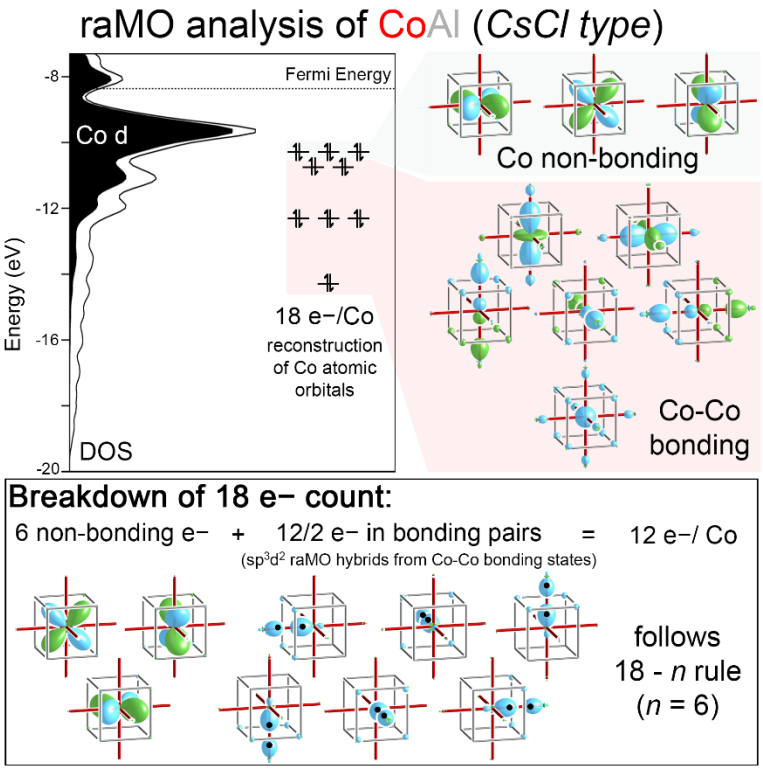

Figure 1.4. raMO analysis of CoAl, showing that despite having only 12 electrons per Co atom, the Fermi level falls into a pseudogap in the density of states curve. This is rationalized through the recreation of 6 isolobal Co-Co bonds, allowing electron pairs to be shared between transition metal atoms and stabilizing the electronics of the structure in accordance with the 18–*n* rule. (adapted from Yannello, V. J. *Proposal Narrative* **2014**)

While the 18−*n* rule is often adhered to, however, many experimentally observed phases do not exactly reach their expected electron counts. As one example, NiAl has the same structure and presence of six isolobal bonds as CoAl, but the additional electron gained in replacing Co atoms with Ni gives NiAl an electron count of 13, one larger than the 12 electrons per T atom predicted by the 18−*n* rule. This deviation, called δ_{VEC}, is measured as the ideal electron count predicted by the 18−*n* rule subtracted from the actual electron count, in this case yielding a value of $\delta_{VEC} = +1$. In figure 1.5, we show an array of T-Al binary compounds, including NiAl, arranged according to δ_{VEC}. While many are electron precise ($\delta_{VEC} = 0$), there is a significant distribution on both sides of the 18−*n* expectation; this value gives us a useful metric for determining if a structure is electron-rich ($\delta_{VEC} > 0$) or electron-poor ($\delta_{VEC} < 0$). A method for the design of frustrated intermetallics suggested by this range of δ_{VEC} values could be to leverage the stabilizing forces associated with a combination of electronically overstable and understable structures.

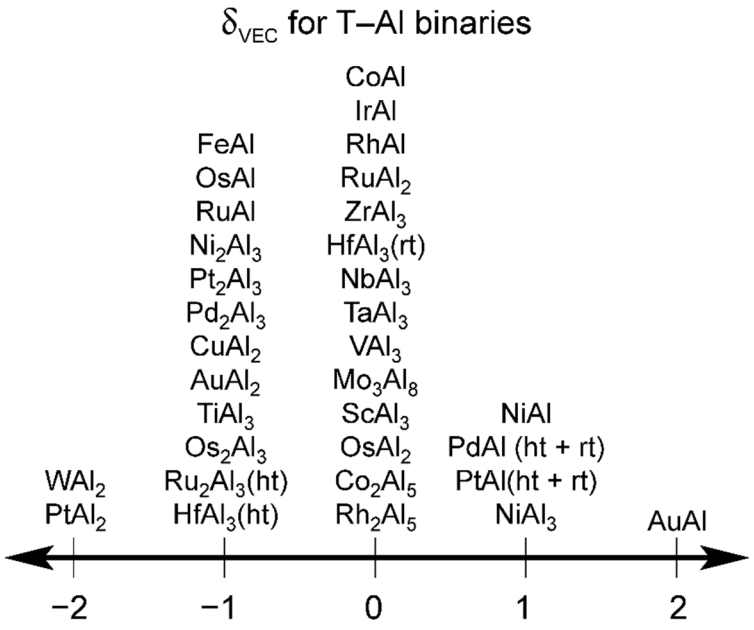

Figure 1.5. Binary T-Al phases (T = transition metal) arranged according to δ_{VEC} deviation from an ideal 18−*n* electron count. Two of these phases, FeAl and PdAl, served as inspiration for the synthesis of the $Fe_{14}Pd_{17}Al_{69}$ phase detailed in Chapter 2.

The last of our Hume-Rothery inspired factors is the use of electronegativity as a driving force for intergrowth of structural domains. In Chapter 4 of this work, we explore one potential mechanism by which electronegativity can influence structure and induce complexity, and consider future synthetic targets based on the similarly primed systems. Explicit analysis of the effects of electrostatic potentials in solids are wrapped up in calculations of the Madelung energy and Madelung constant, and tools for the calculation and assessment of these factors in intermetallics are in the preliminary stages of development, but showing great promise for future studies.

1.3 Outline of Thesis

The remainder of this work focuses on the presentation of complex intermetallic structures that were discovered and analyzed with the tools and methods described above. In each case, theory and chemical intuition inspired and guided synthesis within a ternary system of interest, and through analysis of each compound our methods were refined and our understanding of the forces at work were improved.

Chapter 2 describes the formulation of the electron-hole matching method, the idea that intergrowth structure may be induced by the matching of binary parent structures with complementary δ_{VEC} values. This idea is fleshed out through an investigation of the Ti-Ni-Al phase diagram; the binaries $TiAl_3$ and NiAl are found to have δ_{VEC} values of −1 and +1 respectively, aligning with expectations from the 18−*n* rule and the placement of their Fermi levels below and above pseudogaps in their density of states curves, respectively. The ternary phase $TiNi_{1.5}Al_5$ is known to exist at an intermediate composition between these two binaries and resembles a layered intergrowth of $TiAl_3$- and NiAl-like bonding domains. The ternary, in fact, is found to be electron precise ($\delta_{VEC} = 0$), suggesting that the combination of complementary

electron-rich and electron-poor domains from the binaries has acted to electronically stabilize $TiNi_{1.5}Al_5$ in accordance with the 18−*n* rule. Similar complementary δ_{VEC} values for FeAl and PdAl inspires an investigation of the Fe-Pd-Al phase diagram, revealing the discovery of the ternary phase $Fe_{14}Pd_{17}Al_{69}$. The structure of this compound is be understood as a supercell derivative of $IrAl_{2.75}$, with disorder manifesting in Fe-centered square antiprisms and mixed occupancy of transition metal sites. Reversed approximation Molecular Orbital analysis shows that the electron-poor domain within this structure forms a network of T-T isolobal bonds, allowing it to reach a fulfilled 18−*n* configuration.

In Chapter 3, we discuss the formation of the intermetallic subnitride $Mn_{39}Si_9N_x$. This phase was discovered through a synthetic exploration of the quasicrystal approximant υ-$Mn_{81.5}Si_{18.5}$, and is found to be stabilized through complementary Mn-Mn chemical pressures between domains of Cr_3Si-type Mn_3Si and Mn_4N, analogous to previous work on closely related carbide phases. The solved structure represents an intergrowth between domains of tetrahedrally close-packed Mn-Si interactions, and domains of Mn octahedra centered by N atoms. While its structure is quite intricate, containing 200 atomic positions per unit cell, it can be completely described by the modular arrangement of two building blocks. The first consists of a vertex-sharing triangle of icosahedra encrusted within a partial shell of octahedra, reminiscent of clusters from Mackay-type quasicrystals. The second is a fusion of five interpenetrating icosahedra, forming a single merged tcp cluster. These modules condense into one-dimensional chains along **a**, which stack into layers to construct the full unit cell. This analysis of $Mn_{39}Si_9N_x$ suggests a more general mechanism for the targeted synthesis nitrogen-containing intermetallics, where metals with high N solubility can be combined with binary phases showing negative Mn-Mn chemical pressures to yield new intergrowths.

Finally, in Chapter 4 we present an analysis of the forces acting to stabilize the stuffed $BaHg_{11}$-type phase $Ca_3Cu_{7.8}Al_{26.2}$. A structural description of this compound shows that it can be viewed as a construction of three distinct clusters: Ca-centered polyhedra reminiscent of the $CaAl_4$ structure, $Cu@Al_8$ cubes evoking a fluorite-type arrangement, and 13-atom fragments of the fcc-Al structure. We trace the origin of these modules back the structurally related binary and elemental phases, starting by showing through $CaAl_4$'s electron density distribution how it is primed for reaction with a smaller, more electronegative atom. In the Ca-Cu-Al system, such an atom is available in the form of Cu atoms, which are found to theoretically substitute more easily onto the dumbbell site of the $CaAl_4$ structure, forming a hypothetical $ThCr_2Si_2$-type ternary phase. Once there, however, the structure overly strained by the competing atomic packing effects between the desire to shrink Ca-Cu distances without also shortening the contacts in the surrounding framework. Rearrangement of the structural unit from tetragonal to cubic crystal symmetry results, while also allowing for the nucleation of fragments of a Cu-Al fluorite-type phase at the vertices of the unit cell, and opening space to replace Ca atoms with clusters of fcc-Al. Relative to the hypothetical $CaCu_2Al_2$ structure, the resulting $Ca_3Cu_{7.8}Al_{26.2}$ phase is less strained by chemical presure, and electronic stability has is restored by the donation of electrons by Al atoms. In this structure, we observe how the relatively electronegative Cu atoms act as anchor points for inclusions of fluorite-type domains, implying the potential for the stabilization of more intergrowth phases based on electronegativity-driven reactivity.

1.4 References

(1) Lewis, G. N.; Randall, M. *Thermodynamics and the free energy of chemical substances*; McGraw-Hill, 1923.

(2) Rock, P. A. *Chemical thermodynamics*; University Science Books, 1983.

(3) Yartys, V.; Denys, R. Structure–properties relationship in $RE_{3-x}Mg_xNi_9H_{10-13}$ (RE= La, Pr, Nd) hydrides for energy storage. *J. Alloys Compd.* **2015**, *645*, S412-S418.

(4) Amagai, Y.; Yamamoto, A.; Iida, T.; Takanashi, Y. Thermoelectric properties of semiconductorlike intermetallic compounds $TMGa_3$ (TM= Fe, Ru, and Os). *J. Appl. Phys.* **2004**, *96*, 5644-5648.

(5) Mrotzek, A.; Chung, D. Y.; Hogan, T.; Kanatzidis, M. G. Structure and thermoelectric properties of the new quaternary tin selenide K1-xSn5-xBi11+xSe22. *J. Mater. Chem.* **2000**, *10*, 1667-1672.

(6) Toberer, E. S.; Christensen, M.; Iversen, B. B.; Snyder, G. J. High temperature thermoelectric efficiency in $Ba_8Ga_{16}Ge_{30}$. *Phys. Rev. B* **2008**, *77*, 075203.

(7) Zlatic, V.; Horvatic, B.; Milat, I.; Coqblin, B.; Czycholl, G.; Grenzebach, C. Thermoelectric power of cerium and ytterbium intermetallics. *Phys. Rev. B* **2003**, *68*.

(8) Cava, R. J.; Zandbergen, H.; Batlogg, B.; Eisaki, H.; Takagi, H.; Krajewski, J.; Peck, W.; Gyorgy, E.; Uchida, S. Superconductivity in lanthanum nickel boro-nitride. *Nature* **1994**, *372*, 245-247.

(9) Mochiku, T.; Fujii, H.; Takeya, H.; Wuernisha, T.; Mori, K.; Ishigaki, T.; Kamiyama, T.; Hirata, K. $BaAl_4$-type derivative structure in superconducting La–Pd–Ge system. *Physica C* **2007**, *463*, 182-186.

(10) Fujii, H.; Kasahara, S. Superconductivity in the ternary intermetallics of $La_3Ni_4X_4$ (X = Si and Ge). *Journal of Physics-Condensed Matter* **2008**, *20*.

(11) Coey, J.; Sun, H. Improved magnetic properties by treatment of iron-based rare earth intermetallic compounds in anmonia. *J. Magn. Magn. Mater.* **1990**, *87*, L251-L254.

(12) Grin, Y.; Hiebl, K.; Rogl, P. Crystal structure and magnetism of YbT_xGa_{4-x}, T= Zn, Cd with the $BaAl_4$-type. *J. Alloys Compd.* **1995**, *227*, L4-L5.

(13) Hermann, R.; Wendrock, H.; Rodan, S.; Rößler, U.; Blum, C.; Wurmehl, S.; Büchner, B. Single crystal growth of antiferromagnetic Mn_3Si by a two-phase RF floating-zone method. *J. Cryst. Growth* **2013**, *363*, 1-6.

(14) Li, C.; Yang, Y.; Lv, L.; Huang, H.; Wang, Z.; Yang, S. Fabrication and magnetic characteristic of ferrimagnetic bulk Mn_4N. *J. Alloys Compd.* **2008**, *457*, 57-60.

(15) Wijn, H. P. *Magnetic Properties of Metals: d-elements, alloys and Compounds*; Springer Science & Business Media, 2012.

(16) Zhang, Z. X.; Song, X. Y.; Xu, W. W.; Seyring, M.; Rettenmayr, M. Crystal structure and magnetic performance of single-phase nanocrystalline $SmCo_7$ alloy. *Scripta Mater.* **2010**, *62*, 594-597.

(17) Pecharsky, A. O.; Gschneidner, K. A.; Pecharsky, V. K. The giant magnetocaloric effect of optimally prepared $Gd_5Si_2Ge_2$. *J. Appl. Phys.* **2003**, *93*, 4722-4728.

(18) Wang, C. L.; Zou, J. D.; Liu, J.; Mudryk, Y.; Gschneidner, K. A.; Long, Y.; Smetana, V.; Miller, G. J.; Pecharsky, V. K. Crystal structure, magnetic properties, and the magnetocaloric effect of Gd_5Rh_4 and GdRh. *J. Appl. Phys.* **2013**, *113*.

(19) Vepřek, S.; Reiprich, S. A concept for the design of novel superhard coatings. *Thin Solid Films* **1995**, *268*, 64-71.

(20) Niu, H.; Wang, J.; Chen, X.-Q.; Li, D.; Li, Y.; Lazar, P.; Podloucky, R.; Kolmogorov, A. N. Structure, bonding, and possible superhardness of CrB_4. *Phys. Rev. B* **2012**, *85*, 144116.

(21) Jeitschko, W.; Nowotny, H.; Benesovsky, F. Kohlenstoff-haltige ternäre Phasen (Nb_3Al_2C und Ta_3Al_2C). *Monatshefte für Chemie und verwandte Teile anderer Wissenschaften* **1963**, *94*, 332-333.

(22) Brown, P.; Forsyth, J. The structure of the σ-phase Nb_2Al. *Acta Crystallogr.* **1961**, *14*, 362-364.

(23) Yvon, K.; Nowotny, H.; Kieffer, R. Die Kristallstruktur der Subcarbide von Übergangsmetallen. *Monatshefte für Chemie und verwandte Teile anderer Wissenschaften* **1967**, *98*, 34-44.

(24) Fredrickson, R. T.; Guo, Y.; Fredrickson, D. C. Epitaxial Stabilization between Intermetallic and Carbide Domains in the Structures of $Mn_{16}SiC_4$ and $Mn_{17}Si_2C_4$. *J. Am. Chem. Soc.* **2016**, *138*, 248-256.

(25) Guo, Y.; Fredrickson, D. C. On the Functionality of Complex Intermetallics: Frustration, Chemical Pressure Relief, and Potential Rattling Atoms in $Y_{11}Ni_{60}C_6$. *Inorg. Chem.* **2016**, *55*, 10397-10405.

(26) Grin, Y. N. The intergrowth concept as a useful tool to interpret and understand complicated intermetallic structures In *Nato. Adv. Sci. I. C. - Mat.*; Springer: 1992, p 77-96.

(27) Pani, M.; Fornasini, M. Examples of linear structures of intermetallic compounds described as intergrowth of segments of simple basic structures. *Z. Krist. - Cryst. Mater.* **1990**, *190*, 127-134.

(28) Zeier, W. G.; Pei, Y.; Pomrehn, G.; Day, T.; Heinz, N.; Heinrich, C. P.; Snyder, G. J.; Tremel, W. Phonon Scattering through a Local Anisotropic Structural Disorder in the Thermoelectric Solid Solution $Cu_2Zn_{1-x}Fe_xGeSe_4$. *J. Am. Chem. Soc.* **2013**, *135*, 726-732.

(29) Kumar, H.; Frey, N. C.; Dong, L.; Anasori, B.; Gogotsi, Y.; Shenoy, V. B. Tunable magnetism and transport properties in nitride MXenes. *Acs Nano* **2017**, *11*, 7648-7655.

(30) Kadir, K.; Sakai, T.; Uehara, I. Structural investigation and hydrogen storage capacity of $LaMg_2Ni_9$ and $(La_{0.65}Ca_{0.35})(Mg_{1.32}Ca_{0.68})Ni_9$ of the AB_2C_9 type structure. *J. Alloys Compd.* **2000**, *302*, 112-117.

(31) Fredrickson, D. C. Chemical frustration: Lessons on materials design from complex intermetallics. *Abstr Pap Am Chem S* **2012**, *244*.

(32) Greedan, J. E. Geometrically frustrated magnetic materials. *J. Mater. Chem.* **2001**, *11*, 37-53.

(33) Larsson, E. An X-ray investigation of the Ni-P system and the crystal structures of NiP and NiP_2. *Ark. Kemi* **1965**, *23*, 335-365.

(34) Oryshchyn, S.; Zhak, O.; Guérin, P.; Députier, S.; Kuz'ma, Y. B. Structure of $Mo_{2.0-x}Ni_{1.0+x}P$ (x= 0.2) and Some Crystal-Chemical Features of Ternary Phases in the Mo–Ni–P System. *Inorg. Mater.* **2002**, *38*, 1195-1202.

(35) Guérin, R.; Pivan, J.-Y.; Padiou, J.; Sergent, M. Nouveau type structural dans la chimie des phosphures: le compose ternaire $Ni_{20}Zr_6P_{13}$. Preparation, structure et proprietes. *Mater. Res. Bull.* **1984**, *19*, 1257-1270.

(36) Berns, V. M.; Engelkemier, J.; Guo, Y.; Kilduff, B. J.; Fredrickson, D. C. Progress in Visualizing Atomic Size Effects with DFT-Chemical Pressure Analysis: From Isolated Atoms to Trends in AB_5 Intermetallics. *J. Chem. Theory Comput.* **2014**, *10*, 3380-3392.

(37) Berns, V. M.; Fredrickson, D. C. Structural plasticity: How intermetallics deform themselves in response to chemical pressure, and the complex structures that result. *Inorg. Chem.* **2014**, *53*, 10762-10771.

(38) Hume-Rothery, W. *The metallic state*; Clarendon Press Oxford, 1931.

(39) Fredrickson, D. C. Electronic Packing Frustration in Complex Intermetallic Structures: The Role of Chemical Pressure in Ca_2Ag_7. *J. Am. Chem. Soc.* **2011**, *133*, 10070-10073.

(40) Harris, N. A.; Hadler, A. B.; Fredrickson, D. C. In Search of Chemical Frustration in the Ca-Cu-Cd System: Chemical Pressure Relief in the Crystal Structures of Ca_5Cu_2Cd and $Ca_2Cu_2Cd_9$. *Z. Anorg. Allg. Chem.* **2011**, *637*, 1961-1974.

(41) Hilleke, K. P.; Fredrickson, D. C. Discerning Chemical Pressure amidst Weak Potentials: Vibrational Modes and Dumbbell/Atom Substitution in Intermetallic Aluminides. *J. Phys. Chem. A* **2018**, *122*, 8412-8426.

(42) Engelkemier, J.; Fredrickson, D. C. Chemical Pressure Schemes for the Prediction of Soft Phonon Modes: A Chemist's Guide to the Vibrations of Solid State Materials. *Chem. Mater.* **2016**, *28*, 3171-3183.

(43) Yannello, V. J.; Fredrickson, D. C. Generality of the 18-*n* Rule: Intermetallic Structural Chemistry Explained through Isolobal Analogies to Transition Metal Complexes. *Inorg. Chem.* **2015**, *54*, 11385-11398.

(44) Langmuir, I. Types of valence. *Science* **1921**, *54*, 59-67.

(45) Yannello, V. J.; Kilduff, B. J.; Fredrickson, D. C. Isolobal Analogies in Intermetallics: The Reversed Approximation MO Approach and Applications to $CrGa_4$- and Ir_3Ge_7-Type Phases. *Inorg. Chem.* **2014**, *53*, 2730-2741.

(46) Yannello, V. J.; Fredrickson, D. C. Orbital Origins of Helices and Magic Electron Counts in the Nowotny Chimney Ladders: the 18-n Rule and a Path to Incommensurability. *Inorg. Chem.* **2014**, *53*, 10627-10631.

Chapter 2.

Inducing Complexity in Intermetallics through Electron-Hole Matching: The Structure of $Fe_{14}Pd_{17}Al_{69}$

This chapter has been published: Peterson, G. G. C.; Yannello, V. J.; Fredrickson, D. C.; **2017** *Angew. Chem. Int. Ed., 56,* 10145-10150. Synthesis, structural solution, and experimental analysis were done by Peterson. Computational raMO and CP analyses were done by Yannello. Preparation of the manuscript was done jointly by Peterson and Yannello.

2.1 Abstract

We illustrate how the crystal structure of $Fe_{14}Pd_{17}Al_{69}$ provides an example of an electron-hole matching approach to inducing frustration in intermetallic systems. Its structure contains a framework based on $IrAl_{2.75}$, a binary compound that closely adheres to the 18-*n* rule. Upon substituting the Ir with a mixture of Fe and Pd, a competition arises between maintaining the overall ideal electron concentration and accommodating the different structural preferences of the two elements. A 2×2×2 supercell results, with Pd- and Fe-rich regions emerging. Just as in the original $IrAl_{2.75}$ phase, the electronic structure of $Fe_{14}Pd_{17}Al_{69}$ exhibits a pseudogap at the Fermi Energy arising from an 18-*n* bonding scheme. The electron-hole matching approach's ability to combine structural complexity with electronic pseudogaps offers an avenue to new phonon glass-electron crystal materials.

2.2 Introduction to the Electron-Hole Matching Method

The design of new materials requires both an understanding of structure-property relationships from which promising synthetic targets can be devised, and the ability to experimentally realize those target compounds. Both aspects of this process are challenging for intermetallic phases, the virtually limitless family of solid state compounds formed between metallic elements. Their immense structural diversity not only frustrates attempts to guide or control their crystal structures, but also hinders the creation of the systematic structural series necessary for discerning structure-property relationships. One exception is the area of thermoelectrics, in which materials design efforts are guided by the parameters of the phonon glass-electron crystal model:[1] structures supporting moderate electrical conductivity should be combined with phonon-scattering features.[2]

Intermetallics offer great promise in terms of complex, phonon-scattering structures as some crystallize with inexplicably large unit cells containing thousands of atoms.[3] Such complex arrangements are often associated with a tension between incompatible interactions, much like the frustration encountered in the interactions of amphiphilic molecules. Examples include the interpenetration of polar and non-polar regions in $NaCd_2$,[4,5] the coexistence of radially and periodically packed domains in $Ta_{39.1}Cu_{5.4}Al_{55.4}$,[6] the micelle-like segregation of Ca-Cd and Cu-Cd interactions in the quasicrystal approximant $Ca_{10}Cu_2Cd_{27}$,[7] and the intergrowth of intermetallic and carbide units in $Mn_{16}SiC_4$.[8] Such segregated structures have the added advantage that rattling atoms may emerge at the domain interfaces for enhanced phonon scattering.[9]

Any attempt to induce this type of frustration, of course, needs a means of preventing simple phase segregation of the incompatible domains (analogous to the covalent bond linking the head group and tail

in a surfactant molecule). The desire for closed-shell electron counts can provide one such attractive force. Intermetallic structures are becoming increasingly understandable in terms of bonding schemes, such as the Zintl concept,[10] Mott-Jones model,[11] or the 18-*n* rule.[12-14] Many compounds, however, show deviations from these schemes, indicative of non-optimized bonding that could drive new structural chemistry. Figure 2.1 shows two examples: $TiAl_3$[15] and NiAl,[16] whose Fermi Energies (E_F's) narrowly miss minima in their electronic density of states (DOS) distributions (the intermetallic analogue of a large HOMO-LUMO gap in molecules).

These mismatches can be readily understood from the 18-*n* bonding scheme, the electron counting rule that governs transition metal-main group (T-E) intermetallic phases with E content greater than 50%.[12-14] Here, the electronic structure of the compound is envisioned as being based on filled 18 electron configurations on the T atoms, with each T atom requiring 18-*n* valence electrons for a closed-shell electron configuration, where *n* is the number of T-T bonds it participates in. The E atoms primarily participate through bonding contributions to T-centered orbitals, though separate E-E bonding orbitals may appear, requiring additional electrons.

For $TiAl_3$ and NiAl, the 18-*n* rule is almost obeyed. In $TiAl_3$, the Ti atoms are arranged in square nets, with each Ti atom having four Ti neighbors. This predicts that a pseudogap should appear in the phase's DOS distribution at around 18-4 = 14 electrons per Ti atom, and one does. However, the actual electron count is only 13 (=4 electrons/Ti × 1 Ti + 3 electrons/Al × 3 Al), leading to the E_F falling below the pseudogap, such that the deviation from the ideal 18-*n* electron count, δ_{VEC}, is -1. Similarly, the six Ni neighbors surrounding each Ni atom in NiAl suggests that 18-6 = 12 would be the ideal electron count,

while the phase in fact has 13 (δ_{VEC}=+1). Its E_F then falls above the 18-*n* pseudogap. In the language of semiconductors, we could say that $TiAl_3$ and NiAl are respectively hole and electron rich.

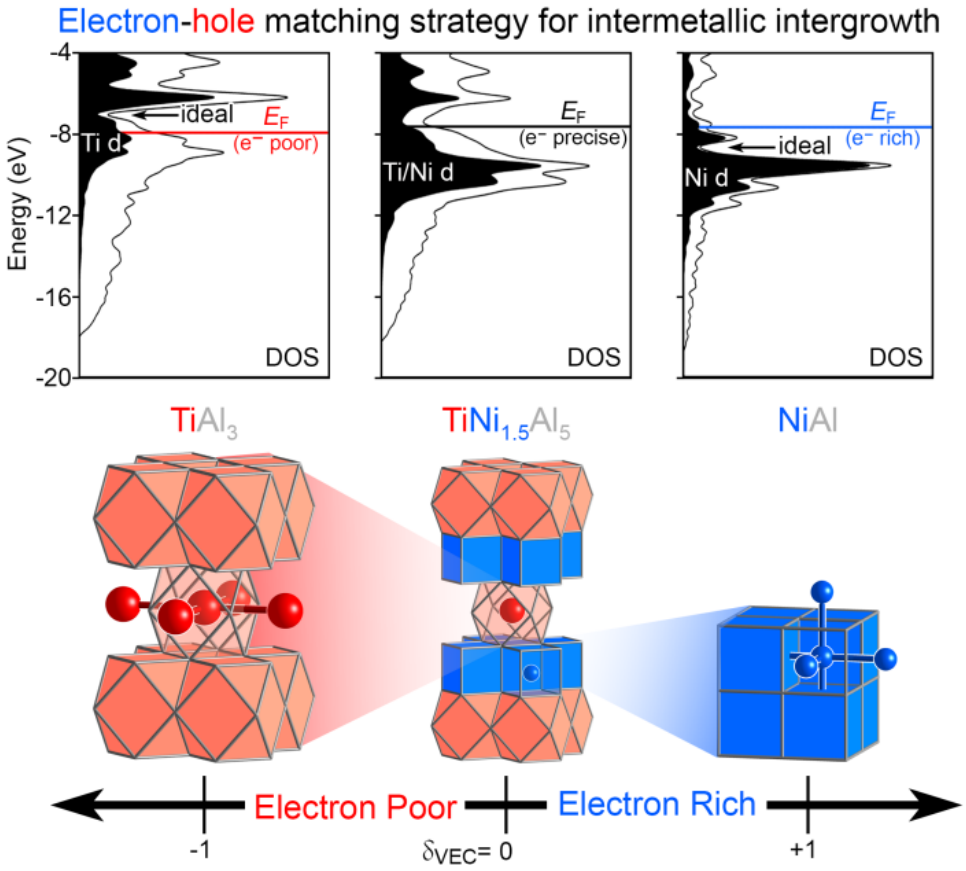

Figure 2.1. The electron-hole matching strategy for creating complex intermetallics from the intergrowth of distinct domains, illustrated with the Ti-Ni-Al system. $TiAl_3$ and NiAl are electron poor and rich relative to their ideal electron counts. δ_{VEC}: deviation from 18-*n* electron count. The differing structural preferences of Ti and Ni prevent them from simply substituting for each other to tune the electron count in either of the binary structures. Instead, an intergrowth is formed: $TiNi_{1.5}Al_5$.

The opposite signs of the δ_{VEC} values exhibited by these two phases suggest that combining them should provide a way for these mismatches to cancel out. For example, a small amount of exchange of Ni and Ti atoms between the two compounds could allow for the electron counts of the $TiAl_3$- and NiAl-based phases to rise and fall, respectively, until the 18-*n* scheme is obeyed by both phases. This Ti/Ni

substitution, however, would require that the Ti and Ni atoms share the same coordination environments, which runs counter to the very different properties of these two elements (as illustrated by their environments in the binary compounds in Figure 2.1).

The experimental Ti-Ni-Al system illustrates how this tension can be resolved. Near the mid-point between the two compounds the phase $TiNi_{1.5}Al_5$ is encountered (Figure 2.1, center).[17,18] Here, rather than Ti and Ni sharing the same sites, they segregate into different layers derived from the binary compounds: sheets of $TiAl_3$ one $Ti@Al_{12}$ polyhedron thick are fused with one-unit-cell thick slabs of NiAl to create an intergrowth structure. The result is a compound that closely follows the 18-*n* scheme (with the support of some Ni vacancies).

This example can be generalized in a design principle for frustrated intermetallic phases, which we term the *electron-hole matching strategy*. Such frustration should be encountered upon mixing crystal structures deviating from the 18-*n* rule in opposite directions when their transition metal atoms are distinct enough to prefer different coordination environments. Tension could alternatively be created by replacing the T atoms in an electron precise phase with incompatible T-T' combinations that preserve the 18-*n* electron count. In either case, structural complexity would emerge as two transition metals attempt to achieve distinct environments while simultaneously needing close proximity for effective electron transfer.

2.3 Results and Discussion

2.3.1 Synthesis and Structural Solution

While searching for possible candidate systems for this effect, the Fe-Pd-Al system caught our attention, as the Fe-Al edge contains an electron-poor phase (FeAl, CsCl-type, $\delta_{VEC} = -1$), while the Pd-Al

edge contains an electron-rich one (PdAl, CsCl-type, $\delta_{VEC} = +1$). Of course, the two phases adopt the same structure type, and an electron precise phase can be obtained by simply alloying Pd and Fe in a pseudo-binary CsCl-type phase.[19-22] However, less structurally trivial phases also appear in the system, including $Fe_{14}Pd_{17}Al_{69}$, whose structure was previously solved,[23] but whose more detailed features related to potential soft vibrational modes, such as anisotropic atomic displacement parameters, were not reported. $Fe_{14}Pd_{17}Al_{69}$'s T:E stoichiometry of 31:69 places $Fe_{14}Pd_{17}Al_{69}$ within the realm of applicability of the 18-*n* rule, while at the same time the structure would need to provide adequate environments for the Fe and Pd (which differ in main group-rich contexts). We thus set out to reinvestigate this compound, with the particular goal of interpreting its structural features in terms of the electron-hole matching scheme (as opposed to its relationship to icosahedral quasicrystals).

After arc-melting and annealing mixtures of the pure elements in ratios lying in the homogeneity range of $Fe_{14}Pd_{17}Al_{69}$, silvery gray ingots were obtained, which were easily crushed and ground to give specimens for single crystal and powder X-ray diffraction analysis, respectively. Wavelength dispersive X-ray spectrometry was used to confirm the composition of the obtained samples as lying within the $Fe_{14}Pd_{17}Al_{69}$ region. Further details regarding the experimental procedures are provided in Appendix A.2.

Single crystals of $Fe_{14}Pd_{17}Al_{69}$ exhibited diffraction patterns with cubic symmetry consistent with the body-centered space group $Im\bar{3}$ and ca. 15.4 Å cubic unit cell previously assigned. The structure solution and refinement (using Superflip[24] and Jana2006,[25] respectively) proceeded smoothly, with the elemental assignments of the mixed sites being judged by comparing the refinements for crystals from batches with different compositions.

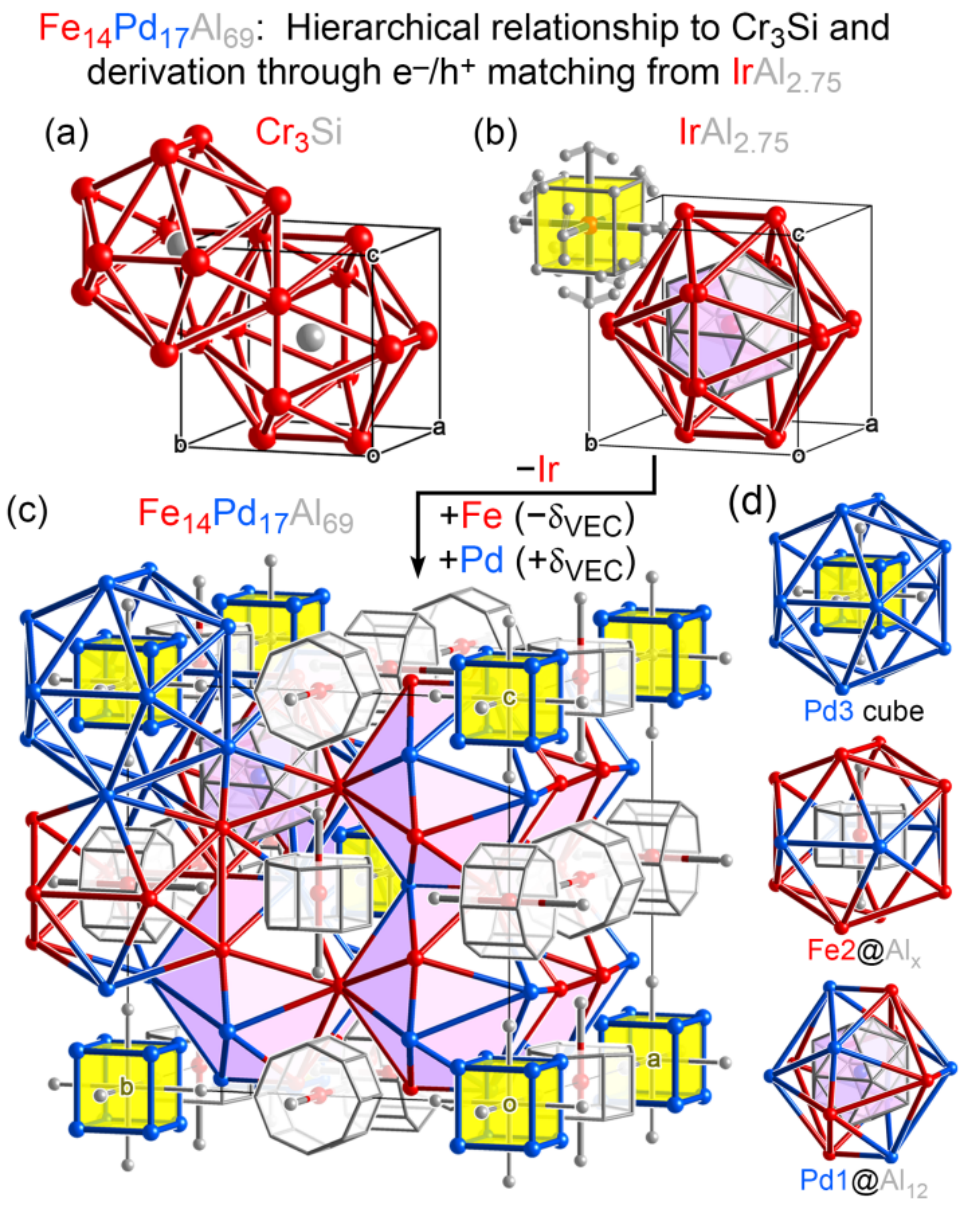

Figure 2.2. The emergence of $Fe_{14}Pd_{17}Al_{69}$ from electron-hole matching. (a) The Cr_3Si structure, from which $Fe_{14}Pd_{17}Al_{69}$ and (b) its 18-*n* electron parent phase $IrAl_{2.75}$ can be derived by placing larger polyhedra at the Si positions. Replacing Ir in the $IrAl_{2.75}$ parent phase with a mixture of Fe and Pd can maintain the overall electron concentration, but requires accommodation of the structural preferences of both elements. (c) The structure of $Fe_{14}Pd_{17}Al_{69}$, with a host framework similar to that of $IrAl_{2.75}$, but (d) different Fe- and Pd-containing clusters in the icosahedral cages.

As suggested by its rather large unit cell, the structure of $Fe_{14}Pd_{17}Al_{69}$ is complex (Figure 2.2). However, it can be readily understood once a few key features are noted. A subset of the Fe and Pd atoms traces out a pseudo-BCC network of fused icosahedra analogous to the Cr sublattice of Cr_3Si (Figure 2.2a). The openings made by this Cr_3Si-based framework are then occupied by a variety of Pd/Al and Fe/Al clusters (Figure 2.2d).

In this sense, $Fe_{14}Pd_{17}Al_{69}$ is one of a number of supercell derivatives of another, more closely related compound, $IrAl_{2.75}$ (Figure 2.2b).[23,26-29] $IrAl_{2.75}$ is thus a useful starting point for a discussion of $Fe_{14}Pd_{17}Al_{69}$'s structure and bonding. In this parent structure, the Cr_3Si-type icosahedral framework is built from Ir atoms, while the icosahedral cages are occupied by two types of Ir-centered polyhedra: an $Ir@Al_{12}$ icosahedron at the cell center and a disordered CsCl-like fragment at the cell corners.

2.3.2 Electronic Structure and Theoretical Analysis of $Fe_{14}Pd_{17}Al_{69}$

The electronic structure of $IrAl_{2.75}$ can be easily interpreted using the 18-*n* bonding scheme. Its unit cell contains eight Ir atoms, six from the icosahedral framework and two at the centers of the Al polyhedra. Each atom in the Ir icosahedral framework has one Ir neighbor at 3.29 Å (long for a classical bond, but reasonable for the multicenter bonding functions isolobal to σ bonds generally found for 18-*n* phases), suggesting that they would require 17 electrons for filled 18-electron configurations. The other two Ir atoms are isolated from Ir neighbors, and would thus be expected to need the full 18 electrons to achieve closed shells. The ideal electron count for the phase is then predicted to be $(17\times6 + 18\times2)/8 = 17.25$ electrons/Ir atom, which agrees with the 17.25 electrons per Ir atom given by the stoichiometry. Indeed,

an electronic DOS curve calculated for an ordered model of $IrAl_{2.75}$ shows a pronounced pseudogap at this electron count (see the SI).

Given that $IrAl_{2.75}$ is essentially electron-precise, moving from this phase to a Fe-Pd analogue sets up an electron-hole matching situation. An approximate 1:1 mixture of Fe and Pd has a similar average electron count as Ir, but with two rather distinct metals: a 3d transition metal and a 4d noble metal. How would the $IrAl_{2.75}$ structure accommodate both of these elements?

As is evident from Figures 2.2c-d, the answer to this question is in varying the clusters occupying the structure's icosahedral cages. A 2×2×2 supercell is formed, with the $Ir@Al_{12}$ icosahedra at the subcell centers being replaced simply by $Pd@Al_{12}$ versions. Six of the eight remaining cavities are filled by disordered $Fe@Al_{10}$ polyhedra, while the remaining two—those at the supercell corners and center—are home to a small fragment of the PdAl CsCl-type phase. The icosahedral cages themselves are built from a mixture of Pd and Fe, with the curious feature that the Pd in this framework tends to concentrate around the PdAl CsCl-type fragment, while the sites around the Fe-centered clusters are enriched with Fe.

Unlike the disorder in $IrAl_{2.75}$, the partial occupancies in the Fe-centered polyhedra of $Fe_{14}Pd_{17}Al_{69}$ have a straightforward interpretation (Figure 2.3a). Each of these Fe sites is surrounded by an octagonal prism of partially occupied Al atoms, with additional Al atoms capping the octagonal faces. The Al-Al distances between neighbors within the octagonal prism range from unphysically to uncomfortably short (1.58-2.45 Å), meaning that only every other atom should be present simultaneously. In this way, the disordered polyhedron is resolved into two half-occupied Al_{10} bicapped square antiprisms, with the two possible orientations being understandable from the pseudo-symmetry mismatch[30] between the polyhedron and its icosahedral cage.

According to the electron-hole matching strategy, the main driving force for combining Fe and Pd within the structure is to maintain a pseudogap at the E_F. DFT calculations[31] on an ordered model of the structure (composition $Fe_{12}Pd_{27}Al_{85}$) in fact show the expected coincidence of the E_F and a DOS minimum (Figure 2.4a). As with $IrAl_{2.75}$, this favorable electron configuration can be understood through 18-*n* arguments, which are buttressed by full reversed approximation Molecular Orbital (raMO) analyses[32] in the SI.

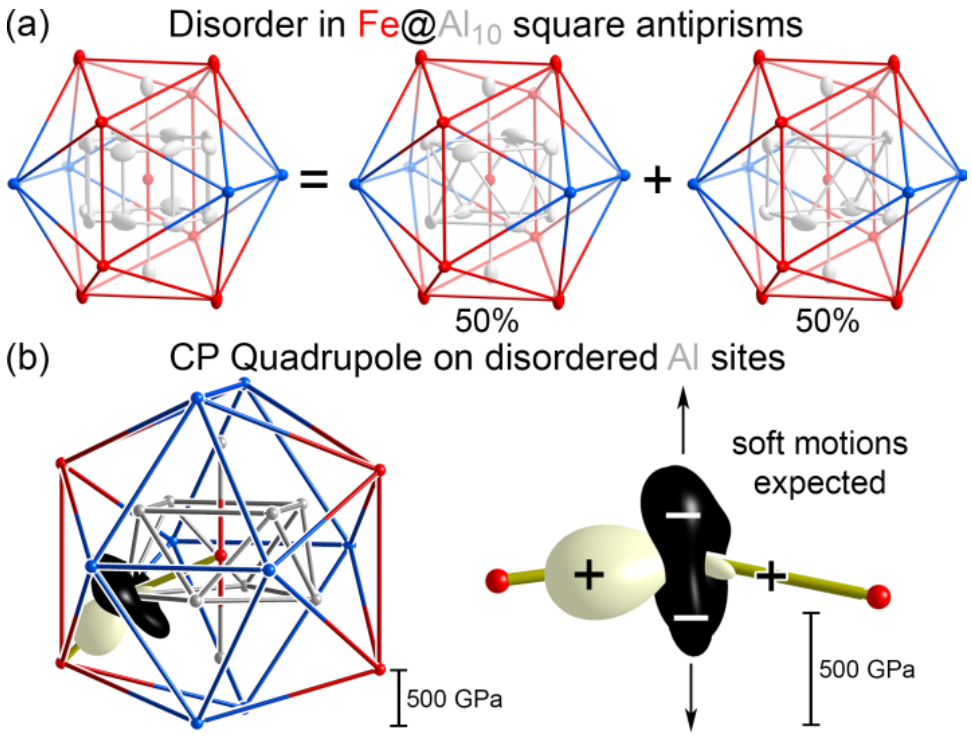

Figure 2.3. Disorder and potential soft vibrational modes in the $Fe@Al_{10}$ filled cavities of $Fe_{14}Pd_{17}Al_{69}$. (a) The resolution of the disordered $Fe@Al_x$ polyhedron into two differently oriented $Fe@Al_{10}$ bicapped square antiprisms. Thermal ellipsoids are shown at the 75% probability level. (b) DFT Chemical Pressure (CP) scheme for an Al atom on the $Fe@Al_{10}$ polyhedron in a simplified model (see SI) illustrating the presence of a CP quadrupole. The CP distribution around the Al is presented with a radial surface, with black corresponding to negative CP (contraction favorable), white to positive CP (expansion favorable).

The $Fe@Al_{10}$ and $Pd@Al_{12}$ polyhedra filling the majority of the icosahedral cavities are n=0 centers, requiring 18 electrons each (Figure 2.4b). The remaining transition metal atoms are closely associated with the PdAl CsCl-type fragments and the surrounding icosahedral framework (Figure 2.4c): the Pd3, Pd2 and Fe1 sites. The Fe1 and Pd2 sites have 1 and 3 transition metal neighbors, respectively, making them n=1 and n=3 centers. The Pd3 site, on the other hand, traces out a Pd cube as part of the CsCl-type fragment, whose edges are capped by Pd2 atoms. This arrangement gives the Pd3 site six Pd neighbors, nominally. However, a raMO analysis of this site indicates that not all of these contacts are equal: whereas each of three Pd3-Pd2 contacts are full bonds, the core-like nature of the Pd 4d orbitals means that a Pd3 atom does not have enough remaining orbitals to make individual bonds to each of its Pd3 neighbors in the cube. Instead, the Pd3 site is better considered as sp^3-hydridized, with three of the hybrids making bonds with the Pd2 bridging atoms, and the fourth pointing toward the center of the Pd3 cube, where an Al atom lies.

The bonding between the Pd atoms of the Pd3 cubes can then be interpreted in terms of the interactions between the sp^3 hybrid orbitals, as is simply done with a raMO analysis. We start by calculating a simple molecular orbital (MO) diagram for a cube of sp^3 hybrid orbitals, which yields the expected pattern of 1+3 bonding MOs below 3+1 antibonding MOs (Figure 2.4d, left). We then use the raMO analysis to create the best reconstructions of the MOs possible from the occupied crystal orbitals of the system. The result is shown on the right side of Figure 2.4d, where the four bonding MOs are all well-reproduced and augmented by bonding contributions from the nearby Al atoms, while the reconstructions of the antibonding MOs bear little relationship to the original functions. The Pd cubes thus have closed shells at 8 electrons, with each Pd3 atom then contributing 1 electron. When we recall that the Pd3 site

also participates in three isolobal bonds to Pd2 neighbors, we see that the Pd3 atoms reach closed shells at 18-(3+1) = 14 electrons.

We are now in a position to make a final tabulation of the electrons in $Fe_{14}Pd_{17}Al_{69}$. Of the 78 transition metal atoms in the unit cell, 14 are $n = 0$ centers, 24 are $n = 1$ centers, 24 are $n = 3$ centers, and 16 are $n = 4$ centers, leading to an average of 15.95 electrons/T atom needed for filled 18-electron configurations throughout the structure. This count lies within the electron count range given by the compound's phase width of ca. 15.91–16.38/T atom, and accounts for the location of the E_F in a DOS pseudogap for the $Fe_{12}Pd_{27}Al_{85}$ model. These results are also consistent with the absence of any pronounced magnetic ordering for the phase, as revealed by magnetization measurements (see Appendix A.2.5).

The position of the E_F near a pseudogap with a small but non-zero DOS suggests that the compound could exhibit a moderate conductivity suitable for thermoelectric applications. The appreciable phase-width for this compound in the phase diagram also suggests the E_F may be tunable to adjust the carrier type and concentration.

Electrical properties are, of course, only one side of the PGEC model; the thermoelectric efficiency for $Fe_{14}Pd_{17}Al_{69}$ would also depend on its ability to act as a phonon-glass for low thermal conductivity. The relatively large unit cell of the phase already bodes well for such hopes, but the details of the structure are particularly promising. The Al atoms in the disordered square antiprisms surrounding the Fe2 positions exhibit disc-like thermal ellipsoids suggestive of vibrational freedom (Figure 2.3). A DFT-Chemical Pressure (CP) analysis on an ordered model of the structure indicates that these Al atoms can have sizeable CP quadrupoles from being squeezed between pairs of transition metal atoms.[33,34] Such features are associated with soft vibrational modes,[35] which may contribute to reduced lattice thermal conductivity.

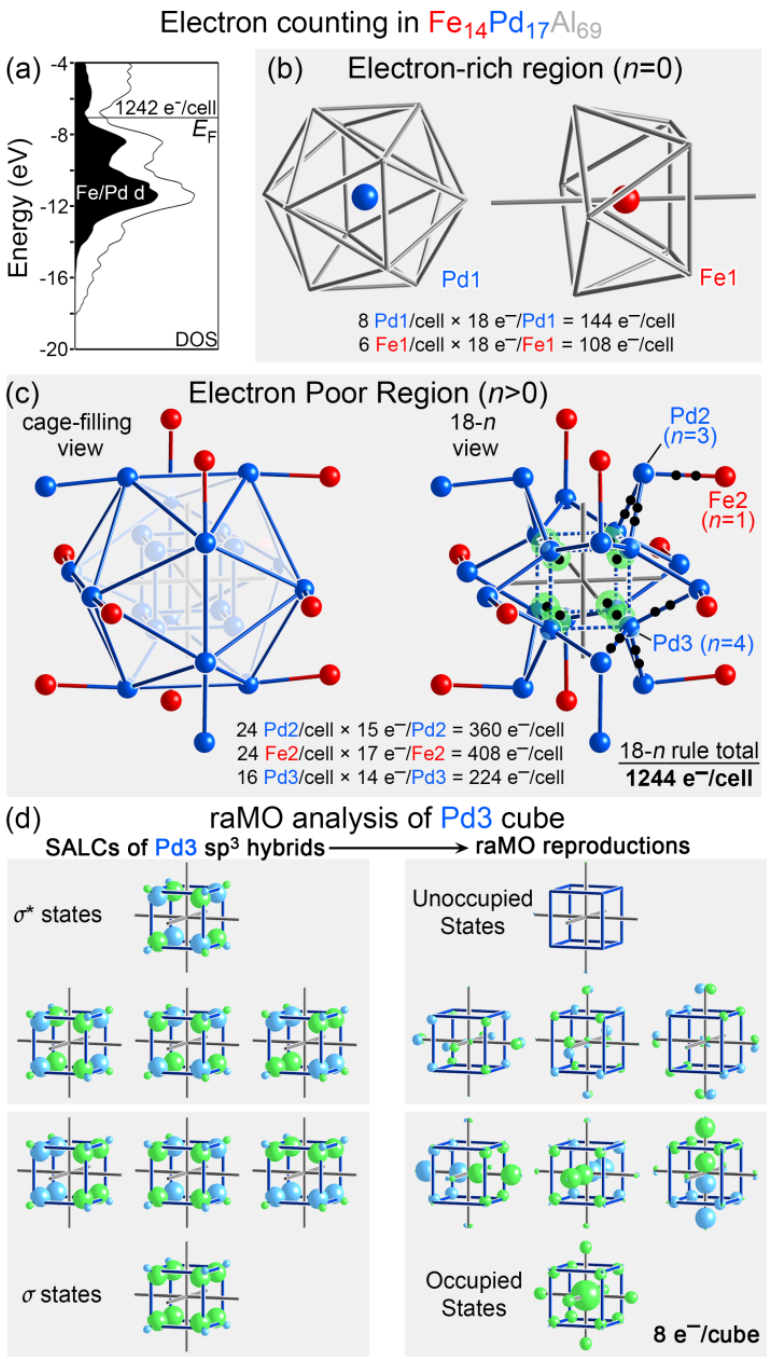

Figure 2.4. 18-*n* bonding scheme for $Fe_{14}Pd_{17}Al_{69}$, based on an ordered model with composition $Fe_{12}Pd_{27}Al_{85}$. (a) The electronic DOS distribution for $Fe_{14}Pd_{17}Al_{69}$. (b) The *n*=0 18-electron centers of the phase, defining electron-rich regions. (c) The electron-poor region defined by transition metal sites with $n > 0$. (d) Symmetry-adapted linear combinations (SALCs) of the Pd sp^3 hybrid orbitals pointing to the center of the Pd3 cube, and their reconstructions from the occupied crystal orbitals using the reversed approximation Molecular Orbital (raMO) method.

This example shows how the electron-hole matching approach can promote combinations of structural and electrical features that are desirable for thermoelectric materials. The thermoelectric figure of merit, however, involves a number of competing relationships among its contributing factors. Properties measurements will be necessary to see exactly how effective this combination is in $Fe_{14}Pd_{17}Al_{69}$. We are now working to synthesize phase pure samples of the compound in sufficient quantities for such measurements to be feasible.

2.4 Conclusions

In this Chapter, we have presented the outline for an approach by which the rattling modes expected for frustrated intermetallic structures can be combined with the electrical properties necessary for thermoelectric applications: the electron-hole matching strategy. Here pairs of transition metals that average to the correct electron count for an 18-*n* bonding scheme but have distinct structural preferences are combined, leading to a conflict between the needs for electron transfer and geometrically differentiated sites. The potential of this scheme is illustrated by the structure and bonding of $Fe_{14}Pd_{17}Al_{69}$, whose complex structure can be seen as the result of electron-hole matching within the framework of a parent compound, $IrAl_{2.75}$. We are looking forward to exploring these expectations through detailed measurements of the physical properties of $Fe_{14}Pd_{17}Al_{69}$ and new syntheses guided by this concept.

2.5 Acknowledgements

We thank Prof. Eric Toberer for insightful discussions regarding the thermoelectric properties of intermetallic materials, Matthew J. Stolt for assistance with the magnetic susceptibility measurements, Anastasiya I. Vinokur for the collection of single crystal X-ray diffraction data, and Dr. John Fournelle for the wavelength dispersive X-ray spectroscopy measurements. We gratefully acknowlege partial support of this research by the National Science Foundation (NSF) through grant DMR-1508496 (for the DFT-CP analysis) and through the University of Wisconsin Materials Research and Engineering Center (DMR-1121288) for the synthetic experiments. The research involved computations using resources supported by NSF grant CHE-0840494.

2.6 References

(1) Slack, G. A. New Materials and Performance Limits for Thermoelectric Cooling In *Thermoelectric Handbook*; Rowe, M., Ed.; CRC Press: Boca Raton, 1995, p 407-440.

(2) Snyder, G. J.; Toberer, E. S. Complex Thermoelectric Materials. *Nat. Mater.* **2008**, *7*, 105-114.

(3) Schmitt, D. C.; Haldolaarachchige, N.; Xiong, Y.; Young, D. P.; Jin, R.; Chan, J. Y. Probing the Lower Limit of Lattice Thermal Conductivity in an Ordered Extended Solid: $Gd_{117}Co_{56}Sn_{112}$, a Phonon Glass–Electron Crystal System. *J. Am. Chem. Soc.* **2012**, *134*, 5965-5973.

(4) Fredrickson, D. C.; Lee, S.; Hoffmann, R. Interpenetrating Polar and Nonpolar Sublattices in Intermetallics: The $NaCd_2$ Structure. *Angew. Chem. Int. Ed.* **2007**, *46*, 1958-1976.

(5) Fredrickson, D. C.; Lee, S.; Hoffmann, R. Sich durchdringende polare und unpolare Untergitter in intermetallischen Phasen: die Struktur von $NaCd_{-2}$. *Angew. Chem.* **2007**, *119*, 2004-2023.

(6) Conrad, M.; Harbrecht, B.; Weber, T.; Jung, D. Y.; Steurer, W. Large, Larger, Largest--A Family of Cluster-based Tantalum Copper Aluminides with Giant Unit Cells. II. The Cluster Structure. *Acta Crystallogr. B* **2009**, *65*, 318-325.

(7) Hadler, A. B.; Harris, N. A.; Fredrickson, D. C. New Roles for Icosahedral Clusters in Intermetallic Phases: Micelle-like Segregation of Ca-Cd and Cu-Cd Interactions in $Ca_{10}Cd_{27}Cu_2$. *J. Am. Chem. Soc.* **2013**, *135*, 17369-17378.

(8) Fredrickson, R. T.; Guo, Y.; Fredrickson, D. C. Epitaxial Stabilization between Intermetallic and Carbide Domains in the Structures of $Mn_{16}SiC_4$ and $Mn_{17}Si_2C_4$. *J. Am. Chem. Soc.* **2016**, *138*, 248-256.

(9) Guo, Y.; Fredrickson, D. C. On the Functionality of Complex Intermetallics: Frustration, Chemical Pressure Relief, and Potential Rattling Atoms in $Y_{11}Ni_{60}C_6$. *Inorg. Chem.* **2016**, *55*, 10397-10405.

(10) Nesper, R. The Zintl-Klemm Concept – A Historical Survey. *Z. Anorg. Allg. Chem.* **2014**, *640*, 2639-2648.

(11) Berger, R. F.; Walters, P. L.; Lee, S.; Hoffmann, R. Connecting the Chemical and Physical Viewpoints of What Determines Structure: From 1-D Chains to γ-Brasses. *Chem. Rev.* **2011**, *111*, 4522-4545.

(12) Yannello, V. J.; Fredrickson, D. C. Orbital Origins of Helices and Magic Electron Counts in the Nowotny Chimney Ladders: the 18 – *n* Rule and a Path to Incommensurability. *Inorg. Chem.* **2014**, *53*, 10627-10631.

(13) Kilduff, B. J.; Yannello, V. J.; Fredrickson, D. C. Defusing Complexity in Intermetallics: How Covalently Shared Electron Pairs Stabilize the FCC Variant $Mo_2Cu_xGa_{6-x}$ ($x \approx 0.9$). *Inorg. Chem.* **2015**, *54*, 8103-8110.

(14) Yannello, V. J.; Fredrickson, D. C. Generality of the 18-*n* Rule: Intermetallic Structural Chemistry Explained through Isolobal Analogies to Transition Metal Complexes. *Inorg. Chem.* **2015**, *54*, 11385-11398.

(15) Brauer, G. Über die Kristallstruktur von $TiAl_3$, $NbAl_3$, $TaAl_3$, und $ZrAl_3$. *Z. Anorg. Allg. Chem.* **1939**, *242*, 1-22.

(16) Becker, K.; Ebert, F. Röntgenspektroskopie an Metallverbindungen. *Z. Physik* **1923**, *16*, 165-169.

(17) Ding, J. J.; Rogl, P.; Schmidt, H. Phase relations in the Al-rich corner of the Ti–Ni–Al system. *J. Alloys Compd.* **2001**, *317–318*, 379-384.

(18) Khan, A. U.; Bursik, J.; Grytsiv, A.; Pomjakushin, V.; Effenberger, H.; Rogl, P. Crystal structure of τ_5–$TiNi_{2-x}Al_5$ (x= 0.48) and isotypic {Zr, Hf} $Ni_{2-x}Al_{5-y}$. *Intermetallics* **2011**, *19*, 1340-1347.

(19) Balanetskyy, S.; Grushko, B.; Velikanova, T. Y.; Urban, K. An investigation of the Al–Pd–Fe phase diagram between 50 and 100 at.% Al: phase equilibria at 750 °C. *J. Alloys Compd.* **2004**, *376*, 158-164.

(20) Balanetskyy, S.; Grushko, B.; Kowalska-Strzęciwilk, E.; Velikanova, T. Y.; Urban, K. An investigation of the Al–Pd–Fe phase diagram between 50 and 100 at.% Al: phase equilibria at 900–1020 °C. *J. Alloys Compd.* **2004**, *364*, 164-170.

(21) Balanetskyy, S.; Grushko, B.; Velikanova, T. Y.; Urban, K. Investigation of the Al–Pd–Fe phase diagram between 50 and 100 at.% Al: ternary phases. *J. Alloys Compd.* **2004**, *368*, 169-174.

(22) Balanetskyy, S.; Velikanova, T. Y.; Grushko, B. An investigation of the Al–Pd–Fe phase diagram between 50 and 100at.% Al: reaction scheme. *J. Alloys Compd.* **2005**, *394*, 219-225.

(23) Sugiyama, K.; Hiraga, K.; Saito, K. Cubic approximants in the Al–Pd–Fe and Al–Pd–Ru systems. *Mater. Sci. Eng. A* **2000**, *294–296*, 345-347.

(24) Palatinus, L.; Chapuis, G. SUPERFLIP - a computer program for the solution of crystal structures by charge flipping in arbitrary dimensions. *J. Appl. Crystallogr.* **2007**, *40*, 786-790.

(25) Petříček, V.; Dušek, M.; Palatinus, L. Crystallographic Computing System JANA2006: General features. *Z. Kristallogr.* **2014**, *229*, 345-352.

(26) Grin, Y.; Peters, K.; Burkhardt, U.; Gotzmann, K.; Ellner, M. The Crystal Structure of the Binary Iridium-Aluminum $IrAl_{2.75}$ and Rhodium-Aluminum $RhAl_{2.63}$ phase. *Z. Kristallogr.* **1997**, *212*, 439-444.

(27) Edler, F. J.; Gramlich, V.; Steurer, W. Structure and disorder phenomena of cubic $Al_{39}Fe_2Pd_{21}$ in comparison with related structures. *J. Alloys Compd.* **1998**, *269*, 7-12.

(28) Mahne, S.; Steurer, W. The crystal structure of the ternary alloy *c*-$Al_{68}Pd_{20}Ru_{12}$. *Z. Kristallogr.* **1996**, *211*, 17-24.

(29) Dshemuchadse, J.; Kuczera, P.; Steurer, W. A new cluster-based cubic phase in the Al–Cu–Ir system. *Intermetallics* **2013**, *32*, 337-343.

(30) Xiong, D.-B.; Okamoto, N. L.; Inui, H. Planar Symmetry Incompatibility in Ru–Sn–Zn Pseudo-Decagonal Approximants Composed of Novel Pentagonal Antiprisms. *Inorg. Chem.* **2011**, *50*, 827-835.

(31) GGA-DFT band energies and DOS distributions calculated with the Vienna Ab Initio Simulation Package (VASP). See: a) G. Kresse, J. Furthmüller, Phys. Rev. B 1996, 54, 11169-11186; b) G. Kresse, J. Furthmüller, Comput. Mater. Sci. 1996, 6, 15-50; and additional references in the SI. These results provided the basis for the refinement of simple Hückel models, on which the reversed approximation Molecular Orbital (raMO) analyses were carried out.

(32) Yannello, V. J.; Kilduff, B. J.; Fredrickson, D. C. Isolobal Analogies in Intermetallics: The Reversed Approximation MO Approach and Applications to $CrGa_4$- and Ir_3Ge_7-Type Phases. *Inorg. Chem.* **2014**, *53*, 2730-2741.

(33) Berns, V. M.; Engelkemier, J.; Guo, Y.; Kilduff, B. J.; Fredrickson, D. C. Progress in Visualizing Atomic Size Effects with DFT-Chemical Pressure Analysis: From Isolated Atoms to Trends in AB_5 Intermetallics. *J. Chem. Theory Comput.* **2014**, *10*, 3380-3392.

(34) The DFT-Chemical Pressure analysis was performed on the output of LDA-DFT calculations made with ABINIT. See: X. Gonze, G.-m. Rignanese, M. Verstraete, J.-m. Beuken, Y. Pouillon, R. Caracas, J.-y. Raty, V. Olevano, F. Bruneval, L. Reining, R. Godby, G. Onida, D. R. Hamann, D. C. Allan, Z. Kristallogr. 2005, 220, 558-562; and additional references in the SI.

(35) Engelkemier, J.; Fredrickson, D. C. Chemical Pressure Schemes for the Prediction of Soft Phonon Modes: A Chemist's Guide to the Vibrations of Solid State Materials. *Chem. Mater.* **2016**, *28*, 3171-3183.

Chapter 3.

$Mn_{39}Si_9N_x$: Epitaxial Stabilization as a Pathway to the Formation of Intermetallic Nitrides

This chapter is currently under review for publication: Initial synthesis and preliminary identification of composition was done by Berns. Synthetic replication, data collection, analysis, and interpretation, computational procedures, and preparation of the manuscript were the work of Peterson.

3.1 Abstract

The realization of the full potential of nitrogen-containing solid state materials is limited by the inert and gaseous nature of N_2. In this Chapter, we describe the simple synthesis yet complex structure of the new phase $Mn_{39}Si_9N_x$ (x=0.84). The formation of this intermetallic subnitride appears to be facilitated by the high solubility of nitrogen in manganese metal, while its structural features are guided by the complementary internal packing strains of Mn-Si and Mn-N domains, an effect known as epitaxial stabilization. These domains intergrow into a composite structure based on the interpenetration of tetrahedrally close-packed (TCP) and Mackay cluster-like modules. We anticipate that other systems combining nitrogen with the TCP packing of metals will be similarly driven toward intergrowth, opening a path to a broader family of intermetallic nitrides.

3.2 Introduction

Materials chemists have long sought a nitride crystal chemistry to parallel the rich diversity found in solid state oxides.[1,2] Indeed, the known nitrides combine unique structural chemistry with applications in catalysis,[3,4] superconductivity,[5-7] solid-state lighting,[8,9] ceramics,[10,11] and permanent magnetism,[12,13] making this class of compounds a highly targeted space for material discovery.[14-16] The fulfillment of this vision, however, has been impeded by the inherent inertness and thermodynamic stability of gaseous N_2, which makes nitride preparation with traditional solid state techniques especially challenging.[17,18] And yet, in some contexts nitrogen offers reaction pathways not accessible to oxygen, such as its relatively high solubility in the mid 3d transition metals,[19-22] which can be leveraged in materials synthesis. In this Chapter, we present the new and complex subnitride $Mn_{39}Si_9N_x$ $(x = 0.84)$, whose facile formation is correlated with this solubility of N in Mn.

The Mn:Si ratio of this compound aligns closely with that of the tetrahedrally close-packed (TCP) υ-$Mn_{81.5}Si_{18.5}$ phase,[23] suggestive of an intercalation of N atoms into a Mn-rich lattice. As illustrated by the structural bedlam of the analogous carbide systems,[24-27] this sets the stage for packing frustration. The tetrahedral holes that dominate TCP structures do not provide sufficient space for the incorporation of interstitial atoms, such as carbon or nitrogen.[28] Such structures as $Mn_{16}SiC_4$ and $Mn_{17}Si_2C_4$[29] reconcile this incompatibility through the intergrowth of TCP domains with metal carbide regions based on C-centered capped trigonal prisms. These structures merge seemingly immiscible domains into single compounds—even as macroscopic phase segregation would seem to be a simpler alternative—making them particularly interesting for materials design.

We recently identified a driving force stabilizing the interface between these domains through the chemical pressure (CP) schemes of the component intermetallic and carbide phases, as summarized in Figures 3.1a-b.[29-31] The CP scheme of a TCP Mn-rich silicide (modeled here as a hypothetical Cr_3Si-type Mn_3Si structure) shows large positive pressures (white lobes) along the shortest Mn-Mn contacts, indicating that these atoms are closer to each other than ideal. However, this drive for the structural expansion is counteracted by negative pressures (black lobes) between the remaining atoms. Here, we see the internal strain caused by competition among atomic contacts: the drive for longer distances between the closest Mn atoms is balanced against the costs of further stretching the other interactions.

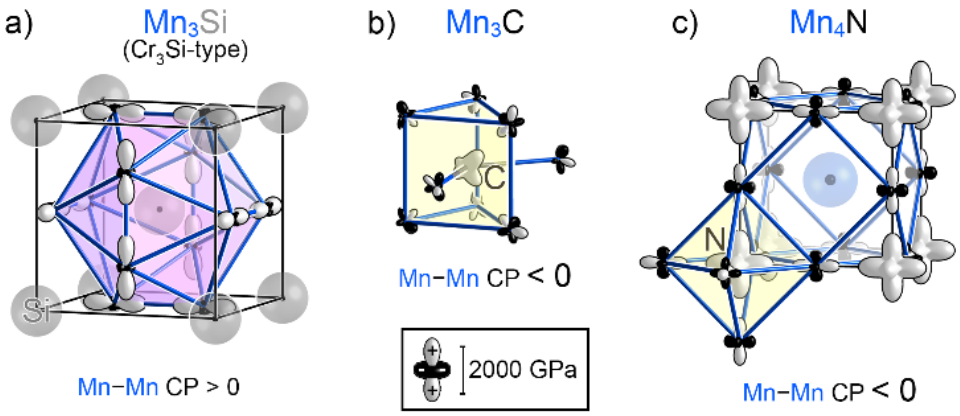

Figure 3.1. Chemical pressure (CP) schemes for (a) hypothetical Cr_3Si-type Mn_3Si, (b) Mn_3C, and (c) Mn_4N. CP surfaces around each atom represent the sums of the pressures experienced by the atom along each direction. White lobes show positive pressures desiring expansion of structure, while black features represent negative pressures calling for contraction.

Similarly, the CP scheme of the carbide Mn_3C also reveals internal tension between competing positive and negative pressures, as shown for the bicapped trigonal prismatic coordination environments of the C atoms in Figure 3.1b. In this case, however, the pressure scheme is inverted relative to Mn_3Si; the shortest Mn-Mn contacts now show substantial negative CPs, which are opposed by Mn-C positive

pressures. This complementary nature of the Mn-Mn CPs in Mn_3Si (positive) and Mn_3C (negative) thus provides an opportunity for beneficial cancellation at the interfaces between Mn-Si and Mn-C domains. We refer to this effect as *epitaxial stabilization*.[29,32]

Here, we explore how such driving forces can also shape the structures of intermetallic nitrides. In Figure 3.1c, we present the CP scheme of Mn_4N. While the N atoms occupy octahedral holes, rather than bicapped trigonal prisms as in the carbide (consistent with N's smaller atomic radius),[33,34] the structure experiences an analogous balance of attractive Mn-Mn and repulsive Mn-N interactions. Mn_4N domains should thus be similarly poised for complementary interactions with Mn_3Si regions, suggesting the potential for Mn-Si-N intergrowth structures.

3.3 Results and Discussion

We encountered an intriguing lead in this direction while synthetically investigating the reported homogeneity range of the quasicrystal approximant υ-$Mn_{81.5}Si_{18.5}$.[23] In one such synthesis, we found crystals which seemed to grow out of the Al_2O_3 fibers used to cap the crucible. An X-ray dataset collected for one of these crystals yielded a structure with refined composition of $Mn_{80}Si_{19}X$, where X corresponded to electron density peaks in octahedral interstices that were attributable to C, N, or O. The structure could not be matched to any known unit cell, and subsequent attempts to create this phase using oxide precursors were unsuccessful.

Several clues pointed to the X positions belonging to N. First, in the related carbide phases, the C atoms exclusively occupy capped trigonal prisms, suggesting that the atoms of X are smaller than those of C. In addition, manganese shows a high solubility of both carbon and nitrogen (~10 at%), whereas the solubility

of oxygen is limited (~1 at%).[19,20,35,36] As these 2nd row elements are difficult to distinguish using X-ray techniques, we set out to synthetically test this idea by including pure N_2 as a starting material.

We loaded ~81.5:18.5 mixtures of Mn and Si powders under 100 to 500 torr of N_2. Annealing these samples at 900 °C for ~300 hours generally resulted in metallic gray ingots, whose powder diffraction patterns reproducibly showed indications of the $Mn_{80}Si_{19}X$ target phase (see Appendix B.2 for experimental details). Single crystals picked from these samples exhibited clean diffraction patterns consistent with the space group *Pnma*, while the structure solution and refinement yielded a model representing a new orthorhombic structure type with composition $Mn_{39}Si_9N_x$ ($x = 0.84$, Z = 4).

Consistent with our expectations of packing tensions in the Mn-Si-N system, the structure of $Mn_{39}Si_9N_x$ is remarkably complex (200 atomic positions per unit cell encoded by 33 symmetry-distinct sites). However, as Figure 3.2 shows, all of these atoms can be captured by just two building block modules. The first consists of a triangle of vertex-sharing $Si@Mn_{12}$ icosahedra (gray) embedded in a network of 23 face-sharing Mn/Si octahedra (yellow). Four of these octahedra are partially N-centered (N occupancies of 58/26%). This arrangement of icosahedra within a shell of face-sharing octahedra is a motif familiar from Mackay-type quasicrystals and their approximants.[37-40] The other module is also built from icosahedra: two Si-centered (gray) and three Mn-centered (lavender), arranged in a trigonal bipyramidal geometry. This module is thus built entirely from face-sharing tetrahedra, making this a TCP domain.

We begin our description of the full $Mn_{39}Si_9N_x$ structure with the icosahedral units within these modules (Figures 3.3a-b). Here, the Mackay modules are represented by their vertex-sharing triangles of icosahedra, while the TCP modules are shown in full. In Figure 3.3c-d, we illustrate how these modules coalesce by type into one-dimensional chains along **a**. For the Mackay modules, this results in a triangular

tiling whose units are linked through shared polyhedral faces, whereas for the TCP modules, the clusters share edges to create a zigzag chain in the **ac** plane.

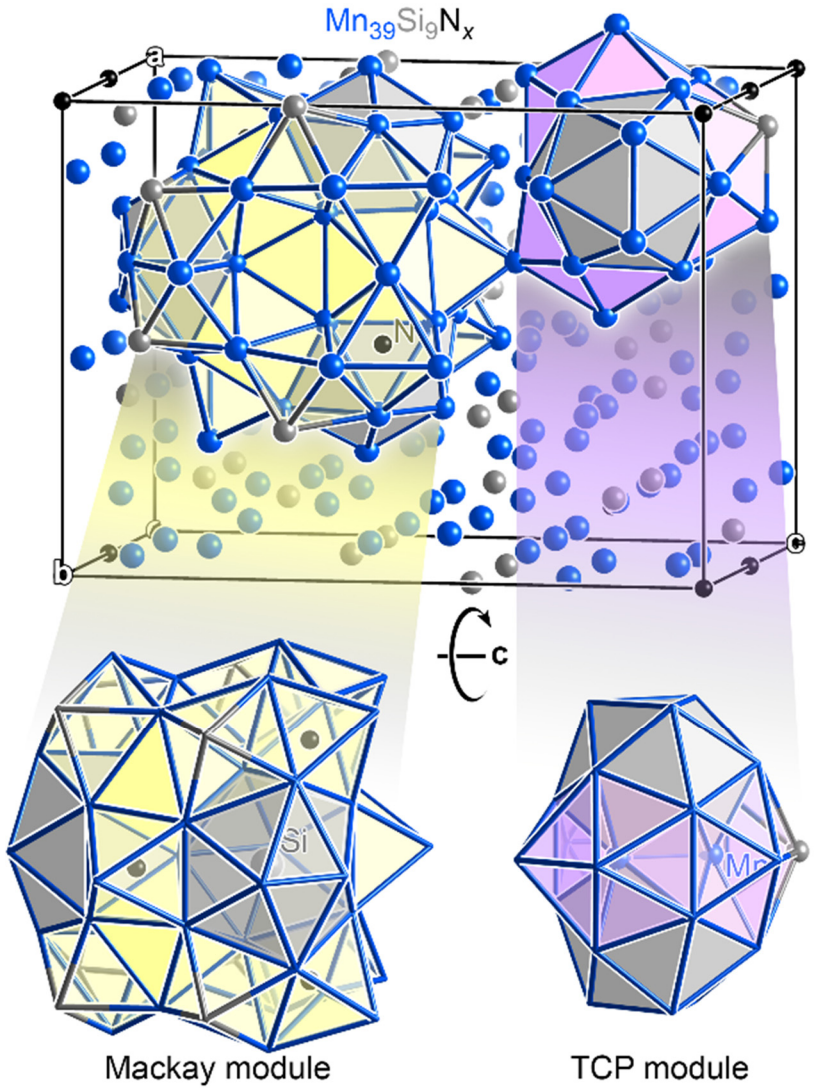

Figure 3.2. The crystal structure of $Mn_{39}Si_9N_x$, with its two modular building blocks highlighted.

The Si atom corners of these zigzag TCP chains provide docking points for condensation with strips of the Mackay modules on both sides (Figure 3.3e), doubling as the center of a Mn_{12} icosahedron in these

neighboring modules. The propagation of this pattern creates a layer centered at $y = 0$, where chains of Mackay and TCP modules alternate along **c**.

These layers have corrugated surfaces, with the apical icosahedra of the TCP modules projecting above and below. This offers a simple way for the layers to stack (Figure 3.3f): the outermost icosahedra of one layer nests within the grooves of the Mackay modules in the layers above and below. The top and bottom triangular faces of the TCP modules become shared with the triangle of vertices at the center of each Mackay module (red triangles in Figures 3.3e-f). Each unit cell contains two such layers, centered at $y = 0$ and $y = ½$, which are related by a 2_1 screw axis.

As one may notice from Figures 3.3e-f, these layers of icosahedra leave behind open spaces. For instance, the border between the triangular Mackay modules form diamond-shaped openings, which are in fact octahedral holes accommodating N atoms (black spheres). This N@Mn_6 octahedron appears to serve as a nucleus for the larger network of face-sharing octahedra that complete the Mackay modules, filling up most of the remaining volume of the structure. In Figure 3.4, we show this assembly in more detail beginning with the now familiar triangular unit of vertex-sharing Si@Mn_{12} icosahedra (Figure 3.4a). We gradually fill in the surrounding octahedra (Figures 3.4b-c) until the full module is formed. These octahedra create a concave hole on the surface of the module, which acts as a docking point for the apical icosahedron of the TCP module above and below along **b** (Figure 3.4d).

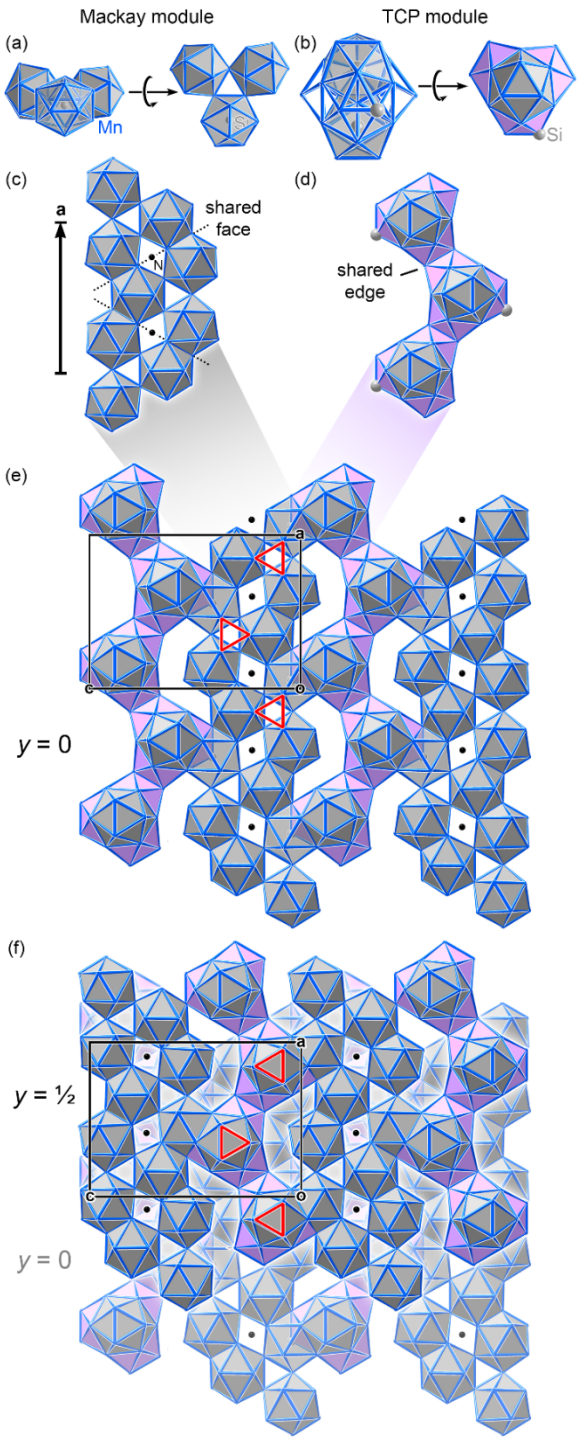

Figure 3.3. The assembly of icosahedra in $Mn_{39}Si_9N_x$. (a) The triangular core of the Mackay module and (b) the TCP module are based on Si-centered (gray) and Mn-centered (lavender) icosahedra, respectively. (c-d) Both modules form zigzag chains along **a**, which (e) interpenetrate to form layers that (f) nest through shared triangles of Mn atoms between the Mackay modules of one layer and the TCP modules of the next (red triangles).

Tracing out the topology of face-sharing octahedra further, we observe that the N-centered octahedra act as bridges between Mackay modules along **a** and **c**, linking the $y = 0$ and $y = ½$ layers and creating a continuous 3D framework that extends through the whole crystal. The continuity of this network suggests a facile path for N diffusion (see Figure B.6 in Appendix B.5), potentially making this structure interesting for catalytic applications.

3.4 Conclusions

Altogether, the $Mn_{39}Si_9N_x$ structure is based on the intergrowth of two different domain types: one based on packing of Mn/Si tetrahedra (the TCP modules and the icosahedra of the Mackay modules), and one built from face-sharing octahedra (the remainders of the Mackay modules) that accommodate N. The individual coordination environments in these regions contain bonding based on either Mn-Si or Mn-N interactions, with the majority of Mn atoms serving as a buffer between these silicide and nitride domains. Zooming out slightly, however, it is clear that these two bonding types do not stray far from each other. Every octahedron in the structure is face-sharing with a Si-centered icosahedron. This aligns with our expectations for epitaxial stabilization between the negative and positive Mn-Mn CPs expected for $N@Mn_6$ and $Si@Mn_{12}$ units, respectively. While the structure strictly avoids direct contact between N and Si, it maximizes the interfacial interactions of their coordination polyhedra.

The complex structural features of $Mn_{39}Si_9N_x$ also hint at the potential for complicated magnetic behavior, as the antiferromagnetic correlations often exhibited by Mn-rich materials may be frustrated by the prevalence of triangular and tetrahedral arrangements.[41-44] As detailed in the Appendix B.4, our measurements show a gradual increase in magnetic moment as the temperature is lowered, down to ~20

K. At this point, the zero-field- and field-cooled curves diverge, with the former turning downwards. These features point to antiferromagnetic or potentially spin-glass character,[45] but given the presence of υ-$Mn_{81.5}Si_{18.5}$ (whose magnetic behavior remains unmeasured) in the samples, more definitive characterization of $Mn_{39}Si_9N_x$'s magnetic structure will require further investigation.

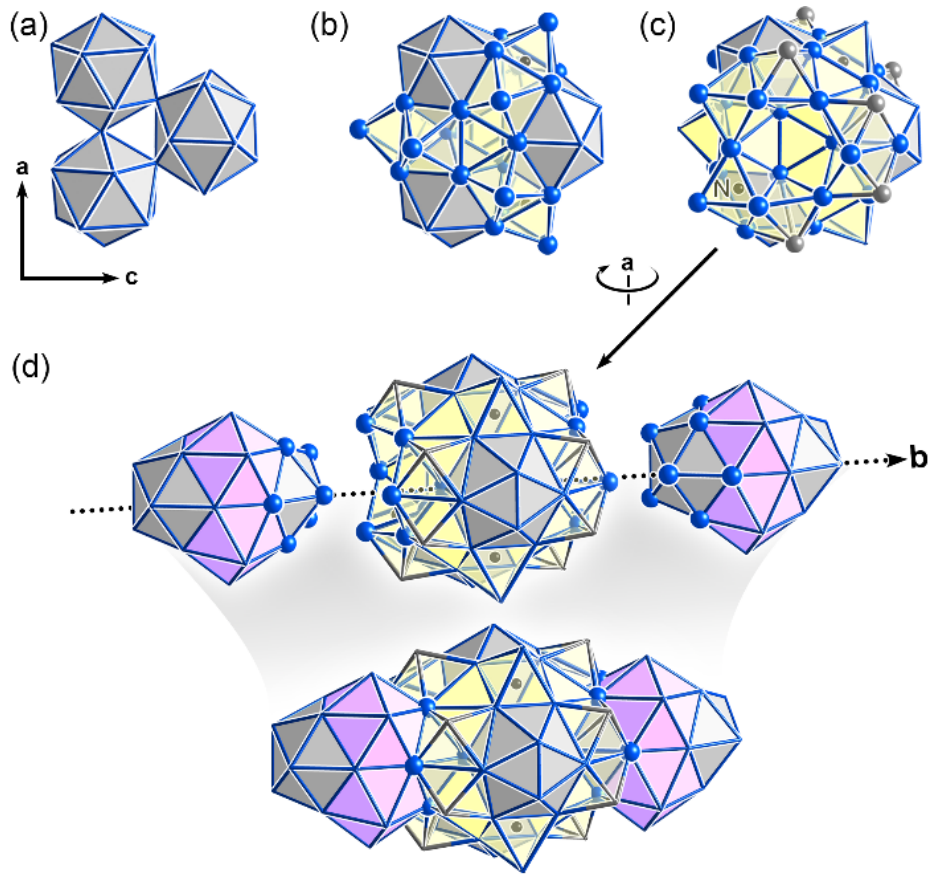

Figure 3.4. The Mackay modules of $Mn_{39}Si_9N_x$. (a) The space within the triangular core of the Mackay module can (b) be filled in with face-sharing octahedra. (c) Adding another layer of octahedra reproduces the full Mackay module, which (d) docks to the apical icosahedra of the TCP module through concavities along **b**.

In this Chapter, we have explored the synthesis and structure of a new intermetallic nitride, in which the solubility of nitrogen in elemental manganese likely facilitates its ability to enter the interstices of a Mn-rich matrix. While the structure of $Mn_{39}Si_9N_x$ is complicated, it can be captured in its entirety through

the assembly of TCP and Mackay cluster-like modules. An intergrowth of silicide and nitride domains emerges, where Mn-Si and Mn-N interactions are separated into $Si@Mn_{12}$ and $N@Mn_6$ coordination environments that nonetheless maximize their interfaces with each other. Such features are a hallmark of the epitaxial stabilization anticipated by the CP schemes of the compound's binary Mn-Si and Mn-N precursors. Of course, they are not limited to the Mn-Si-N system. The generalization of this scenario opens potential pathways to related nitride phases in other systems that combine nitrogen solubility with complementary chemical pressure schemes pointing to the potential for epitaxial stabilization.

3.5 Acknowledgements

We thank Yixu Wang and Michael Roy for insights and advice on the measurement and interpretation of the magnetic properties data. In addition, we are grateful to Ashfia Huq and Katherine Page for discussions and preliminary experiments on the potential for neutron diffraction to distinguish N from C and O in the title phase, Bil Schneider for assistance with the EDS measurements, and the 11-BM mail-in program for collecting synchrotron powder diffraction data. We gratefully acknowledge the financial support of the Department of Energy, Office of Basic Energy Sciences through Grant DE-SC0018938. This work includes calculations that used computing resources supported by NSF Grant CHE-0840494. Use of the Advanced Photon Source at Argonne National Laboratory was supported by the U. S. Department of Energy, Office of Science, Office of Basic Energy Sciences, under Contract No. DE-AC02-06CH11357. A portion of this research used resources at the Spallation Neutron Source, a DOE Office of Science User Facility operated by the Oak Ridge National Laboratory.

3.6 References

(1) Rauch, P. E.; Simon, A. The new subnitride $NaBa_3N$; an extension of alkali metal suboxide chemistry. *Angew. Chem. Int. Ed.* **1992**, *31*, 1519-1521.

(2) Juza, R.; Langer, K.; Von Benda, K. Ternary nitrides, phosphides, and arsenides of lithium. *Angew. Chem. Int. Ed.* **1968**, *7*, 360-370.

(3) Jacobsen, C. J. Novel class of ammonia synthesis catalysts. *Chem. Commun.* **2000**, 1057-1058.

(4) Michalsky, R.; Avram, A.; Peterson, B.; Pfromm, P. H.; Peterson, A. Chemical looping of metal nitride catalysts: low-pressure ammonia synthesis for energy storage. *Chem. Sci.* **2015**, *6*, 3965-3974.

(5) Matthias, B.; Hulm, J. A search for new superconducting compounds. *Phys. Rev.* **1952**, *87*, 799.

(6) Balbarin, V.; Van Dover, R.; DiSalvo, F. The high temperature preparation and property measurements of $CaTaN_2$: A ternary superconducting nitride. *J. Phys. Chem. Solids* **1996**, *57*, 1919-1927.

(7) Cava, R. J.; Zandbergen, H.; Batlogg, B.; Eisaki, H.; Takagi, H.; Krajewski, J.; Peck, W.; Gyorgy, E.; Uchida, S. Superconductivity in lanthanum nickel boro-nitride. *Nature* **1994**, *372*, 245-247.

(8) Amano, H.; Kito, M.; Hiramatsu, K.; Akasaki, I. P-type conduction in Mg-doped GaN treated with low-energy electron beam irradiation (LEEBI). *Jpn. J. Appl. Phys.* **1989**, *28*, L2112.

(9) Pust, P.; Weiler, V.; Hecht, C.; Tücks, A.; Wochnik, A. S.; Henß, A.-K.; Wiechert, D.; Scheu, C.; Schmidt, P. J.; Schnick, W. Narrow-band red-emitting $Sr[LiAl_3N_4]: Eu^{+2+}$ as a next-generation LED-phosphor material. *Nature Mater.* **2014**, *13*, 891-896.

(10) Williams, W. S. The thermal conductivity of metallic ceramics. *JOM* **1998**, *50*, 62-66.

(11) Vepřek, S.; Reiprich, S. A concept for the design of novel superhard coatings. *Thin Solid Films* **1995**, *268*, 64-71.

(12) Miao, M.; Lukashev, P.; Herwadkar, A.; Lambrecht, W. R. Crystal structure, electronic structure and magnetism of transition metal nitrides. *Phys. Status Solidi C* **2005**, *2*, 2516-2519.

(13) Coey, J. M. D.; Smith, P. A. I. Magnetic nitrides. *J. Magn. Magn. Mater.* **1999**, *200*, 405-424.

(14) Sun, W.; Bartel, C. J.; Arca, E.; Bauers, S. R.; Matthews, B.; Orvañanos, B.; Chen, B.-R.; Toney, M. F.; Schelhas, L. T.; Tumas, W.; Tate, J.; Zakutayev, A.; Lany, S.; Holder, A. M.; Ceder, G. A map of the inorganic ternary metal nitrides. *Nature Mater.* **2019**, *18*, 732.

(15) Tareen, A. K.; Priyanga, G. S.; Behara, S.; Thomas, T.; Yang, M. Mixed ternary transition metal nitrides: A comprehensive review of synthesis, electronic structure, and properties of engineering relevance. *Prog. Solid State Chem.* **2019**, *53*, 1-26.

(16) Höhn, P.; Niewa, R. Nitrides of Non-Main Group Elements In *Handbook of Solid State Chemistry* 2017, p 251-359.

(17) Weil, K.; Kumta, P.; Grins, J. Revisiting a rare intermetallic ternary nitride, Ni_2Mo_3N: crystal structure and property measurements. *J. Solid State Chem.* **1999**, *146*, 22-35.

(18) DiSalvo, F. J.; Clarke, S. J. Ternary nitrides: a rapidly growing class of new materials. *Curr. Opin. Solid State Mater. Sci.* **1996**, *1*, 241-249.

(19) Okamoto, H. Comment on Mn-N (Manganese-Nitrogen). *J. Phase Equilib.* **1994**, *15*, 451-452.

(20) Kim, E.-J.; Pak, J.-J.; You, B.-D. Nitrogen solubility in liquid manganese and ferromanganese alloys. *Metall. Mater. Trans. B* **2001**, *32*, 659-668.

(21) Pehlke, R. D.; Elliott, J. F. Solubility of nitrogen in liquid iron alloys. *AIME Transactions* **1960**, *218*, 1088-1101.

(22) Prioux, D.; Bigot, J. Solubility of Nitrogen in High-Purity Chromium at Temperatures Between 400 and 950 Degrees C. *Cr. Acad. Sci. C. Chim.* **1972**, *275*, 1025.

(23) Shoemaker, C.; Shoemaker, D. The crystal structure of the ν phase, $Mn_{81.5}Si_{18.5}$. *Acta Crystallogr. B* **1971**, *27*, 227-235.

(24) Spinat, P.; Herpin, P. Etudes par diffraction de neutrons de la phase Mn_5SiC et des solutions solides $(Mn_{1-x}Mo_x)_5SiC$,$(Mn_{1-x}Fe_x)_5SiC$. Propriétés structurales et magnétiques. *B. Mineral.* **1976**, *99*, 13-20.

(25) Spinat, P.; Brouty, C.; Whuler, A.; Herpin, P. Etude structurale de la phase `Mn_8Si_2C'. *Acta Crystallogr. B* **1975**, *31*, 541-547.

(26) Spinat, P.; Fruchart, R.; Kabbani, M.; Herpin, P. Structure de Mn5 Si C. *B. Mineral.* **1970**, *93*, 171-184.

(27) Kante, S.; Leineweber, A. The iron silicocarbide in cast irons revisited. *J. Alloys Compd.* **2020**, *815*, 152468.

(28) l'He, P.; Chaudoue, P.; Fruchart, R.; Shoemaker, C.; Shoemaker, D. L'analogie des modes d'insertion et d'empilement dans les phases $Nd_2Fe_{14}B$, Mn_5SiC, et Fe_5SiB_2. *J. Solid State Chem.* **1985**, *59*, 54-59.

(29) Fredrickson, R. T.; Guo, Y.; Fredrickson, D. C. Epitaxial Stabilization between Intermetallic and Carbide Domains in the Structures of $Mn_{16}SiC_4$ and $Mn_{17}Si_2C_4$. *J. Am. Chem. Soc.* **2016**, *138*, 248-256.

(30) Hilleke, K. P.; Fredrickson, D. C. Discerning Chemical Pressure amidst Weak Potentials: Vibrational Modes and Dumbbell/Atom Substitution in Intermetallic Aluminides. *J. Phys. Chem. A* **2018**, *122*, 8412-8426.

(31) Berns, V. M.; Engelkemier, J.; Guo, Y.; Kilduff, B. J.; Fredrickson, D. C. Progress in Visualizing Atomic Size Effects with DFT-Chemical Pressure Analysis: From Isolated Atoms to Trends in AB_5 Intermetallics. *J. Chem. Theory Comput.* **2014**, *10*, 3380-3392.

(32) Guo, Y.; Fredrickson, D. C. On the Functionality of Complex Intermetallics: Frustration, Chemical Pressure Relief, and Potential Rattling Atoms in $Y_{11}Ni_{60}C_6$. *Inorg. Chem.* **2016**, *55*, 10397-10405.

(33) Guillaud, C.; Wyart, J. Alliages binaires ferromagnétiques du manganèse (arséniures, azotures). *Rev. Metall.* **1948**, *45*, 271-276.

(34) Bouchard, J. Etude structurale des carbures de manganese. *Ann. Chim.* **1967**, *2*, 353-366.

(35) Kaufman, L.; Nesor, H. Coupled phase diagrams and thermochemical data for transition metal binary systems-IV. *Calphad* **1978**, *2*, 295-318.

(36) Trömel, G.; WD, F.; Koch, K.; Schaberg, F. Das Zustandsdiagramm Des Systems Mangan-Sauerstoff. *Erzmetall* **1976**, *29*, 234.

(37) Elser, V.; Henley, C. L. Crystal and quasicrystal structures in Al-Mn-Si alloys. *Phys. Rev. Lett.* **1985**, *55*, 2883.

(38) Yang, Q. Structures of Ti_2(Ni, V) in crystalline and quasicrystalline phases. *Philos. Mag. Lett.* **1988**, *57*, 171-176.

(39) Janot, C.; De Boissieu, M. Quasicrystals as a hierarchy of clusters. *Phys. Rev. Lett.* **1994**, *72*, 1674.

(40) Mackay, A. L. A dense non-crystallographic packing of equal spheres. *Acta Crystallogr.* **1962**, *15*, 916-918.

(41) Wijn, H. P. *Magnetic Properties of Metals: d-elements, alloys and Compounds*; Springer Science & Business Media, 2012.

(42) Greedan, J. E. Geometrically frustrated magnetic materials. *J. Mater. Chem.* **2001**, *11*, 37-53.

(43) Hermann, R.; Wendrock, H.; Rodan, S.; Rößler, U.; Blum, C.; Wurmehl, S.; Büchner, B. Single crystal growth of antiferromagnetic Mn_3Si by a two-phase RF floating-zone method. *J. Cryst. Growth* **2013**, *363*, 1-6.

(44) Li, C.; Yang, Y.; Lv, L.; Huang, H.; Wang, Z.; Yang, S. Fabrication and magnetic characteristic of ferrimagnetic bulk Mn_4N. *J. Alloys Compd.* **2008**, *457*, 57-60.

(45) Benbow, E. M.; Dalal, N. S.; Latturner, S. E. Spin glass behavior of isolated, geometrically frustrated tetrahedra of iron atoms in the intermetallic $La_{21}Fe_8Sn_7C_{12}$. *J. Am. Chem. Soc.* **2009**, *131*, 3349-3354.

Chapter 4.

Intermetallic Reactivity: $Ca_3Cu_{7.8}Al_{26.2}$ and the Role of Electronegativity in the Stabilization of Modular Structures

This chapter has been accepted for publication in Inorganic Chemistry in Feb. 2020: Synthesis of the $Ca_3Cu_{7.8}Al_{26.2}$ samples and collection of the crystallographic, diffraction, and energy dispersive spectroscopy data described in this chapter was performed by Geisler. Data analysis and interpretation, computational procedures, and preparation of the manuscript were the work of Peterson.

4.1 Abstract

The structural chemistry of intermetallic phases is generally viewed in terms of what crystal structure will be most stable for a given combination of metallic atoms. And yet, individual atoms don't always make the best reference points. As the numbers of elements involved in compounds increases, their structures can often appear to be assembled from structural motifs derived from simpler compounds nearby in the phase diagram rather than a fundamentally new arrangement of atoms. In this Chapter, we explore the notion that complex multinary phases can be viewed productively in terms of motif-preserving reactions between binary compounds, as opposed to as direct reactions of the component elements. We present the targeted synthesis and structure solution of $Ca_3Cu_{7.8}Al_{26.2}$, an intermetallic phase whose placement in the phase diagram is suggestive of a reaction between $CaAl_4$ and $CuAl_2$. Single crystal X-ray diffraction analysis reveals that this compound crystallizes in the $Y_3TaNi_{6+x}Al_{26}$ (or stuffed $BaHg_{11}$) structure type, and is

constructed from three modules: $Ca@(Cu/Al)_{16}$ polyhedra derived from the $BaAl_4$ type, $Cu@Al_8$ cubes, and Al_{13} cuboctahedra. To help understand this arrangement, we identify forces driving the reactivity of one of the supposed starting materials, $CaAl_4$, through visualization of its atomic charge distributions and chemical pressure scheme, which suggest that the Al sites closest to the Ca atoms should show a high affinity for substitution by Cu atoms. Such a process on its own, however, would lead to overly long Ca-Cu distances and electron deficiencies. When Cu is made available to $CaAl_4$ in the Ca-Cu-Al ternary system, its incorporation in the Ca coordination environments instead nucleates domains of a fluorite-like $CuAl_2$ phase, which act as nodes in the primitive cubic framework of $CaAl_4$- and fluorite-like units. The cubic holes created by this framework are occupied by Al_{13} fcc fragments that donate electrons while also resolving negative CPs in the Ca environments. This structural chemistry illustrates how new elements added to a binary compound at sites with conflicting electronic and atomic size preferences can serve as anchor points for the growth of domains of a different bonding type, a notion that can be applied as a more general design strategy for new intermetallic intergrowth structures.

4.2 Introduction

The synthesis of complex molecular compounds generally follows a retrosynthetic approach, in which one works backwards from the target molecule to structurally related and readily available compounds.[1] This is in stark contrast to the approach taken for intermetallic compounds, which are typically viewed as forming from their component elements. Indeed, the synthesis of intermetallics usually involves combining stoichiometric ratios of elemental metals at high temperatures to yield thermodynamically favorable products. However, such phases are often known to exhibit structural fragments or modules

characteristic of simpler compounds,[2-11] such as the nanoscale domains of the $MgCu_2$-type inside the $NaCd_2$ structure[12-15] or the ordered clusters comprising the Al-Cu-Ta structures of unprecedented complexity.[16,17] This observation implies that the chemical and geometrical features of complex intermetallics can be traced back to the structures of simpler compositionally related phases, not unlike the relationship of a molecular precursor and product. In this Chapter, we present the crystal structure determination and theoretical analysis of $Ca_3Cu_{7.8}Al_{26.2}$, whose geometrical features point to a generalizable strategy for harnessing the reactivity of intermetallic compounds to create complex intergrowth phases.

The observation that complexity can emerge from the conglomeration of fragments of simple structures raises the question of what attractive forces drive such assemblies and prevent simple phase segregation. Electron transfer between electron-rich and electron-poor domains is one driving force that has been proposed for the ternary aluminides $TiNi_{1.5}Al_5$ and $Fe_{14}Pd_{17}Al_{69}$.[18] Likewise, the cancelation of complementary atomic packing strains has been evoked to account for the biphasic morphologies of intermetallic carbides[19,20] and the quasicrystal approximant $Ca_{10}Cd_{27}Cu_2$.[21] Still, it remains unclear how comprehensive these mechanisms are, and what other forces may be guiding the formation of complex intergrowth structures.

To build on our understanding of these mechanisms and search for more, we can look to ternary intermetallics that are compositionally positioned between two binary phases. An intriguing case for this study was found in the Ca-Cu-Al ternary system, which contains 10 ternary and 11 binary compounds at a variety of compositions.[22] Perhaps most promising, the Al-rich region shown in Figure 4.1 contains a

phase whose structure remains unknown, but whose composition of $CaCu_2Al_7$ lies almost exactly on the line representing intermetallic compositions between $CaAl_4$ and $CuAl_2$.

As we will see below, a structural determination of this phase reveals a $Y_3TaNi_{6+x}Al_{26}$-type[23] intermetallic of composition $Ca_3Cu_{7.8}Al_{26.2}$ that unites geometrical motifs of $CaAl_4$, fcc-Al, and $CuAl_2$—albeit in the fluorite type—into a single complex structure. Analysis of the chemical forces in $CaAl_4$ reveals an electronegativity-driven reactivity towards a Cu-containing phase. Simple Cu/Al substitution, however, is thwarted by destabilizing atomic packing and electron counting effects. Navigating these challenges leads to structural rearrangements involving the emergence of Al_{13} fcc clusters and the growth of fluorite-type $CuAl_2$ domains in the observed ternary structure. Analysis of this compound suggests a more general model for the anticipation of structural complexity, in which the affinity of one binary intermetallic for a third element offered by a second phase, in this case Cu from $CuAl_2$, can anchor domains of different bonding types to each other, promoting their intergrowth.

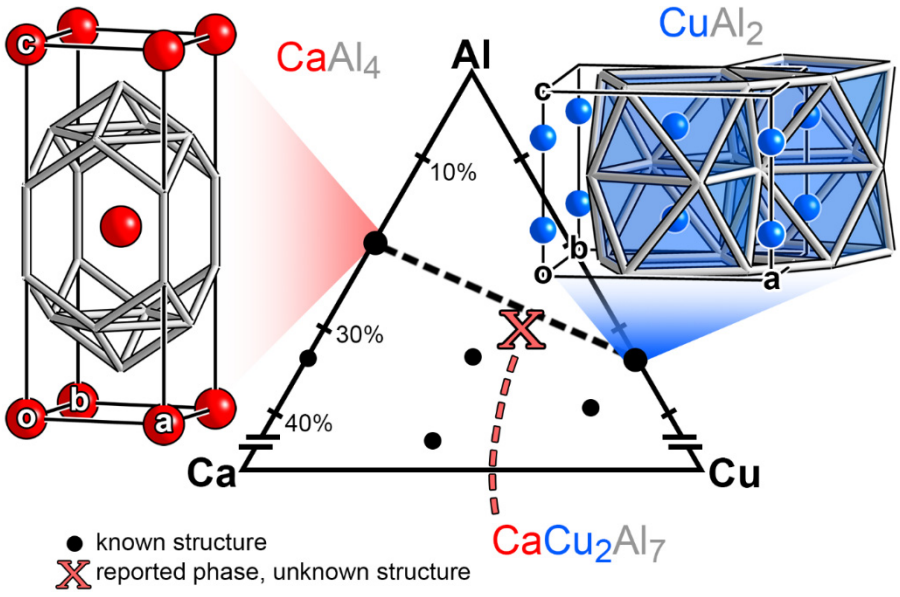

Figure 4.1. Binary and ternary phases in the Ca-Cu-Al system, showing the reported $CaCu_2Al_7$ phase at a composition close to the line between $CaAl_4$ and $CuAl_2$.

4.3 Experimental

4.3.1 Synthetic Procedures

Samples were prepared by mixing of Ca (Alfa Aesar, 99.5%), Cu (Strem, 99.9%), and Al (Strem, 99.7%) powders under argon, and grinding them using an agate mortar and pestle. After mixing, samples were pressed into pellets and melted with an arc welder three times on alternating sides under flowing Ar. Due to the small grain size and vapor pressure of Al, a slight excess of Al powder was used (2% excess) to account for lost mass during mixing, pellet pressing, and arc welding. After arc welding, samples were transferred into fused silica ampoules and sealed under vacuum (<100 mtorr) for heat treatment. Following the synthetic procedure reported in the literature, the samples were first heated to 800 °C and held for 24 h, then cooled over 20 h to 500 °C, annealed for 336 h, and finally cooled to room temperature over the course of 125 h.[22]

4.3.2 Single Crystal X-ray Diffraction

Single crystals were picked from the crushed bulk sample and mounted at the ends of pulled glass fibers. The crystals chosen were metallic gray in color and often exhibited plate-like habits. Single crystal X-ray diffraction data were collected using an Oxford Diffraction Xcalibur E diffractometer with graphite-monochromatized Mo Kα radiation (λ = 0.71073 Å) at room temperature. The CrysAlis Pro software package (version 171.38.43) provided by the manufacturer was used for run list optimization and processing of frame data. The structure was solved using the charge-flipping algorithm[24,25] in the SUPERFLIP program,[26] and refined on F^2 and modeled with JANA2006.[27] The VESTA[28] and Diamond

3[29] programs were used to visualize and analyze the electron density and structural model. Selected crystallographic data is provided in Table 1, while the refined coordinates are listed in Table 2. Further details are provided in the Appendix C.1. A Crystallographic Information File (CIF) can also be obtained from the Cambridge Crystallographic Data Centre upon citing the Deposition Number 1978515.

4.3.3 Powder X-ray Diffraction

The crushed sample was ground into a uniform powder with an agate mortar and pestle, and spread onto a Si Zero-Diffraction plate. Powder X-ray diffraction data were collected under Cu Kα radiation (λ = 1.5419 Å) on a Bruker D8 Advance diffractometer with Lynxeye detector from 2θ = 15°–59.91°. The resulting pattern was analyzed using the Match! version 3.4.2 software.[30]

4.3.4 Energy Dispersive Spectroscopy

Fragments of the sample were fixed in epoxy inside hollow Al bullets, and polished with diamond lapping film to a fineness of 0.5 μm finish to expose flat cross sections. The surface was then coated with a layer of conductive carbon and mounted in a sample holder for analysis with a Hitachi S-3100N scanning electron microscope. Energy dispersive spectroscopy data were collected at an accelerating voltage of 15 keV with an Oxford Instruments X-act detector and analyzed using the Oxford Instruments AZtec software package version 3.2. This analysis showed a predominance of two phases that were determined to be $Ca_{3.00(3)}Cu_{7.61(15)}Al_{28.48(14)}$ (majority) and $Ca_{1.00(2)}Cu_{4.20(21)}Al_{7.87(21)}$ (minority). Back-scattered electron images showing the phases present in the sample are given in Appendix C.2.

Table 1. Selected Crystallographic Data for $Ca_3Cu_{7.8}Al_{26.2}$

refined composition	$Ca_3Cu_{7.82(5)}Al_{26.18(5)}$
EDS composition	$Ca_{3.00(3)}Cu_{7.61(15)}Al_{26.48(14)}$
Pearson symbol	*cP*37
space group	$Pm\bar{3}m$ (No. 221)
a (Å)	8.5152(1)
cell volume (Å^3)	617.43(1)
Z	1
crystal volume (mm^3)	0.017 × 0.056 × 0.091
crystal color, shape	grey, plate
data collection temp.	295 K
radiation source, λ (Å)	Mo Kα, 0.71073
absorption coefficient (mm^{-1})	8.162
absorption correction	analytical
θ_{min}, θ_{max}	3.38, 28.890
refinement method	F^2
$R_{int}(I > 3\sigma)$, R_{int}(all)	8.66, 9.67
no. of reflections ($I > 3\sigma$, all)	5731, 14098
unique reflections ($I > 3\sigma$, all)	157, 207
no. of parameters	17
$R(I > 3\sigma)$, $R_w(I > 3\sigma)$	1.92, 3.57
R(all), R_w(all)	4.10, 4.34
$S(I > 3\sigma$, all)	1.06, 1.11
$\Delta\rho_{max}$, $\Delta\rho_{min}$ (e$^-$/Å^3)	0.73, -0.99

4.3.5 Computational Procedures

DFT-Chemical Pressure (CP) schemes were calculated for $CuAl_2$, $CaAl_4$, $CaCu_2Al_2$, anti-$CaCu_2Al_2$, and a Cu-rich ordered model of the $Ca_3Cu_{7.8}Al_{26.2}$ structure ($Ca_3Cu_{13}Al_{21}$). The unit cell parameters and atomic positions of these structures, as well as of $CuAl_2$ in its own type and the fluorite type, were optimized with LDA-DFT using ABINIT[31-34] and Hartwigsen–Goedecker–Hutter norm-conserving pseudopotentials (valence-only for Ca and Al, semicore for Cu).[35] The energy cutoff was set to 30 Ha for $CaAl_4$, 105 Ha for the Cu-containing ternaries, and 120 Ha for both $CuAl_2$ models. For the CP calculations,

single point ABINIT calculations were done on structures with volumes contracted and expanded slightly (1.5%) to generate the kinetic energy and electron densities, and potential maps used for the creation of the 3D chemical pressure maps.

CPpackage2 was used to generate final chemical pressure maps using the core unwarping procedure[36] and mapping of the nonlocal pseudopotential energies.[37] The localized electron count for Cu was set to 5.50889 eletrons (see Appendix C.3.1 for the localized electron calibration procedure).[37] CP maps were divided into contact volumes using the Hirshfeld-inspired integration scheme,[36] and the resulting pressures between atomic pairs were projected onto atom-centered spherical harmonics ($l \leq 4$) and visualized with the in-house Matlab program *Figuretool2*.

Table 2. Refined atomic coordinates for $Ca_3Cu_{7.8}Al_{26.2}$

Site	Element	Multiplicity	*x*	*y*	*z*	$U_{equivalent}$	Occupancy
Cu1	Cu	1	0	0	0	0.0152(2)	1
Ca2	Ca	3	0.5	0	0	0.0126(4)	1
Al1	Al	12	0.5	0.26379(9)	0.26379(9)	0.0149(3)	1
Al2	Al	1	0.5	0.5	0.5	0.0139(5)	1
Al3	Al	8	0.17035(9)	0.17035(9)	0.17035(9)	0.0118(2)	1
Al4a	Cu	12	0.34102(10)	0.34102(10)	0	0.0121(3)a	0.568(4)
Al4b	Al	12	0.3689(4)	0.3689(4)	0	0.0121(3)a	0.432(4)

To more accurately incorporate the ionic character of the atoms, the Bader program[38-41] was used to calculate atomic charges on each atom, with the core electron density distributions being added to the valence density maps for determination of the Bader volumes. Radial electron density profiles for the free ions were then generated with the Atomic Pseudopotential Engine[42] for 0% and 15% of the Bader charge, beyond which convergence issues were encountered for the free Cu ions. CP schemes presented in this Chapter are shown using the profiles for 15% of the calculated Bader charge. Full chemical pressure

schemes at 0% and 15% ionicity are shown for $CaAl_4$, $CaCu_2Al_2$, anti-$CaCu_2Al_2$, and $Ca_3Cu_{13}Al_{21}$ in Appendix C.3.

Density of states (DOS) curves were generated with the Vienna Ab initio Simulation Package (VASP)[43-46] via single point calculations on the optimized geometries in high-precision mode. These calculations used the projector augmented wave (PAW) potentials provided with the package[47,48] and the generalized gradient approximation (GGA).[49-52]

4.4 Results and Discussion

4.4.1 Synthesis and Characterization

According to the reported Ca-Cu-Al phase diagram at 500 °C, the $CaCu_2Al_7$ phase lies at a composition almost directly between the $CaAl_4$ and $CuAl_2$ binaries,[22] but its crystal structure remains unknown. We thus sought to synthesize this compound with the goal of tracing its structural features to bonding or packing constraints apparent in these nearby binary phases. After pressing pellets of the combined elements under argon, we arc-welded the samples and annealed them for 14 days at 500 °C. Silvery gray ingots emerged from this procedure which were brittle and easily ground in an agate mortar and pestle.

Powder X-ray diffraction data collected on the products (Figure 4.2) exhibited a series of peaks attributable to the ternary phase $CaCu_4Al_8$, a neighbor in the composition space to the target phase, as well as fcc-Al. The remaining peaks were initially assigned to the Cu_9Al_4 binary phase (a = 8.7023 Å), but on closer inspection were found to correspond to an 8.52 Å cubic unit cell that couldn't be matched to any known structure in the system. SEM-BSE imaging and EDS analysis (see Appendix C.2) indicated that the

sample contains a majority phase with a composition of $Ca_{1.00(1)}Cu_{2.54(5)}Al_{8.83(5)}$, which is qualitatively close to the $CaCu_2Al_7$ target phase, with the remainder attributed to the neighboring $CaCu_4Al_8$ phase with a composition of $Ca_{1.00(2)}Cu_{4.20(2)}Al_{7.87(7)}$.

Single crystals picked from the bulk sample yielded clean diffraction patterns which could be indexed to a cubic unit cell of $a \approx 8.52$ Å, suggesting that they correspond to the structurally unknown $CaCu_2Al_7$ phase detected in the powder patterns and EDS data. Full data sets collected on these crystals showed cubic point symmetry and no systematic absences, consistent with the space group $Pm\bar{3}m$.

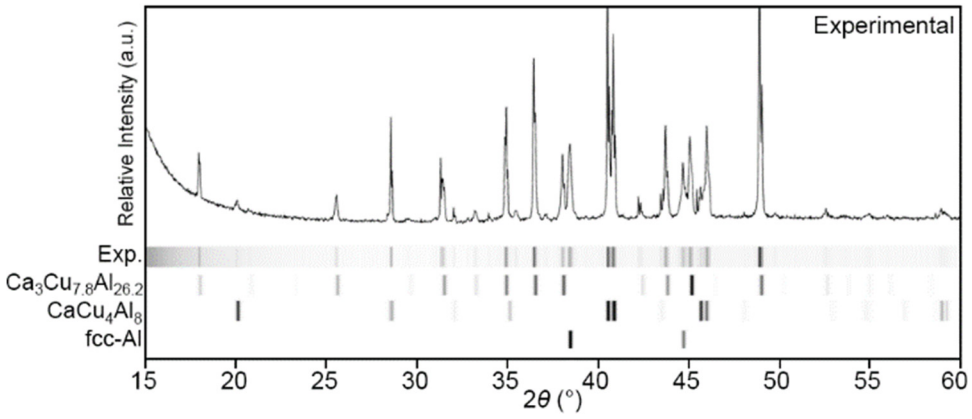

Figure 4.2. Powder X-ray diffraction analysis of a sample with nominal composition of $Ca_3Cu_{7.75}Al_{26.69}$. Below the intensity vs. 2θ profile, film strip representations of the experimental powder data are compared to the simulated patterns of $Ca_3Cu_{7.8}Al_{26.2}$, $CaCu_4Al_8$, and the fcc-Al structure, where peak intensity is indicated by the darkness of the lines.

4.4.2 The Crystal Structure of $Ca_3Cu_{7.8}Al_{26.2}$

The crystallographic model obtained from the data using the charge-flipping algorithm contained 37 atoms per unit cell at 7 crystallographically unique positions. This initial model, however, was quite Ca-rich relative to determined EDS composition, and was substantially improved by reassigning one Ca site with unrealistically short interatomic distances to its neighbors as a Cu/Al mixed site. Anisotropic residual

electron densities and elongated thermal ellipsoids at this location were further indicative of a split atomic position. When allowed to separate during refinement, the Cu and Al components on this site spread apart from each other by 0.34 Å. Attempts to model the other Al and Cu sites as mixed resulted in minority occupancies within the standard uncertainty of zero. The refined model has a composition of $Ca_3Cu_{7.82(6)}Al_{26.18(6)}$—nearly within 2σ of that determined from EDS ($Ca_{3.00(3)}Cu_{7.61(15)}Al_{26.48(14)}$).

Figure 4.3 illustrates the refined model obtained from single crystal analysis. Its structure can be understood in terms of three basic modules: $Cu@Al_8$ cubes at the corners of the cell (blue), $CaAl_4$-like polyhedra on the cell edges (pink), and Al_{13} cuboctahedra at the cell centers (black). Here, the Cu- and Ca- centered units share square Al faces, forming a continuous primitive cubic network. This framework leaves large central vacancies, providing space for the Al_{13} cuboctahedra, a fragment derivable from the structure of fcc-Al. This depiction captures every atomic position in the structure.

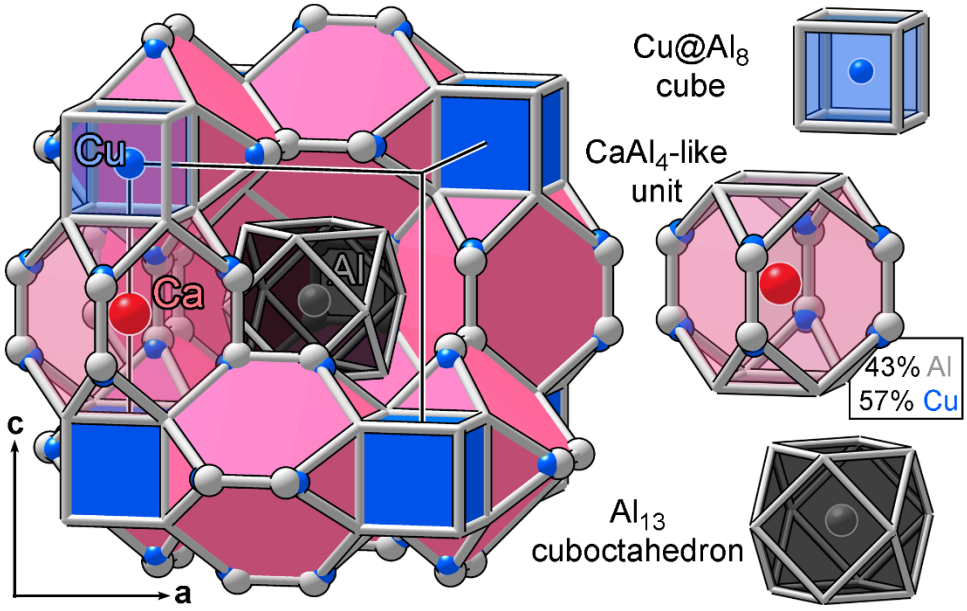

Figure 4.3. The structure of $Ca_3Cu_{7.8}Al_{26.2}$ viewed as an assembly of three modules: $Cu@Al_8$ cubes, $CaAl_4$-like polyhedra, and Al_{13} cuboctahedra.

The Ca coordination environment of $Ca_3Cu_{7.8}Al_{26.2}$ is remarkably similar to that of the $BaAl_4$-type high temperature $CaAl_4$ binary structure.[53] Unlike the binary structure, however, the 8 equatorial dumbbell atoms of the $CaAl_4$-like polyhedron (gray/blue spheres around Ca in Figure 4.3) show positional and occupational disorder. In the refined crystallographic model, this site is occupied 57% by Cu and 43% by Al. Intriguingly, the position of the atom varies depending on its identity: when occupied by Cu, it lies substantially closer to the two nearest Ca atoms (3.20 Å vs. 3.33 Å). This shift is in line with the smaller metallic radius of Cu (1.28 Å) relative to that of Al (1.43 Å), and has the net effect of shrinking the Ca coordination environment in the presence of Cu.

With these geometrical features, $Ca_3Cu_{7.8}Al_{26.2}$ joins a family of R-T-Al phases (R = group II or III metal, T = transition metal) that adopt the $Y_3TaNi_{6+x}Al_{26}$-type structure.[23,54-57] This geometry has been described as a stuffed derivative of the $BaHg_{11}$ structure,[58] in which an atom occupies the interstitial position at the centers of the cubes on the cell corners, in this case Cu atoms centering the Al_8 cubes. One difference from the other compounds of this type, however, is evident in the cuboctahedron in the cell center. In the other $Y_3TaNi_{6+x}Al_{26}$-type structures as well as the related $BaHg_{11}$-type phase $CaAg_4Al_7$,[59] this polyhedron is occupied by a transition metal, creating a fragment of the $AuCu_3$ type. For $Ca_3Cu_{7.8}Al_{26.2}$, this central position is taken by Al, yielding a 13-atom cluster of fcc-Al.

In our synthetic foray into the Ca-Cu-Al system, we were motivated by an interest in how the structure of the unknown compound is reflected in its position in the phase diagram almost directly on the line between $CaAl_4$ and $CuAl_2$. The $Ca_3Cu_{7.8}Al_{26.2}$ structure indeed demonstrates a tendency for segregation between Ca-Al and Cu-Al interactions, and contains structural modules that are clearly reminiscent of the $CaAl_4$ binary structure. However, several elements of this structure are more unexpected: disordered

Cu/Al occupation of dumbbell sites, cubic Cu coordination environments, inclusions of Al_{13} fcc fragments, and an absence of the square antiprisms characteristic of the $CuAl_2$ type. In the next section, we will see how these features are rooted in bonding and packing issues in the $CaAl_4$ compound neighboring $Ca_3Cu_{7.8}Al_{26.2}$ in the phase diagram.

4.4.3 Driving Forces for Reactivity in $CaAl_4$

The high temperature polymorph of $CaAl_4$ is one member of a large family of $BaAl_4$-type binary structures formed in many combinations of electropositive metals (alkali, alkaline earth, lanthanide) with group 13 metals (Al, Ga, In).[60-65] This framework serves as a parent structure to a variety of superstructures, distortions, and colored derivatives across an even broader array of elements.[66-81] The $BaAl_4$-type framework thus seems to be quite structurally responsive to perturbations in electron count, atomic size, and composition.[82] An analysis of how these factors underlie the structure of $CaAl_4$ can then help us understand its evolution with the addition of another compositional dimension as we move into the ternary space of the Ca-Cu-Al system.

In Figure 4.4, we highlight one simple factor that hints at the potential reactivity of $CaAl_4$: the distribution of valence electron density across its atoms. Figure 4.4a shows a slice of the density through the (1 0 0) plane of the structure. The electron density appears to localize into the Al-Al bonding regions, leaving relatively lower density around the Ca atoms. Such charge transfer conforms to our expectations of the electropositive alkaline earth metal within a p-block atom framework.

In this layer of the structure, the number of electrons concentrated around each Al atom appears correlated with the number of Al-Al bonds in which it participates. Indeed, integration of the electron

density within the Bader volume of each atom (black outlines in Figure 4.4a) shows that the Al atoms with three bonding interactions in the (1 0 0) layer are surrounded by significantly more electron density, resulting in an overall negative charge of −0.59. Conversely, the Al atoms lacking the electron-rich bond oriented along **c** are left having a net positive charge of +0.11.

We can visualize this overall effect in 3D by representing Bader charges as atom-centered spheres (Figure 4.4b).[14,83-85] In this scheme, the spheres are volumetrically proportional to the charge magnitudes, while the sphere color corresponds to the sign of the charge: black for cationic, white for anionic. The structure's Ca atoms thus appear as relatively large black spheres corresponding to a large cationic charge (+0.96), while their closest Al neighbors form anionic dumbbells. The rest of the Al atoms form square nets further away from the Ca atoms (3.49 Å vs. 3.18 Å in the LDA optimized structure), and end up slightly cationic overall. The net charge transfer in the structure is then from the Ca atoms to their nearest dumbbell Al neighbors, which also gain electrons from the square net Al sites.

Notably, this plot of the Bader charges shows a clear distinction between the two Al sites in the $CaAl_4$ structure. Despite occupation by the same element, the charges calculated for the dumbbell and square net sites have opposite signs. Such cases often imply a preference for occupation by elements with different electronegativities, a trend rationalized with the notion of topological charge stabilization (TCS).[86,87] Here, we would expect a less electronegative atom to prefer the square net position, while a more electronegative atom should tend toward the dumbbell site. This is in line with earlier theoretical analyses of the $BaAl_4$ type.[76,87,88]

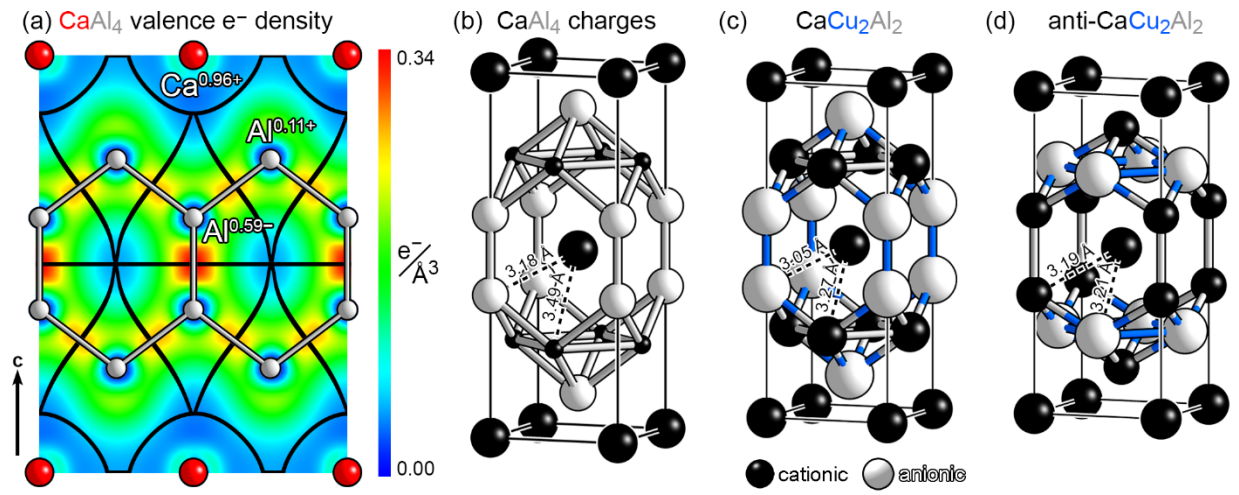

Figure 4.4. LDA-DFT atomic charge distributions in $BaAl_4$-type $CaAl_4$ and two Cu-substituted derivatives. (a) (1 0 0) cross section of the valence electron density of $CaAl_4$, with Bader volume surfaces overlaid in black and integrated charges shown. Calculated Bader charges for (b) $CaAl_4$, (c) $CaCu_2Al_2$, and (d) anti-$CaCu_2Al_2$ represented as spheres whose volumes are proportional to charge magnitude and whose colors indicate the sign of the charge: black for cationic, white for anionic.

A similar story emerges when we consider the atomic size effects in the $CaAl_4$ structure, as revealed by its chemical pressure (CP) scheme (Figure 4.5a). Here, the pressures acting between atoms in the structure are mapped onto spherical harmonics, and visualized with radial plots in which the distance of the surface on each atom from the atomic center is proportional to the sum of the pressure contributions along that direction. The signs of the pressures are given by a color code: white lobes represent positive pressures, where the local arrangement would be stabilized by expansion of the structure, and black lobes correspond to negative pressures, where the atoms are too far apart and would benefit from contraction of the structure.

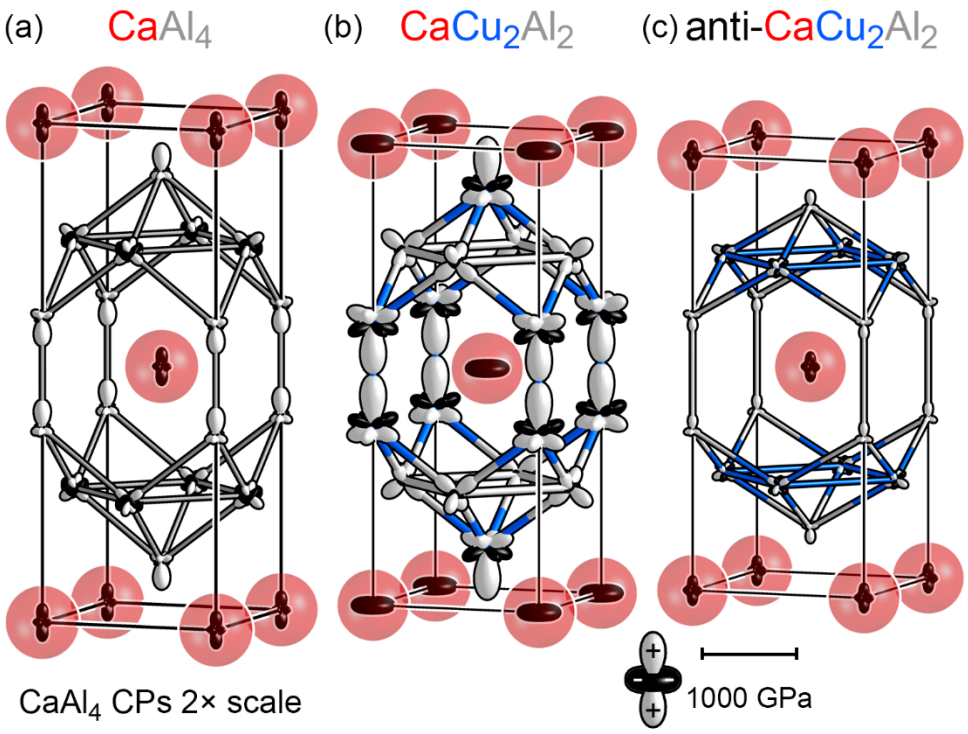

Figure 4.5. Chemical pressure schemes of (a) $CaAl_4$ (shown at 2× scale), (b) $CaCu_2Al_2$, and (c) anti-$CaCu_2Al_2$.

As was seen in our previous CP analysis of the $BaAl_4$ type,[37] there is uniformly negative pressure surrounding the structure's cationic atoms, indicating that their coordination environments are too expansive. In the case of $CaAl_4$, the Ca atoms would prefer tighter coordination by their Al neighbors. This shrinking of the structure around the Ca atoms, however, is prevented by the positive CPs along all of the close Al-Al contacts in the surrounding framework. Relieving the Ca-Al negative CPs through the contraction of the structure would require shortening these already overly-close Al-Al interactions.

Although their general features are similar, the overall pressures experienced by the two Al sites in the structure differ greatly. The positive pressures of the square net atoms are only slightly overbalanced by the negative Ca-Al contacts, resulting in a net CP of −7.66 GPa. On the other hand, dumbbell Al atoms, with their large positive CPs directed toward their partner along **c**, experience positive pressure overall, with a

net CP of +25.70 GPa. From a packing perspective, the two Al sites appear adapted for atoms of different sizes: the square net would prefer a slightly larger atom than Al, while the dumbbell site favors replacement by a smaller atom.

Combining our views of atomic charge and atomic packing, we can develop a picture for potentially favorable atomic substitution patterns in the $CaAl_4$ structure. The square net site is mildly cationic with negative net CP, and so an element that is somewhat larger and more electropositive than Al might substitute favorably onto this position. On the dumbbell site we see the opposite—a smaller, more electronegative atom would be best suited here. Substitution of either site with another atom type is in fact common among $BaAl_4$-type compounds, and at its limit results in the $ThCr_2Si_2$ or anti-$ThCr_2Si_2$ types.[89,90] In our synthetic study of the ternary Ca-Cu-Al system, we have introduced a means to enact this change: the addition of Cu to the system. In the next section, we will explore how the electronic structures of two Cu-substituted models of $CaAl_4$ reflect these expectations, and how such substitution ultimately sets the stage for larger-scale rearrangements to the $Ca_3Cu_{7.8}Al_{26.2}$ structure.

4.4.4 Theoretical Analysis of Cu Substitution into $CaAl_4$

To examine the effects of Cu incorporation into the $CaAl_4$ structure, let's consider derivative structures in which one of the two crystallographic Al sites is occupied by Cu. Because Cu has a smaller metallic radius (1.28 Å for Cu, 1.43 Å for Al) and a higher electronegativity (1.90 for Cu, 1.61 for Al), we expect that it would more favorably substitute onto the $CaAl_4$ dumbbell site, creating a $ThCr_2Si_2$-type derivative which we will simply label "$CaCu_2Al_2$." Alternatively, Cu atoms could substitute into the square net, forming an anti-$ThCr_2Si_2$ structure we will call "anti-$CaCu_2Al_2$." DFT total energy calculations show that

the optimized anti-$CaCu_2Al_2$ arrangement is less energetically favorable by 0.07 eV/atom, aligning with our expectations from the TCS and CP considerations above.

Furthermore, the synergy between the structural topology and atomic electronegativity suggested by TCS analysis of $CaAl_4$ is evident in the charge distributions of the ternary structures (returning to Figure 4.4c). With Cu on the dumbbell sites in $CaCu_2Al_2$, the overall Bader charge scheme qualitatively mirrors that of $CaAl_4$, while showing a quantitative increase in strength of the charges. The electronegativity of the added Cu has supported a large negative charge on the dumbbells, allowing for more stabilizing electrostatic interactions between neighboring atoms.

For anti-$CaCu_2Al_2$ on the other hand, the sites of negative charge accumulation follow the Cu atoms into the square net sites (Figure 4.4d). The charges are again increased, but this time the pattern of anionic and cationic positions has changed to make the Ca atoms and their nearest neighbor Al atoms both positively charged. This distribution runs counter to the arrangement of the Al charges in $CaAl_4$, and places like charges in close proximity to one another. As such, the dumbbell site appears to be a more favorable position for substitution of Cu into the structure.

These trends in the atomic charges are also reflected in the differences in the DFT-optimized geometries of $CaAl_4$ and the two substituted models. In $CaCu_2Al_2$, the attraction between the opposite charges of the Ca and Cu atoms is supported by a shortening of the interatomic contact from 3.18 Å in $CaAl_4$ to 3.05 Å. Conversely, in the anti-$CaCu_2Al_2$ structure, the distances between the dumbbell and Ca atoms—now both cationic—have lengthened to 3.19 Å. Meanwhile, closer Ca-Cu contacts have been obtained through a shortening of the *c*-axis.

The effect of these geometrical differences is also apparent in the CP schemes of our two models, which can also be understood in terms of Cu-induced perturbations on the structure of $CaAl_4$. In both of the model ternary structures, we see contraction of the optimized structure, as we would expect with substitution of Al with smaller Cu atoms. The overall volume change is similar between models, but while $CaCu_2Al_2$ contracts nearly isotropically (~3% shortening of c/a), the anti-$CaCu_2Al_2$ model distorts by shrinking disproportionately along **c** (~12% shortening of c/a).

Figure 4.5b shows the CP scheme for the $CaCu_2Al_2$ structure, where we see qualitatively familiar pressure features to those of $CaAl_4$ (shown at 2× scale in Figure 4.5a), but heavily exacerbated. The negative pressure features in particular are intensified within the **ab** plane of the structure—between Ca and dumbbell Cu atoms—which distorts the negative Ca CPs to a disc-like shape. This intensification of negative pressure within the **ab** plane of $CaCu_2Al_2$ indicates that, although this contact has already shortened through contraction of the unit cell, there is still a strong desire for it to shorten further. This movement, however, is impeded by the competing Cu-Cu and Cu-Al positive pressures in the surrounding framework. From these results, the potential for the relief of positive dumbbell-site CP through substitution of Al with smaller Cu atoms appears to be outweighed by the enhancement of the negative CPs around the Ca atoms.

In contrast to $CaCu_2Al_2$, the CP scheme of anti-$CaCu_2Al_2$ shown in Figure 4.5c is far less intense and appears less strained by atomic packing constraints. The pressure distribution and the shapes of the CP lobes closely mimic those of $CaAl_4$; in fact they are nearly identical. The Ca-Cu negative pressures of this structure are especially dwarfed by comparison to $CaCu_2Al_2$. Does this mean that we should regard the anti-$CaCu_2Al_2$ structure as more favorable? A comparison of the Bader charge distributions and total

energies for the two models hints otherwise. In anti-$CaCu_2Al_2$, the corresponding Ca-Cu distances are actually significantly longer than in $CaCu_2Al_2$ (3.21 Å vs. 3.05 Å), suggesting that the smaller CP magnitudes reflect weaker interactions.[91]

The impact of Cu substitution on $CaAl_4$'s bonding extends beyond the effects of atomic packing. Figure 4.6 compares the density of states (DOS) distributions for $CaAl_4$, $CaCu_2Al_2$, and anti-$CaCu_2Al_2$. For $CaAl_4$, we can see that the Fermi level (E_F) lies near a local DOS minimum, and so we expect the bonding in this structure to be optimized with regard to electron count. In fact, this pseudogap reflects the optimal filling of Al-Al multi-center bonding states as elucidated by Zheng and Hoffmann.[92] The replacement of Al atoms with Cu naturally perturbs this electron-precise situation, as each Cu atom contributes only a single valence electron to the electronic structure, compared to the three valence electrons contributed per Al atom. As a result, in the substituted structures the E_F falls far below this DOS minimum, which is now substantially shallower. These two curves are dominated by peaks corresponding to Cu *d* states, which have only slight mixing into the rest of the electronic structure, and correspond to filled Cu 3*d* subshells.

Overall, the TCS advantages of Cu substitution onto the dumbbell site appears to be obstructed by the atomic packing and electronic issues that result. This observation is supported by the phase diagram[22] and an overview of reported structures in the Inorganic Crystal Structure Database (ICSD),[93,94] which offer no known $ThCr_2Si_2$-type structures in the Ca-Cu-Al ternary system, and no homogeneity range for $CaAl_4$ into the ternary space. However, in the observed $Ca_3Cu_{7.8}Al_{26.2}$, we do in fact see Cu substitution onto the $CaAl_4$-like structural fragment at the dumbbell site as predicted by our TCS and CP analyses of $CaAl_4$. How has the complex ternary structure managed to find a way to simultaneously satisfy the

electronegativity-driven incorporation of Cu without overly disrupting the atomic packing and electronic stability? We will explore this question in the next section, and see how these frustrations are ultimately resolved through structural rearrangement.

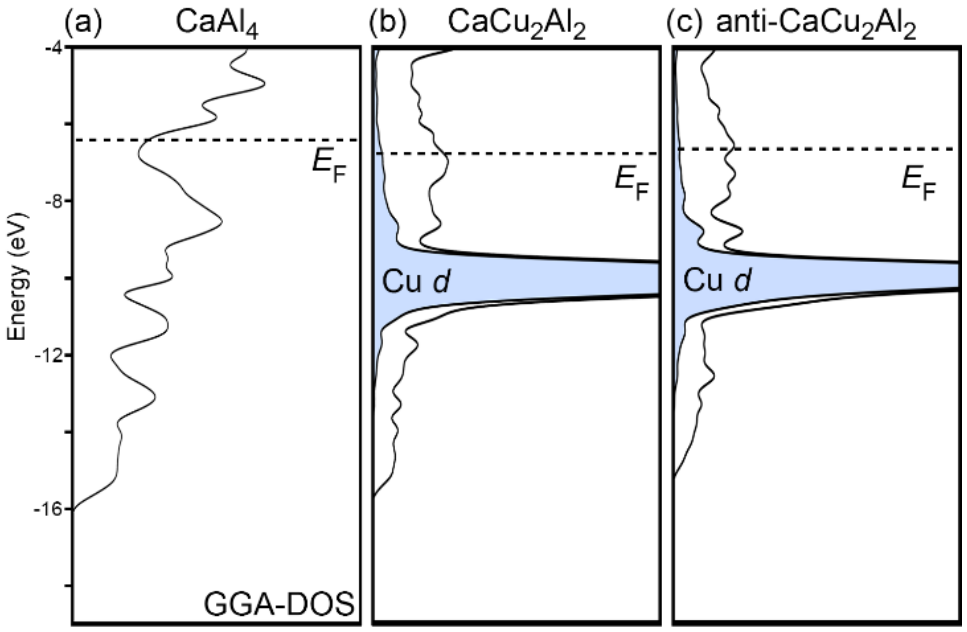

Figure 4.6. Electronic density of states distributions calculated for (a) $CaAl_4$, (b) $CaCu_2Al_2$, and (c) anti-$CaCu_2Al_2$.

4.4.5 Structural Rearrangement to $Ca_3Cu_{7.8}Al_{26.2}$

In our chemical pressure analysis of $CaCu_2Al_2$, we identified intense attractive forces between Ca and Cu atoms manifesting as negative CP in the structure's **ab** plane. To better visualize the aggregation of this stress, in Figure 4.7a-b we take larger slabs of the $CaAl_4$ and $CaCu_2Al_2$ CP schemes along the (1 1 0) direction, displayed such that the Ca and dumbbell Cu atoms are in the plane of the page. CP lobes for just these atoms Ca and Cu atoms are drawn. A comparison of these two schemes shows how the negative pressures aligned horizontally in $CaCu_2Al_2$'s **ab** plane is a defining feature of the structure. Along this

direction, the structure is dominated by the desire to form shorter Ca-Cu distances, in tension with the network of Cu-Al and Cu-Cu interactions already strained by positive pressure.

The vacuities of the $CaCu_2Al_2$ structure—as well as the repulsive interactions that grow in response—cannot be resolved in the $BaAl_4$ type. The Ca atoms are simply not large enough for their coordination by a mixture of Cu and Al atoms, hence the enlarged negative CP. One potential solution to this problem would be to replace Ca with a larger atom. However, none is available in the Ca-Cu-Al system. Instead, the structure finds another solution, using clusters of Al that can occupy larger volumes of space. In the observed structure, one out of every four Ca atoms is replaced with a 13-atom cuboctahedron. The large size and cubic symmetry of this unit is neatly accommodated by rearrangement of the $CaAl_4$-type polyhedra into the primitive cubic framework characteristic of the $BaHg_{11}$ type.

In Figure 4.7c, we show the CP scheme for $Ca_3Cu_{13}Al_{21}$—a Cu-rich ordered model of $Ca_3Cu_{7.8}Al_{26.2}$ in which the Cu/Al mixed sites are completely occupied with Cu—in a layer of polyhedra most closely analogous to that shown for $CaCu_2Al_2$. A comparison of the CP schemes for these two structures reveals the benefits of this rearrangement on the strains in atomic packing. The CPs on the dumbbell Cu atoms have been dramatically relieved, and now show only small negative lobes toward Ca and small positive pressures to their Al neighbors. The dominating Cu-Cu positive pressures of $CaCu_2Al_2$ have completely disappeared, signifying that while these distances have in fact shortened by 0.10 Å relative to $CaCu_2Al_2$, they are well-optimized for their new electronic context. The Ca pressures, while similar in overall magnitude, have changed to a more isotropic shape. This change be correlated with indentations in the Ca CP surface that align with contacts to the atoms in the Al_{13} cluster, which at 2.92 Å are dramatically closer than the Ca neighbors at 3.97 Å in the $CaCu_2Al_2$ structure. Overall, the replacement of a Ca atom with the

Al_{13} fragment and subsequent rearrangement to the stuffed $BaHg_{11}$-type has served to relieve the major atomic packing strains induced through incorporation of Cu. As can be seen in Figure C.2 in Appendix C, the CPs of the $Cu@Al_8$ cube and Al_{13} cluster are also subdued.

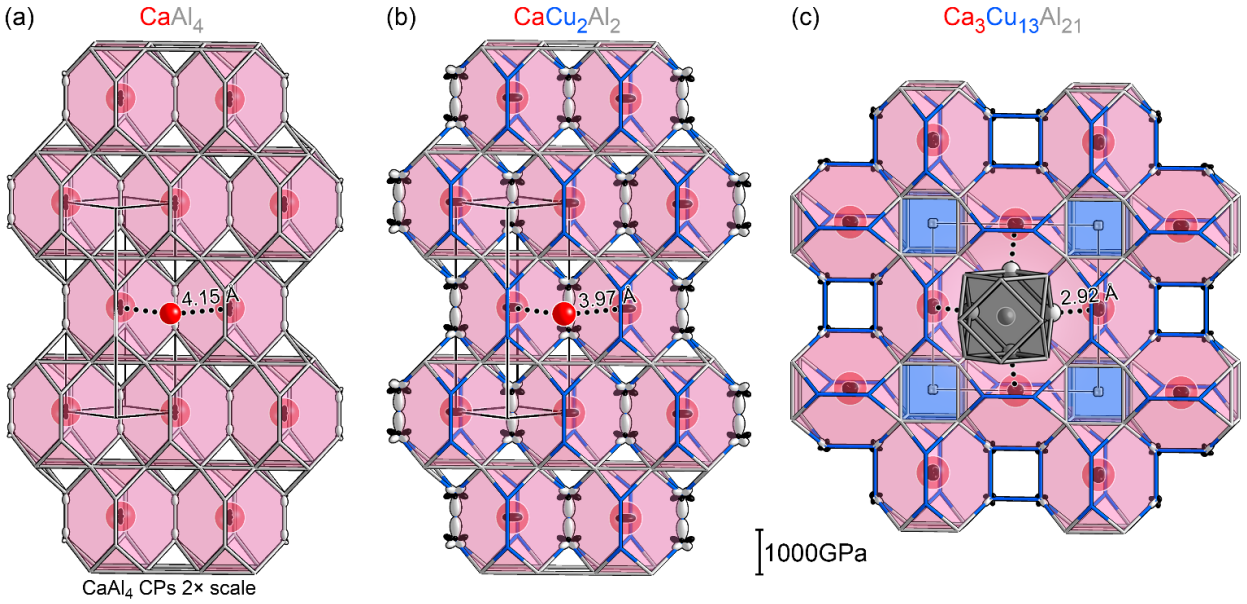

Figure 4.7. Analysis of chemical pressure relief through rearrangement to the $BaHg_{11}$ structure type. (1 1 0) slabs of the (a) $CaAl_4$ and (b) $CaCu_2Al_2$ structures with CP lobes shown for atoms in the Ca-dumbbell plane. (c) An analogous layer of the $Ca_3Cu_{13}Al_{21}$ ordered model of $Ca_3Cu_{7.8}Al_{26.2}$ with CP lobes shown for atoms in the Ca-Cu plane.

In addition to atomic packing issues, we identified the removal of the Fermi level from an electronic pseudogap as a force destabilizing a hypothetical $CaCu_2Al_2$ structure. Figure 4.8a shows that the DOS curve for $Ca_3Cu_7Al_{27}$—an ordered model most closely matching the ternary structure's refined composition—shows that the Fermi level has been restored to a DOS pseudogap. In Figure 4.8b, a possible origin of this can be seen in the distribution of Bader charges for $Ca_3Cu_{13}Al_{21}$ (see Table C.5 in Appendix C). Here, all 13 Al atoms in the fcc-Al cluster are cationic, combining for a total loss of 6.53 electrons. In this way, the added Al_{13} cuboctahedron acts as a source of electrons to the rest of the structure,

compensating for the electrons removed through the substitution of Cu atoms and rectifying the electronic stability of the structure.

4.4.6 $Ca_3Cu_{7.8}Al_{26.2}$ Interpreted as a Reaction Product

In the previous sections, we have seen how chemical factors influence the reactivity and stability of $CaAl_4$ and its potential Cu-substituted derivatives as they ultimately lead to the structure of $Ca_3Cu_{7.8}Al_{26.2}$. Let's now take a broader view of this compound in the context of the Ca-Cu-Al system, particularly its placement almost directly between $CaAl_4$ and $CuAl_2$ in the phase diagram. Is there a way that this structure can be contextualized as the product of a reaction of these binary phases (even if it doesn't necessarily reflect the process by which $Ca_3Cu_{7.8}Al_{26.2}$ crystals grow from the melt)?

Our initial assessment of the Ca-Cu-Al system and the reported $CaCu_2Al_7$ phase showed that it existed in close compositional proximity to the line between $CaAl_4$ and $CuAl_2$ within the Al-rich corner of the phase diagram. In $Ca_3Cu_{7.8}Al_{26.2}$, we have identified $CaAl_4$-like and fcc-Al fragments that make sense with regard to these simple nearby phases, but we have not found an obvious way in which the motifs of $CuAl_2$ have manifested in the ternary structure.

Returning to Figure 4.1, we see that the structure of $CuAl_2$ is based on the vertical stacking of square antiprisms stuffed with 8 coordinate Cu atoms, with domains of tetrahedrally close-packed Al atoms in between. Neither of these motifs are present in the $Ca_3Cu_{7.8}Al_{26.2}$ structure, where instead we see that Cu atoms have been added to cubic coordination environments. These $Cu@Al_8$ cubes evoke another, more common 1:2 structure type found for transition metal/*p*-block metal systems: the fluorite type.[95] From DFT calculations, the total energy of $CuAl_2$ in the fluorite structure is in fact 2.3 meV/atom *lower* than

$CuAl_2$ in its own structure type, meaning there is very little thermodynamic barrier to the formation of local fluorite-like configurations.

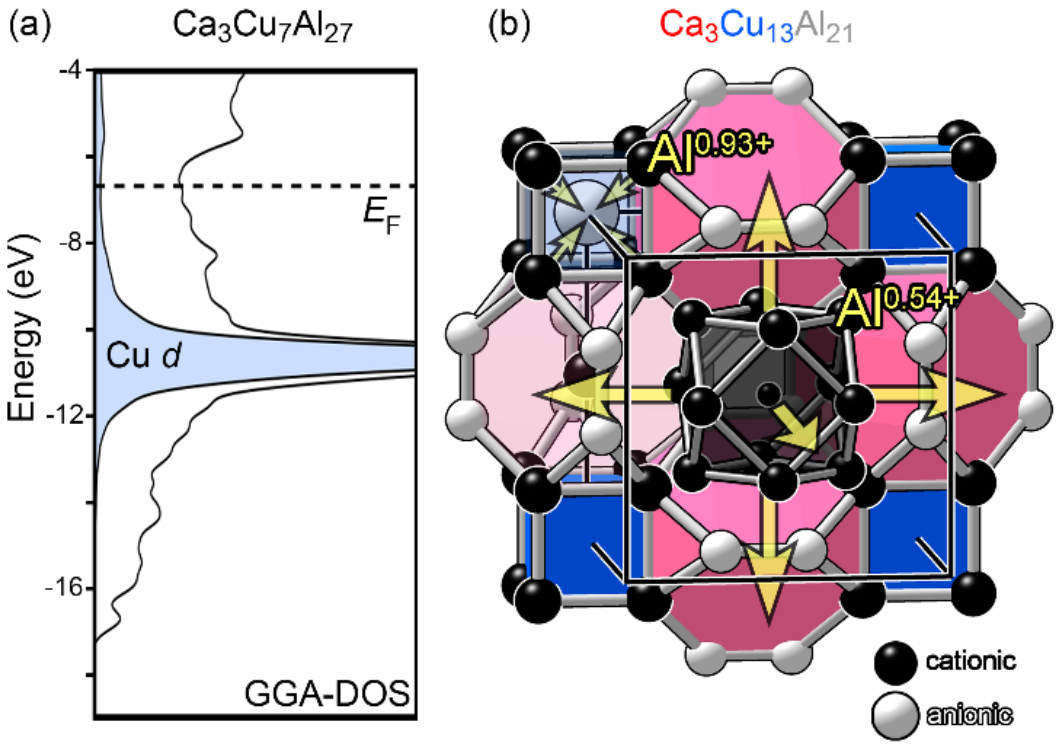

Figure 48. Resolution of electronic stress through incorporation of excess Al. (a) Structural rearrangement to the stuffed $BaHg_{11}$-type structure returns the Fermi level to a pseudogap in the electronic DOS. (b) This electronic stabilization is achieved through the cationic nature of the fcc-Al cluster, which donates a total of 6.53 electrons to the rest of the structure, alleviating the electron shortage caused by substitution of Cu for Al in $CaAl_4$.

Intriguingly, by starting at the center atom of the $Cu@Al_8$ cubes, we can trace out a 21-atom fluorite-type motif, as shown in Figure 4.9a. In this way, the Cu cube can be viewed as a fragment of the fluorite structure intergrown with the familiar motif of $CaAl_4$. Of note is the ease with which these two structural modules fit together: four-fold symmetric $CaAl_4$-like polyhedra match perfectly into the concave holes of the fluorite structure fragment. Such compatibility between the $BaAl_4$ and fluorite types is well known from their lamellar integrowth in $BaMg_4Si_3$- and Ce_2NiGe_{10}-type compounds, among others.[96-98]

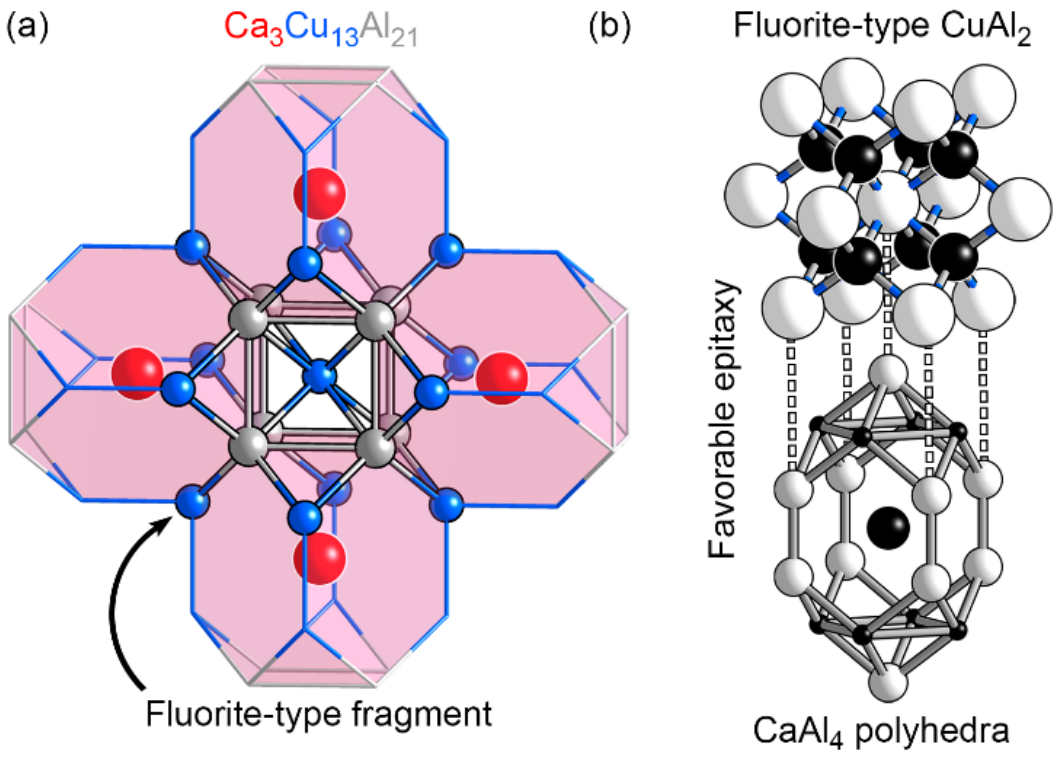

Figure 4.9. The $Ca_3Cu_{7.8}Al_{26.2}$ structure viewed as a reaction product of $CaAl_4$ and $CuAl_2$. (a) Structural fragment of the $Ca_3Cu_{13}Al_{21}$ ordered model with the extended 21-atom fluorite-type arrangement highlighted. (b) Favorable epitaxy between the atomic Bader charges present in fluorite-type $CuAl_2$ and $CaAl_4$.

As illustrated in Figure 4.9b, the favorable epitaxy between these structural motifs extends to their Bader charge schemes. Here, we can see that the alternation of anionic Cu and cationic Al atoms aligns with the Bader charges in the Al framework atoms of $CaAl_4$. The complementary match between these two structures offers a facile way for $CaAl_4$ to join with $CuAl_2$ by nucleating domains of a fluorite-type structure that place the electronegative Cu atoms in close proximity to the cationic Ca.

This interpretation of $Ca_3Cu_{7.8}Al_{26.2}$ as a product of $CaAl_4$ and $CuAl_2$ allows us to construct a conceptual scheme for its formation from intermetallic precursors. In one formula unit, there are a total of 3 equivalents of $CaAl_4$ and 7.8 equivalents of fluorite-type $CuAl_2$. The conjunction of these two species results in vertices of the $CaAl_4$ polyhedra becoming shared with the fluorite fragment, eliminating an

average of 14.4 Al to form a primitive cubic framework with stoichiometry $Ca_3Cu_{7.8}Al_{13.2}$. The system then uses the eliminated Al atoms to create the Al_{13} fcc cluster in the structure's voids, with 1.4 Al atoms left over. This hypothetical reaction, resembling the condensation of two distinct intermetallic phases, is summarized as:

$$3\ CaAl_4 + 7.8\ CuAl_2 \rightarrow Ca_3Cu_{7.8}Al_{26.2} + 1.4\ Al$$

The excess Al product is in line with the finer details of the phase diagram, which shows that the target phase is slightly Al-poor relative to the line between $CaAl_4$ and $CuAl_2$.

4.5 Conclusions

In this Chapter, we have explored how complex structures can be viewed as emerging, at least conceptually, from the reactions of simpler compounds. The unknown structure of $CaCu_2Al_7$ was identified as the product of a potential reaction between the nearby $CaAl_4$ and $CuAl_2$ phases. Targeted synthesis of this stoichiometry yielded the compound $Ca_3Cu_{7.8}Al_{26.2}$, whose modular structure is built of Cu-centered cubes, $CaAl_4$-like polyhedra, and fragments of fcc-Al. We analyzed the electronegativity, atomic size, and electron count factors influencing the reactivity of $CaAl_4$, and determined that topological charge stabilization was the primary driving force for Cu to occupy the dumbbell sites of $CaAl_4$. However, the incorporation of Cu creates atomic packing and electronic instabilities that are largely resolved through rearrangement to the $Y_3TaNi_{6+x}Al_{26}$ structure type. In the final stuffed $BaHg_{11}$-type structure, fragments of fluorite-like $CuAl_2$ and fcc-Al stabilize the structure through relief of chemical pressure and the donation of electrons.

The story of $Ca_3Cu_{7.8}Al_{26.2}$ illustrates how the features of a complex ternary intermetallic can be linked to chemical bonding issues in simpler precursor phases. In this system, the distribution of atomic charges and positive Al-Al CPs favors the substitution of Cu into the $CaAl_4$ structure. However, simply replacing Al atoms with Cu ones in the $CaAl_4$ structure leads to the emergence of negative Ca-Cu CPs and an electron deficiency, demanding larger-scale structural rearrangements. The inserted Cu atoms nucleate the new fluorite-type $CuAl_2$ domains, while Al_{13} fcc clusters replace a selection of Ca atoms to relieve negative CPs in their surroundings.

These observations provide the outlines for a generalizable strategy for the development of new ternary phases with intergrowth character. We hypothesize that binary structures containing minority cations surrounded by negative CP should show the potential for similar structural chemistry. The addition of smaller and more electronegative atoms of a third element are expected to gravitate toward the most anionic and crowded sites in these structures, and serve as electronegativity anchor points for the growth of dissimilar domains. Another example of this electronegativity anchor mechanism can be perceived in the quasicrystal approximant $Ca_{10}Cd_{27}Cu_2$.[21] Here, the incorporation of Cu into the $CaCd_2$ Laves phase results in micelle-like Bergman clusters, following a scheme parallel to that of $Ca_3Cu_{7.8}Al_{26.2}$. We are looking forward to exploring synthetically how this approach may guide the discovery of new chemically frustrated intermetallic phases.

4.6 Acknowledgements

We thank Hillary Mitchell Warden and Katie Hilleke for discussions and insights into the chemical pressure and bonding schemes of $CaAl_4$, as well as Mary Hawgood for identifying the connection to the $CaAg_4Al_7$ structure. We are also grateful to Bil Schneider for assistance with electron microscopy and EDS analysis. The authors gratefully acknowledge the financial support of the Department of Energy, Office of Basic Energy Sciences through Grant DE-SC0018938. This work includes calculations that used computing resources supported by NSF Grant CHE-0840494. This research was performed using the computing resources and assistance of the UW-Madison Center for High Throughput Computing (CHTC) in the Department of Computer Sciences. The CHTC is supported by UW-Madison, the Advanced Computing Initiative, the Wisconsin Alumni Research Foundation, the Wisconsin Institutes for Discovery, and the National Science Foundation, and is an active member of the Open Science Grid, which is supported by the National Science Foundation and the U.S. Department of Energy's Office of Science.

4.7 References

(1) Jones Jr., M.; Fleming, S. A. *Organic Chemistry (Fifth Edition)*; W. W. Norton & Company, 2014.

(2) Andersson, S.; Wadsley, A. The crystal structure of $Na_2Ti_3O_7$. *Acta Crystallogr.* **1961**, *14*, 1245-1249.

(3) Andersson, S.; Wadsley, A. The structures of $Na_2Ti_6O_{13}$ and $Rb_2Ti_6O_{13}$ and the alkali metal titanates. *Acta Crystallogr.* **1962**, *15*, 194-201.

(4) Andersson, S.; Hyde, B. Twinning on the unit cell level as a structure-building operation in the solid state. *J. Solid State Chem.* **1974**, *9*, 92-101.

(5) Parthé, E.; Chabot, B.; Cenzual, K. Complex structures of intermetallic compounds interpreted as intergrowth of segments of simple structures. *Chimia* **1985**, *39*, 164-174.

(6) Pani, M.; Fornasini, M. Examples of linear structures of intermetallic compounds described as intergrowth of segments of simple basic structures. *Z. Krist. - Cryst. Mater.* **1990**, *190*, 127-134.

(7) Grin, Y. N. The intergrowth concept as a useful tool to interpret and understand complicated intermetallic structures In *Nato. Adv. Sci. I. C. - Mat.*; Springer: 1992, p 77-96.

(8) Gladyshevskii, R. E.; Cenzual, K.; Parthé, E. Yttrium-cobalt-aluminum ($Y_2Co_3Al_9$) with yttrium-cobalt-gallium ($Y_2Co_3Ga_9$) type structure: an intergrowth of cesium chloride- and thorium-palladium (Th_3Pd_5)-type slabs. *J. Alloys Compd.* **1992**, *182*, 165-170.

(9) Gladyshevskii, R. E.; Cenzual, K.; Parthé, E. The crystal structure of orthorhombic gadolinium-nickel-aluminum ($Gd_3Ni_5Al_{19}$), a new representative of the structure series $R_{2+m}T_{4+m}Al_{15+4m}$. *J. Solid State Chem.* **1992**, *100*, 9-15.

(10) Viklund, P.; Svensson, C.; Hull, S.; Simak, S. I.; Berastegui, P.; Häußermann, U. From $V_8Ga_{36.9}Zn_{4.1}$ and $Cr_8Ga_{29.8}Zn_{11.2}$ to $Mn_8Ga_{27.4}Zn_{13.6}$: A Remarkable Onset of Zn-Cluster Formation in an Intermetallic Framework. *Chem.-Eur. J.* **2001**, *7*, 5143-5152.

(11) Blatov, V. A.; Ilyushin, G. D.; Proserpio, D. M. Nanocluster model of intermetallic compounds with giant unit cells: β, β′-Mg_2Al_3 polymorphs. *Inorg. Chem.* **2010**, *49*, 1811-1818.

(12) Samson, S. Crystal structure of $NaCd_2$. *Nature* **1962**, *195*, 259-262.

(13) Yang, Q.-B.; Andersson, S.; Stenberg, L. An alternative description of the structure of $NaCd_2$. *Acta Crystallogr. B* **1987**, *43*, 14-16.

(14) Fredrickson, D. C.; Lee, S.; Hoffmann, R. Interpenetrating polar and nonpolar sublattices in intermetallics: The $NaCd_2$ structure. *Angew. Chem. Int. Ed.* **2007**, *46*, 1958-1976.

(15) Shevchenko, V. Y.; Blatov, V.; Ilyushin, G. Intermetallic compounds of the $NaCd_2$ family perceived as assemblies of nanoclusters. *Struct. Chem.* **2009**, *20*, 975.

(16) Weber, T.; Dshemuchadse, J.; Kobas, M.; Conrad, M.; Harbrecht, B.; Steurer, W. Large, larger, largest–a family of cluster-based tantalum copper aluminides with giant unit cells. I. Structure solution and refinement. *Acta Crystallogr. B* **2009**, *65*, 308-317.

(17) Conrad, M.; Harbrecht, B.; Weber, T.; Jung, D. Y.; Steurer, W. Large, larger, largest–a family of cluster-based tantalum copper aluminides with giant unit cells. II. The cluster structure. *Acta Crystallogr. B* **2009**, *65*, 318-325.

(18) Peterson, G. G. C.; Yannello, V. J.; Fredrickson, D. C. Inducing Complexity in Intermetallics through Electron–Hole Matching: The Structure of $Fe_{14}Pd_{17}Al_{69}$. *Angew. Chem. Int. Ed.* **2017**, *56*, 10145-10150.

(19) Fredrickson, R. T.; Guo, Y.; Fredrickson, D. C. Epitaxial Stabilization between Intermetallic and Carbide Domains in the Structures of $Mn_{16}SiC_4$ and $Mn_{17}Si_2C_4$. *J. Am. Chem. Soc.* **2016**, *138*, 248-256.

(20) Guo, Y.; Fredrickson, D. C. On the Functionality of Complex Intermetallics: Frustration, Chemical Pressure Relief, and Potential Rattling Atoms in $Y_{11}Ni_{60}C_6$. *Inorg. Chem.* **2016**, *55*, 10397-10405.

(21) Hadler, A. B.; Harris, N. A.; Fredrickson, D. C. New Roles for Icosahedral Clusters in Intermetallic Phases: Micelle-like Segregation of Ca-Cd and Cu-Cd Interactions in $Ca_{10}Cd_{27}Cu_2$. *Journal of the American Chemical Society* **2013**, *135*, 17369-17378.

(22) Yanson, T. L.; Manyako, N. B.; Zarenchuk, O. S. Features of Component Interaction in the Ternary(Ca, Eu, Sr)--Cu--Al Systems. *Russ. Metall.* **1992**, 161-165.

(23) Gladyshevskii, R. E.; Cenzual, K. Structure of $Y_3TaNi_{6+x}Al_{26}$: a filled-up substitution variant of the $BaHg_{11}$ type. *J. Alloys Compd.* **1996**, *240*, 266-271.

(24) Oszlányi, G.; Sütő, A. Ab initio structure solution by charge flipping. *Acta Crystallogr. A* **2004**, *60*, 134-141.

(25) Oszlányi, G.; Sütő, A. Ab initio structure solution by charge flipping. II. Use of weak reflections. *Acta Crystallogr. A* **2005**, *61*, 147-152.

(26) Palatinus, L.; Chapuis, G. SUPERFLIP - a computer program for the solution of crystal structures by charge flipping in arbitrary dimensions. *J. Appl. Crystallogr.* **2007**, *40*, 786-790.

(27) Petříček, V.; Dušek, M.; Palatinus, L. Crystallographic computing system JANA2006: general features. *Z. Krist. - Cryst. Mater.* **2014**, *229*, 345-352.

(28) Momma, K.; Izumi, F. VESTA 3 for three-dimensional visualization of crystal, volumetric and morphology data. *J. Appl. Crystallogr.* **2011**, *44*, 1272-1276.

(29) Putz, H.; Brandenburg, K. Diamond. *Crystal Impact GbR, Bonn, Germany* **2014**.

(30) Putz, H.; Brandenburg, K. Match! - Phase Identification form Powder Diffraction. *Crystal Impact GbR, Bonn, Germany* **2017**.

(31) Vanderbilt, D. Soft self-consistent pseudopotentials in a generalized eigenvalue formalism. *Phys. Rev. B* **1990**, *41*, 7892-7895.

(32) Gonze, X.; Beuken, J.-M.; Caracas, R.; Detraux, F.; Fuchs, M.; Rignanese, G.-M.; Sindic, L.; Verstraete, M.; Zerah, G.; Jollet, F. First-principles computation of material properties: the ABINIT software project. *Comp. Mater. Sci.* **2002**, *25*, 478-492.

(33) Gonze, X. A brief introduction to the ABINIT software package. *Z. Krist. - Cryst. Mater.* **2005**, *220*, 558-562.

(34) Gonze, X.; Amadon, B.; Anglade, P.-M.; Beuken, J.-M.; Bottin, F.; Boulanger, P.; Bruneval, F.; Caliste, D.; Caracas, R.; Côté, M. ABINIT: First-principles approach to material and nanosystem properties. *Comput. Phys. Commun.* **2009**, *180*, 2582-2615.

(35) Hartwigsen, C.; Gœdecker, S.; Hutter, J. Relativistic separable dual-space Gaussian pseudopotentials from H to Rn. *Phys. Rev. B* **1998**, *58*, 3641-3662.

(36) Berns, V. M.; Engelkemier, J.; Guo, Y.; Kilduff, B. J.; Fredrickson, D. C. Progress in Visualizing Atomic Size Effects with DFT-Chemical Pressure Analysis: From Isolated Atoms to Trends in AB_5 Intermetallics. *J. Chem. Theory Comput.* **2014**, *10*, 3380-3392.

(37) Hilleke, K. P.; Fredrickson, D. C. Discerning Chemical Pressure amidst Weak Potentials: Vibrational Modes and Dumbbell/Atom Substitution in Intermetallic Aluminides. *J. Phys. Chem. A* **2018**, *122*, 8412-8426.

(38) Bader, R. F. Atoms in molecules. *Acc. Chem. Res.* **1985**, *18*, 9-15.

(39) Henkelman, G.; Arnaldsson, A.; Jónsson, H. A fast and robust algorithm for Bader decomposition of charge density. *Comp. Mater. Sci.* **2006**, *36*, 354-360.

(40) Sanville, E.; Kenny, S. D.; Smith, R.; Henkelman, G. Improved grid-based algorithm for Bader charge allocation. *J. Comput. Chem.* **2007**, *28*, 899-908.

(41) Tang, W.; Sanville, E.; Henkelman, G. A grid-based Bader analysis algorithm without lattice bias. *J. Phys.: Condens. Matter* **2009**, *21*, 084204.

(42) Oliveira, M. J.; Nogueira, F. Generating relativistic pseudo-potentials with explicit incorporation of semi-core states using APE, the Atomic Pseudo-potentials Engine. *Comput. Phys. Commun.* **2008**, *178*, 524-534.

(43) Kresse, G.; Hafner, J. Ab initio molecular dynamics for liquid metals. *Phys. Rev. B* **1993**, *47*, 558-561.

(44) Kresse, G.; Hafner, J. Ab initio molecular-dynamics simulation of the liquid-metal–amorphous-semiconductor transition in germanium. *Phys. Rev. B* **1994**, *49*, 14251-14269.

(45) Kresse, G.; Furthmuller, J. Efficiency of ab-initio total energy calculations for metals and semiconductors using a plane-wave basis set. *Comp. Mater. Sci.* **1996**, *6*, 15-50.

(46) Kresse, G.; Furthmüller, J. Efficient iterative schemes for ab initio total-energy calculations using a plane-wave basis set. *Phys. Rev. B* **1996**, *54*, 11169.

(47) Blöchl, P. E. Projector augmented-wave method. *Phys. Rev. B* **1994**, *50*, 17953.

(48) Kresse, G.; Joubert, D. From ultrasoft pseudopotentials to the projector augmented-wave method. *Phys. Rev. B* **1999**, *59*, 1758-1775.

(49) Perdew, J. P.; Chevary, J. A.; Vosko, S. H.; Jackson, K. A.; Pederson, M. R.; Singh, D. J.; Fiolhais, C. Atoms, molecules, solids, and surfaces: Applications of the generalized gradient approximation for exchange and correlation. *Phys. Rev. B* **1992**, *46*, 6671-6687.

(50) Perdew, J. P.; Chevary, J.; Vosko, S.; Jackson, K. A.; Pederson, M. R.; Singh, D.; Fiolhais, C. Erratum: Atoms, molecules, solids, and surfaces: Applications of the generalized gradient approximation for exchange and correlation. *Phys. Rev. B* **1993**, *48*, 4978.

(51) Perdew, J. P.; Burke, K.; Ernzerhof, M. Generalized gradient approximation made simple. *Phys. Rev. Lett.* **1996**, *77*, 3865.

(52) Perdew, J. P.; Burke, K.; Wang, Y. Generalized gradient approximation for the exchange-correlation hole of a many-electron system. *Phys. Rev. B* **1996**, *54*, 16533.

(53) Nowotny, H.; Wormes, E.; Mohrnheim, A. Untersuchungen in den Systemen Aluminium-Kalzium, Magnesium-Kalzium und Magnesium-Zirkon. *Z. Metallkd.* **1940**, *32*, 39-42.

(54) Latturner, S. E.; Kanatzidis, M. G. Formation of Multinary Intermetallics from Reduction of Perovskites by Aluminum Flux: $M_3Au_{6+x}Al_{26}Ti$ (M= Ca, Sr, Yb), a Stuffed Variant of the $BaHg_{11}$ Type. *Inorg. Chem.* **2004**, *43*, 2-4.

(55) Li, B.; Corbett, J. D. Synthesis and Structure of $K_3Mg_{20}In_{14}$, a Stuffed Variant of the $BaHg_{11}$ Structure Type with a Magnesium– Indium Network. *Inorg. Chem.* **2006**, *45*, 3861-3863.

(56) Latturner, S. E.; Bilc, D.; Mahanti, S.; Kanatzidis, M. G. $R_3Au_{6+x}Al_{26}T$ (R= Ca, Sr, Eu, Yb; T= Early Transition Metal): a Large Family of Compounds with a Stuffed $BaHg_{11}$ Structure Type Grown from Aluminum Flux. *Inorg. Chem.* **2009**, *48*, 1346-1355.

(57) Charkin, D. O.; Demchyna, R.; Prots, Y.; Borrmann, H.; Burkhardt, U.; Schwarz, U.; Schnelle, W.; Plokhikh, I. V.; Kazakov, S. M.; Abakumov, A. M. Two new arsenides, $Eu_7Cu_{44}As_{23}$ and $Sr_7Cu_{44}As_{23}$, with a new filled variety of the $BaHg_{11}$ structure. *Inorg. Chem.* **2014**, *53*, 11173-11184.

(58) Peyronel, G. Struttura della fase $BaHg_{11}$. *Gazz. Chim. Ital* **1952**, *82*, 679.

(59) Cordier, G.; Czech, E.; Schäfer, H. Zur kenntnis der verbindungen $Ca_4Cd_5Al_3$, $CaAg_4Al_7$, $CaCu_{6.5}Al_{6.5}$, $SrAg_{6.5}Al_{6.5}$ und $CeCu_{6.5}Al_{6.5}$. *J. Less Common Met.* **1985**, *108*, 225-239.

(60) Nowotny, H. Beitrag zur Kenntnis der Systeme Aluminium-Cer und Aluminium-Lanthan. *Z. Metallkd.* **1942**, *34*, 22.

(61) Kripyakevich, P.; Gladyshevskii, E. Crystal Structure of Compounds in the Nd-Al, Y-Al, and Gd-Fe Systems. *Soviet Phys.-Cryst.* **1961**, *6*, 118.

(62) Zarechnyuk, O.; Kripyakevich, P.; Gladyshevskii, E. Ternary Intermetallic Compounds with a $BaAl_4$-type Superlattice. *Soviet Phys.-Cryst.* **1965**, *9*, 706-708.

(63) Buschow, K.; Van Vucht, J. Systematic arrangement of the binary rare-earth-aluminium systems. *Philips Res. Rep* **1967**, *22*, 233-245.

(64) Frank-Cordier, U.; Cordier, G.; Schäfer, H. Die Struktur des Na_7Ga_{13-I} und ein Konzept zur bindungsmäßigen Deutung. *Z Naturforsch B* **1982**, *37*, 119-126.

(65) Zhang, J.; Bobev, S. Synthesis, structural characterization and properties of $SrAl_{4-x}Ge_x$, $BaAl_{4-x}Ge_x$, and $EuAl_{4-x}Ge_x$ ($x \approx 0.3–0.4$)—Rare examples of electron-rich phases with the $BaAl_4$ structure type. *J. Solid State Chem.* **2013**, *205*, 21-28.

(66) Zarechnyuk, O.; Kripyakevich, P.; Gladyshevskiy, E. Ternary Intermetallic Compounds with a $BaAl_4$ Type Superstructure. *Kristallografiya* **1964**, *9*, 835.

(67) Eisenmann, B.; May, N.; Müller, W.; Schäfer, H. Eine neue strukturelle Variante des $BaAl_4$-Typs: Der $CaBe_2Ge_2$-Typ. *Z Naturforsch B* **1972**, *27*, 1155-1157.

(68) May, N.; Schäfer, H. Neue Verbindungen im $ThCr_2Si_2$-Typ/New Compounds in the $ThCr_2Si_2$-Type. *Z Naturforsch B* **1972**, *27*, 864-865.

(69) Parthé, E.; Chabot, B.; Braun, H.; Engel, N. Ternary $BaAl_4$-type derivative structures. *Acta Crystallogr. B* **1983**, *39*, 588-595.

(70) Bruzzone, G.; Fornasini, M.; Merlo, F. Re-examination of the Ca-Ga system and crystal structure of $CaGa_4$, a monoclinic distortion of the $BaAl_4$ type. *J. Less Common Met.* **1989**, *154*, 67-77.

(71) Grin, Y.; Hiebl, K.; Rogl, P. Crystal structure and magnetism of YbT_xGa_{4-x}, T= Zn, Cd with the $BaAl_4$-type. *J. Alloys Compd.* **1995**, *227*, L4-L5.

(72) Williams, W. M.; Macaluso, R. T.; Moldovan, M.; Young, D.; Chan, J. Y. Synthesis, structure, and magnetoresistance of $SmPd_2Ga_2$. *Inorg. Chem.* **2003**, *42*, 7315-7318.

(73) Liu, S.; Corbett, J. D. Synthesis, Structure, and Bonding of $BaAuTl_3$ and $BaAuIn_3$: Stabilization of $BaAl_4$-Type Examples of the Heavier Triels through Gold Substitution. *Inorg. Chem.* **2004**, *43*, 4988-4993.

(74) Gout, D.; Barker, T. J.; Gourdon, O.; Miller, G. J. A new superstructure for the $BaAl_4$-structure type: an experimental and theoretical study of La_2NiAl_7. *Chem. Mater.* **2005**, *17*, 3661-3667.

(75) Mochiku, T.; Fujii, H.; Takeya, H.; Wuernisha, T.; Mori, K.; Ishigaki, T.; Kamiyama, T.; Hirata, K. $BaAl_4$-type derivative structure in superconducting La–Pd–Ge system. *Physica C* **2007**, *463*, 182-186.

(76) Li, B.; Corbett, J. D. Syntheses and Structures of New Phases AeM_xIn_{4-x} (Ae= Sr, Ba; M= Mg, Zn): Size Effects and Site Preferences in $BaAl_4$-Type Structures. *Inorg. Chem.* **2007**, *46*, 8812-8818.

(77) Tkachuk, A. V.; Mar, A. Electron-poor $SrAu_xIn_{4-x}$ ($0.5 \leqslant x \leqslant 1.2$) and $SrAu_xSn_{4-x}$ ($1.3 \leqslant x \leqslant 2.2$) phases with the $BaAl_4$-type structure. *J. Solid State Chem.* **2007**, *180*, 2298-2304.

(78) Latturner, S. E.; Kanatzidis, M. G. $RE(AuAl_2)_nAl_2(Au_xSi_{1-x})_2$: A New Homologous Series of Quaternary Intermetallics Grown from Aluminum Flux. *Inorg. Chem.* **2008**, *47*, 2089-2097.

(79) Lin, Q.; Corbett, J. D. Formation of nets of corner-shared bicapped gold squares in $SrAu_3Ge$: how a $BaAl_4$-type derivative reconciles fewer valence electrons and the origin of its uniaxial negative thermal expansion. *J. Am. Chem. Soc.* **2012**, *134*, 4877-4884.

(80) Francisco, M. C.; Malliakas, C. D.; Macaluso, R. T.; Prestigiacomo, J.; Haldolaarachchige, N.; Adams, P. W.; Young, D. P.; Jia, Y.; Claus, H.; Gray, K. Structures and Phase Transitions of $CePd_{3+x}Ga_{8-x}$: New Variants of the $BaHg_{11}$ Structure Type. *J. Am. Chem. Soc.* **2012**, *134*, 12998-13009.

(81) Seidel, S.; Hoffmann, R.-D.; Poettgen, R. $SrPdGa_3$–An orthorhombic superstructure of the $ThCr_2Si_2$ type. *Z. Krist. - Cryst. Mater.* **2014**, *229*, 421-426.

(82) Pearson, W. The most populous of all crystal structure types—the tetragonal $BaAl_4$ structure. *J. Solid State Chem.* **1985**, *56*, 278-287.

(83) Schmidt, J. T.; Lee, S.; Fredrickson, D. C.; Conrad, M.; Sun, J.; Harbrecht, B. $Pd_{0.213}Cd_{0.787}$ and $Pd_{0.235}Cd_{0.765}$ structures: Their long c axis and composite crystals, chemical twinning, and atomic site preferences. *Chem.-Eur. J.* **2007**, *13*, 1394-1410.

(84) Fredrickson, D. C.; Lidin, S.; Venturini, G.; Malaman, B.; Christensen, J. Origins of superstructure ordering and incommensurability in stuffed CoSn-Type phases. *J. Am. Chem. Soc.* **2008**, *130*, 8195-8214.

(85) Berns, V. M.; Stacey, T. E.; Sapiro, M.; Fredrickson, D. C. $Mg_{11}Cu_6Al_{12}$, A New Link in the Structural Chemistry of $MgCu_2$-Type Clusters. *Eur. J. Inorg. Chem.* **2011**, *2011*, 3936-3949.

(86) Gimarc, B. M. Topological charge stabilization. *J. Am. Chem. Soc.* **1983**, *105*, 1979-1984.

(87) Miller, G. J. The "coloring problem" in solids: How it affects structure, composition and properties. *Eur. J. Inorg. Chem.* **1998**, *1998*, 523-536.

(88) Burdett, J. K.; Miller, G. J. Fragment formalism in main-group solids: applications to aluminum boride (AlB_2), calcium aluminum silicide ($CaAl_2Si_2$), barium-aluminum ($BaAl_4$), and related materials. *Chem. Mater.* **1990**, *2*, 12-26.

(89) Ban, Z.; Sikirica, M. The crystal structure of ternary silicides ThM_2Si_2 (M= Cr, Mn, Fe, Co, Ni and Cu). *Acta Crystallogr.* **1965**, *18*, 594-599.

(90) Shatruk, M. $ThCr_2Si_2$ structure type: The "perovskite" of intermetallics. *J. Solid State Chem.* **2019**, *272*, 198-209.

(91) Engelkemier, J.; Fredrickson, D. C. Chemical Pressure Schemes for the Prediction of Soft Phonon Modes: A Chemist's Guide to the Vibrations of Solid State Materials. *Chem. Mater.* **2016**, *28*, 3171-3183.

(92) Zheng, C.; Hoffmann, R. An unusual electron count and electron-deficient multi-center bonding in one class of intermetallics: the $BaAl_4$, $CaAl_2Zn_2$, $CeMg_2Si_2$ and fcc Al structures. *Z Naturforsch B* **1986**, *41*, 292-320.

(93) Bergerhoff, G.; Hundt, R.; Sievers, R.; Brown, I. D. The Inorganic Crystal Structures Database. *Chem. Inf. Comput. Sci.* **1983**, 66-69.

(94) Belsky, A.; Hellenbrandt, M.; Karen, V. L.; Luksch, P. New developments in the Inorganic Crystal Structure Database (ICSD): accessibility in support of materials research and design. *Acta Crystallogr. B* **2002**, *58*, 364-369.

(95) Gehlhoff, W.; Ulrici, W. Transition metal ions in crystals with the fluorite structure. *physica status solidi (b)* **1980**, *102*, 11-59.

(96) Yarmolyuk, Y. P.; Grin, Y. N.; Rozhdestvenskaya, I. V.; Usov, O. A.; Kuz'min, A. M.; Bruskov, V. A.; Gladyshevskii, E. I. Crystal chemistry of heterogeneous linear structures. III. Crystal structure of cerium-gallium-nickel ($Ce_2Ga_{10}Ni$) and lanthanum-gallium-nickel ($La_2Ga_{10}Ni$). *Kristallografiya* **1982**, *27*, 999-1001.

(97) Macaluso, R. T.; Nakatsuji, S.; Lee, H.; Fisk, Z.; Moldovan, M.; Young, D.; Chan, J. Y. Synthesis, structure, and magnetism of a new heavy-fermion antiferromagnet, $CePdGa_6$. *J. Solid State Chem.* **2003**, *174*, 296-301.

(98) Engelkemier, J.; Green, L. M.; McDougald, R. N.; McCandless, G. T.; Chan, J. Y.; Fredrickson, D. C. Putting $ScTGa_5$ (T= Fe, Co, Ni) on the Map: How Electron Counts and Chemical Pressure Shape the Stability Range of the $HoCoGa_5$ Type. *Cryst. Growth Des.* **2016**, *16*, 5349-5358.

Appendix A.

Supporting Information for Chapter 2.

Inducing Complexity in Intermetallics through Electron-Hole Matching: The Structure of $Fe_{14}Pd_{17}Al_{69}$

Work shown in Section A.5 was done by Yannello. Work presented in Sections A.1-A.4, A.6 was done by Peterson.

A.1 Crystallographic Tables

Table A.1. Selected crystallographic data for Pd-rich and Fe-rich crystals of $Fe_{14}Pd_{17}Al_{69}$

	Pd-rich Composition	Fe-rich Composition
refined composition	$Fe_{27.715}Pd_{49.413}Al_{170.872}$	$Fe_{34.672}Pd_{42.754}Al_{170.574}$
WDS composition	$Fe_{11.1(1.6)}Pd_{19.0(9)}Al_{69.9(3)}$	–
Pearson symbol	*cI*248	*cI*248
space group	$Im\bar{3}$	$Im\bar{3}$
a (Å)	15.3982(2)	15.3479(3)
cell volume (Å^3), Z	3650.98(8)	3615.32(12)
cryst volume (mm^3)	0.068 × 0.031 × 0.024	0.145 × 0.052 0.018
cryst color, shape	grey, block	grey, block
data collection temp.	293	293
radiation source, λ (Å)	Mo K*a* (0.71073)	Mo K*a* (0.71073)
abs coeff (mm^{-1})	9.622	9.584

abs corr	multi-scan	multi-scan
θmin, θmax	3.24, 28.81	3.25, 28.91
refinement method	F^2	F^2
$R_{int}[I > 3\sigma(I)]$, R_{int}(all)	6.11, 7.19	6.93, 8.13
no. of reflections $[I > 3\sigma(I)$, all]	5306, 11415	11375, 29673
unique reflections $[I > 3\sigma(I)$, all]	585, 864	611, 864
no. of parameters	73	73
$R[I > 3\sigma(I)]$, $R_w[I > 3\sigma(I)]$	2.69, 4.95	2.78, 5.64
R(all), R_w(all)	5.86, 6.33	6.09, 7.02
$S[I > 3\sigma(I)]$, *S(all)*	1.04, 1.07	1.31, 1.35
$\Delta\rho_{max}$, $\Delta\rho_{min}$ ($e^-/Å^3$)	1.28, −1.15	2.12, −1.08

Table A.2. Refined atomic coordinates for the Pd-rich crystal of $Fe_{14}Pd_{17}Al_{69}$

Pd-rich Composition							
Site	Element	Multiplicity	*x*	*y*	*z*	$U_{equivalent}$	Occupancy
Pd1	Pd	8	0.25	0.25	0.25	0.01088(17)	1
Pd2a	Pd	24	0.14842(4)	0.26076(4)	0	0.0100(2)	0.920(7)
Pd2b	Fe	24	0.14842(4)	0.26076(4)	0	0.0100(2)	0.080(7)
Pd3a	Pd	16	0.09679(3)	0.09679(3)	0.09679(3)	0.00964(14)	0.940(5)
Pd3b	Al	16	0.09679(3)	0.09679(3)	0.09679(3)	0.00964(14)	0.060(5)
Fe1a	Fe	24	0.34958(6)	0.24596(7)	0	0.0144(3)	0.821(6)
Fe1b	Pd	24	0.34958(6)	0.24596(7)	0	0.0144(3)	0.179(6)
Fe2	Fe	6	0.5	0	0	0.0078(6)	1
Al1a	Al	2	0	0	0	0.0083(13)	0.96(2)
Al1b	Fe	2	0	0	0	0.0083(13)	0.04(2)
Al2	Al	12	0.5	0.1950(2)	0	0.0182(11)	1
Al3	Al	48	0.24929(10)	0.16257(11)	0.09875(10)	0.0112(5)	1
Al4	Al	12	0	0.1923(2)	0	0.0113(10)	1
Al5	Al	48	0.25641(11)	0.34486(11)	0.09761(11)	0.0132(5)	1
Al6	Al	48	0.4056(2)	-0.0795(2)	0.0954(2)	0.0223(11)	0.5
Al7	Al	24	0.3625(3)	-0.0733(3)	0	0.0218(17)	0.5
Al8	Al	24	0.5	-0.0732(3)	0.1357(3)	0.0280(19)	0.5

Table A.3. Refined harmonic atomic displacement parameters for the Pd-rich crystal of $Fe_{14}Pd_{17}Al_{69}$

Pd-rich Composition						
Site	U_{11}	U_{22}	U_{33}	U_{12}	U_{13}	U_{23}
Pd1	0.0109(3)	0.0109(3)	0.0109(3)	0.0000(2)	0.0000(2)	0.0000(2)
Pd2a	0.0094(3)	0.0114(3)	0.0091(3)	-0.0014(3)	0	0
Pd2b	0.0094(3)	0.0114(3)	0.0091(3)	-0.0014(3)	0	0
Pd3a	0.0096(2)	0.0096(2)	0.0096(2)	-0.00048(17)	-0.00048(17)	-0.00048(17)
Pd3b	0.0096(2)	0.0096(2)	0.0096(2)	-0.00048(17)	-0.00048(17)	-0.00048(17)
Fe1a	0.0096(6)	0.0249(7)	0.0087(6)	0.0010(4)	0	0
Fe1b	0.0096(6)	0.0249(7)	0.0087(6)	0.0010(4)	0	0
Fe2	0.0075(11)	0.0088(11)	0.0070(11)	0	0	0
Al1a	0.008(2)	0.008(2)	0.008(2)	0	0	0
Al1b	0.008(2)	0.008(2)	0.008(2)	0	0	0
Al2	0.0115(18)	0.029(2)	0.0143(18)	0	0	0
Al3	0.0097(9)	0.0133(9)	0.0106(8)	-0.0014(7)	0.0005(7)	0.0021(7)
Al4	0.0076(16)	0.0086(16)	0.0178(18)	0	0	0
Al5	0.0162(9)	0.0117(9)	0.0118(8)	-0.0018(7)	-0.0011(7)	0.0002(7)
Al6	0.0197(19)	0.0165(19)	0.031(2)	0.0042(16)	0.0172(17)	0.0091(17)
Al7	0.013(3)	0.017(3)	0.035(3)	-0.004(2)	0	0
Al8	0.046(4)	0.021(3)	0.017(3)	0	0	0.009(2)

Table A.4. Refined atomic coordinates for the Fe-rich crystal of $Fe_{14}Pd_{17}Al_{69}$

Fe-rich Composition							
Site	Element	Multiplicity	x	y	z	$U_{equivalent}$	Occupancy
Pd1	Pd	8	0.25	0.25	0.25	0.01376(17)	1
Pd2a	Pd	24	0.14910(4)	0.25955(4)	0	0.0121(2)	0.707(6)
Pd2b	Fe	24	0.14910(4)	0.25955(4)	0	0.0121(2)	0.293(6)
Pd3a	Pd	16	0.09624(3)	0.09624(3)	0.09624(3)	0.01207(13)	0.955(5)
Pd3b	Al	16	0.09624(3)	0.09624(3)	0.09624(3)	0.01207(13)	0.045(5)
Fe1a	Fe	24	0.34955(6)	0.24479(7)	0	0.0154(4)	0.896(6)
Fe1b	Pd	24	0.34955(6)	0.24479(7)	0	0.0154(4)	0.104(6)
Fe2	Fe	6	0.5	0	0	0.0090(6)	1
Al1a	Al	2	0	0	0	0.0121(13)	0.93(2)
Al1b	Fe	2	0	0	0	0.0121(13)	0.07(2)
Al2	Al	12	0.5	0.1927(2)	0	0.0190(11)	1
Al3	Al	48	0.24965(10)	0.16193(10)	0.09800(10)	0.0131(5)	1
Al4	Al	12	0	0.1955(2)	0	0.0133(10)	1
Al5	Al	48	0.25629(11)	0.34479(11)	0.09604(11)	0.0151(5)	1

Al6	Al	48	0.4049(3)	-0.0789(2)	0.0954(3)	0.0326(13)	0.5
Al7	Al	24	0.3629(3)	-0.0730(3)	0	0.033(2)	0.5
Al8	Al	24	0.5	-0.0711(4)	0.1366(3)	0.041(2)	0.5

Table A.5. Refined harmonic atmoic displacement parameters for the Fe-rich crystal of $Fe_{14}Pd_{17}Al_{69}$

	Fe-rich Composition					
Site	U_{11}	U_{22}	U_{33}	U_{12}	U_{13}	U_{23}
Pd1	0.0138(3)	0.0138(3)	0.0138(3)	-0.0001(2)	-0.0001(2)	-0.0001(2)
Pd2a	0.0111(4)	0.0137(4)	0.0117(4)	-0.0016(3)	0	0
Pd2b	0.0111(4)	0.0137(4)	0.0117(4)	-0.0016(3)	0	0
Pd3a	0.0121(2)	0.0121(2)	0.0121(2)	-0.00050(16)	-0.00050(16)	-0.00050(16)
Pd3b	0.0121(2)	0.0121(2)	0.0121(2)	-0.00050(16)	-0.00050(16)	-0.00050(16)
Fe1a	0.0103(6)	0.0238(7)	0.0120(6)	0.0010(4)	0	0
Fe1b	0.0103(6)	0.0238(7)	0.0120(6)	0.0010(4)	0	0
Fe2	0.0071(10)	0.0111(11)	0.0088(10)	0	0	0
Al1a	0.012(2)	0.012(2)	0.012(2)	0	0	0
Al1b	0.012(2)	0.012(2)	0.012(2)	0	0	0
Al2	0.0164(18)	0.027(2)	0.0137(17)	0	0	0
Al3	0.0126(9)	0.0135(8)	0.0133(8)	-0.0021(6)	0.0002(6)	0.0011(6)
Al4	0.0115(16)	0.0139(17)	0.0143(17)	0	0	0
Al5	0.0186(9)	0.0127(8)	0.0140(8)	-0.0025(6)	-0.0001(7)	-0.0019(7)
Al6	0.033(2)	0.021(2)	0.044(2)	0.0022(17)	0.027(2)	0.0086(18)
Al7	0.013(3)	0.019(3)	0.069(4)	-0.006(2)	0	0
Al8	0.085(5)	0.025(3)	0.013(3)	0	0	0.007(2)

Table A.6. Table of selected interatomic distances

Site	Neighbor	Pd-rich Composition Distance (Å)	Fe-rich Composition Distance (Å)
Pd1	Al3(×6)	2.6901(16)	2.6961(16)
	Al5(×6)	2.7657(16)	2.7765(16)
Pd2	Al3(×2)	2.6477(17)	2.6246(16)
	Al3(×2)	2.6235(16)	2.6105(16)
	Al4	2.5169(15)	2.4907(14)
	Al5(×2)	2.5887(17)	2.5671(17)
	Al6(×2)	2.672(4)	2.669(4)
Pd3	Al1(×2)	2.5815(4)	2.5584(4)
	Al3(×3)	2.5575(16)	2.5614(15)
	Al4(×3)	2.5700(19)	2.585(2)
	Pd3(×3)	2.9809(6)	2.9542(6)
Fe1	Al2	2.4457(15)	2.4434(15)
	Al3(×2)	2.5190(18)	2.4961(17)
	Al5(×2)	2.5238(17)	2.5245(16)
	Al5(×2)	2.5761(18)	2.5645(18)
	Al7	2.667(5)	2.645(5)
	Al8	2.177(5)	2.190(6)
Fe2	Al6(×8)	2.402(4)	2.397(4)
	Al7(×4)	2.399(5)	2.384(5)
	Al8(×4)	2.373(5)	2.364(5)
Al1	Al4(×6)	2.961(3)	3.000(3)
Al2	Al5(×4)	2.9201(19)	2.9086(19)
	Al6(×4)	2.726(4)	2.707(4)
	Al7(×2)	2.827(6)	2.794(6)
	Al8(×2)	2.807(6)	2.807(6)
	Al8(×2)	2.841(6)	2.838(6)
Al3	Al3(×2)	2.850(2)	2.862(2)
	Al5	2.809(2)	2.808(2)
	Al5	2.805(2)	2.821(2)
	Al6	2.726(4)	2.702(4)
	Al7	2.691(4)	2.674(4)
Al4	Al7(×2)	2.853(6)	2.803(6)
Al5	Al5(×2)	2.876(2)	2.893(2)

	Al6	2.690(4)	2.690(4)
	Al6	2.665(4)	2.649(4)
Al6	Al6	2.938(5)	2.929(5)
	Al6	2.448(5)	2.423(5)
	Al6	2.907(5)	2.920(5)
	Al7	1.615(4)	1.603(4)
	Al7	2.851(5)	2.828(6)
	Al8	1.583(4)	1.595(4)
	Al8	2.832(6)	2.799(6)
Al7	Al7	2.256(7)	2.241(7)
	Al8(×2)	2.974(5)	2.970(5)
Al8	Al8	2.253(8)	2.184(8)

A.2 Experimental Procedures

A.2.1 Synthetic Procedures

Samples of $Fe_{14}Pd_{17}Al_{69}$ were prepared by mixing Fe powder (Strem, 99.9%), Pd powder (filed from a Pd coin), and Al powder (Alfa Aesar, 99.97%) in stoichiometric ratios under an Ar atmosphere with an agate mortar and pestle. In a typical experiment, approximately .38 g of the mixture was pressed (~ 10,000 psi) into a cylindrical pellet 8mm in diameter. This pellet was arc melted under Ar, sealed in an evacuated fused silica tube (~10^{-3} Pa), and placed into a muffle furnace for annealing. The sample was annealed at 950°C for 2 hrs, then cooled and held at 750°C for 504 hrs, and finally cooled at 5°C/hr to room temperature. The tube was broken and the sample was retrieved and crushed into small pieces (~100μm) suitable for single crystal X-ray diffraction studies. The measurements described here were taken on a sample with nominal composition $Fe_{10.20}Pd_{19.60}Al_{70.20}$ (aiming to the Al-rich side of the homogeneity range of the $Fe_{14}Pd_{17}Al_{69}$ phase to account for possible vaporization of the Al during the arc-melting step), with

the exception of the data-collection on the Fe-rich crystal, which was taken from a sample with nominal composition $Fe_{14.19}Pd_{16.01}Al_{69.81}$.

A.2.2 Single Crystal X-ray Diffraction

Single crystals were picked from the bulk sample and mounted on pulled glass fibers attached to goniometer pins. Single-crystal X-ray diffraction data were collected using an Oxford Diffraction Xcalibur E diffractometer with graphite-monochromatized Mo Kα radiation (λ = 0.71069 Å) at room temperature. The software package CrysAlis Pro version 171.38.43 was used for run list optimization and processing of frame data. The structure was solved using the SUPERFLIP program[1] via the charge-flipping algorithm,[2,3] and the structure was refined on F^2 with JANA2006.[4] The programs Diamond 3 and VESTA[5] were used to analyze the solved structural model and experimental electron density, respectively. Crystal data for Pd- and Fe-rich crystals of $Fe_{14}Pd_{17}Al_{69}$ are provided in Table A.1, while refined atomic coordinates and selected interatomic distances are listed in Table A.2 – A.6.

A.2.3 Powder X-ray Diffraction Data Collection and Analysis

To obtain samples for powder x-ray diffraction, a portion of the bulk sample from synthesis was ground in an agate mortar and pestle, and the resulting powder was placed on a zero-diffraction plate. X-ray diffraction data were collected using a Rigaku D/Max Rapid II diffractometer with Mo Kα radiation (λ = 0.710806 Å) at room temperature using a curved two-dimensional imaging plate with peaks integrated

from 2° to 45°. The software Match! version 3.2.1 was used to analyze the measured diffraction data. An example of a powder pattern obtained for $Fe_{14}Pd_{17}Al_{69}$ is given in Figure A.1.

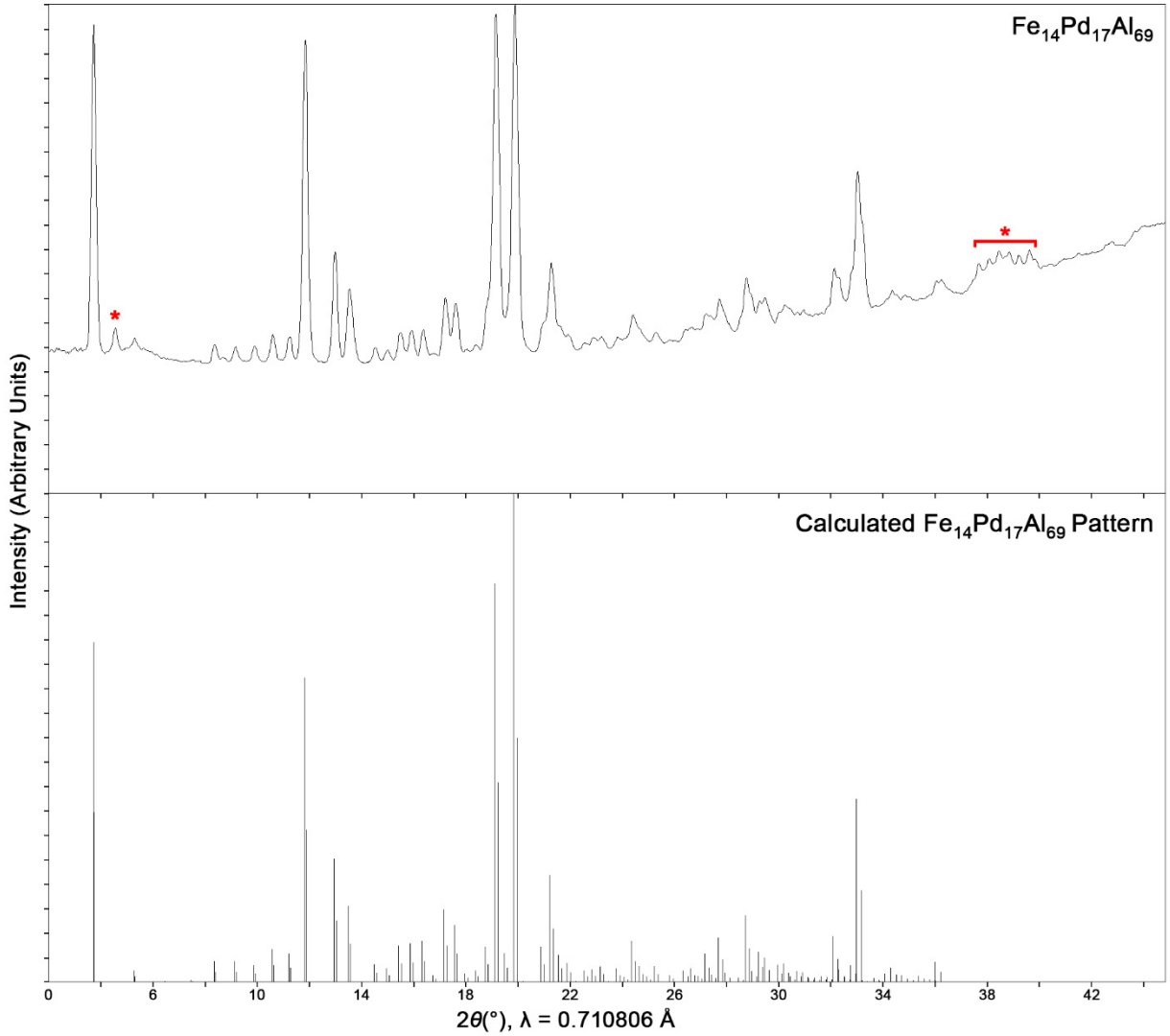

Figure A.1. Powder X-ray Diffraction (PXRD) pattern for the Pd-rich sample of $Fe_{14}Pd_{17}Al_{69}$ (nominal composition: $Fe_{10.20}Pd_{19.60}Al_{70.20}$) compared with the pattern calculated from the structure model. Red asterisks are placed over peaks that are unable to be assigned to $Fe_{14}Pd_{17}Al_{69}$. The unindexed peaks are consistent with a $Fe_{6.41}Al_{12.59}$-type phase, which can be tentatively assigned to the $Fe_7Pd_{29}Al_{64}$ compound (structure unknown) detected in the WDS measurements with composition $Fe_{6.4}Pd_{28.4}Al_{65.2}$.

A.2.4 Elemental Analysis via Wavelength Dispersive Spectroscopy

Polycrystalline fragments of the samples were suspended in epoxy inside hollow aluminum bullets. These bullets were polished with diamond grit solution down to a 1μm finish and coated in a conductive layer of carbon. The polished samples were examined with a Hitachi S-3100N scanning electron microscope, and backscattered electron (BSE) images showing the phases present were taken at 15kV accelerating voltage (shown in Figure A.2). Electron probe micro analysis (EPMA) was done with a CAMECA SX-Five FE electron probe in the UW-Madison Geoscience department. Wavelength dispersive spectrometry (WDS) was performed on the sample using Al Kα (LTAP), Pd Lα (LPET), and Fe Kα (LLIF) crystals. Elemental Fe, elemental Pd, and a 60:40 wt. % Al/Fe alloy were used as standards. From this analysis, the composition of the darker major phase seen in Figure A.2 was determined to be $Fe_{11.1(1.6)}Pd_{19.0(9)}Al_{69.9(3)}$. The composition of the lighter minor phase was determined to be $Fe_{6(2)}Pd_{28.4(8)}Al_{65.2(3)}$, and the presence of this Al-poor phase implies that substantial Al was lost during the arc welding step of sample preparation.

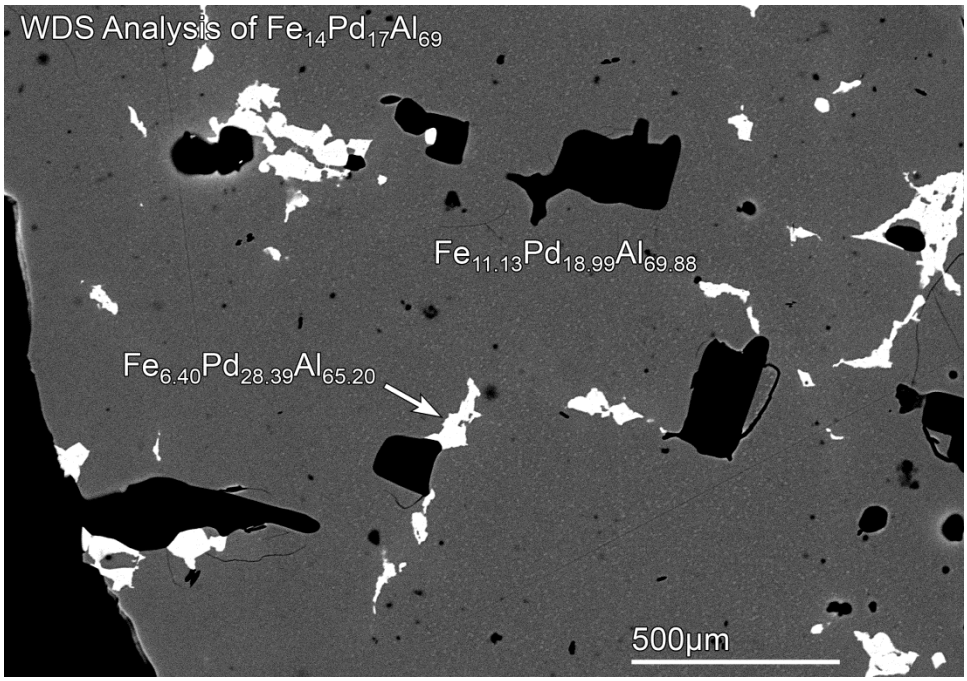

Figure A.2. Backscattered image of a polycrystalline Fe-Pd-Al sample. The majority grey phase is the $Fe_{14}Pd_{17}Al_{69}$ compound, while the minority white phase with composition of $Fe_{6.4}Pd_{28.4}Al_{65.2}$ can be assigned to the $Fe_7Pd_{29}Al_{64}$ phase (structure unknown).

A.2.5 Magnetic Susceptibility and Hysteresis Measurements

Magnetic properties measurements on $Fe_{14}Pd_{17}Al_{69}$ were taken using a Quantum Design Physical Properties Measurement System (PPMS-9T). 0.0989g of finely ground polycrystalline $Fe_{14}Pd_{17}Al_{69}$ were loaded into a Teflon bucket stuffed with glass wool to resist shifting of the sample when attached to the equipped Vibrating Sample Magnetometer. Zero field-cooled (Figure A.3) and 1000 Oe field-cooled (Figure A.4) magnetization scans were run on this sample from 400K to 6K as well as back from 6K to 400K. Additionally, magnetization measurements as a function of field strength were taken at 315K and 100K under an applied magnetic field over the ±10000 Oe range (Figure A.5). An antiferromagnetic transition is evident at around 300 K; however, due to the small magnetic moments involved (maximum

obtained magnetization under applied field = 5×10^{-3} μ_B/Fe atom, with sample diamagnetism beginning to dominate above ~7500 Oe), we attribute this to an impurity, most likely $Fe_7Pd_{29}Al_{64}$.

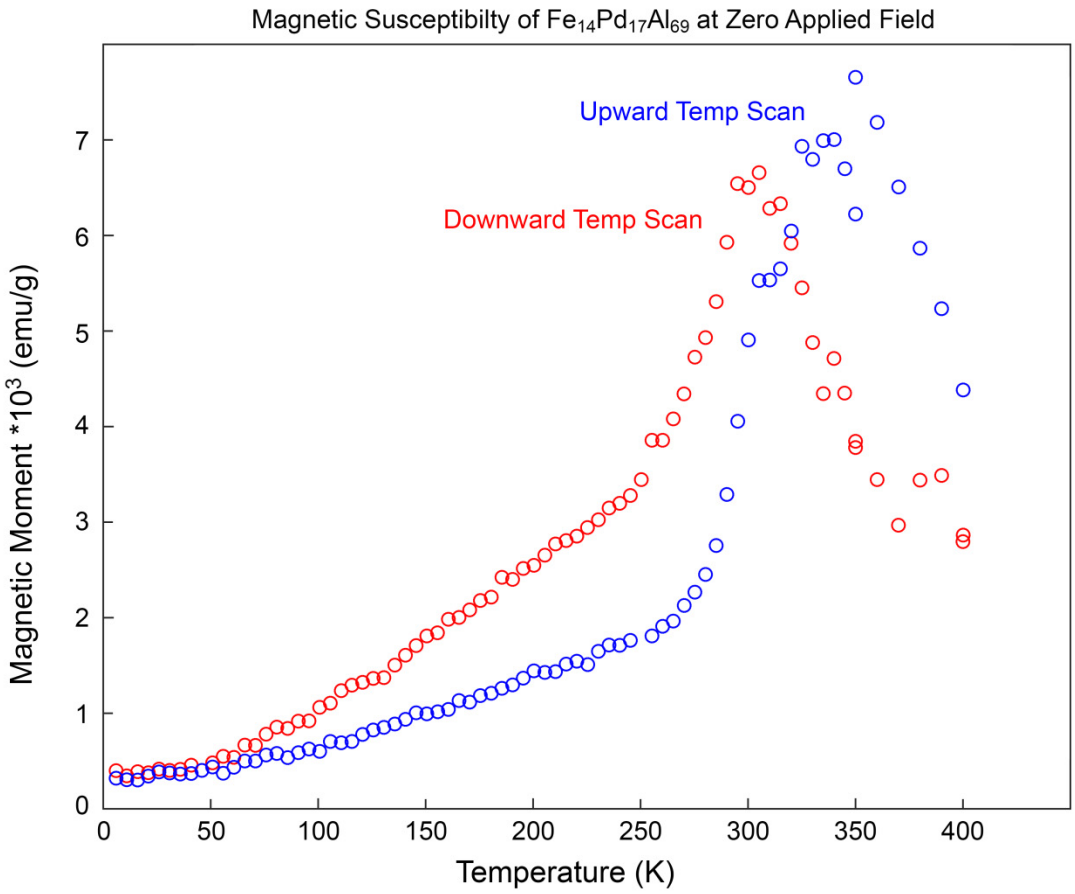

Figure A.3. Magnetic susceptibility plot for $Fe_{14}Pd_{17}Al_{69}$ with no applied external field from 6 K to 400 K in steps of 5 K between 6 K and 350 K, and steps of 10 K between 350 K and 400 K.

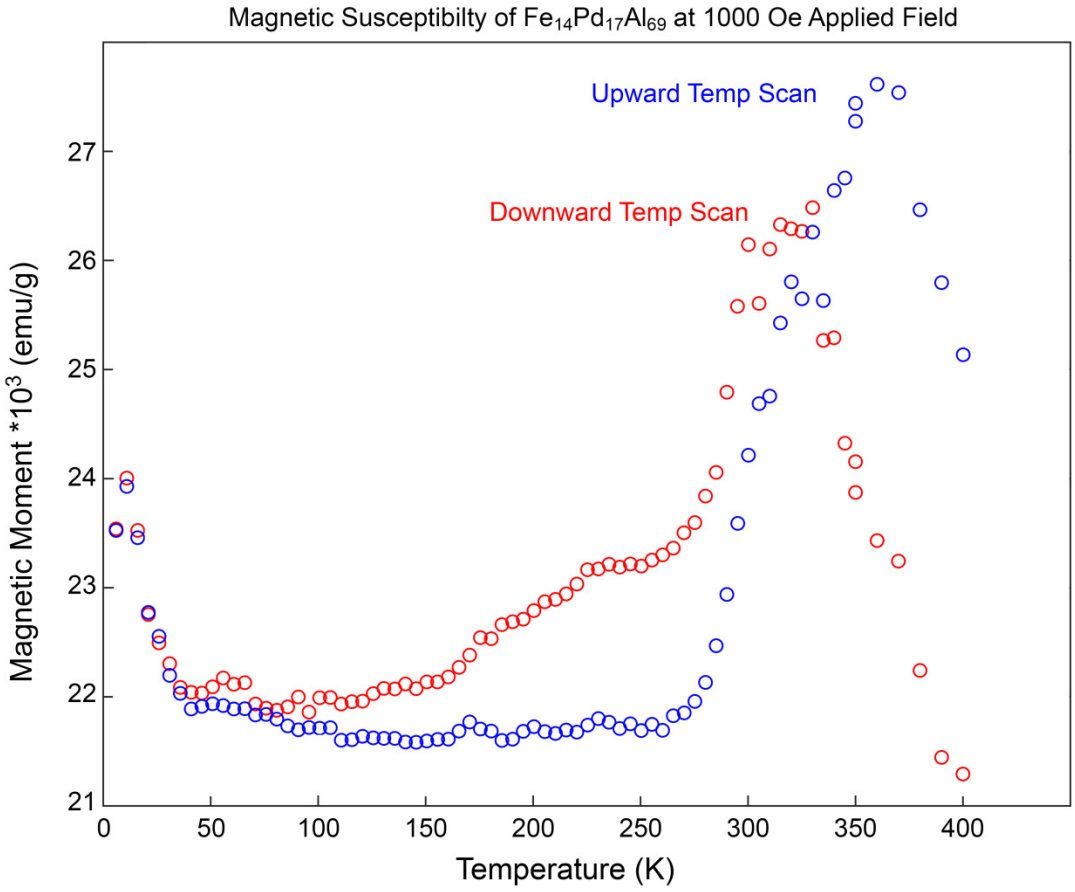

Figure A.4. Magnetic susceptibility plot for $Fe_{14}Pd_{17}Al_{69}$ with a 1000 Oe applied external field from 6 K to 400 K in steps of 5 K between 5 K and 350 K, and steps of 10 K between 350 K and 400 K.

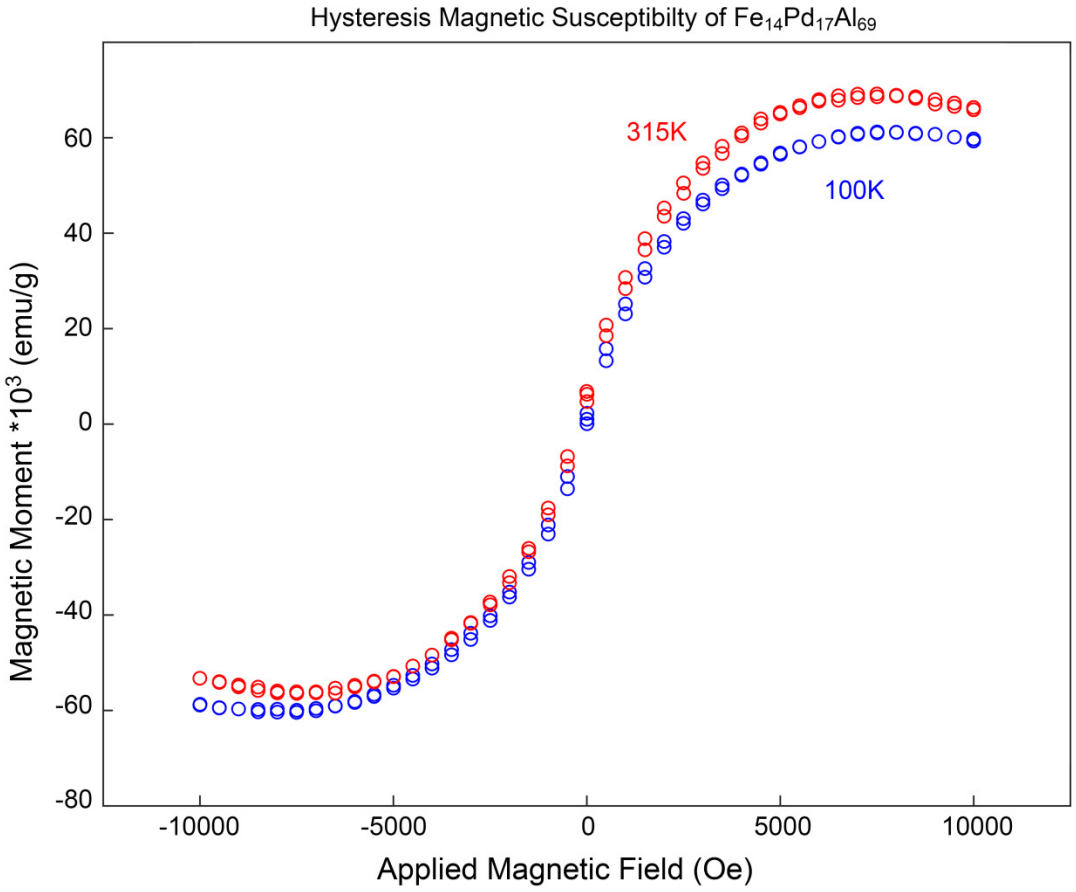

Figure A.5. Hysteresis curves for $Fe_{14}Pd_{17}Al_{69}$ at 315 K and 100 K from -10000 Oe to +10000 Oe using a 500 Oe step size. No significant hysteresis is observed at either temperature.

A.3 Determination of Mixed Site Occupancies

The integrated intensities of the single crystal data collected as described in Section S1 were used in the program SUPERFLIP to determine the initial structural solution $Fe_{30}Pd_{48}Al_{170}$. Immediately, it was clear that the Al6, Al7, and Al8 sites could not all be fully occupied in a reasonable model as the distance between the Al6 and Al7 site (1.615 Å) and the Al6 and Al8 site (1.583 Å) are incompatible with Al—Al distances found in the literature. Additionally, the interatomic distances between neighboring Al6 atoms (2.448 Å), neighboring Al7 atoms (2.256 Å), and neighboring Al8 atoms (2.253 Å), were also significantly

shorter than Al—Al distances previously reported. Thus, we concluded that the central Fe2 atom of these fragments must have a coordination of eight Al atoms in a square antiprismatic arrangement, with two half-occupied antiprisms offset from each other by 90° forming the averaged structure seen in the initial solution (See Figure 2.3 in the Chapter 2). Under this arrangement, all bond distances are in accordance with previously reported Al—Al contact distances. Therefore, Al6, Al7, and Al8 atoms were all assigned to half occupancy to account for only one of the two antiprism arrangements existing around each particular Fe2 atom in the structure.

Upon further refinement of the structure, the behavior of the atomic displacement parameters (ADPs) and deviations from the WDS composition indicated that there were likely several sites in the structure with mixed occupancies. Very small isotropic ADP parameters on the Fe1 and Al1 sites in particular indicated that there was substantial mixing with a heavier atom at these sites. Multiple combinations of Fe, Pd, and Al can give similar average form factors because of their similar atomic radii (1.26 Å, 1.37 Å, and 1.43 Å for Fe, Pd, and Al, respectively). Thus, some ambiguity arises in the assignments of the mixed sites. To address this problem, an additional sample of the same $Fe_{14}Pd_{16}Al_{69}$ structure type was prepared with an Fe-rich loading composition (see Table A.7) with an otherwise identical synthetic method to the original sample. By comparatively refining occupancy models of these two samples against each other, the mixing occupancies of each site were determined to be as shown in Table A.8.

From Table A.8, it can be seen that only the two sites that comprise the icosahedral framework of the structure, Pd2 and Fe1, show minor atom mixing percentages over 10%. At the Pd2 site, the minor atom occupancy percentage is significantly higher in the Fe-rich sample, and so this is expected to be a Pd/Fe mixed site. By the same logic, the Fe1 site can be expected to be a Fe/Pd mixed site because of increased

minority site occupancy percentage in the Pd-rich sample. For Pd3 site, because the minority atom occupancy percentage decreases in the Fe-rich sample, it is expected that the Pd3 site is a Pd/Al mixed site. Finally, the Al1 shows an increase in minority atom occupancy percentage in the Fe-rich sample, and so it is expected that the Al1 site is a mixed site between Al/Fe.

Table A.7. Loading Compositions of Pd-rich and Fe-rich Samples for Mixed Site Determination

Element	Pd-rich Loading Composition	Fe-rich Loading Composition
Fe	10.20%	14.19%
Pd	19.60%	16.01%
Al	70.20%	69.81%

Table A.8. Refined Compositions of Crystallographic Sites for Pd-rich and Fe-rich Samples

Site	Pd-rich Refined Compositions		Fe-rich Loading Compositions	
	Major Atom Occ.	Minor Atom Occ.	Major Atom Occ.	Minor Atom Occ.
Pd2(Pd/Fe)	0.920(7)	0.080(7)	0.707(6)	0.293(6)
Pd3(Pd/Al)	0.940(5)	0.060(5)	0.955(5)	0.045(5)
Fe1(Fe/Pd)	0.821(6)	0.179(6)	0.896(6)	0.104(6)
Al1(Al/Fe)	0.96(2)	0.04(2)	0.93(2)	0.07(2)

A.4 Theoretical and Computational Details

All systems studied theoretically in this work were first structurally optimized with GGA-DFT using the Vienna Ab initio Simulation Package (VASP) in the high-precision mode with the GGA-projector augmented wave potentials provided with the package.[6-9] Further details regarding the VASP calculations are shown in Table A.9, while the optimized cell parameters obtained are given in Table A.10.

Table A.11 – Table A.16 list the optimized atomic positions and total energies for each phase. During the structure optimization of each compound, first the atomic positions were relaxed with a fixed unit cell, then all parameters were released. The DFT DOS curves were then printed for NiAl, $TiAl_3$, and $TiNi_{1.5}Al_5$.

For $Fe_{12}Pd_{27}Al_{85}$ and Ir_4Al_{13}, best-fit Hückel models were refined using the eHtuner program,[10] yielding the parameters listed in Table A.17. The procedure for generating Hückel parameters was consistent between all compounds, using, as a starting point, the optimized parameters for the elemental structure of each element. As needed, the transition metal ζ_p values were constrained to match the ζ_s value to prevent the unrealistic situation where $\zeta_s < \zeta_p$. Reversed approximation Molecular Orbital (raMO) calculations were performed on all symmetry-distinct T sites in $Fe_{12}Pd_{27}Al_{85}$. Briefly, a raMO calculation involves generating a supercell of the conventional cell (2×2×2 in this case) in order to fold multiple high-symmetry k-points onto the Γ point. The Hamiltonian matrix is then generated using YAeHMOP,[11] and analyzed using in-house Matlab programs. The raMO results, as well as any necessary Linear Combination of raMOs (LCraMOs) to illustrate the bonding on each site, are shown in Figure A.6 – Figure A.44. The DOS curve calculated for Ir_4Al_{13} (an ordered model of $IrAl_{2.75}$) is presented in Figure A.45, with the Fermi Energy adjusted to match the number of electrons in $IrAl_{2.75}$.

For the Chemical Pressure (CP) calculations, an ordered version of $Fe_{14}Pd_{17}Al_{69}$ (structure shown in Figure A.46), was geometrical optimized in VASP (using LDA and the ultrasoft pseudopotentials provided with the package[12]), single point calculations were then carried out with ABINIT[13,14] at three different volumes (equilibrium, and slightly expanded and contracted volumes). ABINIT calculations used the LDA exchange correlation functional of Goedecker, Teter, and Hutter,[15] and Hartswigen–Goedecker–Hutter norm-conserving pseudopotentials.[16] CP analysis was then performed

with in-house programs. The core undistorting procedure and Hirshfeld-inspired integration schemes were employed [17] using electron density profiles for free ions modeled after the structure's Hirshfeld charges. The Hirshfeld charges were obtained by first running a calculation with neutral atomic profiles obtained from the ABINIT homepage, with the charges as output of this calculation. These Hirshfeld charges were then input into the Atomic Pseudopotentials Engine (APE)[18] to generate ionic profiles. The ABINIT calculation used a 6×6×6 k-point grid shifted by ½×½×½, an energy cutoff of 90 Ha, and a 125×125×125 FFT grid (0.0607 Å voxel spacing), yielding a total energy of -253.6440 Ha/cell.

Table A.9. Details of the VASP-DFT calculations on structures serving as bases for the parameterization of Hückel models.

Structure	Geo Optimized	Pseudopotentials	Energy Cut-off	k-point mesh[a]
$Fe_{12}Pd_{27}Al_{85}$[b]	Yes	PAW GGA	334.9 eV	3×3×3, Γ-centered
NiAl	Yes	PAW GGA	337.0 eV	12×12×12, Γ-centered
$TiAl_3$	Yes	PAW GGA	300.5 eV	16×16×12, Γ-centered
$TiNi_{1.5}Al_5$	Yes	PAW GGA	337.0 eV	16×16×4, Γ-centered
Ir_4Al_{13}	Yes	PAW GGA	300.5 eV	6×6×6, Γ-centered
$Fe_3Pd_5Al_{22}$[c]	Yes	LDA Ultrasoft	297.0 eV	6×6×6, Γ-centered

[a]All k-point grids were converged to a total energy of <1meV/atom
[b]Ordered model of $Fe_{14}Pd_{17}Al_{69}$ used for the raMO analysis.
[c]Ordered model of $Fe_{14}Pd_{17}Al_{69}$ used for the CP analysis.

Table A.10. Cell parameters for all VASP-DFT optimized structures

	a (Å)	b (Å)	c (Å)	α (°)	β (°)	γ (°)
$Fe_{12}Pd_{27}Al_{85}$	13.3358	13.3358	13.3358	109.47	109.47	109.47
NiAl	2.8915	2.8915	2.8915	90.00	90.00	90.00
$TiAl_3$	3.8446	3.8446	5.0931	112.18	112.18	90.00
$TiNi_{1.5}Al_5$	3.9556	3.9556	14.1016	90.00	90.00	90.00
Ir_4Al_{13}	8.0501	8.0501	8.0501	90.00	90.00	90.00
$Fe_3Pd_5Al_{22}$	7.6716	7.5072	7.6018	90.00	90.00	90.00

Table A.11. Atomic coordinates and total energy for the GGA-DFT optimized structure of $Fe_{12}Pd_{27}Al_{85}$

Element	x	y	z
Pd	0.650480	0.896480	0.246000
Pd	0.896480	0.246000	0.650480
Pd	0.595520	0.246000	0.349520
Pd	0.500000	0.500000	0.500000
Pd	0.000000	0.000000	0.500000
Pd	0.000000	0.500000	0.000000
Pd	0.500000	0.000000	0.000000
Pd	0.260790	0.148440	0.409230
Pd	0.739210	0.851560	0.590770
Pd	0.260790	0.851560	0.112350
Pd	0.739210	0.148440	0.887650
Pd	0.409230	0.260790	0.148440
Pd	0.590770	0.739210	0.851560
Pd	0.112350	0.260790	0.851560
Pd	0.887650	0.739210	0.148440
Pd	0.148440	0.409230	0.260790
Pd	0.851560	0.590770	0.739210
Pd	0.851560	0.112350	0.260790
Pd	0.148440	0.887650	0.739210
Pd	0.193600	0.193600	0.193600
Pd	0.806400	0.806400	0.806400
Pd	0.000000	0.000000	0.806400
Pd	0.000000	0.000000	0.193600
Pd	0.000000	0.806400	0.000000
Pd	0.000000	0.193600	0.000000
Pd	0.806400	0.000000	0.000000
Pd	0.193600	0.000000	0.000000
Al	0.000000	0.000000	0.000000
Al	0.194700	0.500000	0.694700
Al	0.805300	0.500000	0.305300
Al	0.694700	0.194700	0.500000
Al	0.305300	0.805300	0.500000
Al	0.500000	0.694700	0.194700
Al	0.500000	0.305300	0.805300
Al	0.261050	0.347840	0.411710
Al	0.738950	0.652160	0.588290
Al	0.936130	0.849340	0.588290
Al	0.063870	0.150660	0.411710

Al	0.063870	0.652160	0.913210
Al	0.936130	0.347840	0.086790
Al	0.738950	0.150660	0.086790
Al	0.261050	0.849340	0.913210
Al	0.411710	0.261050	0.347840
Al	0.588290	0.738950	0.652160
Al	0.588290	0.936130	0.849340
Al	0.411710	0.063870	0.150660
Al	0.913210	0.063870	0.652160
Al	0.086790	0.936130	0.347840
Al	0.086790	0.738950	0.150660
Al	0.913210	0.261050	0.849340
Al	0.347840	0.411710	0.261050
Al	0.652160	0.588290	0.738950
Al	0.849340	0.588290	0.936130
Al	0.150660	0.411710	0.063870
Al	0.652160	0.913210	0.063870
Al	0.347840	0.086790	0.936130
Al	0.150660	0.086790	0.738950
Al	0.849340	0.913210	0.261050
Al	0.192300	0.000000	0.192300
Al	0.807700	0.000000	0.807700
Al	0.192300	0.192300	0.000000
Al	0.807700	0.807700	0.000000
Al	0.000000	0.192300	0.192300
Al	0.000000	0.807700	0.807700
Al	0.442550	0.353910	0.601180
Al	0.557450	0.646090	0.398820
Al	0.752730	0.841370	0.398820
Al	0.247270	0.158630	0.601180
Al	0.247270	0.646090	0.088640
Al	0.752730	0.353910	0.911360
Al	0.557450	0.158630	0.911360
Al	0.442550	0.841370	0.088640
Al	0.601180	0.442550	0.353910
Al	0.398820	0.557450	0.646090
Al	0.398820	0.752730	0.841370
Al	0.601180	0.247270	0.158630
Al	0.088640	0.247270	0.646090
Al	0.911360	0.752730	0.353910

Al	0.911360	0.557450	0.158630
Al	0.088640	0.442550	0.841370
Al	0.353910	0.601180	0.442550
Al	0.646090	0.398820	0.557450
Al	0.841370	0.398820	0.752730
Al	0.158630	0.601180	0.247270
Al	0.646090	0.088640	0.247270
Al	0.353910	0.911360	0.752730
Al	0.158630	0.911360	0.557450
Al	0.841370	0.088640	0.442550
Al	0.174800	0.689900	0.673900
Al	0.984000	0.499100	0.673900
Al	0.984000	0.310100	0.484900
Al	0.174800	0.500900	0.484900
Al	0.673900	0.174800	0.689900
Al	0.673900	0.984000	0.499100
Al	0.484900	0.984000	0.310100
Al	0.484900	0.174800	0.500900
Al	0.689900	0.673900	0.174800
Al	0.499100	0.673900	0.984000
Al	0.310100	0.484900	0.984000
Al	0.500900	0.484900	0.174800
Al	0.926600	0.362500	0.289100
Al	0.926600	0.637500	0.564100
Al	0.289100	0.926600	0.362500
Al	0.564100	0.926600	0.637500
Al	0.362500	0.289100	0.926600
Al	0.637500	0.564100	0.926600
Al	0.790900	0.364100	0.426800
Al	0.062700	0.635900	0.426800
Al	0.426800	0.790900	0.364100
Al	0.426800	0.062700	0.635900
Al	0.364100	0.426800	0.790900
Al	0.635900	0.426800	0.062700
Fe	0.246000	0.349520	0.595520
Fe	0.754000	0.650480	0.404480
Fe	0.246000	0.650480	0.896480
Fe	0.754000	0.349520	0.103520
Fe	0.404480	0.754000	0.650480
Fe	0.103520	0.754000	0.349520

Fe	0.349520	0.595520	0.246000
Fe	0.650480	0.404480	0.754000
Fe	0.349520	0.103520	0.754000
Fe	0.000000	0.500000	0.500000
Fe	0.500000	0.000000	0.500000
Fe	0.500000	0.500000	0.000000
Total Energy:	-621.229833 eV/cell		

Table A.12. Atomic coordinates and total energy for the GGA-DFT optimized structure of NiAl

Element	*x*	*y*	*z*
Ni	0.500000	0.500000	0.500000
Al	0.000000	0.000000	0.000000
Total Energy:	-10.509074eV/cell		

Table A.13. Atomic coordinates and total energy for the GGA-DFT optimized structure of $TiAl_3$

Element	*x*	*y*	*z*
Al	0.000000	0.500000	0.000000
Al	0.250000	0.250000	0.500000
Al	0.750000	0.750000	0.500000
Ti	0.500000	0.000000	0.000000
Total Energy:	-20.412511 eV/cell		

Table A.14. Atomic coordinates and total energy for the GGA-DFT optimized structure of $TiNi_{1.5}Al_5$

Element	*x*	*y*	*z*
Ti	0.000000	0.000000	0.005695
Ti	0.500000	0.500000	0.498689
Ni	0.000000	0.000000	0.240041
Ni	0.000000	0.000000	0.760155
Ni	0.500000	0.500000	0.741276
Al	0.000000	0.500000	0.147954
Al	0.000000	0.500000	0.859141
Al	0.500000	0.000000	0.147954
Al	0.500000	0.000000	0.859141
Al	0.500000	0.000000	0.641992
Al	0.500000	0.000000	0.347946
Al	0.000000	0.500000	0.641992
Al	0.000000	0.500000	0.347946
Al	0.000000	0.000000	0.493975
Al	0.500000	0.500000	0.005084
Total Energy:	-76.394839 eV/cell		

Table A.15. Atomic coordinates and total energy for the GGA-DFT optimized structure of Ir_4Al_{13}

Element	*x*	*y*	*z*
Ir	0.500000	0.500000	0.500000
Ir	0.000000	0.000000	0.000000
Ir	0.500000	0.000000	0.721354
Ir	0.500000	0.000000	0.278646
Ir	0.721354	0.500000	0.000000
Ir	0.278646	0.500000	0.000000
Ir	0.000000	0.721354	0.500000
Ir	0.000000	0.278646	0.500000
Al	0.202568	0.499999	0.666707
Al	0.797432	0.500001	0.666707
Al	0.797432	0.499999	0.333293
Al	0.202568	0.500001	0.333293
Al	0.666707	0.202568	0.499999
Al	0.666707	0.797432	0.500001
Al	0.333293	0.797432	0.499999
Al	0.333293	0.202568	0.500001
Al	0.499999	0.667074	0.202568

Al	0.500001	0.666707	0.797432
Al	0.499999	0.333293	0.797432
Al	0.500001	0.333293	0.202568
Al	0.801635	0.801635	0.801635
Al	0.198365	0.198365	0.801635
Al	0.198365	0.801635	0.198365
Al	0.801635	0.198365	0.198365
Al	0.348272	0.000000	0.000000
Al	0.651728	0.000000	0.000000
Al	0.000000	0.348272	0.000000
Al	0.000000	0.651728	0.000000
Al	0.000000	0.000000	0.348272
Al	0.000000	0.000000	0.651728
Al	0.801634	0.198366	0.801634
Al	0.198366	0.801634	0.801634
Al	0.198366	0.198366	0.198366
Al	0.801634	0.801634	0.198366
Total Energy:	-176.809468 eV/cell		

Table A.16. Atomic coordinates and total energy for the LDA-DFT optimized structure of $Fe_3Pd_5Al_{22}$

Element	*x*	*y*	*z*
Fe	0.000000	0.000000	0.000190
Fe	0.500000	0.000000	0.660103
Fe	0.500000	0.000000	0.272860
Pd	0.000000	0.291980	0.507221
Pd	0.720371	0.500000	0.995154
Pd	0.500000	0.500000	0.493885
Pd	0.279629	0.500000	0.995154
Pd	0.000000	0.708020	0.507221
Al	0.214597	0.499999	0.672314
Al	0.785403	0.500001	0.672314
Al	0.804899	0.499999	0.318156
Al	0.195101	0.500001	0.318156
Al	0.679814	0.185274	0.490607
Al	0.679814	0.814726	0.490610
Al	0.320186	0.814726	0.490607
Al	0.320186	0.185274	0.490610
Al	0.499999	0.679621	0.197240
Al	0.500001	0.698794	0.797247

Al	0.499999	0.301206	0.797247
Al	0.500001	0.320380	0.197240
Al	0.298944	0.000000	0.871553
Al	0.000000	0.305535	0.884071
Al	0.701056	0.000000	0.871553
Al	0.000000	0.694465	0.884071
Al	0.000000	0.000000	0.347025
Al	0.000000	0.000000	0.685259
Al	0.208839	0.817505	0.148083
Al	0.791161	0.182495	0.148083
Al	0.208840	0.182495	0.148084
Al	0.791160	0.817505	0.148084
Total Energy:	-166.287897 eV/cell		

Table A.17. DFT-calibrated Hückel parameters used in this Chapter

Compound, RMS deviation[a]	Element	Orbital	H_{ii} (eV)	c_1	ζ_1 (a_o^{-1})	c_2	ζ_2 (a_o^{-1})
$Fe_{12}Pd_{27}Al_{85}$, 0.060795 eV	Fe	Fe 4s	-4.525		2.3972		
		Fe 4p	-3.000		2.1930		
		Fe 3d	-7.467	0.5680	6.4187	0.9887	2.2290
	Pd[b]	Pd 5s	-5.201		2.5984		
		Pd 5p	-2.840		2.5984		
		Pd 4d	-10.413	1.0000	4.9663	3.2730	2.6747
	Al	Al 3s	-7.830		1.9836		
		Al 3p	-4.502		1.8103		
		Al 3d	-1.405	0.5000	6.1077	2.1975	1.6113
Ir_4Al_{13}, 0.086633 eV	Ir[b]	Ir 6s	-4.197		2.6575		
		Ir 6p	-1.901		2.6575		
		Ir 5d	-8.668	1.0000	6.2954	5.6145	2.9429
	Al	Al 3s	-6.499		1.8782		
		Al 3p	-4.473		1.7731		
		Al 3d	-0.981	0.5000	7.0814	2.2701	1.4209

[a] Root-mean-squared deviations between Hückel and GGA-DFT band energies for bands up to 1 eV above E_F.

[b]This element's ζ_s and ζ_p values were constrained to be equal.

A.5 raMO Analyses of the Symmetry-Distinct T sites in $Fe_{12}Pd_{27}Al_{85}$

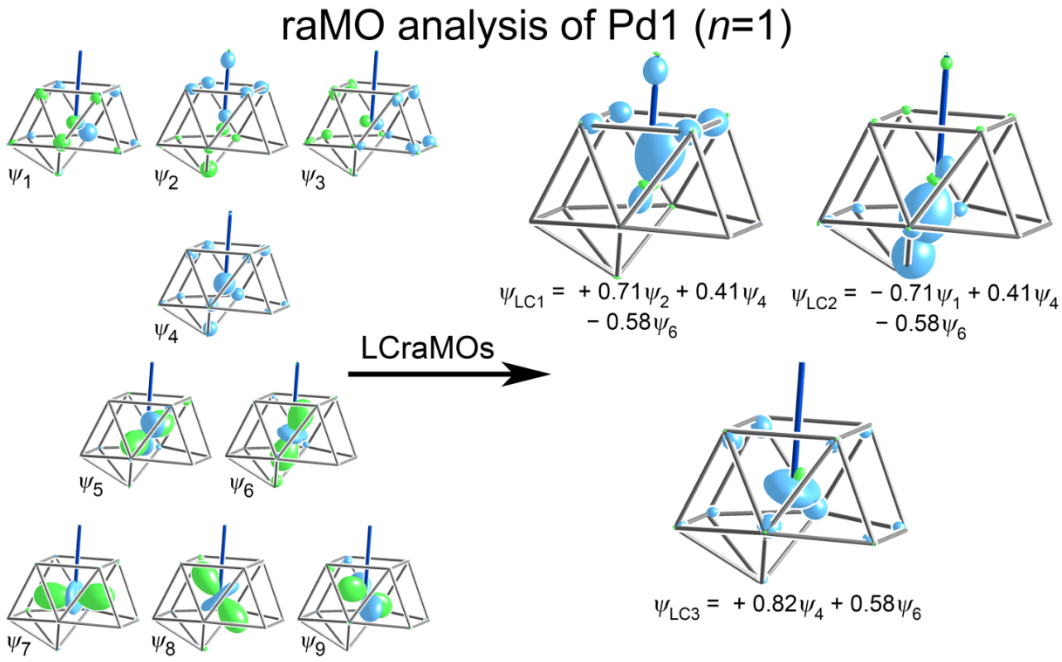

Figure A.6. raMO reconstructions of the spd valence orbitals of Pd1 (from the list of atoms in Table A.11), along with linear combinations of raMOs (LCraMOs) showing the Pd-Pd isolobal bond it participates in. This Pd is an example of the Fe1 site (mixed Fe/Pd) in the experimental structure, modeled here as Pd atom.

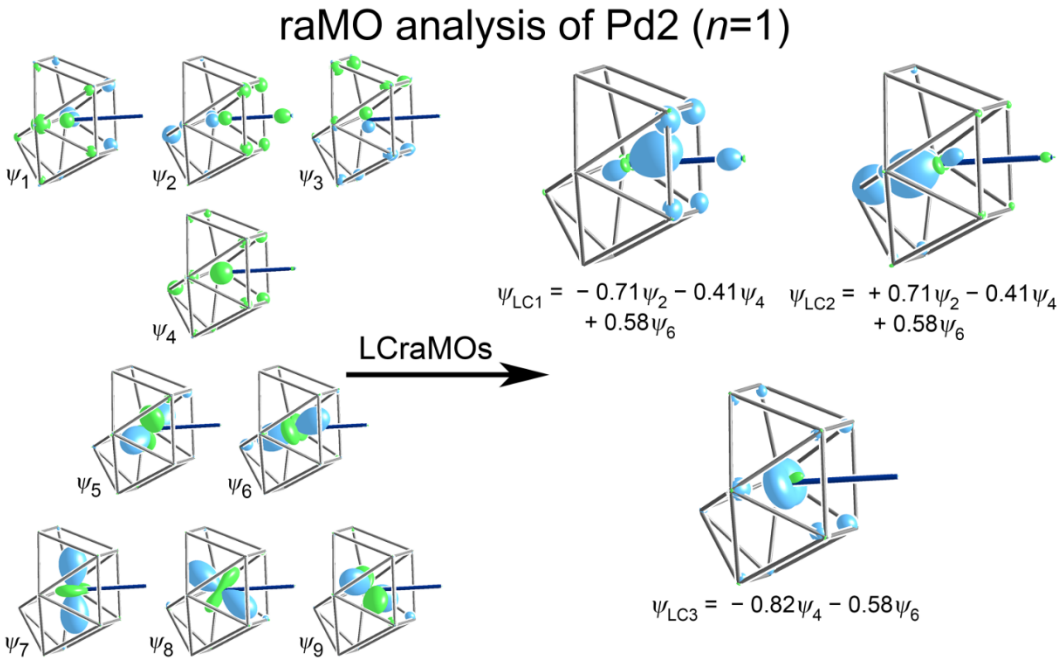

Figure A.7. raMOs and LCramos for Pd2. This atom lies on the Fe1 site (mixed Fe/Pd) from the experimental structure.

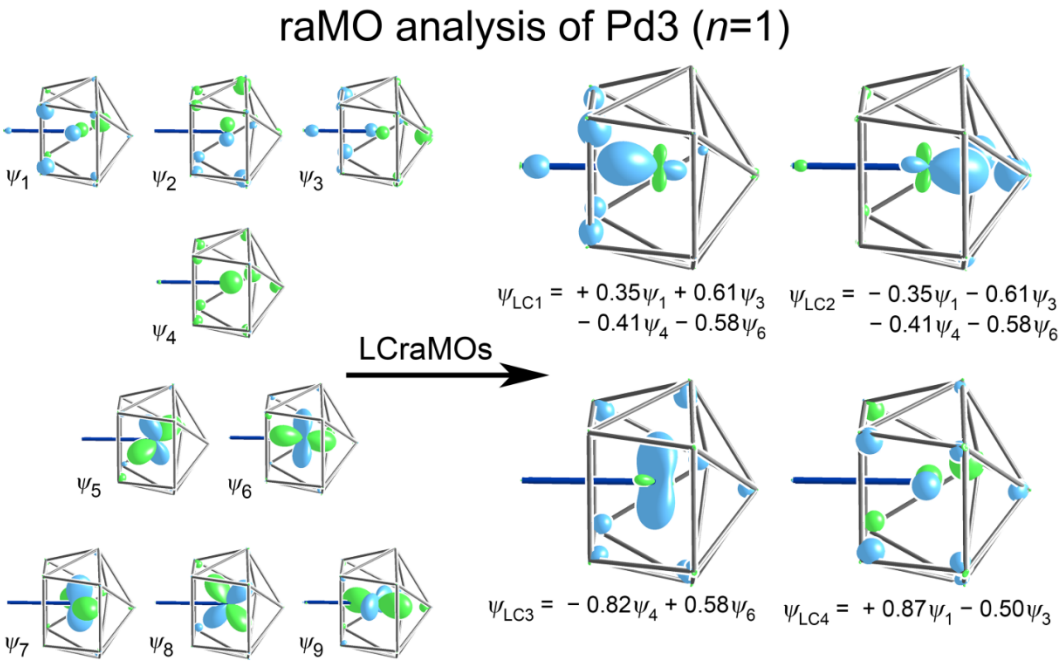

Figure A.8. raMOs and LCramos for Pd3. This atom is lies on the Fe1 site (mixed Fe/Pd) from the experimental structure.

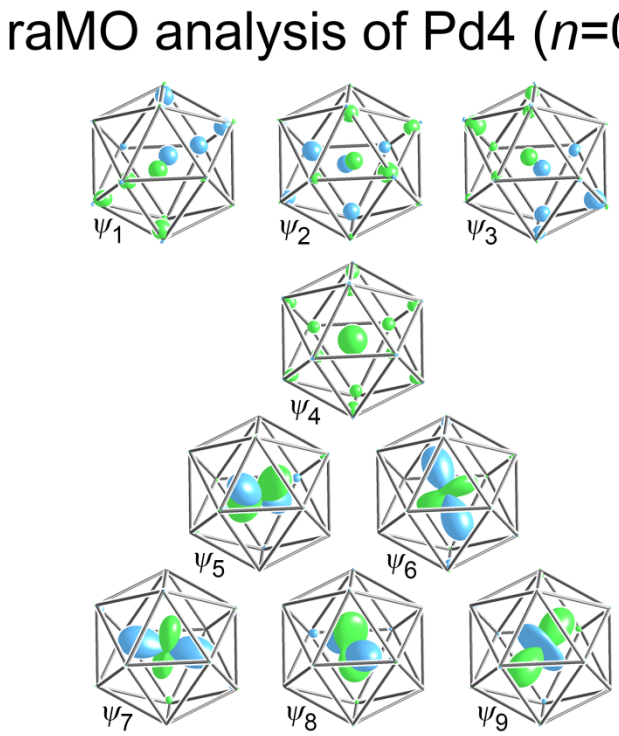

Figure A.9. raMOs for Pd4. The atom lies on a Pd1 site from the experimental structure.

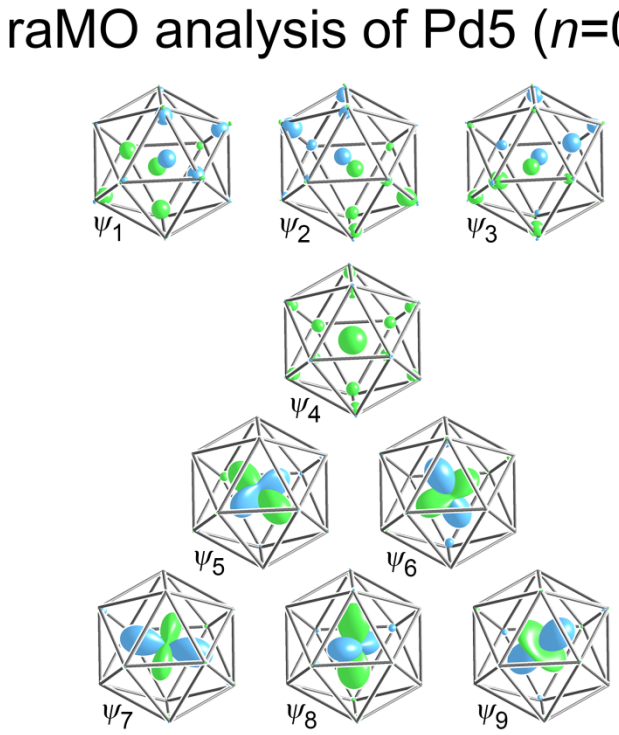

Figure A.10. raMOs for Pd5. This atom lies on a Pd1 site from the experimental structure.

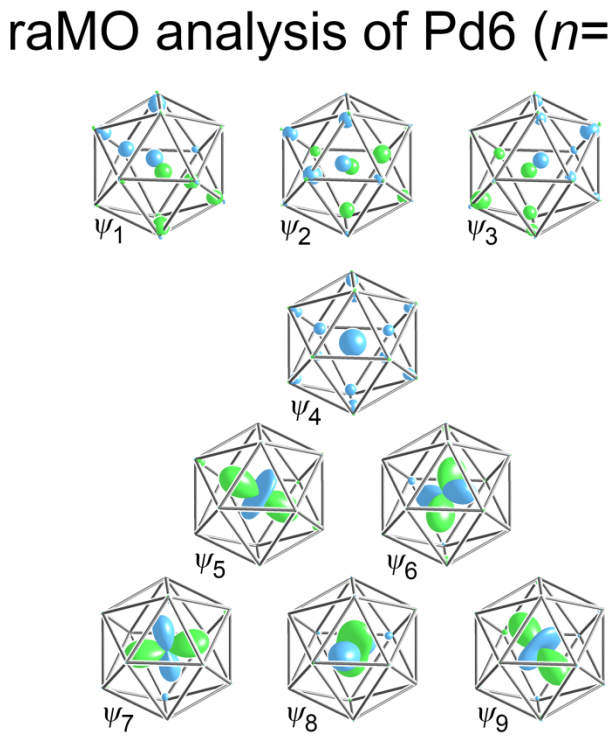

Figure A.11. raMOs for Pd6. This atom lies on a Pd1 site from the experimental structure.

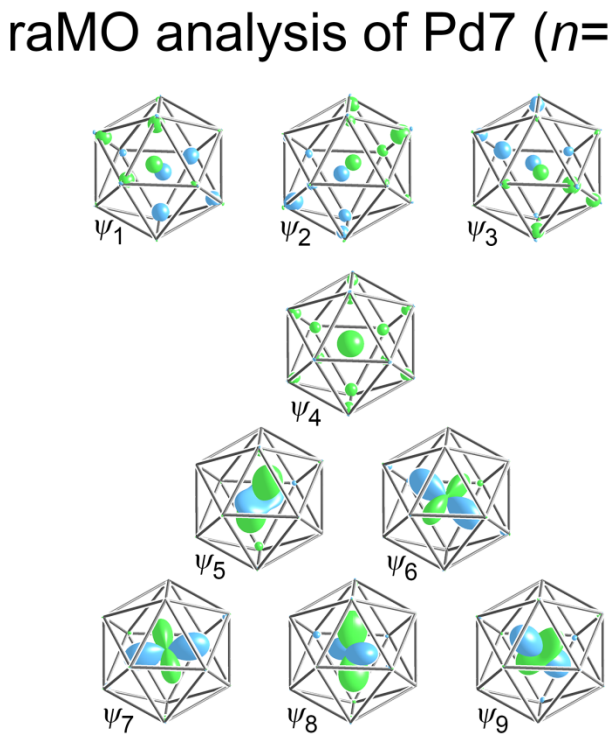

Figure A.12. raMOs for Pd7. This atom lies on a Pd1 site from the experimental structure.

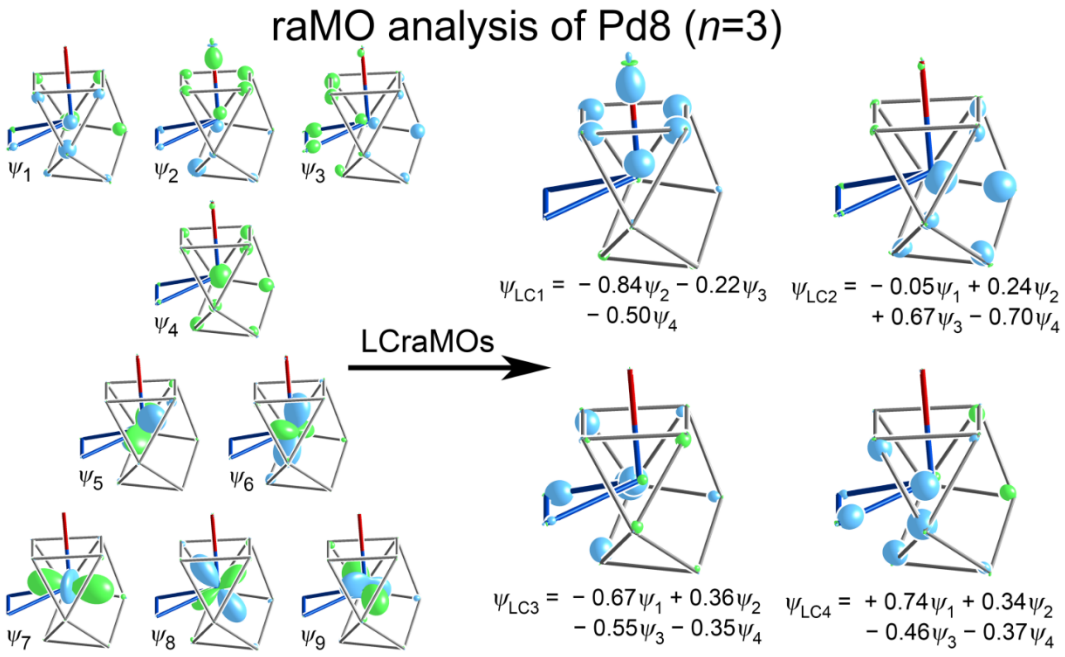

Figure A.13. raMOs and LCramos for Pd8. This atom lies on a Pd2 site from the experimental structure.

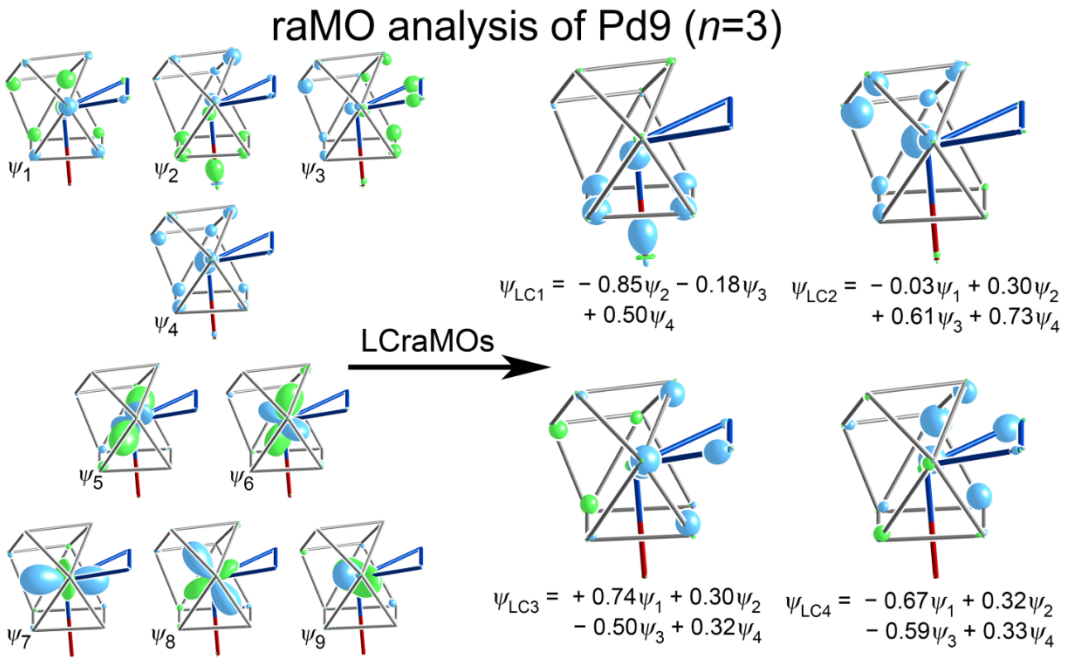

Figure A.14. raMOs and LCramos for Pd9. This atom lies on Pd2 site from the experimental structure.

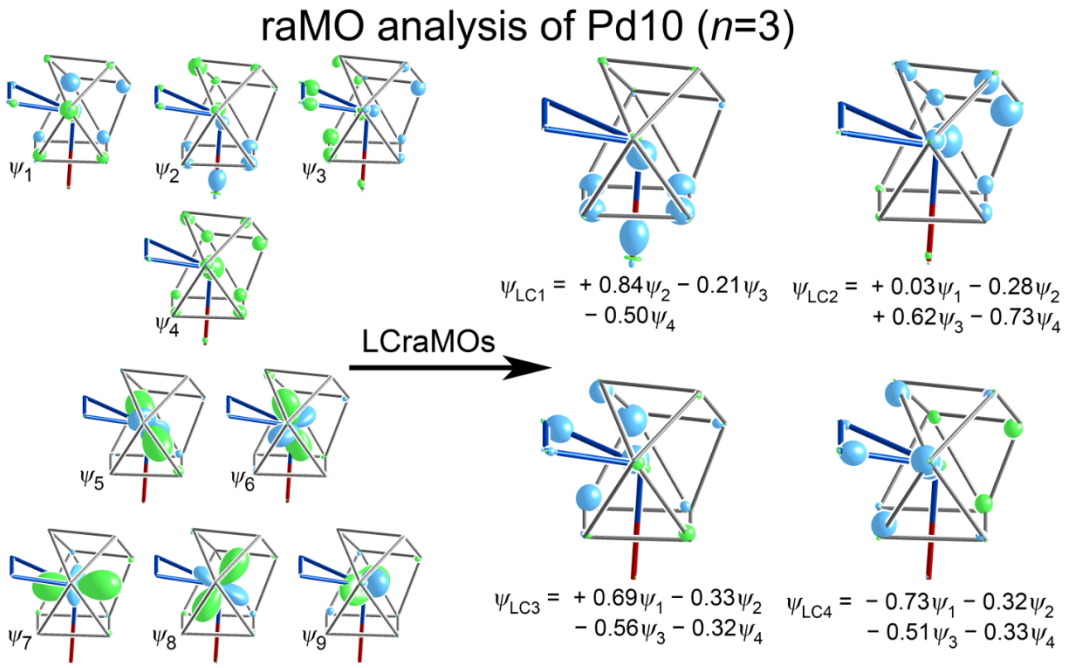

Figure A.15. raMOs and LCramos for Pd10. This atom lies on a Pd2 site from the experimental structure.

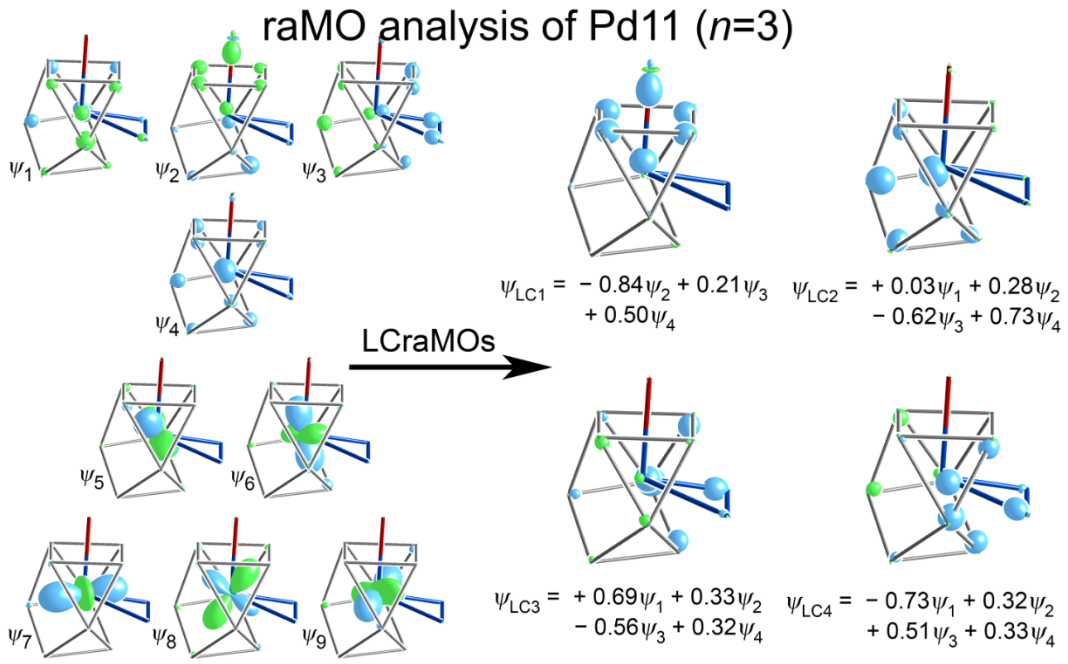

Figure A.16. raMOs and LCramos for Pd11. This atom lies on a Pd2 site from the experimental structure.

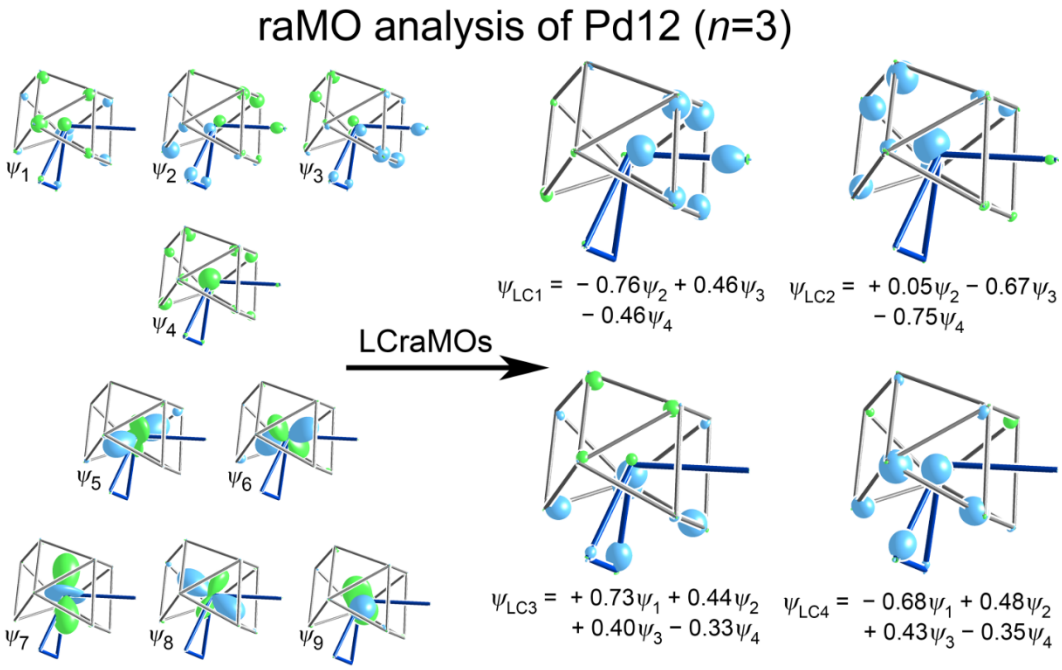

Figure A.17. raMOs and LCramos for Pd12. This atom lies on a Pd2 site from the experimental structure.

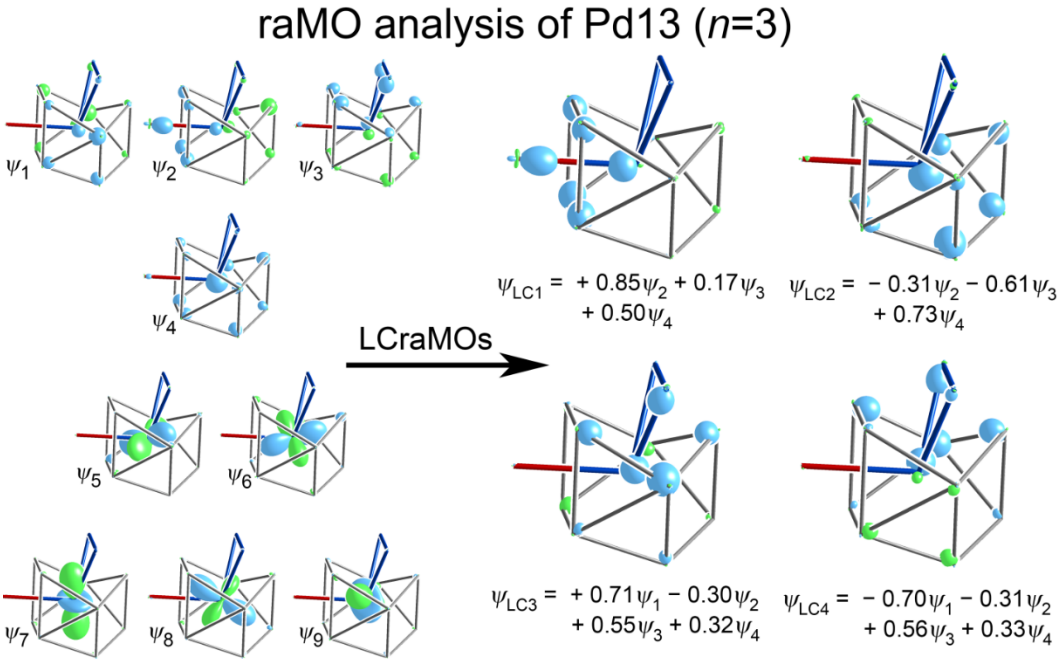

Figure A.18. raMOs and LCramos for Pd13. This atom lies on a Pd2 site from the experimental structure.

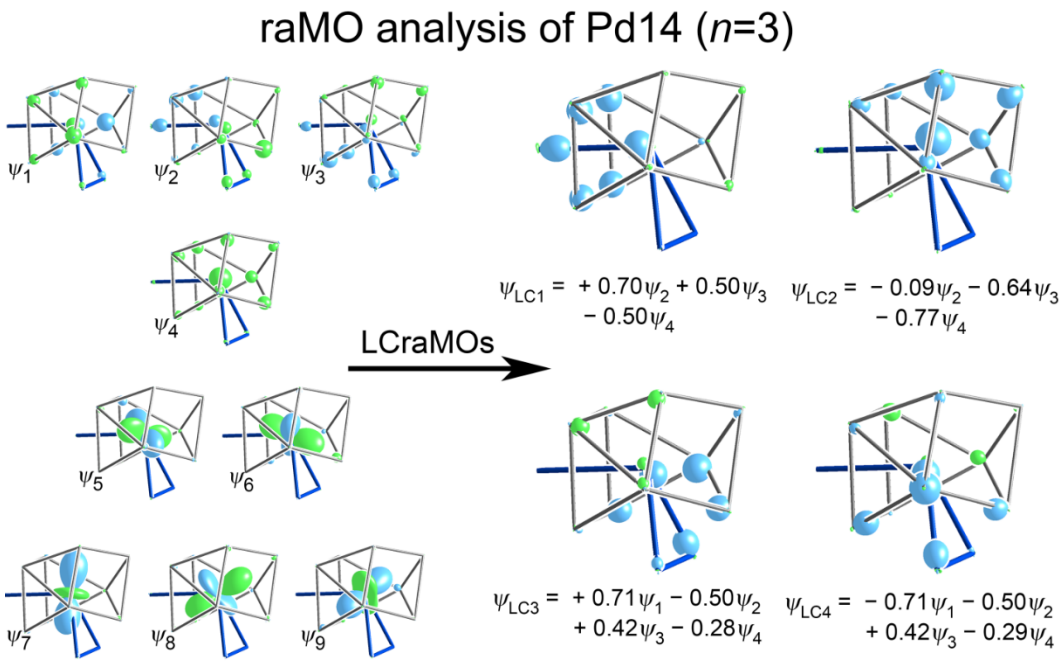

Figure A.19. raMOs and LCramos for Pd14. This atom lies on a Pd2 site from the experimental structure.

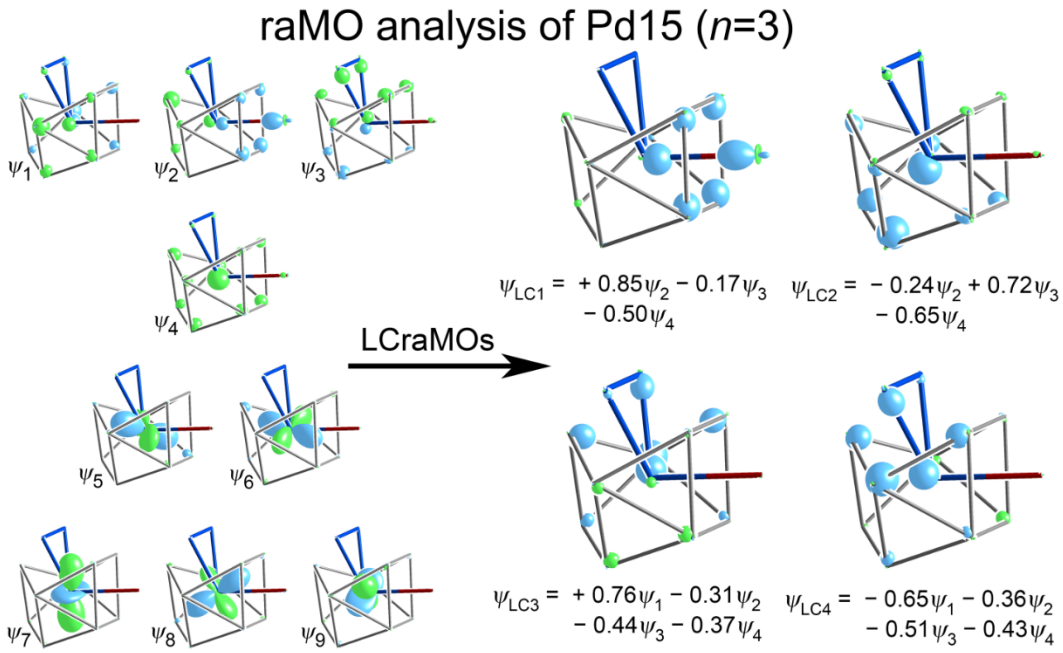

Figure A.20. raMOs and LCramos for Pd15. This atom lies on an Pd2 site from the experimental structure.

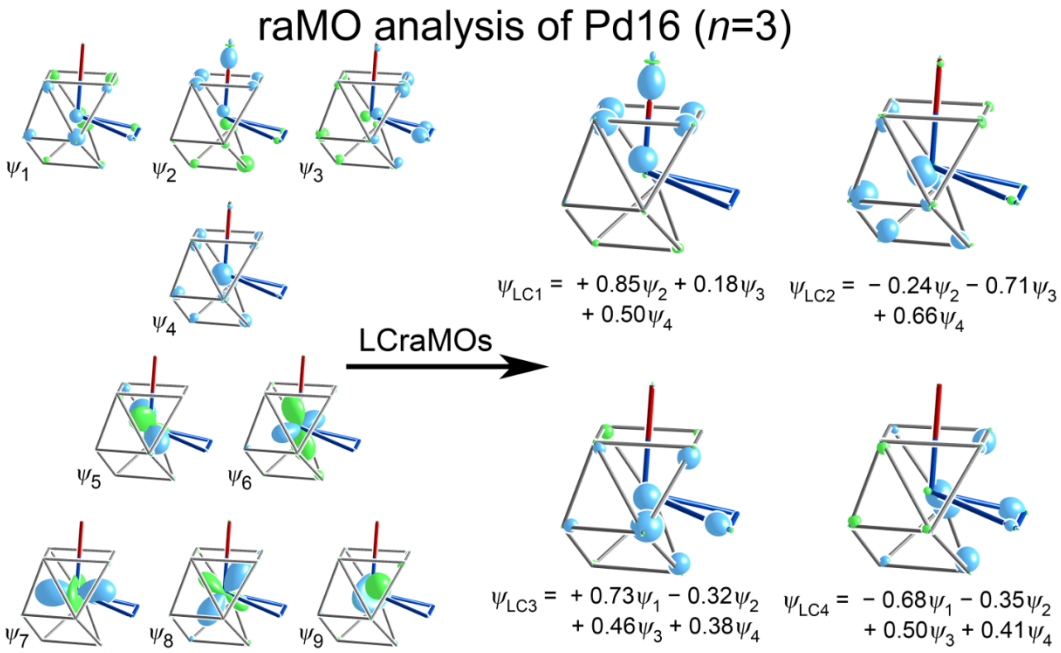

Figure A.21. raMOs and LCramos for Pd16. This atom lies on a Pd2 site from the experimental structure.

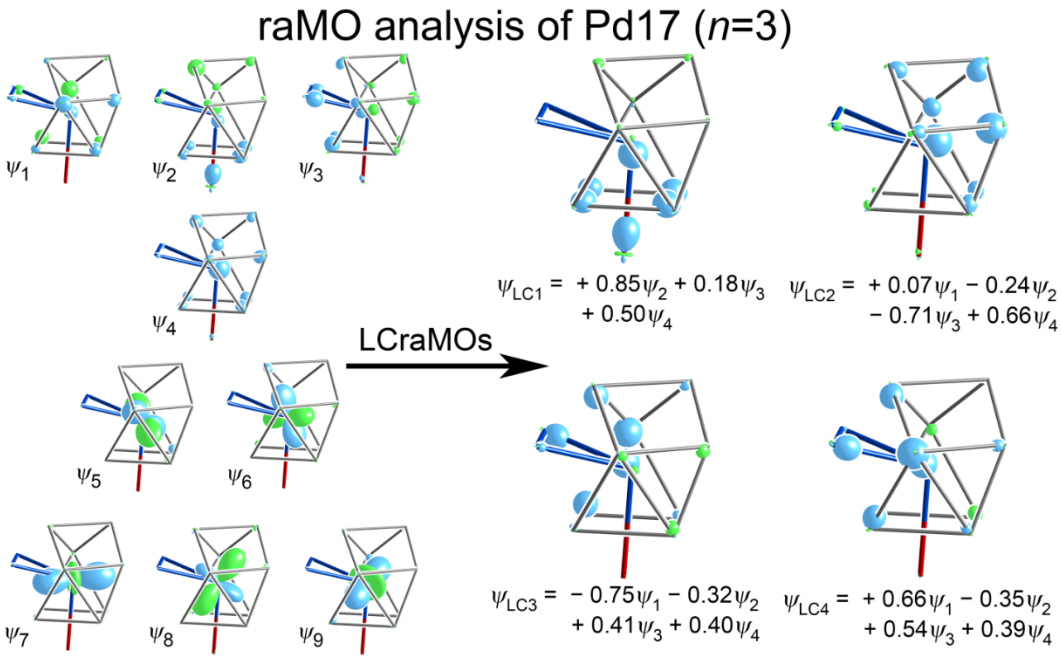

Figure A.22. raMOs and LCramos for Pd17. This atom lies on an Pd2 site from the experimental structure.

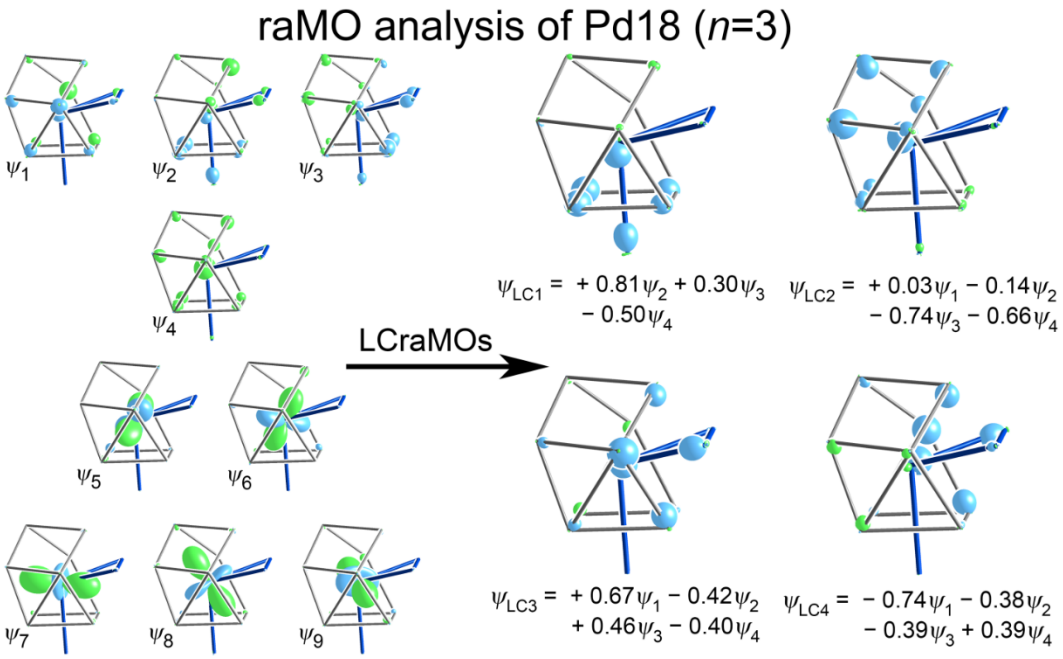

Figure A.23. raMOs and LCramos for Pd18. This atom lies on a Pd2 site from the experimental structure.

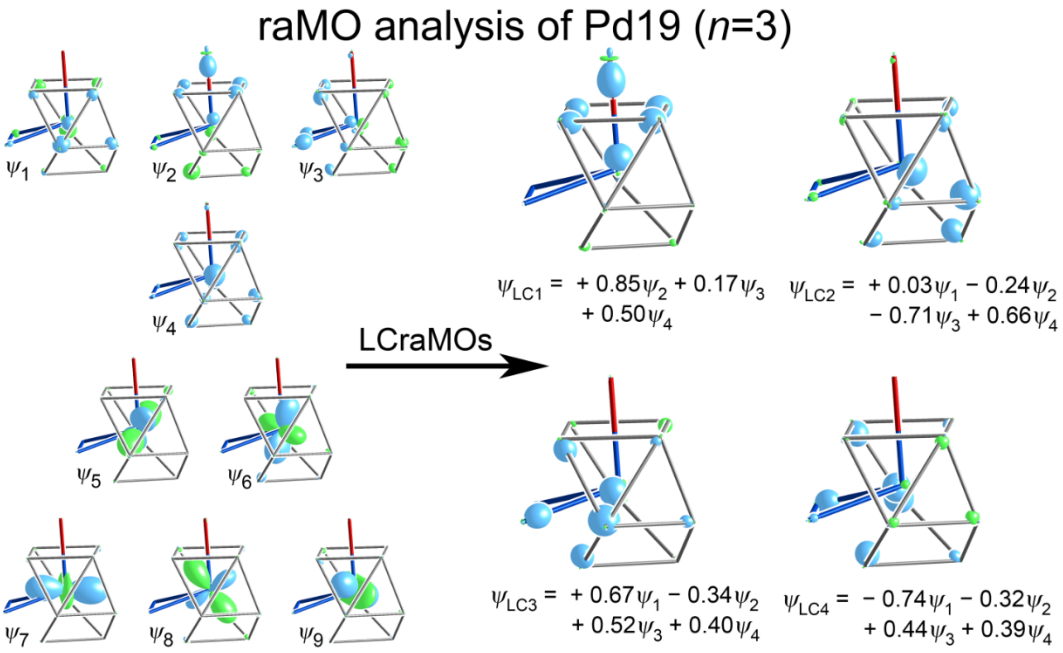

Figure A.24. raMOs and LCramos for Pd19. This atom lies on a Pd2 site from the experimental structure.

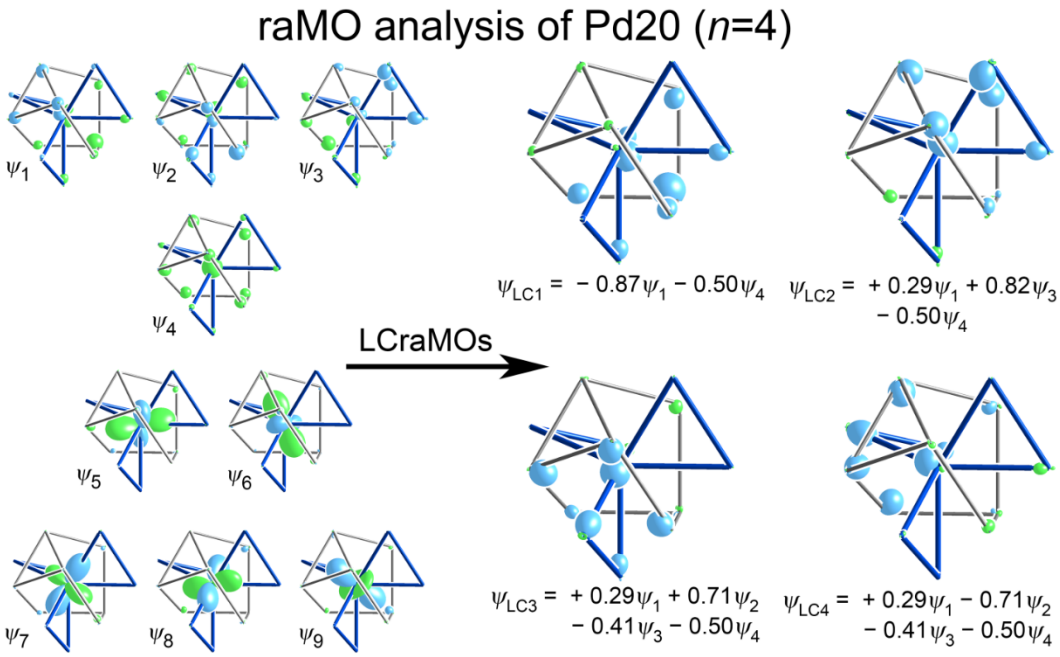

Figure A.25. raMOs and LCramos for Pd20. This atom lies on a Pd3 site from the experimental structure. The fourth bonding state contributes to the Pd_8 cube states shown in Figure 2.4 in Chapter 2.

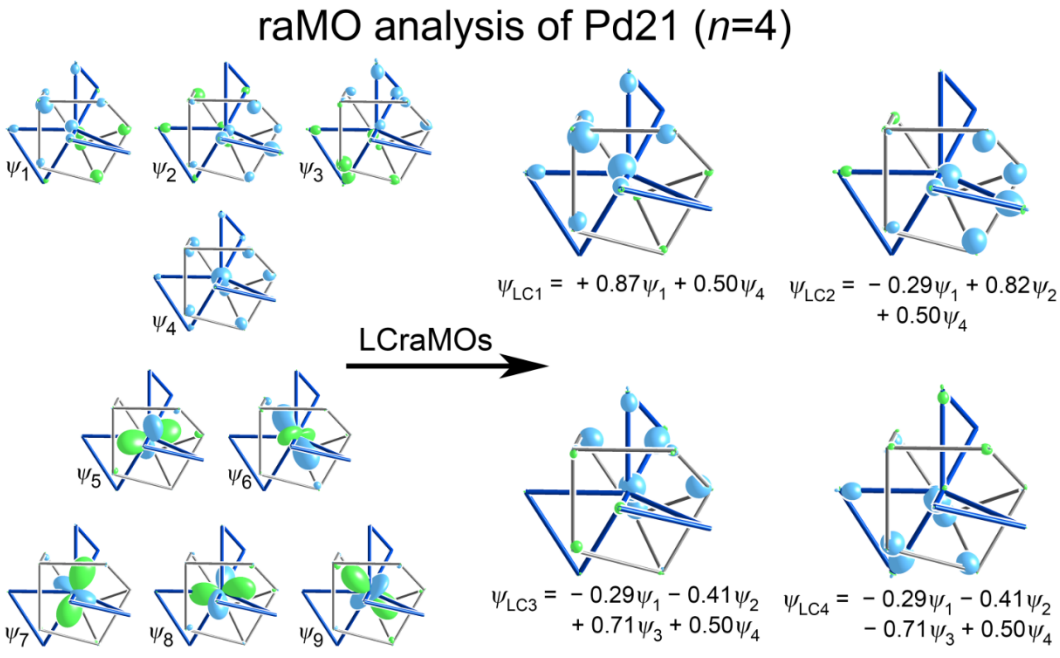

Figure A.26. raMOs and LCramos for Pd21. This atom lies on a Pd3 site from the experimental structure.

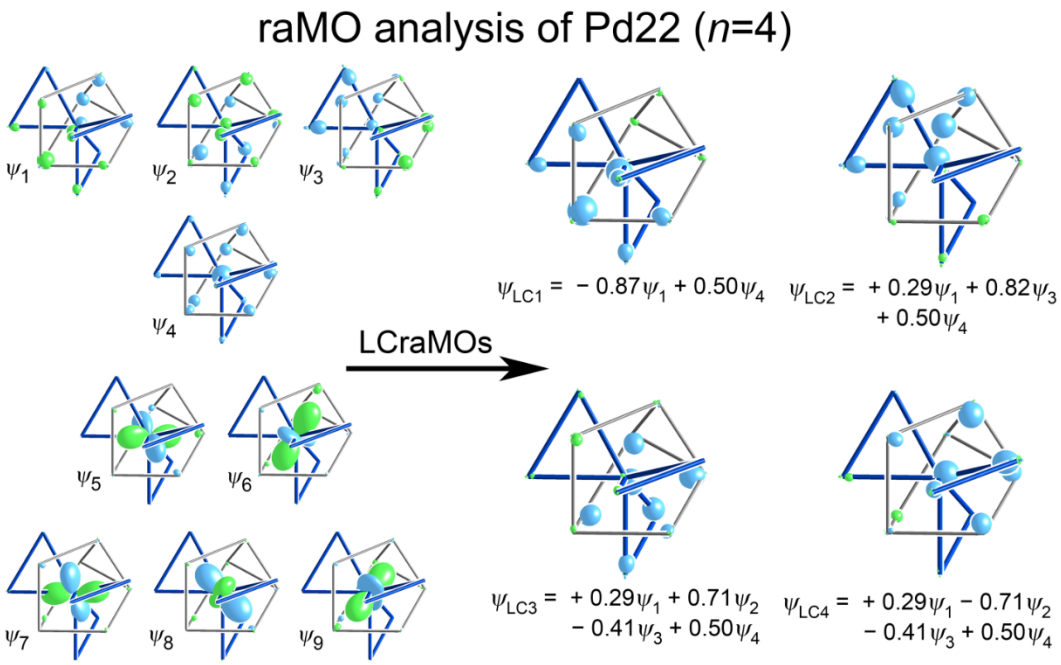

Figure A.27. raMOs and LCramos for Pd22. This atom is derived from a Pd3 site in the experimental structure.

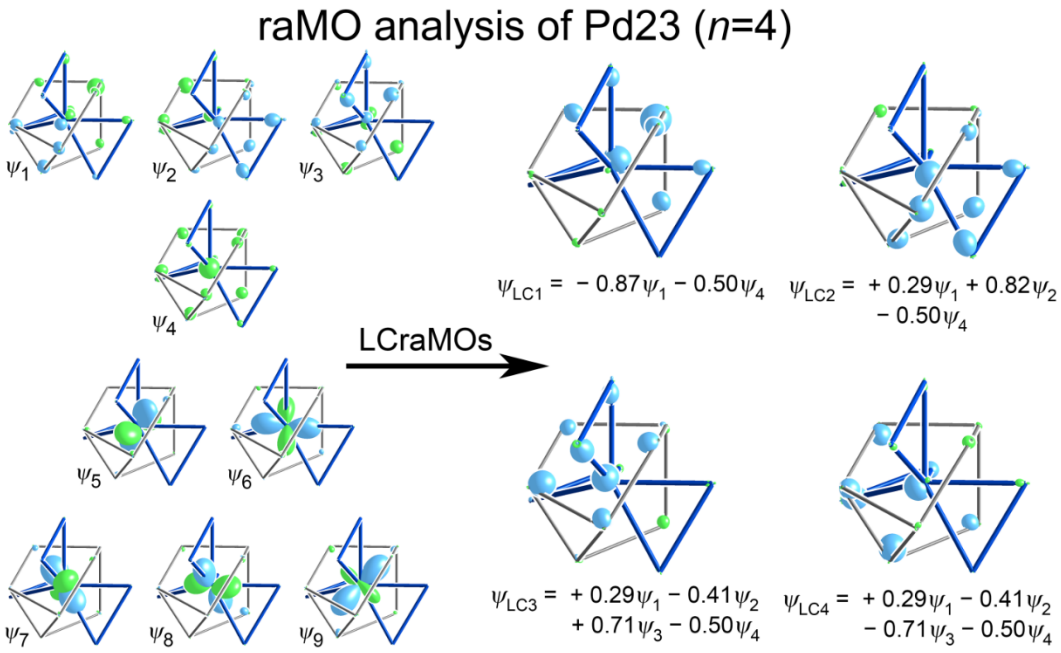

Figure A.28. raMOs and LCramos for Pd23. This atom is derived from a Pd3 site in the experimental structure.

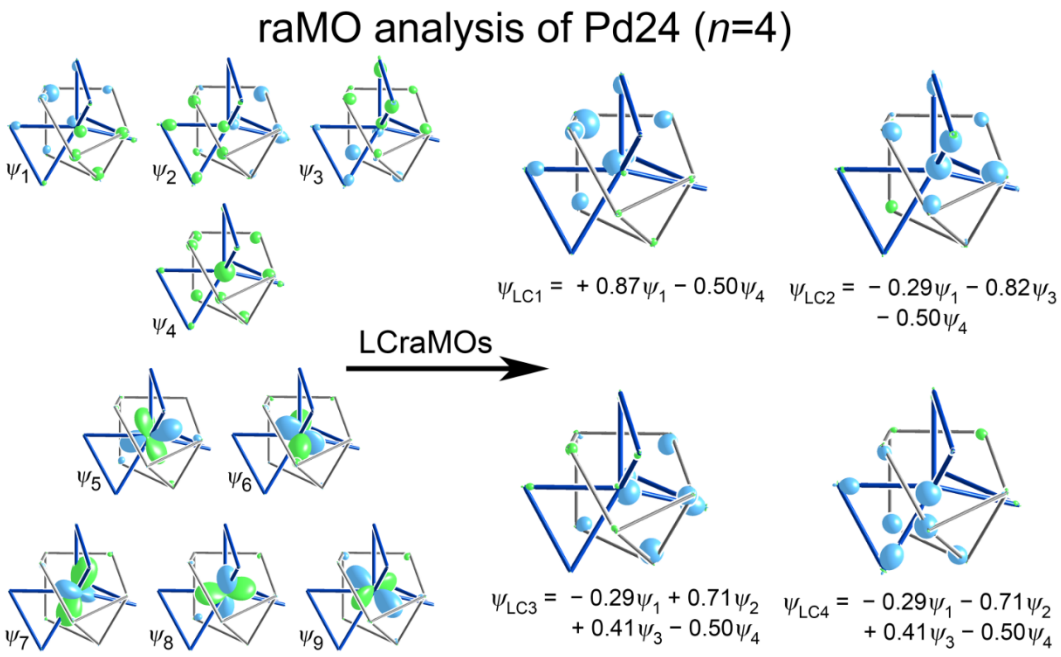

Figure A.29. raMOs and LCramos for Pd24. This atom lies on a Pd3 site from the experimental structure.

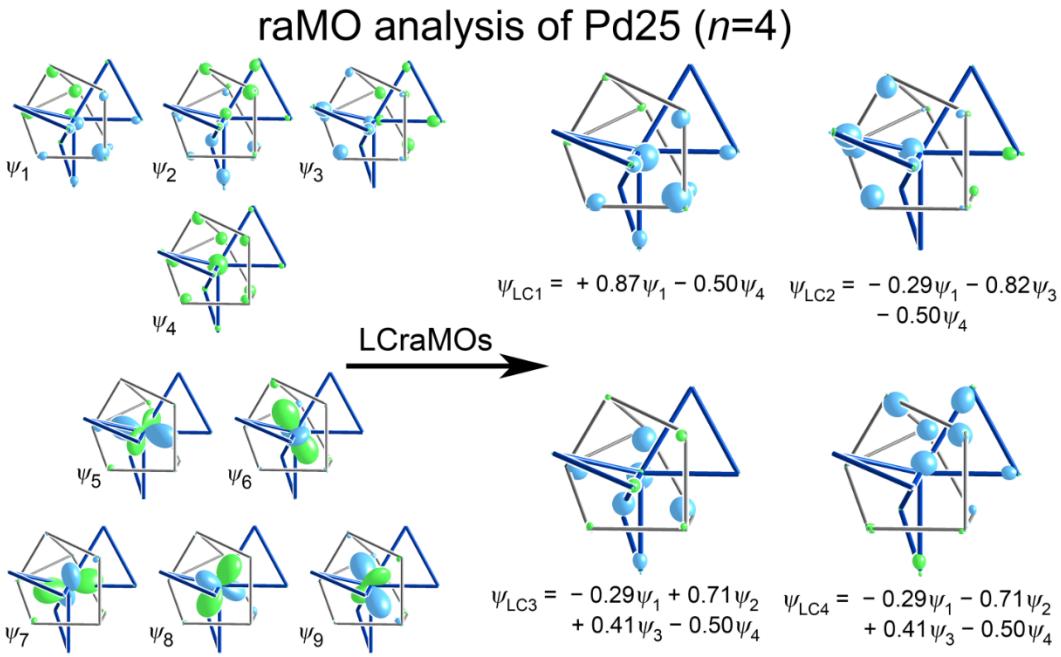

Figure A.30. raMOs and LCramos for Pd25. This atom lies on a Pd3 site from the experimental structure.

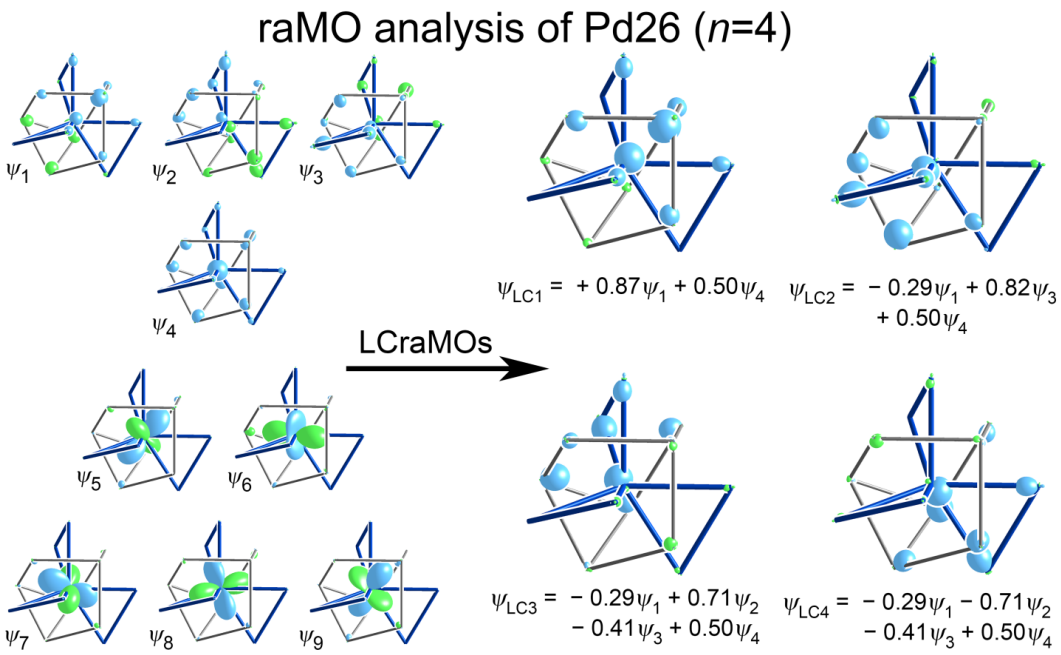

Figure A.31. raMOs and LCramos for Pd26. This atom is derived from a Pd3 site in the experimental structure.

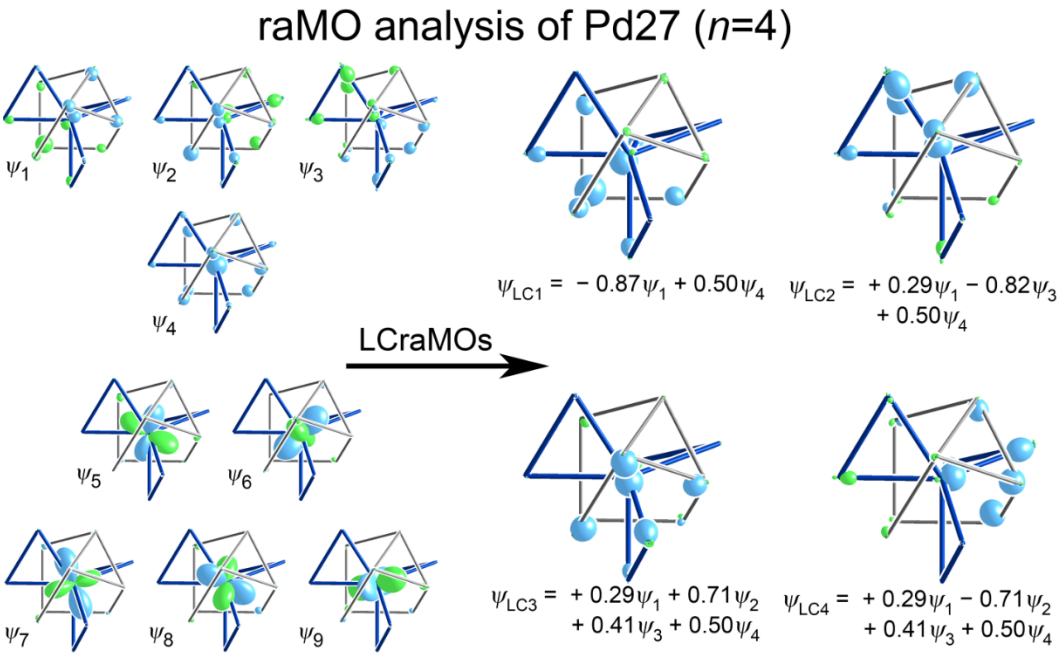

Figure A.32. raMOs and LCramos for Pd27. This atom corresponds to a Pd3 site in the experimental structure.

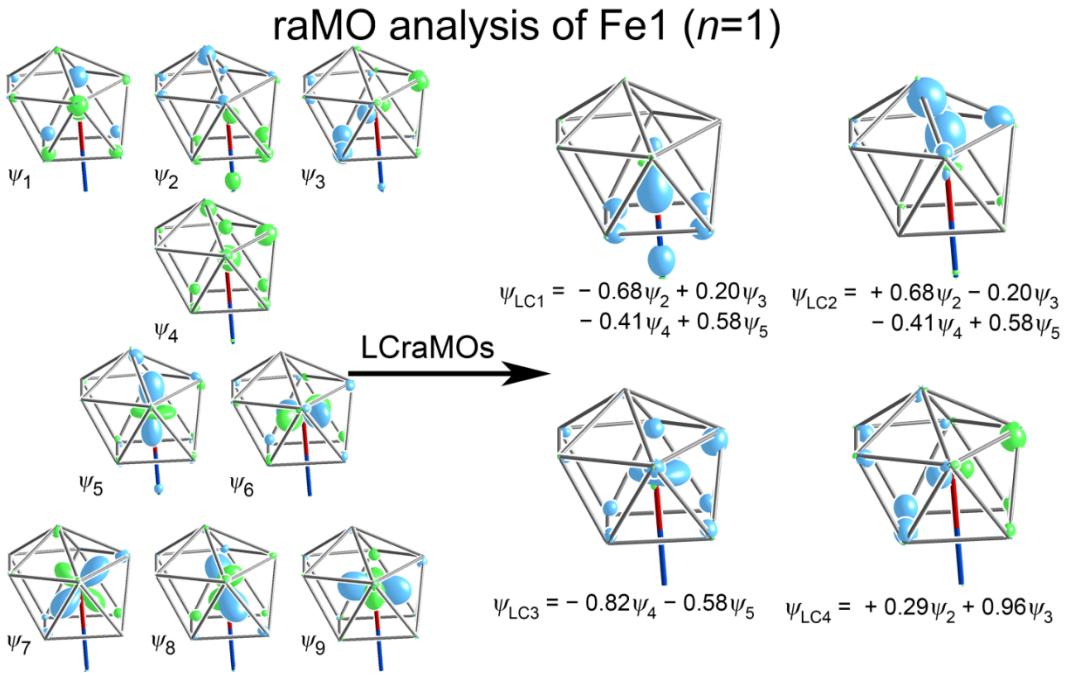

Figure A.33. raMOs and LCramos for Fe1. This atom is derived from an Fe1 site in the experimental structure.

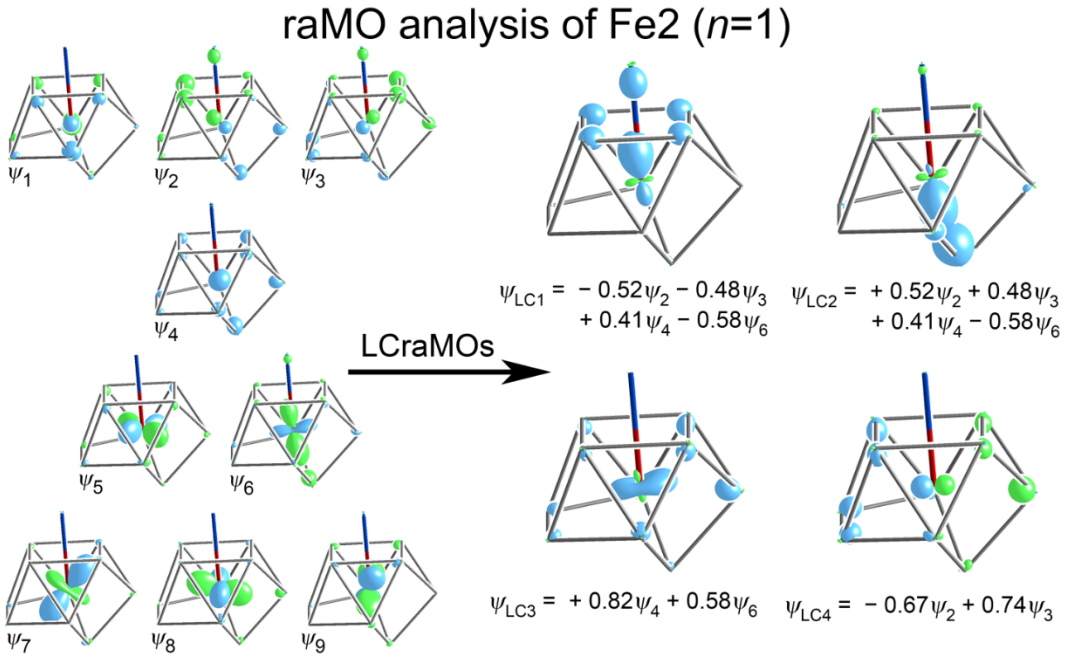

Figure A.34. raMOs and LCramos for Fe2. This atom is derived from an Fe1 site in the experimental structure.

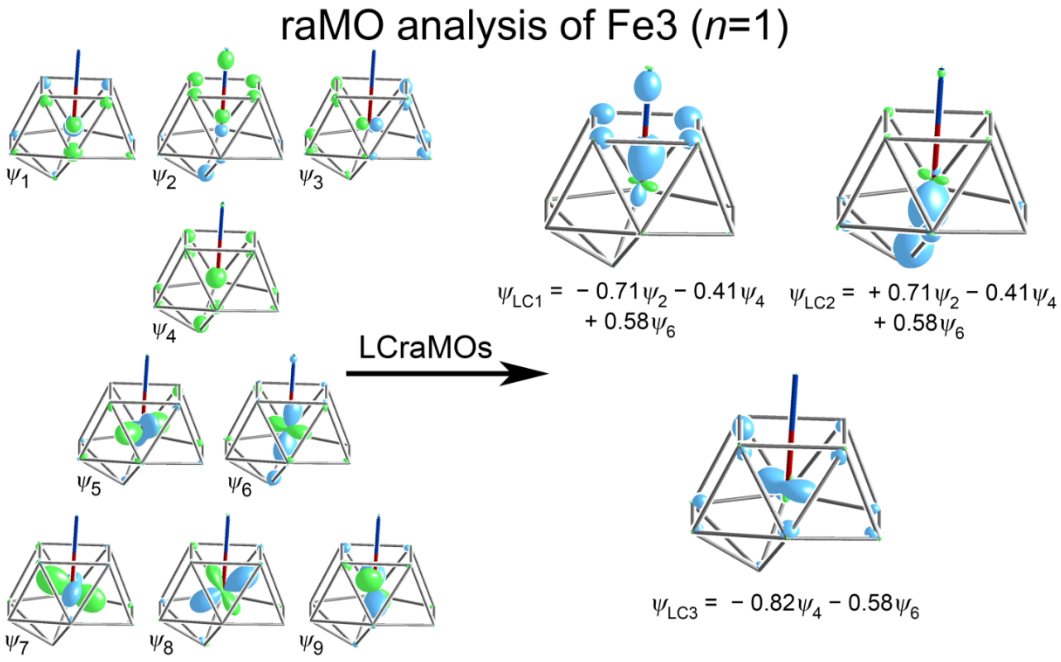

Figure A.35. raMOs and LCramos for Fe3. This atom is derived from an Fe1 site in the experimental structure.

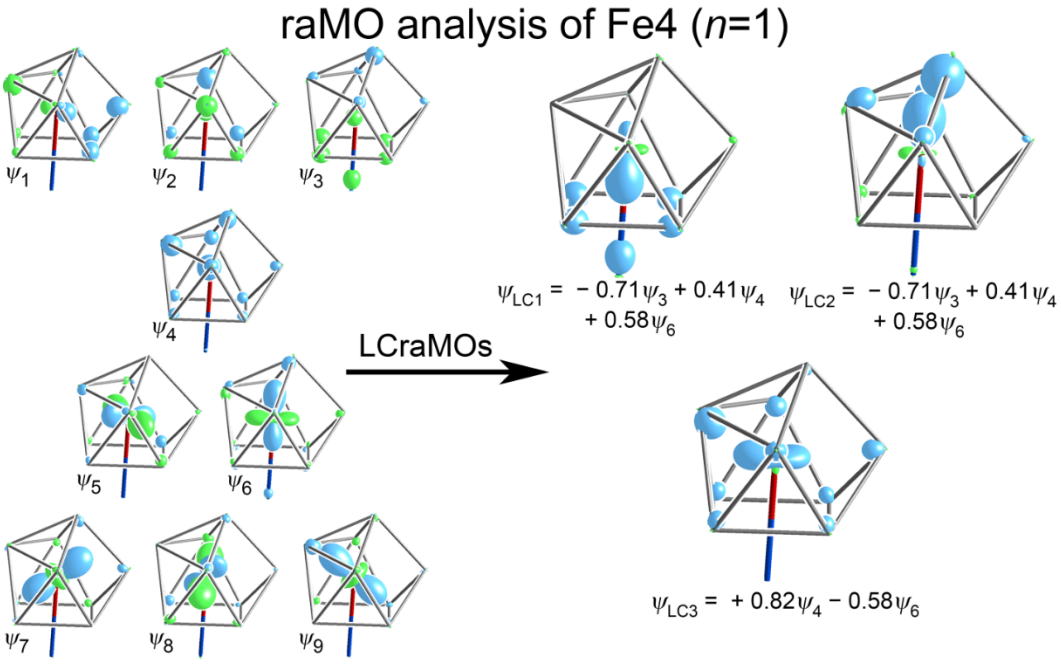

Figure A.36. raMOs and LCramos for Fe4. This atom is derived from an Fe1 site in the experimental structure.

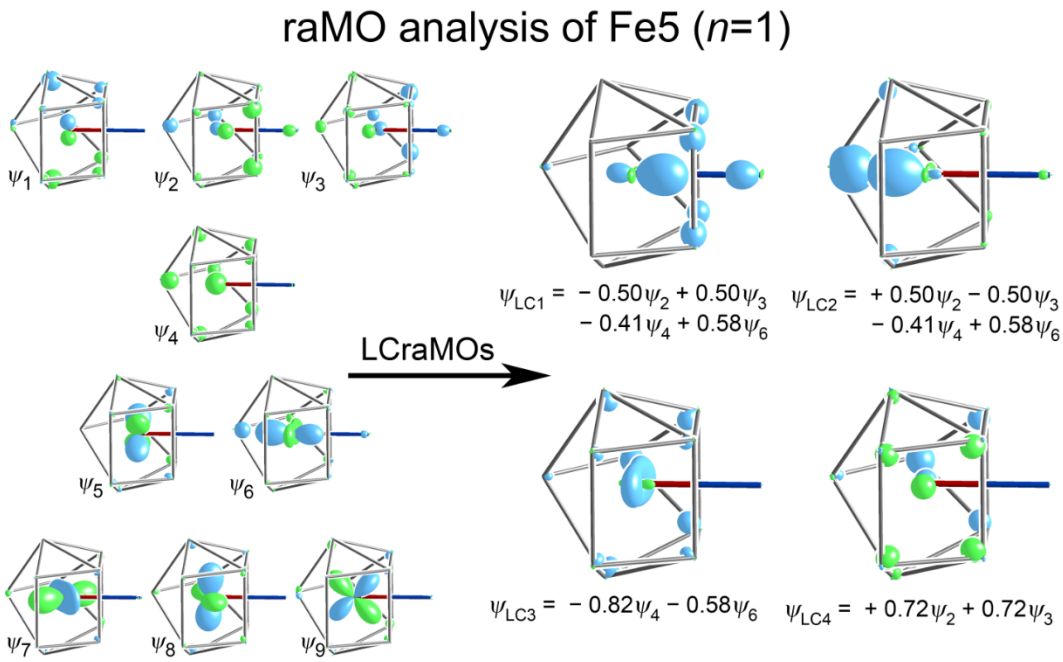

Figure A.37. raMOs and LCramos for Fe5. This atom is derived from an Fe1 site in the experimental structure.

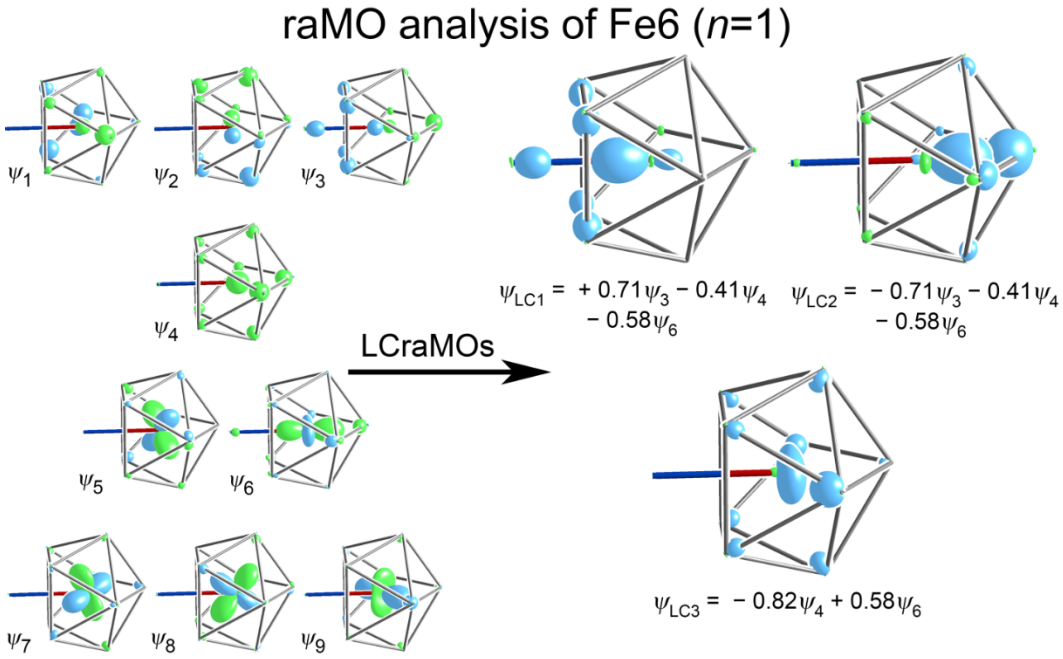

Figure A.38. raMOs and LCramos for Fe6. This atom is derived from an Fe1 site in the experimental structure.

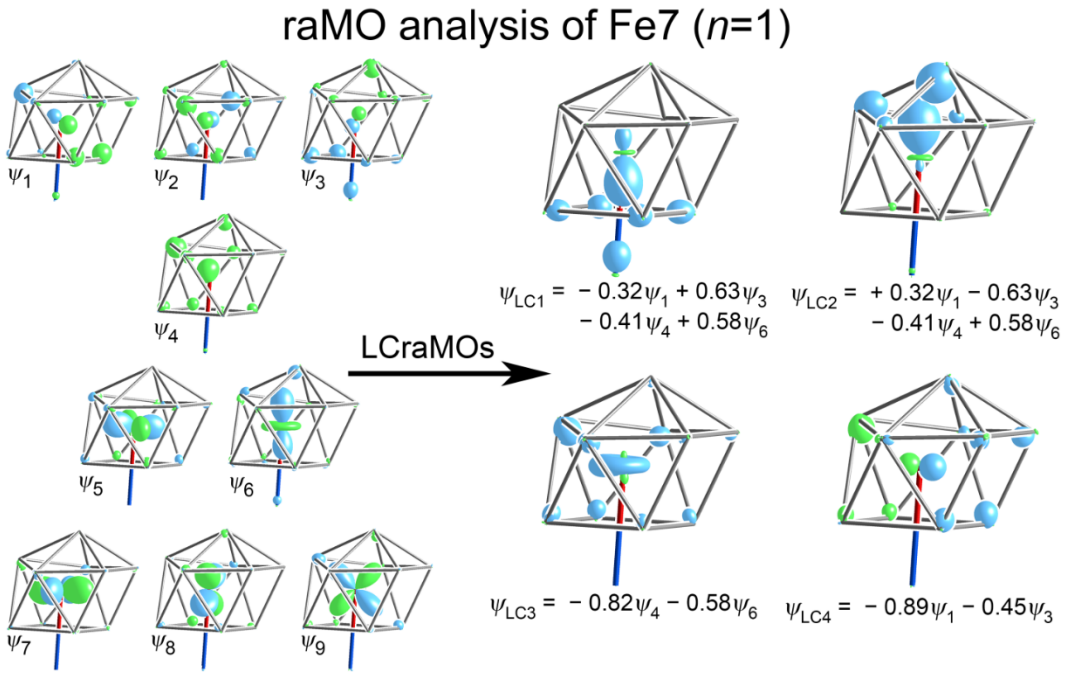

Figure A.39. raMOs and LCramos for Fe7. This atom is derived from an Fe1 site in the experimental structure.

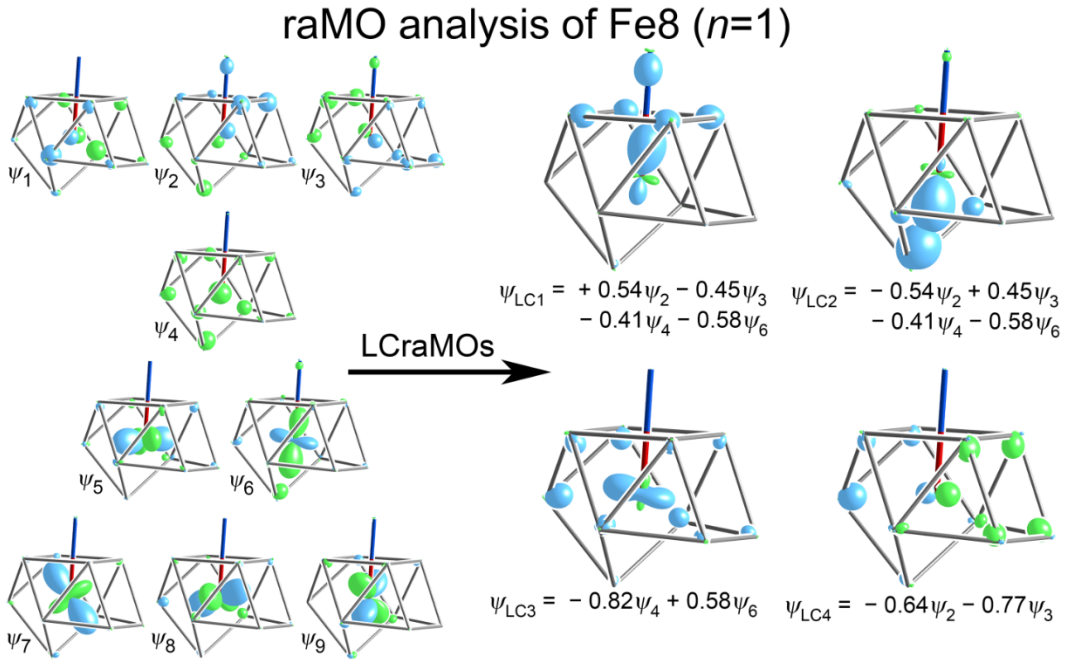

Figure A.40. raMOs and LCramos for Fe8. This atom is derived from an Fe1 site in the experimental structure.

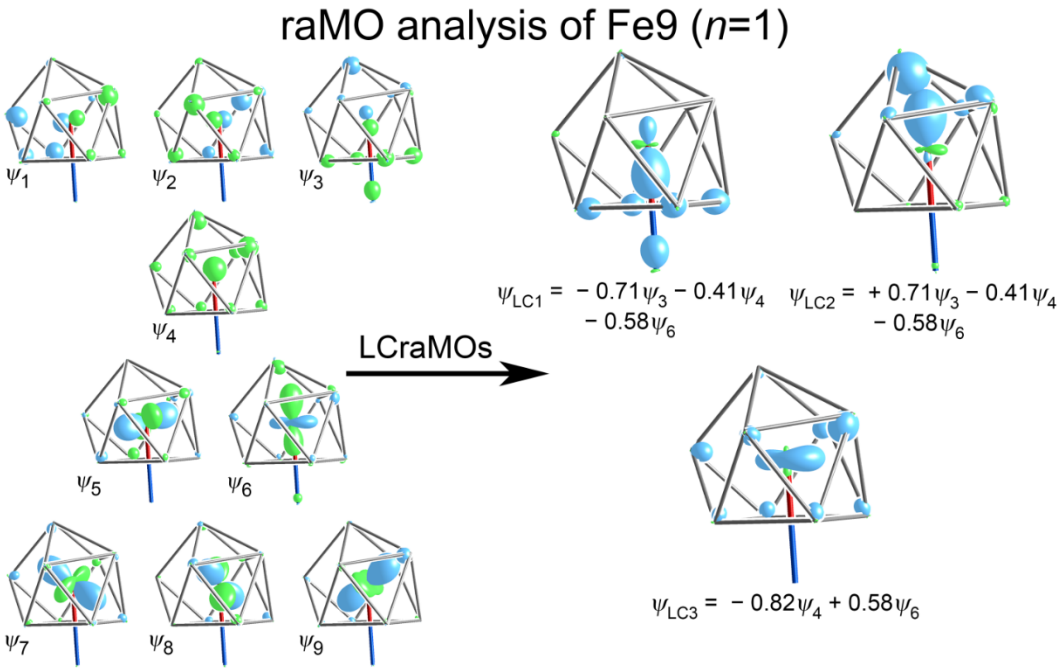

Figure A.41. raMOs and LCramos for Fe9. This atom is derived from an Fe1 site in the experimental structure.

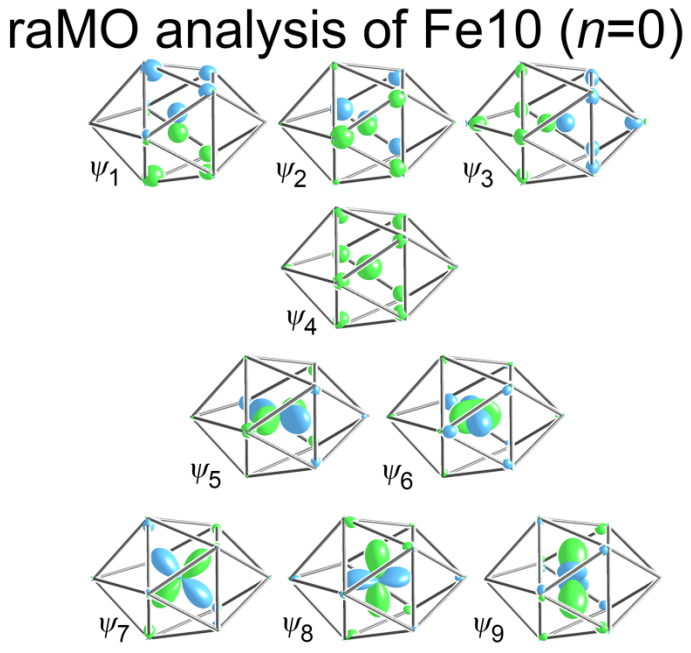

Figure A.42. raMOs for Fe10. This atom is derived from an Fe2 site in the experimental structure.

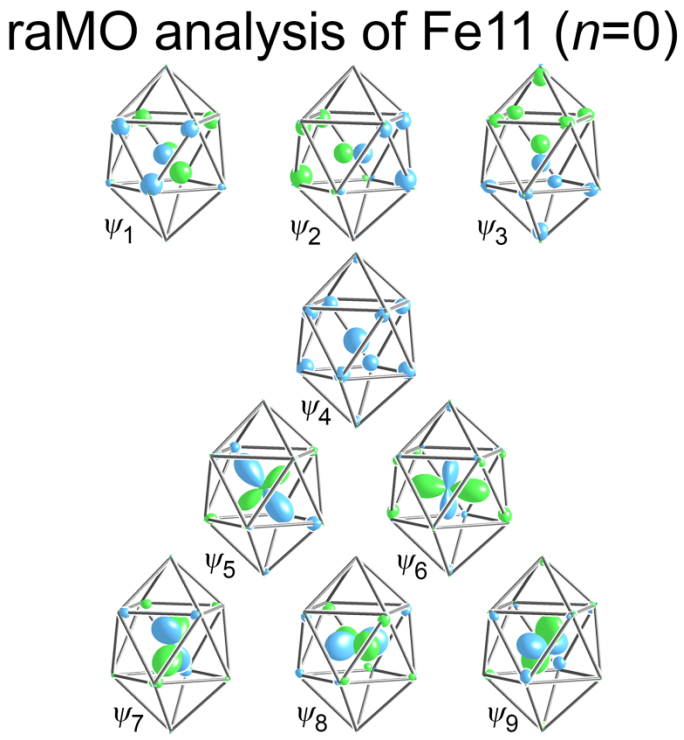

Figure A.43. raMOs for Fe11. This atom is derived from an Fe2 site in the experimental structure.

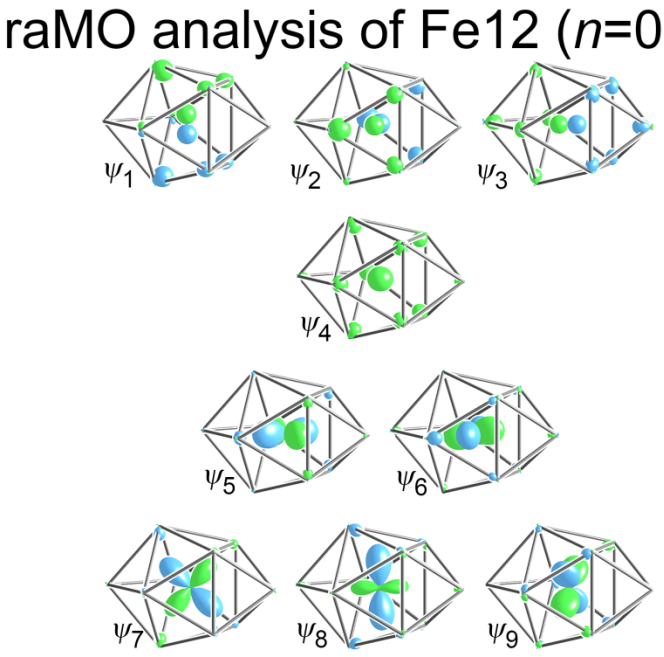

Figure A.44. raMOs for Fe12. This atom is derived from an Fe2 site in the experimental structure.

A.6 Additional Theoretical Figures

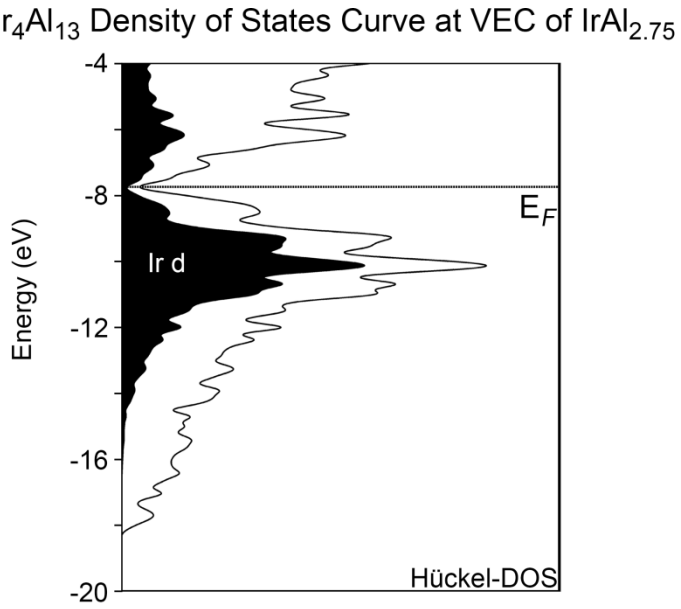

Figure A.45. Density of States(DOS) curve for Ir_4Al_{13}, one ordered variant of $IrAl_{2.75}$, with the Fermi Energy being placed at the valence electron concentration of $IrAl_{2.75}$. An extremely deep pseudogap is seen at the Fermi Energy, indicating the stability and strong preference for this electron count (17.25 e^-/Ir).

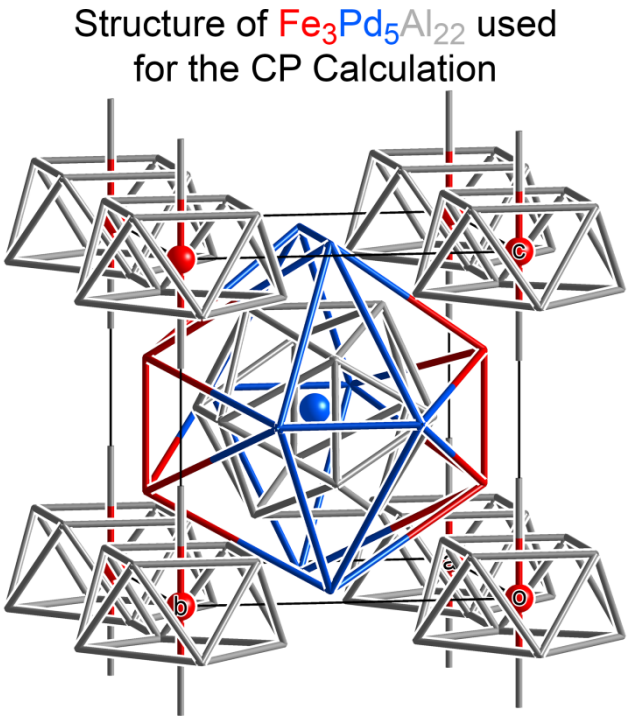

Figure A.46. Structural picture for the model system $Fe_3Pd_5Al_{22}$, the basis of the CP calculation shown in Figure 2.3 in Chapter 2, with structural parameters in Table A.16.

A.7 References

(1) Palatinus, L.; Chapuis, G. SUPERFLIP - a computer program for the solution of crystal structures by charge flipping in arbitrary dimensions. *J. Appl. Crystallogr.* **2007**, *40*, 786-790.

(2) Oszlányi, G.; Sütő, A. Ab initio structure solution by charge flipping. *Acta Crystallogr. Sect. A: Found. Crystallogr.* **2004**, *60*, 134-141.

(3) Oszlányi, G.; Sütő, A. Ab initio structure solution by charge flipping. II. Use of weak reflections. *Acta Crystallogr. Sect. A: Found. Crystallogr.* **2005**, *61*, 147-152.

(4) Petříček, V.; Dušek, M.; Palatinus, L. Crystallographic Computing System JANA2006: General features. *Z. Kristallogr.* **2014**, *229*, 345-352.

(5) Momma, K.; Izumi, F. VESTA 3 for three-dimensional visualization of crystal, volumetric and morphology data. *J. Appl. Crystallogr.* **2011**, *44*, 1272-1276.

(6) Blöchl, P. E. Projector Augmented-wave Method. *Phys. Rev. B* **1994**, *50*, 17953-17979.

(7) Kresse, G.; Furthmüller, J. Efficient Iterative Schemes for Ab Initio Total-Energy Calculations using a Plane-Wave Basis Set. *Phys. Rev. B* **1996**, *54*, 11169-11186.

(8) Kresse, G.; Furthmüller, J. Efficiency of Ab-Initio Total Energy Calculations for Metals and Semiconductors using a Plane-Wave Basis Set. *Comput. Mater. Sci.* **1996**, *6*, 15-50.

(9) Kresse, G.; Joubert, D. From Ultrasoft Pseudopotentials to the Projector Augmented-wave Method. *Phys. Rev. B* **1999**, *59*, 1758-1775.

(10) Stacey, T. E.; Fredrickson, D. C. Perceiving Molecular Themes in the Structures and Bonding of Intermetallic Phases: The Role of Hückel Theory in an *ab initio* Era. *Dalton Trans.* **2012**, *41*, 7801-7813.

(11) G. A. Landrum; W. V. Glassey. YAeHMOP: Yet Another extended Hückel Molecular Orbital Program. YAeHMOP is freely available via the Internet at URL: https://sourceforge.net/projects/yaehmop/ [Last Accessed: Feb. 27, 2017].

(12) Vanderbilt, D. Soft self-consistent pseudopotentials in a generalized eigenvalue formalism. *Phys. Rev. B* **1990**, *41*, 7892-7895.

(13) Gonze, X.; Rignanese, G.-m.; Verstraete, M.; Beuken, J.-m.; Pouillon, Y.; Caracas, R.; Raty, J.-y.; Olevano, V.; Bruneval, F.; Reining, L.; Godby, R.; Onida, G.; Hamann, D. R.; Allan, D. C. A Brief Introduction to the ABINIT Software Package. *Z. Kristallogr.* **2005**, *220*, 558-562.

(14) Gonze, X.; Amadon, B.; Anglade, P.-M.; Beuken, J.-M.; Bottin, F.; Boulanger, P.; Bruneval, F.; Caliste, D.; Caracas, R.; Côté, M.; Deutsch, T.; Genovese, L.; Ghosez, P.; Giantomassi, M.; Goedecker, S.; Hamann, D. R.; Hermet, P.; Jollet, F.; Jomard, G.; Leroux, S.; Mancini, M.; Mazevet, S.; Oliveira, M. J. T.; Onida, G.; Pouillon, Y.; Rangel, T.; Rignanese, G.-M.; Sangalli, D.; Shaltaf, R.; Torrent, M.; Verstraete, M. J.; Zerah, G.; Zwanziger, J. W. ABINIT: First-principles approach to material and nanosystem properties. *Comput. Phys. Commun.* **2009**, *180*, 2582-2615.

(15) Goedecker, S.; Teter, M.; Hutter, J. Separable dual-space Gaussian pseudopotentials. *Phys. Rev. B* **1996**, *54*, 1703-1710.

(16) Hartwigsen, C.; Goedecker, S.; Hutter, J. Relativistic separable dual-space Gaussian pseudopotentials from H to Rn. *Phys. Rev. B* **1998**, *58*, 3641-3662.

(17) Berns, V. M.; Engelkemier, J.; Guo, Y.; Kilduff, B. J.; Fredrickson, D. C. Progress in Visualizing Atomic Size Effects with DFT-Chemical Pressure Analysis: From Isolated Atoms to Trends in AB_5 Intermetallics. *J. Chem. Theory Comput.* **2014**, *10*, 3380-3392.

(18) Oliveira, M. J. T.; Nogueira, F. Generating relativistic pseudo-potentials with explicit incorporation of semi-core states using APE, the Atomic Pseudo-potentials Engine. *Comput. Phys. Commun.* **2008**, *178*, 524-534.

Appendix B.

Supporting Information for Chapter 3.

$Mn_{39}Si_9N_x$: Epitaxial Stabilization as a Pathway to the Formation of Intermetallic Nitrides

Work in this Appendix was done by Peterson

B.1 Tables of Crystallographic Data for $Mn_{39}Si_9N_x$

Table B.1. Selected Crystallographic Data for $Mn_{39}Si_9N_x$

refined composition	$Mn_{38.869(12)}Si_{9.131(12)}N_{0.84(3)}$
EDS composition	$Mn_{39.00(14)}Si_{9.14(4)}$
Pearson symbol	*oP*195.36(12)
space group	*Pnma* (62)
a (Å)	12.0826(2)
b (Å)	11.9195(2)
c (Å)	16.5709(3)
cell volume (Å^3), Z	2386.52(7), 4
crystal volume (mm^3)	0.098 × 0.048 × 0.015
crystal color, shape	gray, plate
data collection temp. (K)	295
radiation source, λ (Å)	Mo Kα, 0.71069
absorption coefficient (mm^{-1})	20.152
absorption correction	analytical
θ_{min}, θ_{max} (°)	2.98, 28.92

refinement method	F^2
$R_{int}(I > 3\sigma)$, R_{int}(all)	7.90, 10.06
no. of reflections ($I > 3\sigma$, all)	12048, 40425
unique reflections ($I > 3\sigma$, all)	1858, 3173
no. of parameters	245
$R(I > 3\sigma)$, $R_w(I > 3\sigma)$	3.11, 5.69
R(all), R_w(all)	8.39, 7.98
$S(I > 3\sigma$, all)	0.96, 1.00
$\Delta\rho_{max}$, $\Delta\rho_{min}$ ($e^-/Å^3$)	1.59, −1.88

Table B.2. Refined atomic coordinates for $Mn_{39}Si_9N_x$

Site	Element	Wyckoff	x	y	z	$U_{equiv.}$	Occupancy
Mn1	Mn	4c	0.04420(13)	0.75	0.19320(9)	0.0053(5)	1
Mn2	Mn	4c	0.55753(12)	0.75	0.05630(9)	0.0039(5)	1
Mn3	Mn	4c	0.65641(13)	0.75	-0.32874(9)	0.0051(4)	1
Mn4	Mn	4c	0.84512(13)	0.75	-0.05708(9)	0.0042(4)	1
Mn5	Mn	8d	0.46322(9)	0.63311(10)	0.17762(6)	0.0061(3)	1
Mn6	Mn	8d	0.34255(10)	0.13692(10)	0.05655(6)	0.0058(3)	1
Mn7	Mn	4c	0.54621(13)	0.75	-0.18931(9)	0.0056(5)	1
Mn8	Mn	4c	0.15211(14)	0.75	0.05517(9)	0.0067(5)	1
Mn9	Mn	4c	0.26525(13)	0.75	0.19420(9)	0.0055(5)	1
Mn10	Mn	4c	0.45020(13)	0.75	-0.07008(9)	0.0050(5)	1
Mn11	Mn	8d	0.32756(9)	0.43910(10)	0.20913(6)	0.0057(3)	1
Mn12	Mn	4c	0.75162(13)	0.75	0.06114(9)	0.0035(5)	1
Mn13	Mn	8d	0.65572(10)	0.56417(10)	0.09682(6)	0.0057(3)	1
Mn14	Mn	8d	0.65887(9)	0.56759(10)	0.25772(6)	0.0068(3)	1
Mn15	Mn	8d	0.45191(9)	0.57646(10)	0.02041(6)	0.0052(3)	1
Mn16	Mn	8d	0.26736(9)	0.57217(10)	0.09950(6)	0.0067(3)	1
Mn17	Mn	8d	0.84375(9)	0.85675(9)	-0.29576(6)	0.0049(3)	1
Mn18	Mn	8d	0.84828(10)	0.64303(10)	0.17783(6)	0.0072(3)	1
Mn19	Mn	8d	0.53845(9)	0.57025(10)	0.40140(6)	0.0071(3)	1
Mn20	Mn	8d	0.84654(9)	0.55521(10)	0.01544(6)	0.0061(3)	1
Mn21	Mn	8d	0.48992(9)	0.44111(10)	0.28106(6)	0.0059(3)	1
Mn22	Mn	8d	0.96523(9)	0.13782(10)	0.06015(6)	0.0055(3)	1
Mn23	Mn	8d	0.27249(9)	0.64284(10)	-0.04701(6)	0.0065(3)	1
Mn24	Mn	4c	0.74405(13)	0.75	-0.18429(9)	0.0057(5)	1
Mn25a	Mn	4c	0.44996(13)	0.75	-0.31588(9)	0.0041(5)	0.869(12)
Mn25b	Si	4c	0.44996(13)	0.75	-0.31588(9)	0.0041(5)	0.131(12)
Si1	Si	4c	0.3587(2)	0.75	0.06592(16)	0.0032(8)	1

Si2	Si	8d	0.15506(17)	0.08607(16)	0.13681(11)	0.0031(5)	1
Si3	Si	4c	0.9502(2)	0.75	0.06184(17)	0.0053(9)	1
Si4	Si	4c	0.6526(3)	0.75	0.18371(15)	0.0054(8)	1
Si5	Si	8d	0.81818(17)	0.04441(18)	0.14664(12)	0.0067(6)	1
Si6	Si	8d	0.50319(17)	0.06037(19)	0.12958(12)	0.0054(6)	1
N1	N	4c	-0.0953(13)	0.75	0.2516(9)	0.010(5)[a]	0.58(3)
N2	N	4a	0.5	0.5	0.5	0.013(12)[a]	0.26(3)

[a]modeled with isotropic atomic displacement parameters

Table B.3. Refined harmonic displacement parameters for $Mn_{39}Si_9N_x$

Site	U_{11}	U_{22}	U_{33}	U_{12}	U_{13}	U_{23}
Mn1	0.0049(8)	0.0070(9)	0.0042(8)	0	-0.0006(6)	0
Mn2	0.0023(8)	0.0041(9)	0.0053(8)	0	-0.0005(6)	0
Mn3	0.0049(8)	0.0051(8)	0.0055(7)	0	-0.0014(7)	0
Mn4	0.0042(7)	0.0048(8)	0.0036(7)	0	-0.0007(6)	0
Mn5	0.0059(6)	0.0052(6)	0.0072(6)	0.0001(5)	-0.0001(5)	0.0002(5)
Mn6	0.0043(5)	0.0071(6)	0.0062(5)	0.0003(5)	-0.0003(5)	0.0011(4)
Mn7	0.0047(8)	0.0067(9)	0.0054(8)	0	0.0011(6)	0
Mn8	0.0037(8)	0.0095(9)	0.0068(8)	0	-0.0003(7)	0
Mn9	0.0049(8)	0.0083(9)	0.0034(7)	0	0.0016(6)	0
Mn10	0.0067(8)	0.0044(9)	0.0039(8)	0	0.0014(6)	0
Mn11	0.0045(6)	0.0072(6)	0.0053(5)	-0.0006(5)	0.0005(4)	-0.0007(5)
Mn12	0.0038(8)	0.0037(9)	0.0032(8)	0	0.0003(6)	0
Mn13	0.0048(5)	0.0055(6)	0.0068(5)	-0.0006(5)	-0.0009(5)	0.0009(4)
Mn14	0.0079(6)	0.0062(6)	0.0062(5)	0.0007(5)	0.0000(5)	0.0010(4)
Mn15	0.0055(6)	0.0057(6)	0.0043(5)	-0.0001(5)	-0.0003(4)	0.0003(5)
Mn16	0.0071(6)	0.0051(6)	0.0077(6)	-0.0021(5)	0.0002(4)	0.0015(5)
Mn17	0.0038(5)	0.0049(6)	0.0062(5)	-0.0005(5)	0.0002(5)	0.0006(4)
Mn18	0.0080(6)	0.0049(6)	0.0088(6)	-0.0009(5)	0.0017(5)	-0.0002(4)
Mn19	0.0083(6)	0.0058(6)	0.0072(6)	0.0018(5)	0.0006(5)	-0.0010(5)
Mn20	0.0057(5)	0.0069(6)	0.0057(5)	0.0010(5)	0.0000(5)	0.0007(4)
Mn21	0.0041(6)	0.0087(6)	0.0049(6)	0.0005(5)	-0.0006(4)	-0.0002(5)
Mn22	0.0064(6)	0.0048(6)	0.0052(6)	-0.0004(5)	0.0010(5)	-0.0003(4)
Mn23	0.0058(6)	0.0078(6)	0.0059(6)	-0.0008(5)	-0.0012(4)	-0.0012(5)
Mn24	0.0040(8)	0.0069(9)	0.0062(8)	0	-0.0004(6)	0
Mn25a	0.0042(9)	0.0054(10)	0.0027(9)	0	-0.0006(6)	0
Mn25b	0.0042(9)	0.0054(10)	0.0027(9)	0	-0.0006(6)	0
Si1	0.0015(14)	0.0041(14)	0.0042(13)	0	0.0008(11)	0
Si2	0.0041(9)	0.0016(10)	0.0036(9)	-0.0003(9)	0.0015(8)	0.0008(7)

Si3	0.0039(15)	0.0061(16)	0.0059(15)	0	-0.0007(11)	0
Si4	0.0067(14)	0.0067(15)	0.0026(13)	0	-0.0018(12)	0
Si5	0.0081(11)	0.0065(11)	0.0056(10)	-0.0007(8)	-0.0022(8)	0.0002(8)
Si6	0.0066(10)	0.0038(11)	0.0059(10)	-0.0005(8)	0.0000(8)	-0.0019(9)

Table B.4. Selected interatomic distances

Site	Neighbor	Distance (Å)
Mn1	Mn5 (×2)	2.7351(17)
	Mn8	2.633(2)
	Mn9	2.671(2)
	Mn14 (×2)	2.7034(14)
	Mn18 (×2)	2.7008(18)
	Mn19 (×2)	2.6557(15)
	Si3	2.455(3)
	Si4	2.424(3)
	N1	1.944(15)
Mn2	Mn5 (×2)	2.6984(17)
	Mn6 (×2)	2.6021(17)
	Mn10	2.463(2)
	Mn12	2.346(2)
	Mn13 (×2)	2.6009(14)
	Mn15 (×2)	2.5022(14)
	Si1	2.407(3)
	Si4	2.403(3)
Mn3	Mn7	2.667(2)
	Mn17 (×2)	2.6535(18)
	Mn22 (×2)	2.7089(17)
	Mn23 (×2)	2.7996(17)
	Mn24	2.617(2)
	Mn25a	2.504(2)
	Mn25b	2.504(2)
	Si5 (×2)	2.503(2)
Mn4	Mn6 (×2)	2.6379(18)
	Mn12	2.261(2)
	Mn20 (×2)	2.6144(13)
	Mn22 (×2)	2.6536(18)
	Mn24	2.436(2)
	Mn25a	2.457(2)
	Mn25b	2.457(2)
	Si2 (×2)	2.359(2)
	Si3	2.344(3)
Mn5	Mn1	2.7351(17)
	Mn2	2.6984(17)
	Mn5	2.7866(17)
	Mn9	2.7818(17)
	Mn13	2.8067(16)
	Mn14	2.8214(16)
	Mn15	2.6947(15)
	Mn16	2.7935(16)
	Mn18	2.7713(15)
	Mn21	2.8774(16)
	Si1	2.638(3)
	Si4	2.6809(33)
	Si6	2.487(2)
	N1	1.953(11)
Mn6	Mn2	2.6021(17)
	Mn4	2.6379(18)
	Mn6	2.6958(16)
	Mn10	2.8526(18)
	Mn11	2.6920(15)
	Mn12	2.6296(17)
	Mn13	2.6854(15)
	Mn16	2.7465(16)
	Mn20	2.7552(16)
	Mn24	2.7189(17)
	Si2	2.6959(23)
	Si6	2.463(2)
Mn7	Mn3	2.667(2)
	Mn10	2.291(2)
	Mn11 (×2)	2.7412(14)
	Mn17 (×2)	2.7685(18)

Site	Neighbor	Distance (Å)
	Mn21 (×2)	2.7733(14)
	Mn24	2.392(2)
	Mn25a	2.398(2)
	Mn25b	2.398(2)
	Si6 (×2)	2.539(2)
Mn8	Mn1	2.633(2)
	Mn9	2.679(2)
	Mn16 (×2)	2.6404(15)
	Mn19 (×2)	2.6446(15)
	Mn22 (×2)	2.7295(17)
	Mn23 (×2)	2.5717(17)
	Si1	2.503(3)
	Si3	2.442(3)
Mn9	Mn1	2.671(2)
	Mn5 (×2)	2.7818(17)
	Mn8	2.679(2)
	Mn14 (×2)	2.6485(14)
	Mn16 (×2)	2.6375(14)
	Mn18 (×2)	2.6701(17)
	Si1	2.407(3)
	Si4	2.439(3)
	N1	1.909(15)
Mn10	Mn2	2.463(2)
	Mn6 (×2)	2.8526(18)
	Mn7	2.291(2)
	Mn15 (×2)	2.5549(14)
	Mn17 (×2)	2.8664(17)
	Mn23 (×2)	2.5275(17)
	Si1	2.510(3)
	Si6 (×2)	2.529(2)
Mn11	Mn6	2.6920(15)
	Mn7	2.7412(14)
	Mn14	2.6080(16)
	Mn16	2.5190(16)
	Mn17	2.7034(15)
	Mn21	2.2956(15)
	Mn24	2.4492(13)
	Si2	2.423(2)
	Si5	2.401(2)

Site	Neighbor	Distance (Å)
	Si6	2.498(2)
Mn12	Mn2	2.346(2)
	Mn4	2.261(2)
	Mn6 (×2)	2.6296(17)
	Mn13 (×2)	2.5688(14)
	Mn18 (×2)	2.5939(17)
	Mn20 (×2)	2.6980(14)
	Si3	2.399(3)
	Si4	2.357(3)
Mn13	Mn2	2.6009(14)
	Mn5	2.8067(16)
	Mn6	2.6854(15)
	Mn12	2.5688(14)
	Mn14	2.6668(14)
	Mn15	2.7729(15)
	Mn15	2.8766(15)
	Mn18	2.8459(16)
	Mn20	2.6732(16)
	Mn23	2.7427(17)
	Si4	2.6421(18)
	Si5	2.492(2)
	Si6	2.428(2)
Mn14	Mn1	2.7034(14)
	Mn5	2.8214(16)
	Mn9	2.6485(14)
	Mn11	2.6080(16)
	Mn13	2.6668(14)
	Mn16	2.7055(15)
	Mn17	2.6650(16)
	Mn18	2.7927(16)
	Mn19	2.7904(15)
	Mn21	2.5670(16)
	Si2	2.532(2)
	Si4	2.4975(17)
Mn15	Mn2	2.5022(14)
	Mn5	2.6947(15)
	Mn10	2.5549(14)
	Mn13	2.7729(15)
	Mn13	2.8766(15)

Site	Neighbor	Distance (Å)
	Mn15	2.2651(16)
	Mn16	2.5870(15)
	Mn23	2.5639(15)
	Si1	2.4729(19)
	Si6	2.551(2)
	Si6	2.513(2)
Mn16	Mn5	2.7935(16)
	Mn6	2.7465(16)
	Mn8	2.6404(15)
	Mn9	2.6375(14)
	Mn11	2.5190(16)
	Mn14	2.7055(15)
	Mn15	2.5870(15)
	Mn19	2.7659(16)
	Mn20	2.7976(15)
	Mn23	2.5704(15)
	Si1	2.4538(18)
	Si2	2.404(2)
Mn17	Mn3	2.6535(18)
	Mn7	2.7685(18)
	Mn10	2.8664(17)
	Mn11	2.7034(15)
	Mn14	2.6650(16)
	Mn17	2.5448(16)
	Mn21	2.5828(15)
	Mn23	2.7441(15)
	Mn24	2.5460(17)
	Mn25a	2.5862(17)
	Mn25b	2.5862(17)
	Si2	2.7207(21)
	Si5	2.475(2)
	Si6	2.435(2)
Mn18	Mn1	2.7008(18)
	Mn5	2.7713(15)
	Mn9	2.6701(17)
	Mn12	2.5939(17)
	Mn13	2.8459(16)
	Mn14	2.7927(16)
	Mn18	2.5500(16)

Site	Neighbor	Distance (Å)
	Mn19	2.7849(16)
	Si3	2.614(3)
	Si4	2.6880(34)
	Si5	2.322(2)
	N1	1.894(11)
Mn19	Mn1	2.6557(15)
	Mn8	2.6446(15)
	Mn14	2.7904(15)
	Mn16	2.7659(16)
	Mn18	2.7849(16)
	Mn20	2.7818(16)
	Mn20	2.7033(16)
	Mn21	2.5865(16)
	Mn22	2.7091(17)
	Mn22	2.7516(15)
	Si2	2.420(2)
	Si3	2.4697(18)
	N2	1.8938(11)
Mn20	Mn4	2.6144(13)
	Mn6	2.7552(16)
	Mn12	2.6980(14)
	Mn13	2.6732(16)
	Mn16	2.7976(15)
	Mn19	2.7818(16)
	Mn19	2.7033(16)
	Mn22	2.7769(16)
	Mn22	2.8106(16)
	Mn23	2.8133(17)
	Si2	2.550(2)
	Si3	2.7478(18)
	Si5	2.501(2)
	N2	1.9841(11)
Mn21	Mn5	2.8774(16)
	Mn7	2.7733(14)
	Mn11	2.2956(15)
	Mn14	2.5670(16)
	Mn17	2.5828(15)
	Mn19	2.5865(16)
	Mn22	2.8101(15)

Site	Neighbor	Distance (Å)
	Mn25a	2.4595(13)
	Mn25b	2.4595(13)
	Si2	2.437(2)
	Si5	2.402(2)
	Si6	2.515(2)
Mn22	Mn3	2.7089(17)
	Mn4	2.6536(18)
	Mn8	2.7295(17)
	Mn19	2.7091(17)
	Mn19	2.7516(15)
	Mn20	2.7769(16)
	Mn20	2.8106(16)
	Mn21	2.8101(15)
	Mn22	2.6743(17)
	Mn25a	2.6566(17)
	Mn25b	2.6566(17)
	Si2	2.6935(23)
	Si3	2.630(3)
	Si5	2.540(2)
	N2	1.9669(11)
Mn23	Mn3	2.7996(17)
	Mn8	2.5717(17)
	Mn10	2.5275(17)
	Mn13	2.7427(17)
	Mn15	2.5639(15)
	Mn16	2.5704(15)
	Mn17	2.7441(15)
	Mn20	2.8133(17)
	Mn23	2.5545(18)
	Si1	2.494(3)
	Si5	2.303(2)
Mn24	Mn3	2.617(2)
	Mn4	2.436(2)
	Mn6 (×2)	2.7189(17)
	Mn7	2.392(2)
	Mn11 (×2)	2.4492(13)
	Mn17 (×2)	2.5460(17)
	Mn25a	2.488(2)
	Mn25b	2.488(2)
	Si2 (×2)	2.434(2)
Mn25a	Mn3	2.504(2)
	Mn4	2.457(2)
	Mn7	2.398(2)
	Mn17 (×2)	2.5862(17)
	Mn21 (×2)	2.4595(13)
	Mn22 (×2)	2.6566(17)
	Mn24	2.488(2)
	Mn25b	0
	Si2 (×2)	2.458(2)
Mn25b	Mn3	2.504(2)
	Mn4	2.457(2)
	Mn7	2.398(2)
	Mn17 (×2)	2.5862(17)
	Mn21 (×2)	2.4595(13)
	Mn22 (×2)	2.6566(17)
	Mn24	2.488(2)
	Mn25a	0
	Si2 (×2)	2.458(2)
Si1	Mn2	2.407(3)
	Mn5 (×2)	2.638(3)
	Mn8	2.503(3)
	Mn9	2.407(3)
	Mn10	2.510(3)
	Mn15 (×2)	2.4729(19)
	Mn16 (×2)	2.4538(18)
	Mn23 (×2)	2.494(3)
Si2	Mn4	2.359(2)
	Mn6	2.6959(23)
	Mn11	2.423(2)
	Mn14	2.532(2)
	Mn16	2.404(2)
	Mn17	2.7207(21)
	Mn19	2.420(2)
	Mn20	2.550(2)
	Mn21	2.437(2)
	Mn22	2.6935(23)

Site	Neighbor	Distance (Å)
	Mn24	2.434(2)
	Mn25a	2.4582(22)
	Mn25b	2.4582(22)
Si3	Mn1	2.455(3)
	Mn4	2.344(3)
	Mn8	2.442(3)
	Mn12	2.399(3)
	Mn18 (×2)	2.614(3)
	Mn19 (×2)	2.4697(18)
	Mn20 (×2)	2.7478(18)
	Mn22 (×2)	2.630(3)
Si4	Mn1	2.424(3)
	Mn2	2.403(3)
	Mn5 (×2)	2.6809(33)
	Mn9	2.439(3)
	Mn12	2.357(3)
	Mn13 (×2)	2.6421(18)
	Mn14 (×2)	2.4975(17)
	Mn18 (×2)	2.6880(34)
Si5	Mn3	2.503(2)
	Mn11	2.401(2)
	Mn13	2.492(2)
	Mn17	2.475(2)
	Mn18	2.322(2)
	Mn20	2.501(2)
	Mn21	2.402(2)
	Mn22	2.540(2)
	Mn23	2.303(2)
Si6	Mn5	2.487(2)
	Mn6	2.463(2)
	Mn7	2.539(2)
	Mn10	2.529(2)
	Mn11	2.498(2)
	Mn13	2.428(2)
	Mn15	2.551(2)
	Mn15	2.513(2)
	Mn17	2.435(2)
	Mn21	2.515(2)
N1	Mn1	1.944(15)
	Mn5 (×2)	1.953(11)
	Mn9	1.909(15)
	Mn18 (×2)	1.894(11)
N2	Mn19 (×2)	1.8938(11)
	Mn20 (×2)	1.9841(11)
	Mn22 (×2)	1.9669(11)

B.2 Experimental Procedures

B.2.1 Synthetic Procedures

Samples were made by the stoichiometric mixing of Mn (Alfa Aesar, 99.95%) and Si (Alfa Aesar, 99.99%) powders under argon atmosphere, and grinding them together with an agate mortar and pestle. The powder mixtures were transferred to crucibles cut from alumina tubes, and capped with a cement base. These crucibles were placed within ½ inch diameter capped quartz tubes. Outside the box, the ½ inch tubes were placed within a larger quartz tube (sealed at the top with a Teflon stopper) for annealing (~100 mL volume), and immediately placed under active vacuum.

The line and samples were then flushed with ultra-high purity N_2 gas three times for 30 seconds each, and then left under vacuum for several hours (<200 mtorr). Next, while still under vacuum, the line and tube were flushed three more times with N_2 gas, then N_2 levels were adjusted to the desired level (100 – 500 torr for various samples), and the large tube containing the samples was sealed at this pressure.

The large quartz tube was placed inside a tube furnace for annealing, with the Teflon stopper sticking out. Samples yielding the desired $Mn_{39}Si_9N_x$ product were generally heated to 1100 °C for 24 hours, followed by annealing at 900 °C for 336 hours. Some samples deviating from this heating profile were still confirmed to produce the target phase (see Table B.5). After annealing, the samples tended to appear as solid metallic gray chunks, which were crushed to release single crystals.

Table B.5. Synthetic conditions and results for selected samples

N_2 pressure (torr)	1100 °C treatment (hr)	900 °C treatment (hr)	Major phase	Minor phase
433	24	270	$Mn_{39}Si_9N_x$	Mn_3Si
173	24	272	$Mn_{39}Si_9N_x$	υ-$Mn_{81.5}Si_{18.5}$
176	24	272	Mn_3Si	$Mn_{39}Si_9N_x$
101	24	336	$Mn_{39}Si_9N_x$	Mn_3Si
180	24	240	Mn_3Si	$Mn_{39}Si_9N_x$
422	3	300	$Mn_{39}Si_9N_x$	–
322	3	300	$Mn_{39}Si_9N_x$	–
0[a]	20	336	Mn_3Si	Mn_5Si_3

[a]Sample was run under vacuum as a control for possible air exposure during annealing. Only Mn-Si phases were observed in the product.

B.2.2 Single Crystal X-ray Diffraction

Single crystals were picked from the crushed bulk sample and mounted on the end of glass fibers for single crystal X-ray diffraction analysis. These crystals were metallic gray in color, and usually exhibited block- or plate-like habits. Data were collected using an Oxford Diffraction Xcalibur E diffractometer with graphite monochromatized Mo Kα radiation (λ = 0.71073 Å) at ambient temperature (295 K). The CrysAlis Pro version 171.38.43 software package was used for run list optimization and processing of frame data. The integrated data was exported to JANA2006,[1] where the structure was solved using the charge-flipping algorithm[2,3] with SUPERFLIP program.[4] This structural model was refined in JANA2006 on F^2. A Crystallographic Information File (CIF) has been deposited to the Cambridge Crystallographic Data Centre (Deposition Number: 1982735).

B.2.3 Backscattered Electron Imaging and Energy Dispersive Spectroscopy

Polycrystalline fragments of the samples were suspended inside hollow aluminum bullets in epoxy, polished with a diamond grit, and coated in a conductive layer of carbon. These samples were examined with a Hitachi S-3100N scanning electron microscope (SEM) with an energy dispersive spectroscopy (EDS) detector. Backscattered-electron (BSE) images were taken at an accelerating voltage of 15 keV. The EDS compostion was assigned based on an averaging of data for the most phase pure sample (sample BSE image and EDS spectrum for this phase are shown in Figure B.1a below), and was found to be $Mn_{39.00(11)}Si_{8.98(9)}$. Some samples, such as that shown in Figure B.1b, showed the presence of a minority phase within the matrix of the target phase. In this case the inclusion's stoichiometry ($Mn_{79.34(29)}Si_{18.32(16)}$) is compositionally well-matched to the quasicrystal approximant $Mn_{81.5}Si_{18.5}$ (υ-phase). Mn_3Si was also found as a minority phase in some samples. Nitrogen X-ray emission lines were not able to be quantified by the AZtec program; this is not surprising given its low abundance in the sample and the obfuscation of the N Kα_1 emission line at 392.4 eV by the large Mn Lα_1 emission at 637.4 eV, which causes it to appear as a small shoulder in EDS spectra (Figure B.1c).

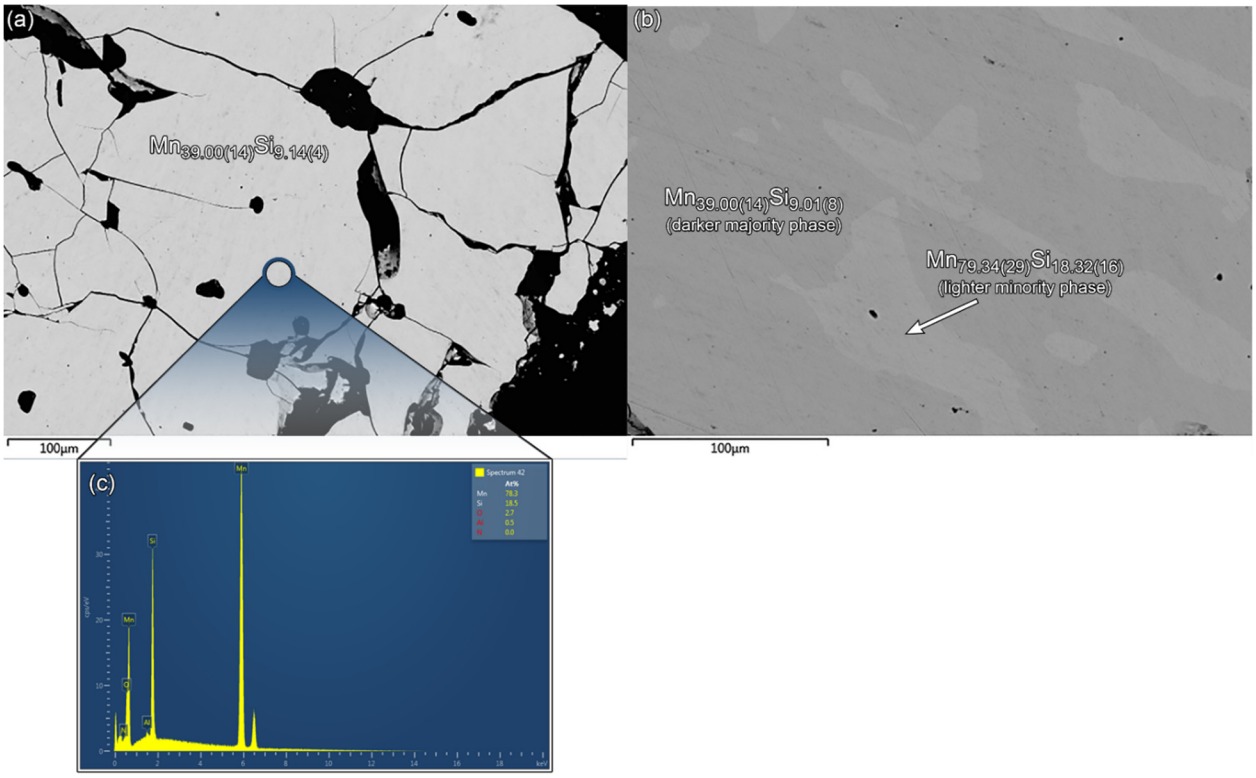

Figure B.1. Two samples used for SEM and EDS analysis. (a) The sample from which the single crystal used for refinement of the structural model was picked. This sample showed little or no presence of a minority phase in the SEM images. (b) The sample for which powder X-ray diffraction data is presented in Figure B.2a, showing the presence of a minority phase compositionally matched to υ-$Mn_{81.5}Si_{18.5}$.

B.2.4 Powder X-ray Diffraction Analysis

Samples were crushed and ground into a uniform powder with an agate mortar and pestle. Powder X-ray diffraction patterns were collected using synchrotron radiation (λ = 0.412682 Å) at ambient temperature using the 11-BM beamline at the Advanced Photon Source. The data were analyzed using the Match! Version 3.4.2 software.[5] From these patterns, $Mn_{39}Si_9N_x$ was found to be present by comparison to a calculated pattern based on the refined crystallographic model, as illustrated in Figure B.2a. This sample among others was found via EDS to contain a minority phase compositionally matched to υ-$Mn_{81.5}Si_{18.5}$ (Figure B.1b), which shares a great deal of peak overlap with $Mn_{39}Si_9N_x$. However, the

locations of the strongest reflections are closely aligned with those calculated from the refined structural model, and slightly offset from those of $Mn_{81.5}Si_{18.5}$. Several samples also contained Mn_3Si, either as a very small minority (Figure B.2a), or as the majority phase (Figure B.2b).

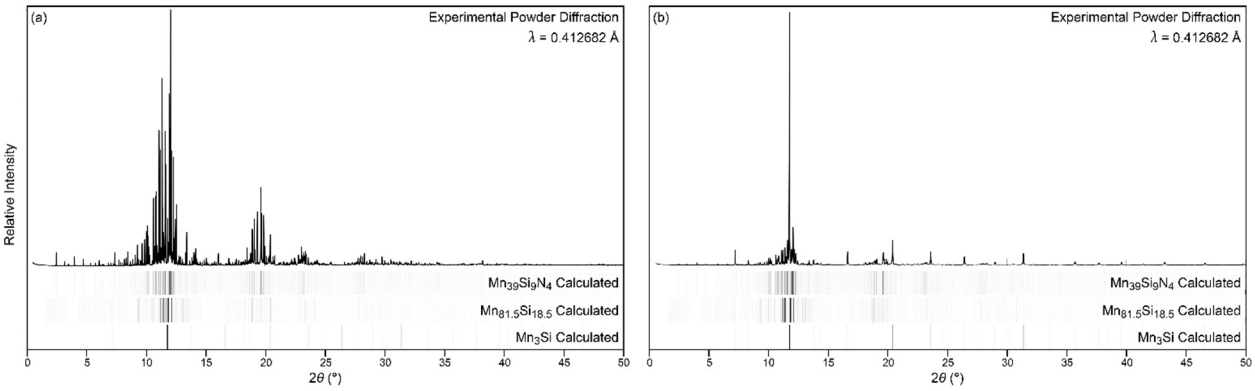

Figure B.2. Experimental powder X-ray diffraction patterns collected for two $Mn_{39}Si_9N_x$-containing samples compared to the calculated patterns for $Mn_{39}Si_9N_x$, $Mn_{81.5}Si_{18.5}$, and Mn_3Si. (a) A sample containing a majority of the target phase, $Mn_{39}Si_9N_x$, with small minorities of υ-$Mn_{81.5}Si_{18.5}$ and Mn_3Si. (b) A sample containing a majority of Mn_3Si, with $Mn_{39}Si_9N_x$ present as a minority.

B.3 Chemical Pressure Computational Procedure

DFT-Chemical Pressure (CP) schemes were produced for Mn_3Si, Mn_3C, and Mn_4N based on LDA-DFT calculations performed with ABINIT[6-8] using Hartwigsen–Goedecker–Hutter norm-conserving pseudopotentials.[9] Valence-only profiles were used for all atoms. Energy cutoff values of 75 Ha were used for Mn_3Si and Mn_3C, while 110 Ha was used for Mn_4N. First, atomic positions were optimized holding the unit cell constant, then atomic positions and the unit cell were optimized simultaneously. Next, single point ABINIT calculations were done on expanded and contracted (1.5%) structure to generate the kinetic energy and electron densities, as well as potential maps used for the creation of 3D chemical pressure maps. The nonlocal pseudopotential energies as well as the localized components of E_{Ewald} and E_{α}

were mapped and core unwarping was performed with the *CPpackage2* program to generate chemical pressure maps,[10,11] which were divided into contact volumes following the Hirschfeld-inspired integration scheme.[10] The resulting pressures were projected onto atom-centered spherical harmonics ($l \leq 4$), and visualized using the in-house Matlab program *Figuretool2*.

The localized electron counts of each atom in each structure were independently calibrated by creating contracted (0.8× scale) and expanded (1.2× scale) structural models of the DFT-optimized Mn_3Si, Mn_3C, and Mn_4N structures. Single-point ABINIT calculations were run, and chemical pressure maps were generated as detailed above for each model, and net CPs were obtained by integrating the CP maps within each Bader volume, as determined with the Bader program.[12-15] The number of localized electrons on each atom for each model was adjusted until pressures were balanced across atoms, with the assumption that at these extreme volumes the macroscopic internal pressures should overwhelm local forces (see Table B.6-B.8). The expanded and contracted values for each atomic position were averaged, and were used for CP calculations done on the 1× scale unit cell.

To account for the ionic character of the atoms, the Bader charge program was used to calculate atomic charges on each atom. Radial electron density profiles accounting for 0%, 25%, and 50% of the Bader charges were created using the Atomic Pseudopotential Engine.[16] As the ionicity changes, as shown in Figure B.3 below, there are few if any differences between CP schemes, except for small increases in the magnitudes of pressure features as the ionicity is increased. Qualitatively, however, the schemes do not change in response to changes in ionicity. The schemes presented in the Chapter 3 are shown for 25% ionicity.

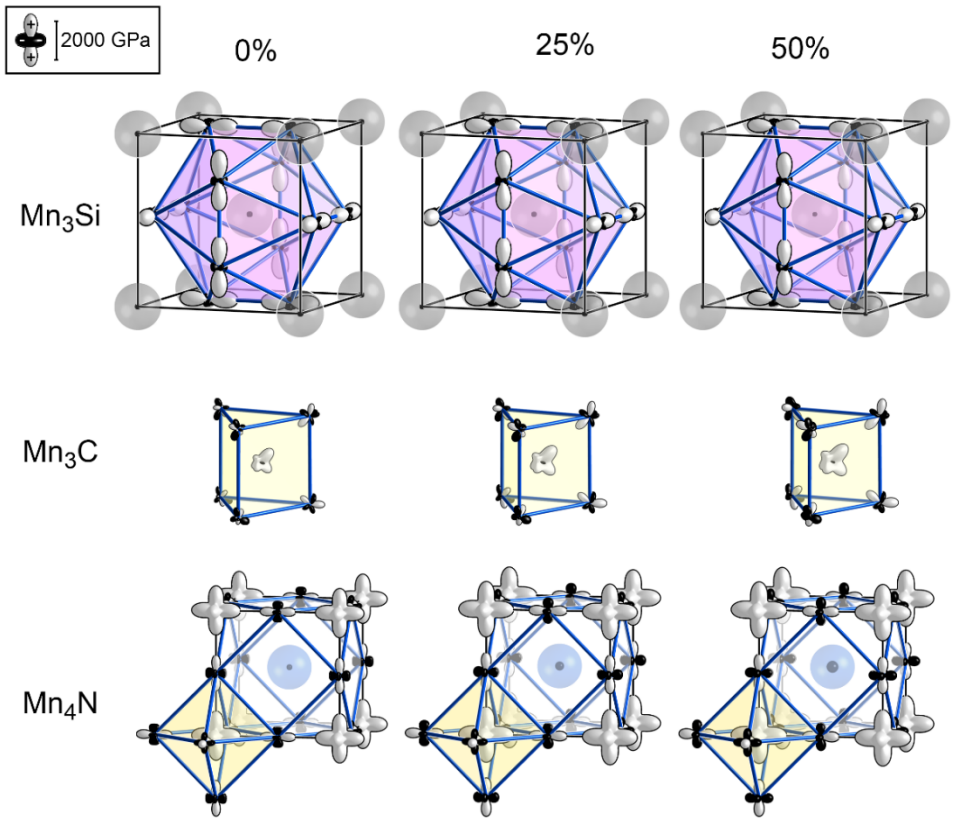

Figure B.3. Comparison of chemical pressure schemes at 0%, 25%, and 50% ionicity for Mn_3Si, Mn_3C, and Mn_4N. As the ionicity used in the calculations is increased, there is a very mild increase in the overall magnitude of pressure features, but the qualitative aspects of each scheme do not change.

Table B.6. Localized electron calibration for Mn_3Si

	0.8 × scale	average	1.2 × scale
Mn1 localized e^- #	0.82676	1.59048	2.3542
Si1 localized e^- #	0	0	0
Mn1 net CPs	741.03	–	-46.54
Si1 net CPs	741.03	–	-46.54

Table B.7. Localized electron calibration for Mn_3C

	0.8 × scale	average	1.2 × scale
Mn1 localized e^- #	0.855699	1.33471	1.81372
Mn2 localized e^- #	0.82788	1.314465	1.80105
C1 localized e^- #	0	0	0
Mn1 net CPs	947.54	–	-59.35
Mn1 net CPs	947.54	–	-59.35
C1 net CPs	947.54	–	-59.35

Table B.8. Localized electron calibration for Mn_4N

	0.8 × scale	average	1.2 × scale
Mn1 localized e^- #	0.3531	0.865595	1.37809
Mn2 localized e^- #	0.4344	0.92614	1.41788
N1 localized e^- #	0	0	0
Mn1 net CPs	861.27	–	-51.59
Mn1 net CPs	861.27	–	-51.59
N1 net CPs	861.32	–	-51.59

Table B.9. k-point meshes used for chemical pressure calculations (LDA-DFT, ABINIT)

Structure	k-point vectors[a]			k-point shift
Mn_3Si	8	0	0	
	0	8	0	
	0	0	8	0.5 0.5 0.5
Mn_3C	6	0	0	
	0	5	0	
	0	0	7	0.5 0.5 0.5
Mn_4N	8	0	0	
	0	8	0	
	0	0	8	0.5 0.5 0.5

[a]Three vectors that define a real-space super-lattice whose reciprocal lattice defines the k-point grid

Table B.10. DFT-calculated total energies (LDA-DFT, ABINIT)

Structure	Total energy (Ha)	Total energy (eV)	Energy per atom (eV/at)
Mn_3Si	-95.8189	-2607.36	-325.92
Mn_3C	-198.5273	-5402.21	-337.638
Mn_4N	-68.5055	-1864.13	-372.826

Table B.11. Unit cell parameters for the LDA-DFT optimized geometries of Mn_3Si, Mn_3C, and Mn_4N

	Mn_3Si (Å)	Mn_3C (Å)	Mn_4N (Å)
a	4.3491	4.8475	3.6223
b	4.3491	6.5495	3.6223
c	4.3491	4.3529	3.6223

Table B.12. Atomic coordinates for the LDA-DFT optimized geometry of Mn_3Si

Site	Wyckoff Pos.	*x*	*y*	*z*
Mn1	6c	0	0.5	0.25
Si1	2a	0	0	0

Table B.13. Atomic coordinates for the LDA-DFT optimized geometry of Mn_3C

Site	Wyckoff Pos.	*x*	*y*	*z*
Mn1	8d	0.18582	0.06528	0.15661
Mn2	4c	0.03097	0.25	0.65900
C1	4c	0.37803	0.25	0.43502

Table B.14. Atomic coordinates for the LDA-DFT optimized geometry of Mn_4N

Site	Wyckoff Pos.	*x*	*y*	*z*
Mn1	1a	0	0	0
Mn2	3c	0	0.5	0.5
N1	1b	0.5	0.5	0.5

B.4 Magnetic Properties Measurements

Magnetic properties of a sample known to contain a majority of $Mn_{39}Si_9N_x$ as well as a small amount of υ-$Mn_{81.5}Si_{18.5}$ (corresponding to Figure B.1b and Figure B.2a) were measured using a Quantum Design Magnetic Properties Measurment System (MPMS) 3 EverCool Superconducting QUantum Interference Device (SQUID). Magnetic moment versus temperature measurements were gathered at 0.01 T, 0.1 T, 1 T, and 7 T applied fields (Figure B.4), and magnetic moment versus applied field isotherms were measured

at 5 K, 150 K, 300K, and 400K (Figure B.5). The divergence of the field-cooled and zero-field-cooled below ~20 K is potentially indicative of antiferromagnetic or spin-glass character, however the identification of the source of this transition, or the one noticeable at 200 K in the low-field curves, is muddled by the presence of υ-$Mn_{81.5}Si_{18.5}$ in these samples, whose magnetic properties have not been reported. Further investigation of the magnetic structure of $Mn_{39}Si_9N_x$ is needed.

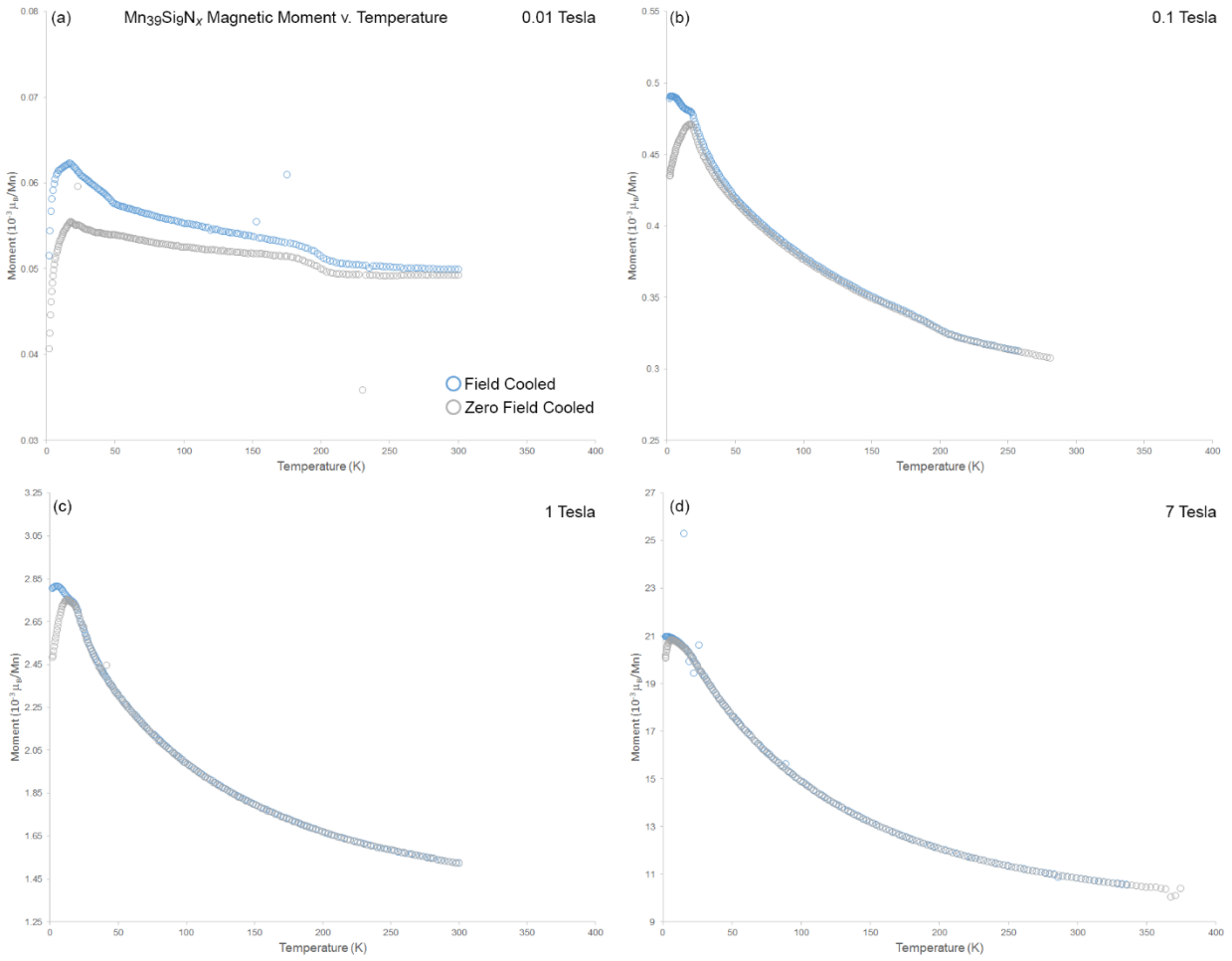

Figure B.4. Magnetic moment (10^{-3} μ_B/Mn atom) vs. Temperature (K) curves of $Mn_{39}Si_9N_x$ samples. Curves for (a) 0.01 Tesla, (b) 0.1 Tesla, (c) 1 Tesla, and (d) 7 Tesla.

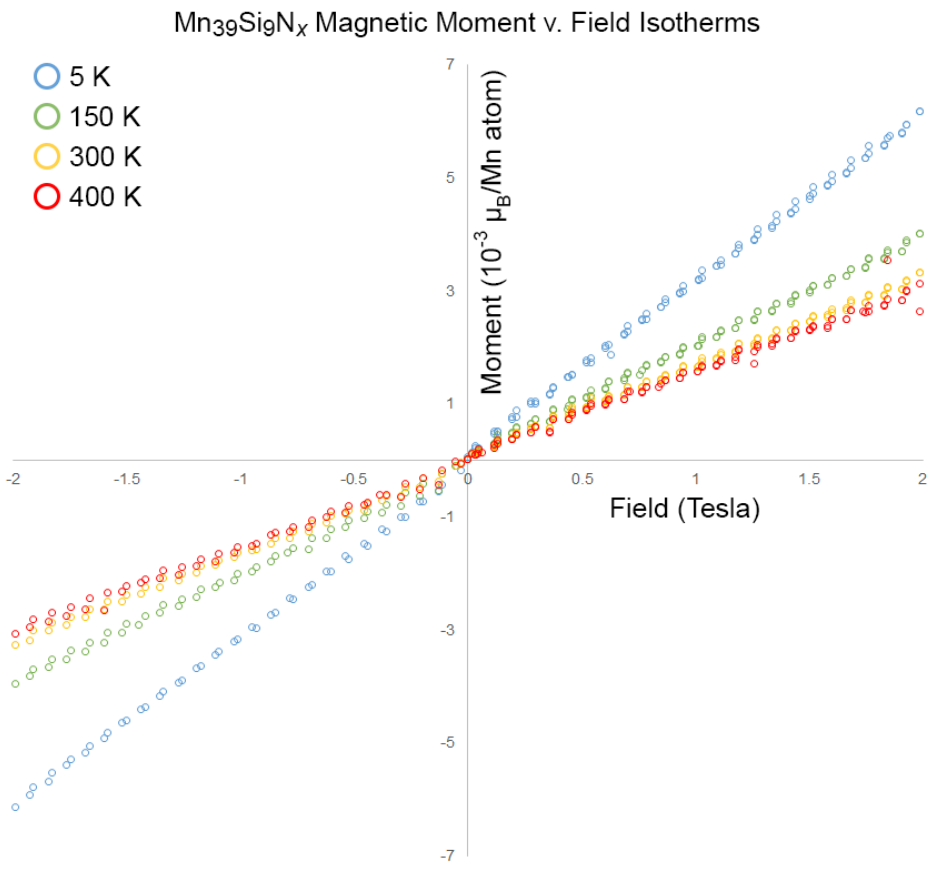

Figure B.5. Magnetic moment vs. field isotherms, showing relatively little hysteresis or saturation of the sample with increasing field.

B.5 Additional Figures

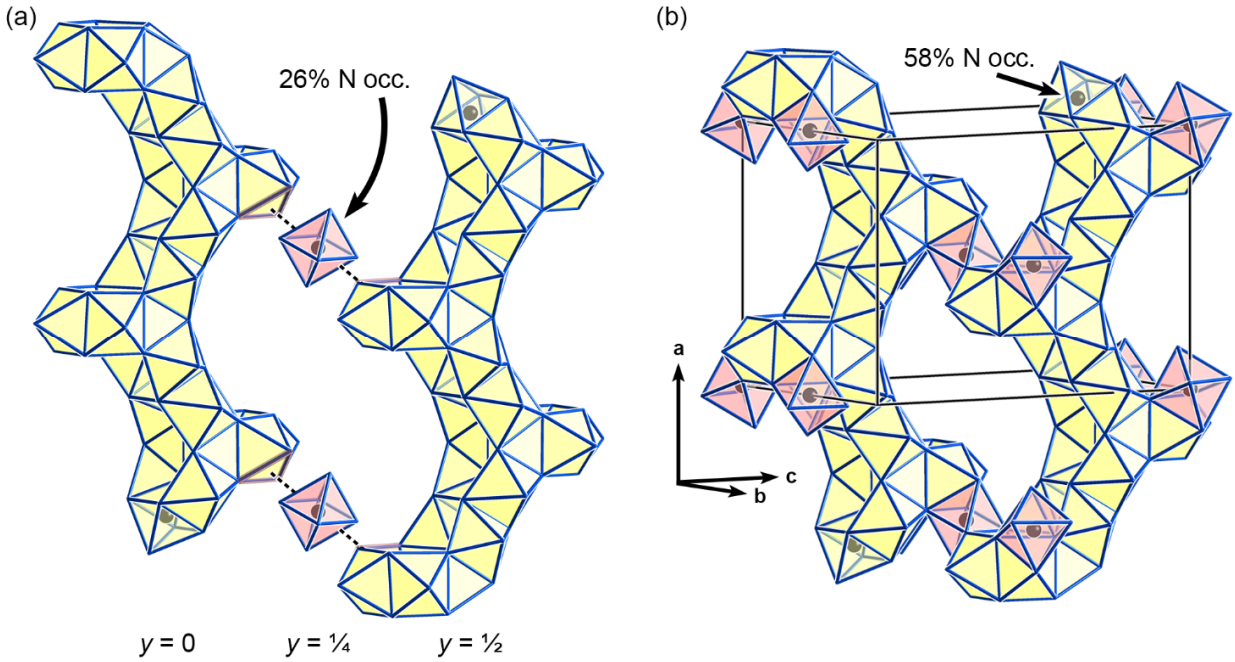

Figure B.6. N-containing octahedra as bridges in a continuous octahedral network throughout the $Mn_{39}Si_9N_x$ structure. (a) Face-sharing zigzag chains of octahedra along **a** (yellow) are joined through N-centered octahedra (58% occupancy) between Mackay clusters. The other N containing octahedra in the structure (26% occupancy, red) joins neighboring chains to each other, creating a network of face-sharing octahedra. This connectivity suggests the potential for a path for N diffusion throughout the structure.

B.6 References

(1) Petříček, V.; Dušek, M.; Palatinus, L. Crystallographic computing system JANA2006: general features. *Z. Krist. - Cryst. Mater.* **2014**, *229*, 345-352.

(2) Oszlányi, G.; Sütő, A. Ab initio structure solution by charge flipping. *Acta Crystallogr. A* **2004**, *60*, 134-141.

(3) Oszlányi, G.; Sütő, A. Ab initio structure solution by charge flipping. II. Use of weak reflections. *Acta Crystallogr. Sect. A: Found. Crystallogr.* **2005**, *61*, 147-152.

(4) Palatinus, L.; Chapuis, G. SUPERFLIP - a computer program for the solution of crystal structures by charge flipping in arbitrary dimensions. *J. Appl. Crystallogr.* **2007**, *40*, 786-790.

(5) Putz, H.; Brandenburg, K.; 3.5.2.104 ed.; Kreuzherrenstr: Bonn, Germany, 2017.

(6) Gonze, X. A brief introduction to the ABINIT software package. *Z. Krist. - Cryst. Mater.* **2005**, *220*, 558-562.

(7) Gonze, X.; Amadon, B.; Anglade, P.-M.; Beuken, J.-M.; Bottin, F.; Boulanger, P.; Bruneval, F.; Caliste, D.; Caracas, R.; Côté, M. ABINIT: First-principles approach to material and nanosystem properties. *Comput. Phys. Commun.* **2009**, *180*, 2582-2615.

(8) Gonze, X.; Beuken, J.-M.; Caracas, R.; Detraux, F.; Fuchs, M.; Rignanese, G.-M.; Sindic, L.; Verstraete, M.; Zerah, G.; Jollet, F. First-principles computation of material properties: the ABINIT software project. *Comp. Mater. Sci.* **2002**, *25*, 478-492.

(9) Hartwigsen, C.; Gœdecker, S.; Hutter, J. Relativistic separable dual-space Gaussian pseudopotentials from H to Rn. *Phys. Rev. B* **1998**, *58*, 3641-3662.

(10) Berns, V. M.; Engelkemier, J.; Guo, Y.; Kilduff, B. J.; Fredrickson, D. C. Progress in Visualizing Atomic Size Effects with DFT-Chemical Pressure Analysis: From Isolated Atoms to Trends in AB_5 Intermetallics. *J. Chem. Theory Comput.* **2014**, *10*, 3380-3392.

(11) Hilleke, K. P.; Fredrickson, D. C. Discerning Chemical Pressure amidst Weak Potentials: Vibrational Modes and Dumbbell/Atom Substitution in Intermetallic Aluminides. *J. Phys. Chem. A* **2018**, *122*, 8412-8426.

(12) Bader, R. F. Atoms in molecules. *Acc. Chem. Res.* **1985**, *18*, 9-15.

(13) Henkelman, G.; Arnaldsson, A.; Jónsson, H. A fast and robust algorithm for Bader decomposition of charge density. *Comp. Mater. Sci.* **2006**, *36*, 354-360.

(14) Sanville, E.; Kenny, S. D.; Smith, R.; Henkelman, G. Improved grid-based algorithm for Bader charge allocation. *J. Comput. Chem.* **2007**, *28*, 899-908.

(15) Tang, W.; Sanville, E.; Henkelman, G. A grid-based Bader analysis algorithm without lattice bias. *J. Phys.: Condens. Matter* **2009**, *21*, 084204.

(16) Oliveira, M. J.; Nogueira, F. Generating relativistic pseudo-potentials with explicit incorporation of semi-core states using APE, the Atomic Pseudo-potentials Engine. *Comput. Phys. Commun.* **2008**, *178*, 524-534.

Appendix C.

Supporting Information for Chapter 4.

Intermetallic Reactivity: $Ca_3Cu_{7.8}Al_{26.2}$ and the Role of Electronegativity in the Stabilization of Modular Structures

Work in this Appendix was done by Peterson.

C.1 Tables of Crystallographic Data for $Ca_3Cu_{7.8}Al_{26.2}$

Table C.1. Refined harmonic atomic displacement parameters for $Ca_3Cu_{7.8}Al_{26.2}$

Site	U_{11}	U_{22}	U_{33}	U_{12}	U_{13}	U_{23}
Cu1	0.0152(4)	0.0152(4)	0.0152(4)	0	0	0
Ca2	0.0174(8)	0.0102(5)	0.0102(5)	0	0	0
Al1	0.0173(7)	0.0136(4)	0.0136(4)	0	0	-0.0008(5)
Al2	0.0139(9)	0.0139(9)	0.0139(9)	0	0	0
Al3	0.0118(4)	0.0118(4)	0.0118(4)	0.0003(3)	0.0003(3)	0.0003(3)

Table C.2. Selected interatomic distance

Site	Neighbor	Distance (Å)
Cu1	Al3 (×8)	2.5125(8)
Ca2	Al1 (×4)	3.1766(8)
	Al3 (×8)	3.4767(8)
	Al4a (×8)	3.2039(9)
	Al4b (×8)	3.334(3)
Al1	Ca2 (×1)	3.1766(8)
	Al1 (×4)	2.8445(8)
	Al2 (×1)	2.8445(8)
	Al3 (×2)	3.0242(11)
	Al4a (×4)	2.7038(8)
	Al4b (×4)	2.6632(18)
Al3	Cu1 (×1)	2.5125(8)
	Ca2 (×3)	3.4767(8)
	Al1 (×3)	3.0242(11)
	Al3 (×3)	2.9011(11)
	Al4a (×3)	2.5156(10)
	Al4b (×3)	2.797(3)
Al4a	Ca2 (×2)	3.2039(9)
	Al1 (×4)	2.7038(8)
	Al3 (×2)	2.5156(10)
	Al4a (×2)	2.7075(12)
	Al4b (×1)	0.336(3)
	Al4b (×2)	2.481(3)
Al4b	Ca2 (×2)	3.334(3)
	Al1 (×4)	2.6632(18)
	Al3 (×2)	2.797(3)
	Al4a (×1)	0.336(3)
	Al4a (×2)	2.481(3)
	Al4b (×2)	2.232(4)

C.2 Backscattered Electron Imaging and Energy Dispersive Spectroscopy

Polycrystalline fragments of the samples were suspended in epoxy inside hollow aluminum bullets. These bullets were polished with diamond grit solution down to a 1μm finish and coated in a conductive layer of carbon. The polished samples were examined with a Hitachi S-3100N scanning electron microscope with an EDS attachment, and backscattered electron (BSE) images showing the phases present were taken at 15 keV accelerating voltage. From this analysis the composition of the darker majority phase was determined to be $Ca_{3.00(3)}Cu_{7.61(15)}Al_{26.48(14)}$ and was attributed to the structurally unknown $CaCu_2Al_7$ phase and eventually the $Ca_3Cu_{7.8}Al_{26.2}$ ternary. The composition of the lighter minority phase was determined to be $Ca_{1.00(2)}Cu_{4.20(21)}Al_{7.87(21)}$, and was assigned to the neighboring ternary phase $CaCu_4Al_8$.

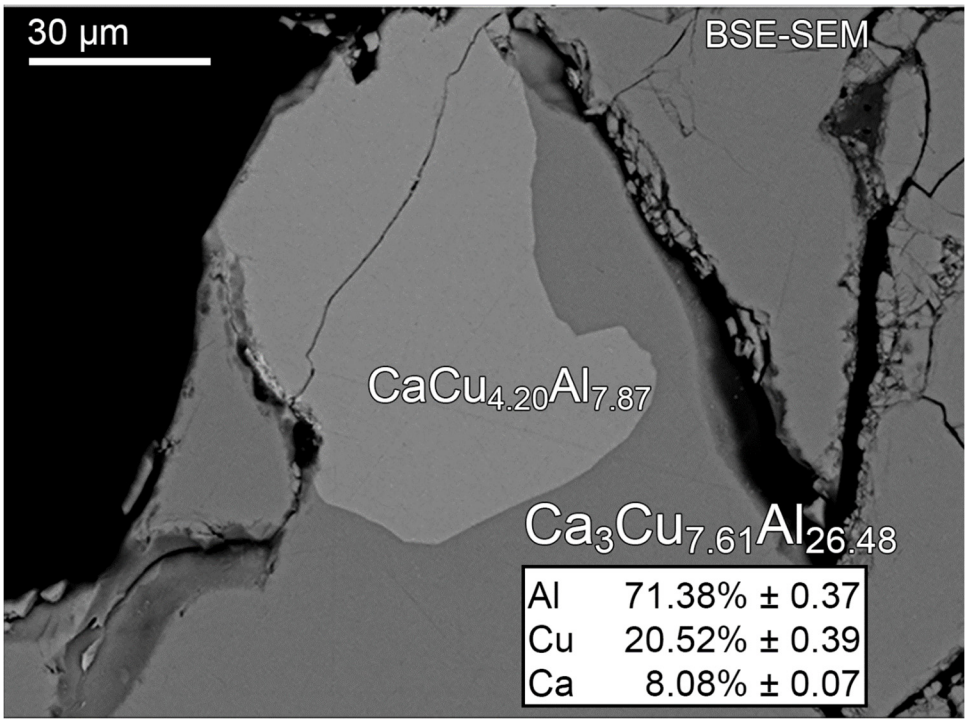

Figure C.1. Elemental Analysis via Energy Dispersive Spectroscopy. BSE image of polished surface of a fragment of the reaction product, with the compositions determined from EDS for the two phases given.

C.3 Additional Computational Details and Results

Table C.3. k-point meshes (LDA-DFT, ABINIT)

Structure	k-point vectors[a]			k-point shift
$CaAl_4$	0	-10	-10	
	-10	0	-10	
	4	4	0	0.5 0.5 0.5
$CuAl_2$ (own type)	0	10	10	
	-10	0	-10	
	-12	-12	0	0.5 0.5 0.5
$CuAl_2$ (fluorite type)	8	8	-8	
	-8	8	-8	
	-8	8	8	0.5 0.5 0.5
$CaCu_2Al_2$	0	-10	-10	
	-10	0	-10	
	4	4	0	0.5 0.5 0.5
anti-$CaCu_2Al_2$	0	-10	-10	
	-10	0	-10	
	5	5	0	0.5 0.5 0.5
$Ca_3Cu_{13}Al_{21}$	8	0	0	
	0	8	0	
	0	0	8	0.5 0.5 0.5

[a]Three vectors that define a real-space super-lattice whose reciprocal lattice defines the k-point grid.

Table C.4. DFT-calculated total energies (LDA-DFT, ABINIT)

Structure	Total energy (Ha)	Total energy (eV)	Energy per atom (eV/at)
$CaAl_4$	-9.1859	-249.9600	-49.9920
$CuAl_2$ (own type)	-104.6227	-2846.9301	-474.4883
$CuAl_2$ (fluorite type)	-104.6292	-2847.1077	-474.5180
$CaCu_2Al_2$	-101.1931	-2753.6050	-550.7210
anti-$CaCu_2Al_2$	-101.1802	-2753.2546	-550.6509
$Ca_3Cu_{13}Al_{21}$	-671.9498	-18284.6956	-494.1810

Table C.5. Calculated Bader charges for $Ca_3Cu_{13}Al_{21}$ (LDA-DFT, ABINIT)

Site	Bader charge
Cu1	-2.37
Cu2	-1.55
Ca1	0.90
Al1	-0.17
Al2	1.15
Al3	0.77

Table C.6. Unit cell parameters for LDA-DFT optimized $CaAl_4$, $CuAl_2$ (own and fluorite type), $CaCu_2Al_2$, anti-$CaCu_2Al_2$, and $Ca_3Cu_{13}Al_{21}$

	$CaAl_4$ (Å)	$CuAl_2$ (own) (Å)	$CuAl_2$ (fluorite) (Å)	$CaCu_2Al_2$ (Å)	anti-$CaCu_2Al_2$ (Å)	$Ca_3Cu_{13}Al_{21}$ (Å)
a	4.1464	5.9398	5.67011	3.9714	4.1266	8.1419
b	4.1464	5.9398	5.67011	3.9714	4.1266	8.1419
c	11.2147	4.7890	5.67011	10.3916	9.8556	8.1419

Table C.7. Atomic coordinates for LDA-DFT optimized $CaAl_4$

Site	Wyckoff Pos.	*x*	*y*	*z*
Ca1	2a	0	0	0
Al1	4d	0	0.5	0.25
Al2	4e	0	0	0.38988

Table C.8. Atomic coordinates for LDA-DFT optimized $CuAl_2$ (own type)

Site	Wyckoff Pos.	*x*	*y*	*z*
Cu1	4a	0	0	0.25
Al1	8h	0.15910	0.65910	0

Table C.9. Atomic coordinates for LDA-DFT optimized $CuAl_2$ (fluorite type)

Site	Wyckoff Pos.	*x*	*y*	*z*
Cu1	4a	0	0	0
Al1	8c	0.25	0.25	0.25

Table C.10. Atomic coordinates for LDA-DFT optimized $CaCu_2Al_2$

Site	Wyckoff Pos.	*x*	*y*	*z*
Ca1	2a	0	0	0
Al1	4d	0	0.5	0.25
Cu1	4e	0	0	0.38578

Table C.11. Atomic coordinates for LDA-DFT optimized anti-$CaCu_2Al_2$

Site	Wyckoff Pos.	*x*	*y*	*z*
Ca1	2a	0	0	0
Cu1	4d	0	0.5	0.25
Al1	4e	0	0	0.36965

Table C.12. Atomic coordinates for LDA-DFT optimized $Ca_3Cu_{13}Al_{21}$

Site	Wyckoff Pos.	*x*	*y*	*z*
Cu1	1a	0	0	0
Cu2	12i	0	0.65182	0.65182
Ca1	3d	0	0	0.5
Al1	1b	0.5	0.5	0.5
Al2	8g	0.82627	0.82627	0.82627
Al3	12j	0.74617	0.74617	0.5

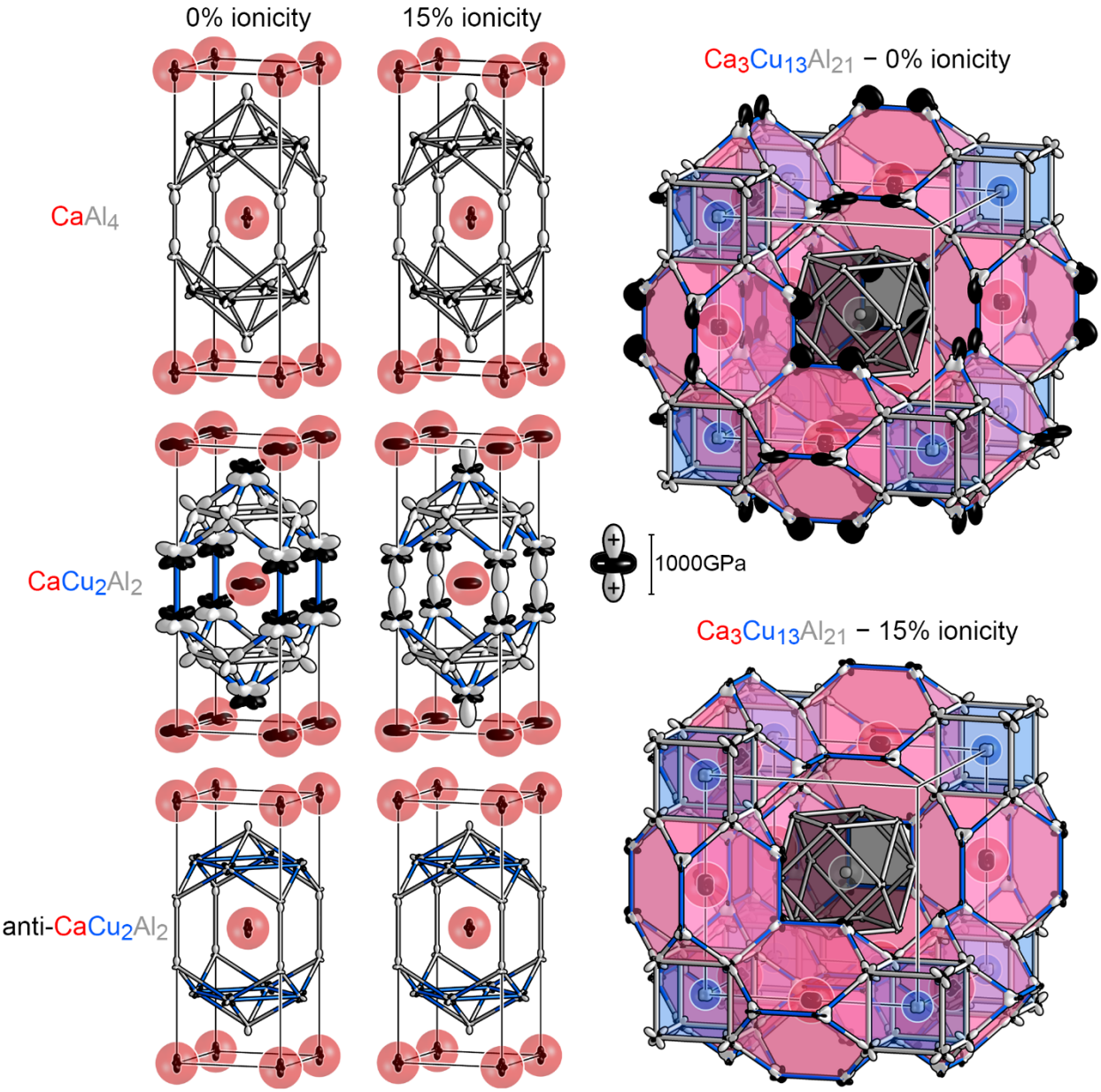

Figure C.2. Chemical pressure schemes of $CaAl_4$, $CaCu_2Al_2$, anti-$CaCu_2Al_2$, and $Ca_3Cu_{13}Al_{21}$ calculated using *CPpackage2* with free ion electron densities of both 0% and 15% of total Bader charge used for the construction of the contact volumes.

Table C.13. k-point meshes (GGA-DFT)

	$CaAl_4$	$CaCu_2Al_2$	anti-$CaCu_2Al_2$	$Ca_3Cu_{13}Al_{21}$	$Ca_3Cu_7Al_{27}$
center	Γ	Γ	Γ	Γ	Γ
grid	$20 \times 20 \times 8$	$10 \times 10 \times 10$	$10 \times 10 \times 10$	$8 \times 8 \times 8$	$8 \times 8 \times 8$

Table C.14. Atomic coordinates and unit cell parameters for GGA-DFT optimized $CaAl_4$

cell vectors	**a**	**b**	**c**
	6.4126	0.0143	0.0000
	3.4398	5.4120	0.0000
	-4.9262	-2.7132	3.0811
element	*x*	*y*	*z*
Ca	0.0000	0.0000	0.0000
Al	0.7500	0.2500	0.5000
Al	0.2500	0.7500	0.5000
Al	0.3863	0.3863	1.0000
Al	0.6137	0.6137	0.0000

Table C.15. Atomic coordinates and unit cell parameters for GGA-DFT optimized $CaCu_2Al_2$

cell vectors	**a**	**b**	**c**
	4.0990	0.0000	0.0000
	0.0000	4.0990	0.0000
	0.0000	0.0000	4.0990
element	*x*	*y*	*z*
Ca	0.0000	0.0000	0.0000
Ca	0.5000	0.5000	0.5000
Cu	0.0000	0.0000	0.3839
Cu	0.0000	0.0000	0.6161
Cu	0.5000	0.5000	0.8839
Cu	0.5000	0.5000	0.1161
Al	0.0000	0.5000	0.2500
Al	0.0000	0.5000	0.7500
Al	0.5000	0.0000	0.2500
Al	0.5000	0.0000	0.7500

Table C.16. Atomic coordinates and unit cell parameters for GGA-DFT optimized anti-$CaCu_2Al_2$

cell vectors	**a**	**b**	**c**
	4.3654	0.0000	0.0000
	0.0000	4.3654	0.0000
	0.0000	0.0000	9.7954
element	*x*	*y*	*z*
Ca	0.0000	0.0000	0.0000
Ca	0.5000	0.5000	0.5000
Al	0.0000	0.0000	0.3647
Al	0.0000	0.0000	0.6353
Al	0.5000	0.5000	0.8647
Al	0.5000	0.5000	0.1353
Cu	0.0000	0.5000	0.2500
Cu	0.0000	0.5000	0.7500
Cu	0.5000	0.0000	0.2500
Cu	0.5000	0.0000	0.7500

Table C.17. Atomic coordinates and unit cell parameters for GGA-DFT optimized $Ca_3Cu_{13}Al_{21}$

cell vectors	**a**	**b**	**c**
	8.3680	0.0000	0.0000
	0.0000	8.3680	0.0000
	0.0000	0.0000	8.3680
element	*x*	*y*	*z*
Cu	0.5000	0.5000	0.5000
Cu	0.5000	0.1519	0.1519
Cu	0.5000	0.8481	0.8481
Cu	0.5000	0.8481	0.1519
Cu	0.5000	0.1519	0.8481
Cu	0.1519	0.5000	0.1519
Cu	0.8481	0.5000	0.8481
Cu	0.1519	0.5000	0.8481
Cu	0.8481	0.5000	0.1519
Cu	0.1519	0.1519	0.5000
Cu	0.8481	0.8481	0.5000
Cu	0.8481	0.1519	0.5000
Cu	0.1519	0.8481	0.5000
Ca	0.5000	0.5000	0.0000
Ca	0.0000	0.5000	0.5000
Ca	0.5000	0.0000	0.5000

Al	0.0000	0.0000	0.0000
Al	0.3256	0.3256	0.3256
Al	0.6744	0.6744	0.6744
Al	0.6744	0.6744	0.3256
Al	0.3256	0.3256	0.6744
Al	0.6744	0.3256	0.6744
Al	0.3256	0.6744	0.3256
Al	0.3256	0.6744	0.6744
Al	0.6744	0.3256	0.3256
Al	0.2431	0.2431	0.0000
Al	0.7569	0.7569	0.0000
Al	0.7569	0.2431	0.0000
Al	0.2431	0.7569	0.0000
Al	0.0000	0.2431	0.2431
Al	0.0000	0.7569	0.7569
Al	0.0000	0.7569	0.2431
Al	0.0000	0.2431	0.7569
Al	0.2431	0.0000	0.2431
Al	0.7569	0.0000	0.7569
Al	0.2431	0.0000	0.7569
Al	0.7569	0.0000	0.2431

Table C.18. Atomic coordinates and unit cell parameters for GGA-DFT optimized $Ca_3Cu_7Al_{27}$

cell vectors	**a**	**b**	**c**
	8.5501	-0.0411	-0.0411
	-0.0411	8.5501	0.0411
	-0.0411	0.0411	8.5501
element	*x*	*y*	*z*
Cu	0.5000	0.5000	0.5000
Cu	0.8403	0.5060	0.1597
Cu	0.8403	0.1597	0.5060
Cu	0.4940	0.1597	0.1597
Cu	0.1597	0.4940	0.8403
Cu	0.5060	0.8403	0.8403
Cu	0.1597	0.8403	0.4940
Al	0.5000	0.1331	0.8669
Al	0.5000	0.8669	0.1331
Al	0.8669	0.5000	0.8669
Al	0.1331	0.5000	0.1331

Al	0.8669	0.8669	0.5000
Al	0.1331	0.1331	0.5000
Al	0.0110	0.7628	0.7628
Al	0.9890	0.2372	0.2372
Al	0.0000	0.2326	0.7674
Al	0.0000	0.7674	0.2326
Al	0.2372	0.9890	0.7628
Al	0.7628	0.0110	0.2372
Al	0.7674	0.0000	0.7674
Al	0.2326	0.0000	0.2326
Al	0.7674	0.7674	0.0000
Al	0.2326	0.2326	0.0000
Al	0.2372	0.7628	0.9890
Al	0.7628	0.2372	0.0110
Al	0.0000	0.0000	0.0000
Al	0.6710	0.6707	0.6707
Al	0.3290	0.3293	0.3293
Al	0.3293	0.3290	0.6707
Al	0.6707	0.6710	0.3293
Al	0.3313	0.6687	0.6687
Al	0.6687	0.3313	0.3313
Al	0.6707	0.3293	0.6710
Al	0.3293	0.6707	0.3290
Ca	0.0000	0.5000	0.5000
Ca	0.5000	0.0000	0.5000
Ca	0.5000	0.5000	0.0000

C.3.1 Localized Electron Calibration Procedure

The number of localized electrons used when calculating chemical pressure schemes with *CPpackage2* was calibrated for Cu atoms used in the calculations. For this calibration, ABINIT chemical pressure calculations were done on the structures of both a contracted (0.8 × scale) and expanded (1.2 × scale) unit cell of $CuAl_2$ (own type). Calculations of the Ewald, E_α, and nonlocal components of the energy were done on each of the cells, and the atomic Bader volumes were determined. Next, CP calculations were performed integrating the CP maps within the Bader volumes to obtain net atomic CPs, with the idea that when properly calibrated at these extreme volumes, the macroscopic internal pressures should overwhelm the local differences in coordination. The number of localized Cu electrons was adjusted for the contracted and expanded unit cells until the pressures across all atoms were balanced (see Table C.17). The values for which these pressures were balanced were found to be 4.35678 electrons for the contracted $CuAl_2$ cell (pressures of +307.28 GPa), and 6.66100 electrons for the expanded cell (−16.47 GPa). Averaging these two values gives 5.50889 localized Cu electrons, which was the value used for all further CP calculations. The localized electron counts for other elements were all left to be 0.

Table C.19. Localized electron calibration for Cu in $CuAl_2$

$CuAl_2$	0.8 × scale	1.2 × scale
Cu localized e^-	4.356780	6.661000
Al localized e^-	0.000000	0.000000
Cu net CPs	+307.28 GPa	−16.47 GPa
Al net CPs	+307.28 GPa	−16.47 GPa